

AFRL-MN-EG-TR-2003-7111

Nanoscience Technology

Ronald W. Armstrong

Air Force Research Laboratory

Munitions Directorate

Ordnance Division

Energetic Materials Branch

Eglin AFB, FL 32542-5910



September 2003

FINAL REPORT FOR PERIOD October 2000 – August 2003

DISTRIBUTION A. Approved for public release; distribution unlimited.

AIR FORCE RESEARCH LABORATORY, MUNITIONS DIRECTORATE

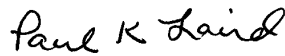
Air Force Materiel Command ■ United States Air Force ■ Eglin Air Force Base

NOTICE

When Government drawings, specifications, or other data are used for any purpose other than in connection with a definitely Government-related procurement, the United States Government incurs no responsibility or any obligation whatsoever. The fact that the Government may have formulated or in any way supplied the said drawings, specifications, or other data, is not to be regarded by implication, or otherwise as in any manner construed, as licensing the holder, or any other person or corporation; or as conveying any rights or permission to manufacture, use or sell any patented invention that may in any way be related thereto.

This report has been reviewed and is approved for publication.

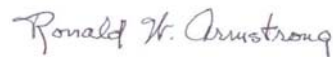
FOR THE COMMANDER



PAUL K. LAIRD
Technical Director,
Ordnance Division



ROBERT L. MCKENNEY Jr.
Technical Advisor
Energetic Materials Branch



RONALD W. ARMSTRONG
Senior Scientist
Energetic Materials Branch

Even though this report may contain special release rights held by the controlling office, please do not request copies from the Air Force Research Laboratory/Munitions Directorate. If you qualify as a recipient, release approval will be obtained from the originating activity by DTIC. Address your request for additional copies to:

Defense Technical Information Center
8725 John J. Kingman Road Suite 0944
Fort Belvoir VA 22060-6218

If your address has changed, if you wish to be removed from our mailing list, or if your organization no longer employs the addressee, please notify AFRL/MNME, 2306 Perimeter Rd., Eglin AFB FL 32542-5910, to help us maintain a current mailing list.

Do not return this report unless contractual obligations or notice on a specific document requires that it be returned.

| | | | | |
|---|--|---|--|--|
| REPORT DOCUMENTATION PAGE | | | Form Approved OMB No. 0704-0188 | |
| Public reporting burden for this collection of information is estimated to average 1 hour per response, including the time for reviewing instructions, searching existing data sources, gathering and maintaining the data needed, and completing and reviewing the collection of information. Send comments regarding this burden estimate or any other aspect of this collection of information, including suggestions for reducing this burden, to Washington Headquarters Services, Directorate for Information Operations and Reports, 1215 Jefferson Davis Highway, Suite 1204, Arlington, VA 22202-4302, and to the Office of Management and Budget, Paperwork Reduction Project (0704-0188), Washington, DC 20503. | | | | |
| 1. AGENCY USE ONLY (Leave blank) | | 2. REPORT DATE September 2003 | | 3. REPORT TYPE AND DATES COVERED Final Report October 2000 – August 2003 |
| 4. TITLE AND SUBTITLE Nanoscience Technology | | | 5. FUNDING NUMBERS PE: 61102F PR: 2306 TA: AM WU: 01 | |
| 6. AUTHOR(S) Ronald W. Armstrong | | | | |
| 7. PERFORMING ORGANIZATION NAME(S) AND ADDRESS(ES) Air Force Research Laboratory/Munitions Directorate Ordnance Division Energetic Materials Branch (AFRL/MNME) Eglin AFB FL 32542-5910 Technical Advisor: Dr. Robert L. McKenney Jr. | | | 8. PERFORMING ORGANIZATION REPORT NUMBER AFRL-MN –EG-TR-2003-7111 | |
| 9. SPONSORING/MONITORING AGENCY NAME(S) AND ADDRESS(ES) Same as Block 7 | | | 10. SPONSORING/MONITORING AGENCY REPORT NUMBER Same as Block 8 | |
| 11. SUPPLEMENTARY NOTES | | | | |
| 12a. DISTRIBUTION/AVAILABILITY STATEMENT DISTRIBUTION A: Approved for public release; distribution unlimited | | | 12b. DISTRIBUTION CODE | |
| 13. ABSTRACT (Maximum 200 words) This technical report is a compilation of unclassified articles, presentations, briefings, etc., produced by R.W. Armstrong, Senior Scientist, AFRL/MNME, mostly in collaboration with Air Force Research Laboratory, Munitions Directorate, Energetic Materials Branch and external national and international colleagues, during the three year period: October 2000 through August 2003. The topical items are mostly centered on dislocation mechanics model descriptions of the total deformation and cracking behaviors of energetic materials and/or structural metals, in the latter case, subjected to high rate loading conditions as experienced in explosive detonations. Additional items referenced are: (1) the forthcoming textbook in print "Deformable Bodies and Their Material Behaviors", co-authored with Henry W. Haslach, Jr.; and, (2) an article on "The Seeds of Tornado Prevention", co-authored with Joseph G. Glenn, and associated with the listed patent disclosure "Tornadic Disruption Through Nanometric Sized Cloud Seeding". The latter items represent a "spin-off" connection of Eglin Air Force Base research interest in the strength and energy release rate properties of energetic/reactive nanomaterials, as shown here to relate to an appreciable number of the described items. | | | | |
| 14. SUBJECT TERM Dislocation Mechanics, Energetic Crystals, Constitutive Equations, Plastic Deformation, Cracking and Fracture, Micro-to-Nano-Structural Modeling, Hot Spots, Shock Deformations, Crystal/Grain Size Effects, Atomic Force Microscopy, Hardness Testing, Nanometric Material Properties, X-ray Diffraction. | | | 15. NUMBER OF PAGES 194 | |
| | | | 16. PRICE CODE | |
| 17. SECURITY CLASSIFICATION OF REPORT UNCLASSIFIED | 18. SECURITY CLASSIFICATION OF THIS PAGE UNCLASSIFIED | 19. SECURITY CLASSIFICATION OF ABSTRACT UNCLASSIFIED | 20. LIMITATION OF ABSTRACT SAR | |

PREFACE

This report was prepared by the Energetic Materials Branch of the Ordnance Division, Air Force Research Laboratory, Munitions Directorate (AFRL/MNME), Eglin Air Force Base, Florida 32542-5910, and covers work performed during the period from October 2000 through August 2003.

ACKNOWLEDGMENTS

It is a great pleasure for me to thank my collegial colleagues at the Air Force Research Laboratory, Munitions Directorate, Energetic Materials Branch, Eglin Air Force Base, for the considerable support received during my happy three-year tenure and, particularly, I want to thank Ms. Karen Clayton and Mr. Byron Allmon, for their generously-supplied assistance, and, also, Mr. J. Greg Glenn, for involving me in his project "Disruption of a Vortex".

Table of Contents

| <u>Title</u> | <u>Page</u> |
|---|-------------|
| R. W. Armstrong Biography..... | 1 |
| List of Articles/Presentations/Briefings/etc. during 10/2000 through 9/2003..... | 3 |
| Grain size dependent alumina fracture mechanics stress intensity (AAC/PA 01-098)..... | 11 |
| Micro-to-nano structural modeling of composite material deformation properties (AAC/PA 01-277)..... | 18 |
| Air Force research in nano-energetics – potential advantages and challenges (AAC/PA 01-130)..... | 20 |
| Nanoscience mechanics of materials (AAC/PA 01-367)..... | 47 |
| The power of energetic nanomaterials (AAC/PA 01-504)..... | 53 |
| Dislocation mechanics based constitutive relations for dynamic deformation of polycrystals (Some charts contain data from publications in the open literature prior to MNME appointment and others are cleared via AAC/PA 01-361, -02-287, and -02-291)..... | 55 |
| The power (and strength) of energetic/reactive nanomaterials (Some charts contain data from from publications in the open literature prior to MNME appointment, one chart approved by NSWC IH (Log number not available), and others are cleared via AAC/PA 01-504, -02-404, -02-287, -01-502, -02-291, -02-301, and -01-098)..... | 67 |
| Enhanced propellant combustion with nanoparticles (AAC/PA 02-401)..... | 89 |
| Grain size dependence of shock-induced twinning stresses for Armco iron (AAC/PA 02-291)..... | 92 |
| Dislocation mechanics aspects of impact/shock initiation of detonation (AAC/PA 02-291).... | 98 |
| Dislocations in energetic crystals (AAC/PA 01-502)..... | 104 |
| Crystal imperfections seen by x-ray diffraction topography (AAC/PA 02-551)..... | 150 |
| The seeds of tornado prevention (AAC/PA03-187)..... | 160 |
| Comparative model x-ray diffraction characteristics of RDX and aluminum (AAC/PA 03-272)..... | 169 |
| Coating and recrystallization of energetic/reactive nanomaterials (AAC/PA 03-361)..... | 173 |

| | |
|---|-----|
| The Power and Strength of Energetic/Reactive Nanomaterials (AAC/PA 03-269)..... | 174 |
| Presentation: Dislocation mechanics activities (AAC/PA 02-178 and –02-287)..... | 176 |



BIOGRAPHY

UNITED STATES AIR FORCE



DR. RONALD W. ARMSTRONG

Dr. Ronald W. Armstrong, a member of the scientific and professional cadre of senior executives, is Senior Scientist in Energetic Materials, Munitions Directorate, Air Force Research Laboratory, Eglin Air Force Base, Fla. He is responsible for contributing technical leadership to the Air Force basic research mission of sustaining superiority in the science and engineering of energetic and related materials properties and performances. In this activity, he provides technical reviews, assesses programs, establishes research strategies for new study areas, and performs theoretical and experimental research. He interacts with other Air Force and government agencies relating to energetic material technologies, and promotes collaboration with foreign governments and organizations, other services and agencies, universities and industry, as relevant to the directorate's thrusts and long-range goals involving energetic materials and their uses. Research topics include fundamental aspects of the mechanics, physics and chemistry of high explosives; the mechanical and initiation behavior of nanoparticle systems; and the high-deformation-rate and shock behavior of condensed matter.



Dr. Armstrong has spent sabbatical leave, summer and consulting appointments at U.S. Steel Research Laboratory, Monroeville, Pa.; Oak Ridge National Laboratory, Tenn.; Lawrence Livermore National Laboratory, Calif.; Institute for Defense Analyses, Washington, D.C.; and the United Technologies Research Center, East Hartford, Conn. Additional appointments include the U.S. National Science Foundation, Science Education Directorate, Bethesda, Md.; Naval Surface Weapons Center, Silver Spring, Md.; National Institute of Standards and Technology, Gaithersburg, Md.; Naval Research Laboratory, Washington, D.C.; U.S. Office of Naval Research, London, England; University of Cambridge, England; and the University of Strathclyde, Glasgow, Scotland. Other appointments include the Naval Ship Research and Development Center, Annapolis, Md.; Laboratory for Physical Sciences, College Park, Md.; Johns Hopkins University, Baltimore, Md.; and the Naval Surface Warfare Center, Indian Head, Md.

During his career, Dr. Armstrong published approximately 275 research periodical and book articles, including 48 invited articles. He has edited several books, has been awarded two patents, and has organized a number of national and international conferences in association with colleagues and students.

EDUCATION

1955 Bachelor of engineering science degree, Johns Hopkins University, Baltimore, Md.
 1957 Master of science degree in metallurgical engineering, Carnegie Institute of Technology, Pittsburgh, Pa.
 1958 Doctor of philosophy degree in metallurgical engineering, Carnegie Institute of Technology, Pittsburgh, Pa.

CAREER CHRONOLOGY

1. 1958 - 1959, DSIR post-doctoral fellow, Houldsworth School of Applied Science, Leeds University, England
2. 1959 - 1964, research metallurgist, Westinghouse Research Laboratory, Pittsburgh, Pa.
3. 1964 - 1965, Westinghouse sabbatical fellow, CSIRO Division of Tribophysics, University of Melbourne, Australia
4. 1965 - 1968, Associate Professor, Brown University, Providence, R.I. (1966 - 1968, Associate Professor with tenure, Brown University)
5. 1968 - 1999, Professor, with tenure, University of Maryland, College Park, Md.

6. 1999 - 2000, Professor Emeritus and Director, Center for Energetic Concepts Development, University of Maryland, College Park, Md.
7. 2000 - present, Senior Scientist in Energetic Materials, Munitions Directorate, Air Force Research Laboratory, Eglin Air Force Base, Fla.

AWARDS AND HONORS

1995 Honorary member, Materials Research Society of India
1996 Honorary member, Indian Institute of Metals

PROFESSIONAL MEMBERSHIPS AND ASSOCIATIONS

American Society for Materials
American Crystallographic Association
American Physical Society
Materials Research Society
Reviewer, Journal of Applied Physics; Acta Materialia; Philosophical Magazine; International Journal of Fracture; Metallurgical Transactions; Scripta Materialia; Materials Science and Engineering; Mechanics of Materials; and Nanostructured Materials

(Current as of January 2002)

**List of Articles/Presentations/Lectures/Briefings/Graduate Degree
Associations/Patent Disclosure/Associated Symposia**

A. Documented Scientific Articles/Presentations

I. Previously listed publications, 2001-2002 (AFRL-MN-EG-2002-7002)

1. J. Sharma, R.W. Armstrong, W.L. Elban, C.S. Coffey, and H.W. Sandusky, "Nanofractography of shocked RDX explosive crystals with atomic force microscopy (AFM)", *Applied Physics Letters*, **78**, 457 (2001).
2. R.W. Armstrong, "Grain size dependent alumina fracture mechanics stress intensity", *International Journal of Refractory Metals and Hard Materials*, **19**, 251 (2001) (AAC/PA 01-098).
3. *R.W. Armstrong and F.J. Zerilli, "Dislocation aspects of shock-wave and high strain-rate phenomena", in Fundamental Issues and Applications of Shock-Wave and High-Strain-Rate Phenomena, edited by K.P. Staudhammer, L.E. Murr and M.A. Meyers, (Elsevier Science Limited, London, 2001), Chapter 15, p. 115.
4. R.W. Armstrong, M.P. Kramer, W.H. Wilson, and F.J. Zerilli, "Micro-to-nano structural modeling of composite material deformation properties", in Eighth International Conference on Composites Engineering (ICCE/8), edited by D. Hui, (University of New Orleans, LA, 2001) p. 41 (AAC/PA 01-277).
5. R.W. Armstrong, C.F. Clark, and W.L. Elban, "Influence of microcracking on pressure dependent energetic crystal combustion", in Combustion of Energetic Materials, edited by K.K. Kuo and L.T. DeLuca, (Begell House, Inc., N.Y., 2002), p. 354.
6. J. Sharma, C.S. Coffey, R.W. Armstrong, W.L. Elban, and S.M. Hoover, "Sub-molecular fracture steps in shock-shattered RDX crystals and follow-on nano-indentation evaluation of early stage plasticity", in Shock Compression of Condensed Matter - 2001, edited by M.D. Furnish, N.N. Thadhani, and Y. Horie, (American Institute of Physics Press, N.Y., 2002), Conference Proceedings 620, Part 1, p. 657.
7. F.J. Zerilli and R.W. Armstrong, "Thermal activation constitutive model for polymers applied to polytetrafluoroethylene (PTFE)", in Shock Compression of Condensed Matter - 2001, edited by M.D. Furnish, N.N. Thadhani, and Y. Horie, (American Institute of Physics Press, N.Y., 2002), Conference Proceedings 620, Part 2, p. 657.
8. *R.W. Armstrong, H.L. Ammon, W.L. Elban, and D.H. Tsai, "Investigation of hot spot characteristics in energetic crystals", *Thermochimica Acta*, **384**, 303 (2002).

9. *R.W. Armstrong, "Plasticity: grain size effects", in Encyclopedia of Materials: Science and Technology, (Elsevier Science Publications, N.Y., 2001), p. 7103.

II. Added publications, 2001-2003

10. *F.J. Zerilli and R.W. Armstrong, "Thermal activation based constitutive equations for polymers", *Journal of Physics IV. France*, **10**, 3 (2001).

11. J. Sharma, C.S. Coffey, R.W. Armstrong, W.L. Elban, and M.Y.D. Lanzerotti, "AFM observations of growth sector structure on a cleaved RDX crystal", *Chemical Physics (Russian)*, **20**, 50 (2001).

12. R.W. Armstrong and F.J. Zerilli, "Dislocation mechanics based analysis of material dynamics behavior: deformation twinning, dynamic recovery, shear instabilities, shock deformation", *Chemical Physics (Russian)*, **20**, 104 (2001).

13. R.W. Armstrong, G.P. Chambers, M.A. Erickson-Natishan, H.W. Sandusky, M. Wagenhofer, and F.J. Zerilli, "Deformation properties of Al-Mg alloy 5086 in laboratory and explosive tests", *Materials Science Forum*, (Trans Tech Publications, SW, 2002) **331-337**, p. 501.

14. *F.J. Zerilli and R.W. Armstrong, "Dislocation mechanics/microstructural based descriptions of strength properties of metals and alloys", THERMEC 2000, (Elsevier Science Publications, N.Y., 2001), CD-ROM.

15. *W.H. Wilson, M.P. Kramer, and R.W. Armstrong, "Air Force research in nano-energetics - potential advantages and challenges", American Chemical Society (ACS) Symposium on Defense Applications of Nanomaterials and Nanoenergetics, 2001, CD-ROM, Presentation 1-2 (AAC/PA 01-130).

16. *R.W. Armstrong, "AFRL strategic workshop on nanoscience and nanotechnology", Universal Technology Corporation Workshop, Dayton, OH, 2001, CD-ROM (Proprietary).

17. R.W. Armstrong, "Nanoscience mechanics of materials (1)", AFOSR Joint Metallic and Ceramic Materials Programs Review: Metallic Materials, edited by C.S. Hartley and J. Fuller, (AFOSR, Arlington, VA, 2001), p.8 (AAC/PA 01-367).

18. *R.W. Armstrong, "Nanometric aspects of energetic crystal properties/testing", Nanotechnology at the Interface of Information Technology, Program and Abstracts, edited by P. Vashishta, (Louisiana State University, Baton Rouge, LA, 2002), p. 24.

19. *R.W. Armstrong and F.J. Zerilli, "Dislocation mechanics based description of dynamic deformation and fracturing", in Contemporary Research in Theoretical and Applied Mechanics, Proceedings, edited by R.C. Batra and E.G. Henneke, (Virginia Polytechnic and State University, Blacksburg, VA, 2002), p. 94.

20. R.W. Armstrong, K.L. Kline, M.P. Kramer, and W.H. Wilson, “The power of energetic nanomaterials”, in Twenty-Ninth International Pyrotechnics Seminar Proceedings, edited by F.J. Schelling, (IPSUSA, 2002, CO) p. 239 (AAC/PA 01-504).
21. R.W. Armstrong, “Nanoscience mechanics of materials (2)”, in AFOSR Joint Metallic and Ceramic Materials Programs Reviews, (AFOSR, Arlington, VA, 2002), CD-ROM.
22. *R.W. Armstrong, “Dislocation mechanics based constitutive relations for dynamic deformation of polycrystals”, in U.S. - Korea Workshop on Advances in Metallic Structural Materials, edited by K.C. Goretti, S.L. Semiatin, and C.S. Hartley, AFOSR/AOARD, Kehee, HI, 2003), CD-ROM (Some charts contain data from publications in the open literature prior to MNME appointment and others are cleared via AAC/PA 01-361, -02-287, and -02-291).
23. *R.W. Armstrong, “The power (and strength) of energetic/reactive nanomaterials”, in 2003 Nano Materials for Aerospace Applications Symposium: Expanding the Envelope, (Corpus Christi, TX, 2003), CD-ROM (Some charts contain data from publications in the open literature prior to MNME appointment and others are cleared via AAC/PA 01-504, -02-404, -02-287, -01-502, -02-291, -02-301, and -01-098).
24. R.W. Armstrong, B. Baschung, D.W. Booth, and M. Samirant, “Enhanced propellant combustion with nanoparticles”, *Nano Letters*, **3**, 253 (2003) (AAC/PA 02-401).

III. Articles in process of publication

25. *R.W. Armstrong, W. Arnold, and F.J. Zerilli, “Grain size dependence of shock-induced twinning stresses for Armco iron”, *Chemical Physics (Russian)*, 2003 (AAC/PA 02-291).
26. *R.W. Armstrong, “Dislocation mechanics aspects of impact/shock initiation of detonation”, *Chemical Physics (Russian)*, 2003, in print (AAC/PA 02-291).
27. *R.W. Armstrong and W.L. Elban, “Dislocations in energetic crystals”, in Dislocations in Solids, edited by F.R.N. Nabarro and J.P. Hirth, (Elsevier Science Limited, London, 2003), **12**, in print (AAC/PA 01-502).
28. R.B. Clough, S.C. Webb, and R.W. Armstrong, “Dynamic hardness measurements using a dropped ball: with application to 1018 steel”, *Materials Science and Engineering*, 2003, in print.
29. R.W. Armstrong, “Crystal imperfections seen by x-ray diffraction topography”, in Nano and Microstructural Design of Advanced Materials, edited by M.A. Meyers, R.O. Ritchie, and M. Sarikaya, (Elsevier Science Publications, N.Y., 2003) (AAC/PA 02-551).

30. H.W. Haslach, Jr., and R.W. Armstrong, "Deformable Bodies and Their Deformation Behaviors", (John Wiley and Sons, Publishers, N.Y., 2003), in print.

IV. Articles/Presentations submitted/to be submitted

31. M.Y.D. Lanzerotti, J. Sharma, and R.W. Armstrong, "AFM studies of fracture surfaces of composition B energetic materials", article submitted to *Metallurgical and Materials Transactions*, 2003.

32. J.G. Glenn and R.W. Armstrong, "The seeds of tornado prevention", article submitted to *Atmospheric Science Letters*, 2003 (AAC/PA 03-187).

33. P. Rodriguez, R.W. Armstrong, and S.L. Mannan, "The dependence of activation area on grain size in cadmium", article submitted to *Transactions of the Indian Institute of Metals*, 2003.

34. K.L. Kline, R.W. Armstrong, D.W. Richards, and M.P. Kramer, "Comparative model x-ray diffraction characteristics of RDX and aluminum", article submitted to Shock Compression of Condensed Matter - 2003, American Institute of Physics Meeting, Portland, OR, July 20-25, 2003 (AAC/PA 03-272).

35. M.P. Kramer, A.E.D.M. van der Heijden, D.W. Richards, W.H. Wilson, R.W. Armstrong, and A.C. van der Steen, "Coating and recrystallization of energetic/reactive nanomaterials", abstract submitted for the Sixth International Workshop on Crystal Growth of Organic Materials (6-ICGOM), Glasgow, U.K., August 17-21, 2003 (AAC/PA 03-361).

36. *R.W. Armstrong, M.P. Kramer, and W.H. Wilson, "The Power and Strength of Energetic/Reactive Nanomaterials", abstract submitted for the International Workshop on Novel Energetic Materials and Applications (9-IWCP), Lerica, La Spezia, IT, September 14-18, 2003 (AAC/PA 03-269).

37. W.R. Grise and R.W. Armstrong, "1-D to 3-D dislocation pile-ups adiabatically released", abstract submitted for The Minerals, Metals, and Materials Society (TMS) 3-Dimensional Materials Science Symposium, Chicago, IL, November 9-12, 2003.

38. *R.W. Armstrong, H. Conrad, and F.R.N. Nabarro, "Meso-to-nano-scopic polycrystal/composite strengthening", abstract submitted for the Materials Research Society (MRS) Symposium Q: Mechanical Properties of Nanostructured Materials and Nanocomposites, Boston, MA, December 1-5, 2003.

39. M.Y.D. Lanzerotti, J. Sharma, and R.W. Armstrong, "Nanofractography of composition B fracture surfaces with AFM", abstract submitted for the Materials Research Society (MRS) Symposium AA: Synthesis, Characterization, and Properties of Energetic/Reactive Nanomaterials, Boston, MA, December 1-5, 2003.

40. W.R. Grise and R.W. Armstrong, “Hot spots from crystal size dependent dislocation pile-up avalanches in energetic materials”, abstract submitted for the Materials Research Society (MRS) Symposium AA: Synthesis, Characterization, and Properties of Energetic/Reactive Nanomaterials, Boston, MA, December 1-5, 2003.
41. L. Ferranti, Jr., R.W. Armstrong, and Naresh N. Thadhani, “Elastic/plastic deformation behavior in a continuous ball indentation test”, draft article prepared for submittal to Materials Science and Engineering A, August, 2003.

B. Lectures/Briefings

1. “Energetic crystal properties and model analyses”; Invitational Workshop on Nano-, energetics, University of Florida Graduate Engineering and Research Center, Shalimar, FL; November 16, 2000.
2. * “Dislocation mechanics/microstructural descriptions of strength properties of metals and alloys”; THERMEC’2000, International Conference on Processing and Manufacturing of Advanced Materials, Las Vegas, NV; December 5, 2000 (see **A.II.14**).
3. “Nanosciences technology”; AFOSR Program Officers’ Visit, Eglin Air Force Base, FL; February 8, 2001.
4. * “Characterization of electronic device and energetic crystal properties” (presented by M. Dudley); International Workshop on Properties and Characterizations of Technologically Important Single Crystals (PCSC – 2001); New Delhi, India; February 27, 2001.
5. “Grain size dependent alumina fracture mechanics stress intensity”; International Conference on the Science of Hard Materials (ICSHM7); Ixtapa, Mexico; March 5, 2001 (see **A.I.2**) (AAC/PA 01-098).
6. * “Air Force research in nano-energetics - potential advantages and challenges” (presented by W.H. Wilson); 221st American Chemical Society National Meeting, San Diego, CA; April 3, 2001 (see **A.II.15**) (AAC/PA 01-130).
7. “Nanoenergetics” (with W.H. Wilson and M.P. Kramer); AFOSR visit of Lyle Schwartz, AFRL/MNME, Eglin Air Force Base, FL; April 10, 2001.
8. “Nanoscience technology”, AFOSR Presentation, Arlington, VA; May 29, 2001.
9. * “AFRL strategic workshop on nanoscience and technology”, Universal Technology Corporation, Dayton, OH; May 30, 2001 (Proprietary).
10. * “Energetic crystal research activity”; Institut Saint-Louis (ISL), France; June 18, 2001.

11. *“Constitutive equation research activity”; Fraunhofer Institut für Kurzzeiddynamik, Ernst-Mach-Institut (EMI), Freiburg, Germany; June 19, 2001.
12. (Poster) “Nanoscience mechanics”; AFOSR Joint Metallic and Ceramic Materials Programs Review, Snowbird, UT; August 21, 2001 (see **A.II.17**) (AAC/PA 01-367).
13. *“Impact of nanoenergetics”; National Academy of Science/National Research Council (NAS/NRC) Committee on Implications of Energetic Micro- and Nano-Technologies; Albuquerque, NM; November 8, 2001; listed in “Implications of Emerging Micro- and Nanotechnologies”, National Research council of The National Academies, Washington, D.C., 2002, p.241.
14. “6.1 nanoenergetics”; Scientific Advisory Board (SAB) Review, High Explosives Research and Development (HERD), Eglin Air Force Base, FL; November 29, 2001 (Proprietary).
15. “Advanced energetics briefing”; General Chedister, Air Armament Command (AAC), High Explosives Research and Development (HERD), Eglin Air Force Base, FL; January 3, 2002 (Proprietary).
16. *“Nanometric aspects of energetic crystal properties/testing”; Mardi Gras: Biotechnology Conference, Louisiana State University, Baton Rouge, LA; February 8, 2002 (see **A.II.18**).
17. *“Armco iron twinning/grain size dependence”; Shock Wave Processes in Condensed Matter, Edinburgh, Scotland; May 20, 2002 (see **A.III.25**) (AAC/PA 02-291).
18. *“Model studies of explosive crystal impacts/shocks”; Shock Wave Processes in Condensed Matter, Edinburgh, Scotland; May 21, 2002 (see **A.III.26**) (AAC/PA 02-291).
19. *“Dislocation mechanics activities”; Physics and Chemistry of Solids Colloquium Series, Cavendish Laboratory, University of Cambridge, U.K., May 30, 2002 (AAC/PA 02-178 and -02-287).
20. *“Discussant overview: energetic nanomaterials”; Gordon Research Conference: Energetic Materials, Tilton, NH; June 16, 2002.
21. *“Dislocation mechanics for dynamic plasticity/fracturing”; 14th National Theoretical and Applied Mechanics Congress, Virginia Polytechnic Institute and State University, Blacksburg, VA; June 24, 2002 (see **A.II.19**).
22. (Poster) “The power of nano-energetics” (presented by M.P. Kramer); 29th International Pyrotechnics Seminar, Westminster, CO; July 16, 2002 (see **A.II.20**).

23. (Poster) “Nanoscience mechanics of materials” (presented by S.L. Semiatin); AFOSR Joint Materials Programs Reviews, Bar Harbor, ME; August 10, 2002 (see **A.II.21**).
24. “Crystal imperfections seen by x-ray topography”; The Minerals, Metals, and Materials Society (TMS) Fall Meeting, Columbus, OH; October 9, 2002 (see **A.III.29**) (AAC/PA 02-551).
25. *(Poster) “Dislocation mechanics based constitutive equations”, US – Korea Workshop on Advances in Metallic Structural Materials, AFOSR Advanced Computing Center, Kehei, Maui, HI; January 21, 2003 (see **A.II.22**) (AAC/PA 01-361, -02-287, and -02-291).
26. * “The power of energetic/reactive nano-materials”; 2003 Nano Materials for Aerospace Applications; Expanding the Envelope, Corpus Christi, TX; January 29, 2003 (see **A.II.23**) (AAC/PA 01-504, -02-404, -02-287, -01-502, -02-291, -02-301, and -01-098).
27. * “The wonders of high strain rate dislocation mechanics?”; Chemistry Division, Los Alamos National Laboratory, Los Alamos, NM; February 19, 2003.

* invited participations

C. Degree Associations

1. External examiner: Ph.D. thesis of Dr. John Corley, “Characterization and modeling of the dynamic mechanical properties of a particulate composite material”, Universitat der Bundeswehr Munchen, Germany, June 28, 2002.
2. Advisory Committee: M.Sc. thesis of Kinnan L. Kline, “Comparative Model Powder X-ray Diffraction Characteristics of Aluminum and Cyclotetramethylene-tetranitramine (RDX)”, University of Florida, Graduate Engineering and Research Center, November 26, 2002.

D. Patent Disclosure

J.G. Glenn and R.W. Armstrong, “Tornado disruption through nanometric sized cloud seeding”, OMB-No. 900 – 0095, May, 2002.

E. Associated Symposia

1. M.P. Kramer, W.H. Wilson and R.W. Armstrong, “Invitational Workshop on Nano-energetics”, University of Florida, Graduate Engineering and Research Center, Shalimar, FL, November 15-16, 2000.

2. G.T. Gray, M.A. Meyers, N.N. Thadhani, and K.S. Vecchio, "Symposium in honor of Professor Ronald W. Armstrong, Dynamic deformation: constitutive modeling, grain size, and other effects", The Minerals, Metals, and Materials Society (TMS) Annual Meeting, San Diego, CA, March 3-5, 2003.
3. N.N. Thadhani, R.W. Armstrong, W.H. Wilson, J.J. Gilman, Z. Munir, and R.L. Simpson, co-organizers of Materials Research Society (MRS) Symposium AA: Synthesis, Characterization, and Properties of Energetic/Reactive Nanomaterials, Boston, MA, December 1-5, 2003.



GRAIN SIZE DEPENDENT ALUMINA FRACTURE MECHANICS STRESS INTENSITY

R.W. Armstrong

AFRL/MNME
2306 Perimeter Road
Eglin AFB, FL 32542-5910, U.S.A.

Abstract

Various grain size dependent hardness test results obtained on alumina materials are brought together on a Hall-Petch (H-P) inverse square root of grain diameter basis to illustrate the normal expectation of greater strengthening for finer grained material, not unrelated to the observation that structural ceramic materials are employed often in a very much finer grain size condition than counterpart structural metals and alloys. Here, the H-P dependence is shown to carry over to describing recent, mutually confirming, hardness-based measurements of the fracture mechanics stress intensity of alumina materials at small grain sizes. The somewhat surprising dependence relates to the frequent observation that an increase in plastic flow strength of a structural material is associated with a decrease in its fracture toughness. For the case of strengthening by grain size refinement, however, the fracture stress of a material is raised more than the plastic flow stress and so greater local plastic work is required for fracturing.

1. Hardness/grain size/cracking dependencies

Considerable results are available to show that the hardnesses of both cubic and non-cubic ceramic materials are greater for materials of finer polycrystalline grain sizes, for example, as established from various measurements made on cubic magnesia and rhombohedral alumina polycrystals. The dependence is often demonstrated on an inverse square root of grain diameter basis as shown for polycrystalline alumina materials in Figure 1 that has been adapted from measurements reported by Rice, Wu and Borchelt [1]. The adapted Figure contains from the original work only the Vickers hardness measurements reported at two applied load values for mainly hot pressed alumina material, as open and closed triangle points, but to which have been added newer measurements reported by Krell [2] for pressureless sintered material (open circle points) and by Franco, Roberts and Warren [3] for three grain sizes (closed circle points). Franco et al. employed pressureless sintering for their two largest grain size materials and hot pressing during sintering for their smallest grain size material.

The lines in Figure 1 are those drawn by Rice et al. [1] for their measurements at the indicated applied loads of 100 and 500 g. Rice et al. associated the lowest hardness values obtained at 500 g, shown at the break in the hardness lines, with cracking and observed crack sizes being comparable to the material grain size. The upper closed circle points of Franco et al. were obtained at a smallest applied load of 500 g and the lower closed circle points were obtained as essentially constant hardness values over a range of loads from 1.0 to 25 kg. Cracking was reported for all of the measurements reported by Franco et al., with comparable crack and hardness indentation diagonal lengths occurring at the smallest 500g load. The results shown from Krell, for ground surfaces on pure alumina microstructures, were obtained at a load of 10 kg. Krell obtained slightly lower hardnesses at the same applied load for polished materials.

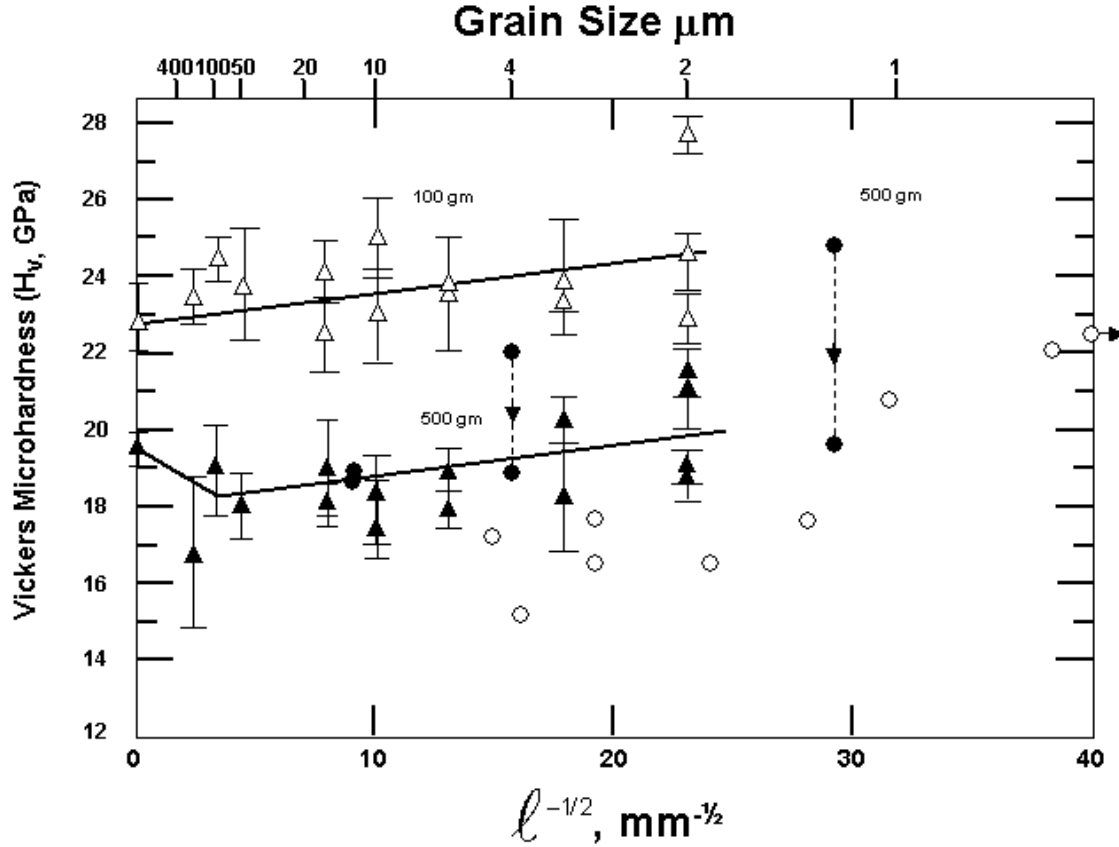


Fig. 1. The Vickers microhardness dependence on grain size, adapted from results reported by Rice, Wu and Borchelt [1], and incorporating additional measurements from Krell [2] and Franco, Roberts and Warren [3].

The new results added to Figure 1 appear to be in agreement with the emphasis given by Rice et al. to the importance of cracking in affecting the determined hardness values. A similar effect of cracking on reducing the hardness of MgO single crystals was demonstrated for reported single crystal measurements [4]. However, such cracking is only one consideration relating to the increase in hardness that occurs with reduced applied load. Detailed measurements made on residual indentations in the {100} cleavage surface of an MgO crystal [5] and computation of the expected Hertzian elastic contribution to the load bearing capability [6] have provided evidence for an important elastic influence on this so-called indentation size effect (ISE). Cracking reduces the contribution of elastic recovery to the ISE. Otherwise, the occurrence of controlled indentation cracking experiments has led to the method of indentation fracture mechanics, either by employing Vickers hardness measurements or Hertzian ball-type ring cracking methods for

determining the fracture toughness of alumina polycrystals [3,7]. In the present report, recent indentation fracture mechanics stress intensities determined for both testing methods are shown to follow predictions of an H-P inverse square root of grain diameter dependence [8,9].

2. A Hall-Petch dependence for the fracture mechanics stress intensity.

2.1. Collected experimental results

Franco et al. [3] measured the fracture mechanics stress intensities for their materials by the two methods of Hertzian ring cracking and Vickers indentation tests. For the Hertzian case, well-defined ring cracks were obtained in the minimum load range of 30 to 50 kg applied at a rate of 0.14 mm/min to a 2.5 mm radius alumina sphere. The investigators gave emphasis to smaller individual crack sizes being obtained in the Hertzian tests, say, at about 5 micrometer crack lengths or smaller, as compared to larger crack sizes occurring in the Vickers test results obtained at applied loads of 0.5 to 25 kg. The Vickers measurements showed a decrease in the grain size dependence of the fracture mechanics stress intensity at greater loads until reaching a negligible dependence for crack sizes of about 40 micrometers and thereafter showing a negative H-P dependence.

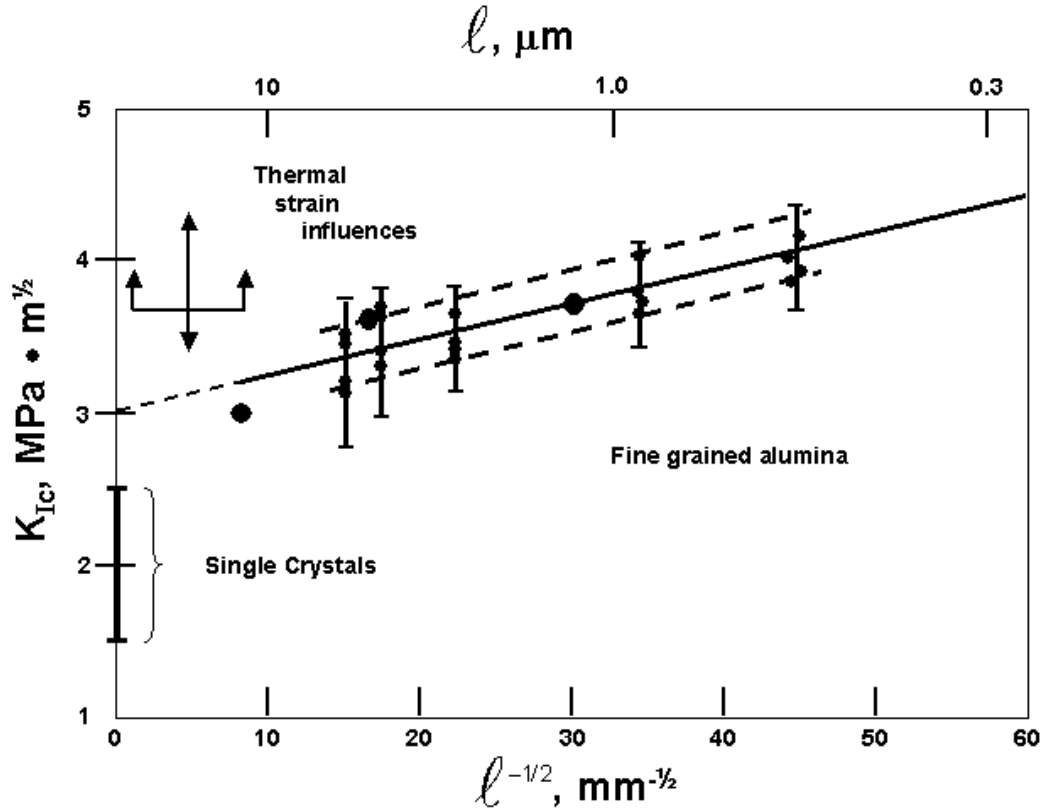


Fig. 2. A Hall-Petch description of the Hertzian-determined indentation fracture mechanics stress intensity dependence on grain size for fine grained alumina as measured by Franco, Roberts and Warren [3] and, for low-load Vickers measurements, comparable measurements reported by Muchtar and Lim [7], also including in the Figure a range of single crystal values reported by Rice [10] along with indication of thermal strain influence complications at large grain sizes.

The Hertzian fracture mechanics stress intensity results obtained by Franco et al. shown in Figure 2 are compared with other Vickers stress intensity determinations reported by Muchtar and Lim [7] for indenter load values of 0.3, 0.5, 1.0 and 2.0 kg. The latter measurements give essentially parallel H-P dependencies that are raised at increasing applied loads. Also shown in Figure 2 along the vertical ordinate axis is a bracketed range of single crystal hardness values reported in a recent compilation by Rice [10]. In the same compilation, widely varying stress intensity values were indicated at larger values of polycrystalline grain diameters, say, greater than ten micrometers, as is meant to be indicated in the Figure by the vertical arrows, and appears attributable to thermal strain influences. The total range in stress intensity values shown in Figure 2 may be compared with a value of $3.7 \text{ MPa}\cdot\text{m}^{1/2}$ quoted by Congleton [11] for dynamic fracturing studies conducted on pre-cracked thin plates.

2.2 Model Hall-Petch interpretation

Returning to Figure 1, it is important that an increase in the alumina yield stress with reduction in grain size is indicated for the H-P type hardness dependence. Generally, an increase in the yield stress of a material is associated with a reduction in the fracture mechanics stress intensity. The reason is that such changes often do not affect the material fracture stress and so, during loading of a pre-cracked tensile specimen, less strain hardening is necessary at the crack tip in order to reach the material fracture stress [9]. For strengthening produced by grain size refinement, however, the yield stress is raised but the fracture stress is raised more on an H-P basis than the yield stress and, so, the counter result of greater strain hardening must occur at the crack tip before the fracture stress is reached. The basis for a greater H-P dependence for the fracture stress, compared to the yield stress, rests on the theoretical association of dislocation coalescence with formation of a crack nucleus.

For alumina, as in the brittle cleavage of steel, microyielding is presumed to occur at the crack tip in order to promote further crack growth and/or to nucleate new cracks at about the same size scale as the grains themselves. Evidence for a substantial plastic work contribution to the experimentally measured fracture mechanics stress intensity comes from evaluation of the theoretical surface energy term. Congleton pointed out that the stress intensity determined value of approximately 18 J/m^2 was far larger than indicated for the theoretical value. Recently, a value of 2.15 J/m^2 has been reported for alumina [12], in agreement with the previous conjecture.

For crack sizes very much larger than the material grain size, the plastic zone size at the tip of the larger crack should connect with the material grain size and, thus, a reversal from the H-P dependence may occur [8]. Thus, the reversed H-P dependence shown by application of the higher loads in the Vickers tests of Franco et al. may be explained on this basis.

3. (Grain/plastic zone) size influences on the flexural strength.

To connect with the grain size dependent stress intensity measurements, several features of the flexural (bend) strength dependence on grain size for variously machined alumina materials are shown on an H-P basis in Figure 3, also adapted from a compilation of measurements reported by Rice [13]; see his Figure 3 that compares a great amount of data and builds onto earlier work. First, in the present Figure 3, the steep line through the origin with slope of $3.5 \text{ MPa}\cdot\text{m}^{1/2}$ was shown to describe the fracture stress dependence on grain size at relatively large grain sizes. The pair of lines with relatively lower slopes and turned down segments at their large grain size ends were chosen to describe two flexural strength features: (1) in the case of the lower line, a lower limiting boundary that was established for smaller grain size fracture strength measurements from a previous survey; and, (2) for the higher segmented line, a chosen dependence for numerous but scattered fracture strength measurements when the plotted grain diameters were determined at the fracture origins. It should be noted that the collected measurements included fracture strength values following the line with steepest slope to a flexural strength value of approximately 600 MPa at a grain size of approximately 35 micrometers.

It seems reasonable to take the steep line in Figure 3 as the fracture stress dependence on Rice's suggestion of the material crack size being determined in depth by one-half of the material grain size, and, on this basis, the slope value of $3.5 \text{ MPa}\cdot\text{m}^{1/2}$ is in reasonable agreement with the stress intensity values

shown in Figure 2. The dashed line of lesser slope through the origin in Figure 3 has been newly computed for a fracture stress dependence on crack size, also taken in depth equal to one-half of the material grain diameter, and with a theoretical value of the stress intensity employing a Young's modulus of 420 GPa and theoretical fracture surface energy of 2.15 J/m²; see the Figure legend. As mentioned earlier, Congleton had pointed out that the measured stress intensity even for rapid fracturing in his macroscopic dynamic fracture tests gave indication of a significant plastic flow contribution to the alumina material fracture toughness, as apparently confirmed on the H-P basis of Figure 3.

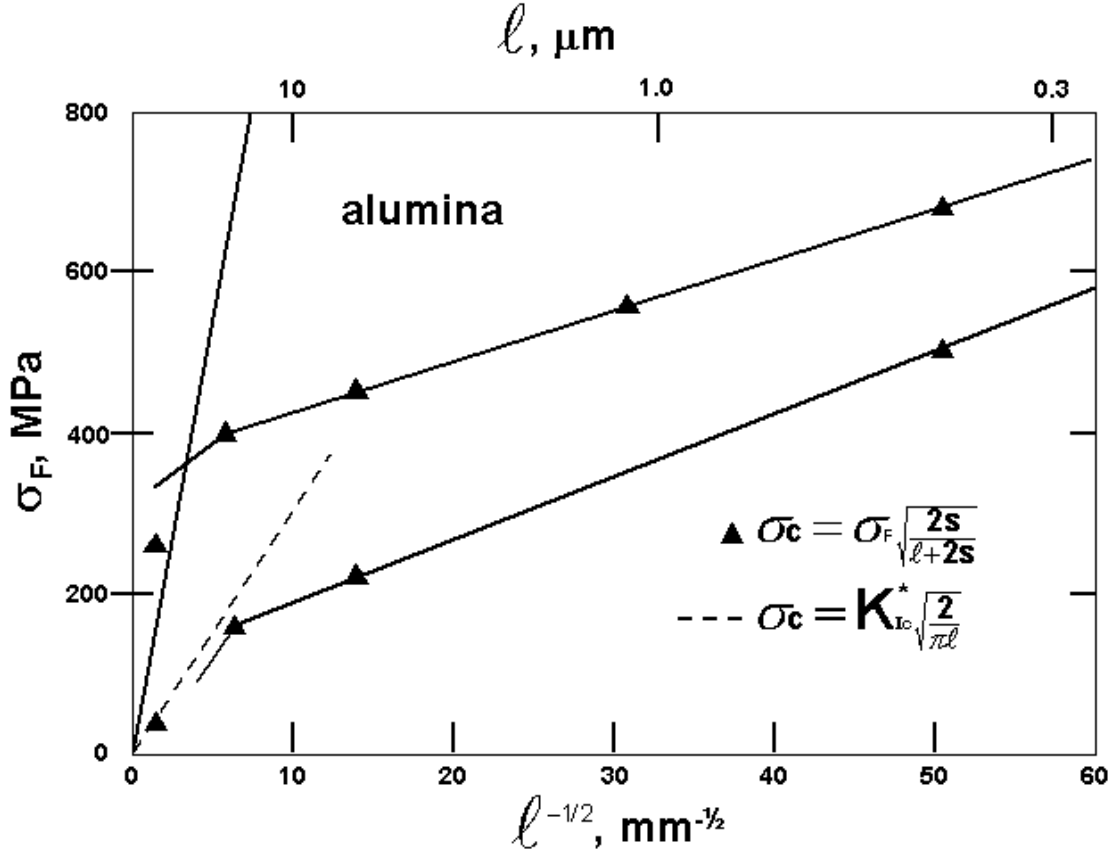


Fig. 3. Linear indications from collected measurements of the flexural (bend) strength dependence on grain size, as adapted from Rice [13], in comparison with: (1) a lower limiting (dashed) theoretical fracture stress dependence on grain size when determining the material crack size; and, (2) a model description fitted to the observed fracture stress dependencies and incorporating influence of a plastic zone size correction at the crack tip.

Also shown in Figure 3, via closed triangular points, are pre-cracked fracture stress values computed in terms of a reference crack-free fracture stress and the material crack radius, c , with an associated plastic zone extension, s , at the crack tip [8,14]; see the legend in Figure 3. For this model description, a limiting small value of s applies for the theoretical surface energy and s becomes increasingly larger to match the greater stress intensity values shown in Figure 2. The higher computed fracture stress (filled triangular) points in Figure 3 were arrived at by a two-step procedure. First, a relevant value of the fracture stress intensity, K , was selected from Figure 2, along with an estimated crack-free fracture stress taken a large grain size from the upper line in Figure 3, to provide an estimated plastic zone size, s . Then, an appropriate pre-cracked fracture stress was computed from the selected crack-free fracture stress and s .

Such pre-cracked plastic- zone-size-determined fracture stresses rapidly converged to the crack-free fracture stress values. The values of s decreased from 0.026 mm at a grain diameter of 0.25 mm to a smallest size of 0.012 mm at the smallest grain size limit of just less than 0.0003 mm in the Figure, thus, indicative for the smallest grain size material of significant microyielding. For the lower triangular points in Figure 3, match was made, first, at the largest grain size, with the dashed theoretical stress intensity line for $K = 1.34 \text{ MPa m}^{1/2}$ and an estimated crack-free fracture stress of 130 MPa to give a plastic zone size, $s = 0.19 \text{ mm}$ for the 0.25mm grain size, and so on.

For the foregoing model description then, the (crack/plastic zone) sizes are shown to tie stress intensity and fracture stresses together, so as to give at large crack sizes, taken approximately equal to the material grain size, a conventional fracture mechanics type dependence on the material grain size; and, at small grain sizes, a plastic zone size substantially larger than the material grain size and so giving an apparent H-P dependence of the fracture stress measurements.

Acknowledgements

Appreciation is expressed to Byron Allmon for help with the construction of Figures and to Robert Sierakowski for directing attention to the recent book by Roy Rice, reference 10.

References

- [1] Rice RW, Wu CCm, Borchelt F. Hardness - grain-size relations in ceramics. J. Amer. Ceram. Soc. 1994;77(10):2539-2553.
- [2] Krell A. Improved hardness and hierarchic influences on wear in submicron sintered alumina. Mater. Sci. Eng. 1995; A209 (1-2):156-163.
- [3] Franco A, Roberts SG, Warren PD. Fracture toughness, surface flaw sizes, and flaw densities in alumina. Acta mater. 1997;45(3):1009-1015.
- [4] Armstrong RW, Elban WL. Cracking at hardness microindentations in RDX explosive and MgO single crystals. Mater. Sci. Eng. 1989; A111:35-43.
- [5] Armstrong RW, Wu CCm. Lattice misorientation and displaced volume for hardness indentations in MgO crystals. J. Amer. Ceram. Soc. 1978; 61:102-106.
- [6] Hammond BL, Armstrong RW. Recovered elastic and plastic strains at residual microindentations in an MgO crystal. Philos. Mag. 1988; 57:41-46.
- [7] Muchtar A, Lim LC. Indentation fracture toughness of high purity submicron alumina. Acta mater. 1998; 46(5):1683-1690.
- [8] Armstrong RW. The (cleavage) strength of pre-cracked polycrystals. Eng. Fract. Mech. 1987;28(5-6):529-538.
- [9] Petch NJ, Armstrong RW. Work-hardening in cleavage fracture toughness. Acta metall. 1989;37(8):2279-2285.
- [10] Rice RW. Mechanical Properties of Ceramics and Composites: Grain and Particle Effects. Marcel Dekker, Inc., NY, 2000:80.
- [11] Congleton J. Crack branching in the fracture of alumina. In: Baker TN, editor. Yield, Flow and Fracture of Polycrystals, Applied Science Publ., London, UK, 1983:101-121.
- [12] Smith JR, Zhang W. Stoichiometric interfaces of Al and Ag with alumina. Acta Mater. 2000;48:4395-4403.

[13] Rice RW. Review: Ceramic tensile strength – grain size relations; grain sizes, slopes and branch intersections. J. Mater. Sci. 1997;32:1673-1692.

[14] Armstrong RW. Grain size: the fabric of (brittle) fracture of polycrystals. In: Taplin DMR, editor. Fracture 1977, Fourth International Conference on Fracture (ICF4), University of Waterloo Press, Waterloo, Ontario, Canada, 1977;4:83-96.

Micro-to-Nano-Structural Modeling of Composite Material Deformation Properties

R.W. Armstrong*, M.P. Kramer*, W.H. Wilson,* and F.J. Zerilli**

*AFRL/MNME, 2306 Perimeter Road, Eglin AFB, FL 32542

**Naval Surface Warfare Center, Indian Head, MD 20640

ABSTRACT

The experimental observation of an inverse square root of grain size influence on the strength properties of reasonably single phase polycrystalline materials has been explained by model calculations of grain boundaries blocking temporarily the egress of dislocation pile-ups in embryonic slip bands or deformation twins [1].

Metallurgical composite connection

Extension of the inverse square root of grain size dependence to metallurgical composite materials has been arguably successful on the basis of determining an effective grain size for the overall composite through measurement of the mean free intercept line length involving both interphase boundaries and grain boundaries [2,3]. Significant applications have been to very small effective grain sizes for patented eutectoid steel (piano) wire [4] and unidirectionally-solidified eutectic, superlattice (candidate turbine blade), materials [5].

Nanoscale strength connection

Extrapolation of the effective grain size analysis to nanoscale dimensions has produced a number of interesting consequences: (i) the achievement of experimental strength levels near to the theoretical limiting strength of defect-free material [6] as shown in Figure 1; (ii) theoretical prediction of discontinuous strength level changes at limiting small grain sizes [7]; and, (iii) suggestion of a reverse trend to effective grain size weakening caused by activation of grain boundary deformation mechanisms at the smallest grain sizes [8]. The last mentioned consideration relates to the observation of effective high temperature creep deformation mechanisms [9].

Thermally-activated flow

Distinction between low-temperature, dislocation-based, model descriptions of viscoplastic behavior

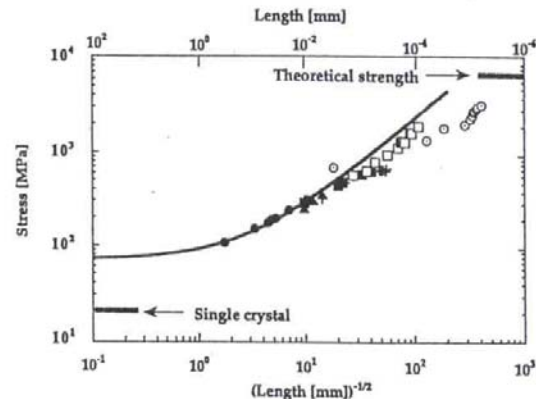


Figure 1. Inverse square root of grain size dependence for iron and steel materials [6].

and higher temperature diffusion-based flow apparently rests on direct consideration in the former case of an appropriate stress influence on the required Gibbs free energy for dislocation activation, G [10]. Such consideration enters generally into the so-called friction resistance force that operates on each dislocation within an embryonic slip band, rather than being an influence on the microstructural stress intensity coefficient of the reciprocal square root of grain size dependence.

The thermally-activated dislocation model description provides for significant differences in crystal-structure-dependent flow, for example, between strain-independent thermal stress terms for iron and other bcc metal deformation as compared with a strain-dependent thermal stress for copper and related fcc metals [11]. Such thermally-activated description has been shown to be applicable, as well, to certain polymer material deformation properties, as shown below in Figure 2 for reported compression results on PMMA [12].

Shear banding

Beyond consideration of the stress-assisted thermal energy influence on individual dislocation or flow

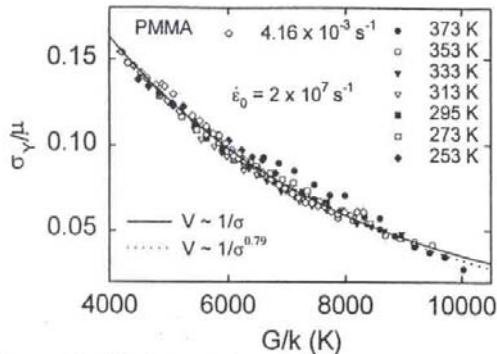


Figure 2. Yield stress/shear modulus ratio versus G/k , [Boltzmann's constant], for PMMA [12].

unit creation and movement, there is the aforementioned important added influence of local stress elevations caused by the collective action of the multiple flow units in the embryonic shear zones blocked at internal obstacles. The latter influence is a minor consideration for aluminum and a major

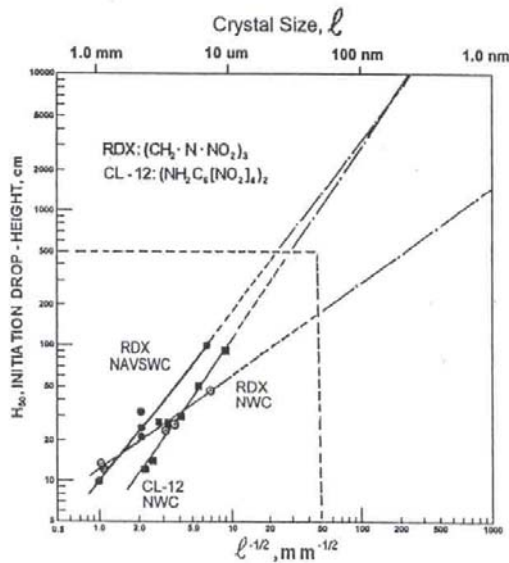


Figure 3. Crystal size dependence of the drop-weight impact initiation of explosives [13].

one for steel, and is even more important for understanding the deformation properties of energetic (explosive) materials, such as RDX (cyclotrimethylenetrinitramine), for which the

mechanical initiation of chemical decomposition in drop-weight impact tests is shown in Figure 3 to be dependent on crystal size [13].

Ductility connection

Although both reduction in crystal or grain size and addition of particles add to material strengthening, the influence on ductility is potentially increased in the former case and clearly reduced in the latter case [14], thus composite material strengthening with particles, even at nanocrystalline grain sizes, is obtained at the price of ductility reduction. One model consideration being further investigated is based on the proposal that the true fracture strain is determined by the particles being brought by plastic deformation to a smaller critical spacing [15].

References

1. RW Armstrong, "Grain size effects in plasticity", in The Encyclopedia of Materials Science and Technology, Elsevier Science Ltd., Oxford, 2001, in press.
2. CT Liu, J Gurland, Trans. ASM **61**, 156 (1968); TMS-AIME **242**, 1535 (1968).
3. E Erginer, J Gurland, Z. Metall. **61**, 606 (1970).
4. JD Embury, RM Fisher, Acta Metall. **14**, 147 (1966).
5. RW Armstrong, FD Lemkey, ER Thompson, in Second Intern. Conf. on "in-Situ" Composites, 2, Xerox Publ., NY, 1976, p. 476.
6. CS Pande, RA Masumura, RW Armstrong, Nanostructured Mater. **2**, 323 (1993).
7. RW Armstrong, YT Chou, RM Fisher, N Louat, Philos. Mag. **14**, 943 (1966).
8. RA Masumura, PM Hazzledine, CS Pande, Acta Mater. **46**, 4527 (1998).
9. RW Armstrong, Canad. Metall. Quart. **13**, 187 (1974).
10. A Seeger, Kristallplastizität, in Handbk. der Physik, VII/2, Crystal Physics II, Springer, Berlin, 1958, p. 541.
11. FJ Zerilli, RW Armstrong, J. Appl. Phys. **61**, 1816 (1987).
12. FJ Zerilli, RW Armstrong, J. Phys. IV France **10**, Pr9-3 (2000).
13. RW Armstrong, CS Coffey, VF DeVost, WL Elban, J. Appl. Phys. **68**, 979 (1990).
14. RW Armstrong, Trans. Indian Inst. Met. **50**, 521 (1997).
15. FJ Zerilli, RW Armstrong, J. Mater. Process. Tech. 2001, in press.

AIR FORCE RESEARCH IN NANOENERGETICS – POTENTIAL ADVANTAGES AND CHALLENGES

3 April 2001



W.H. Wilson, R.W. Armstrong, M.P. Kramer
Energetic Materials Branch
Munitions Directorate
Air Force Research Laboratory
Eglin AFB, FL 32542



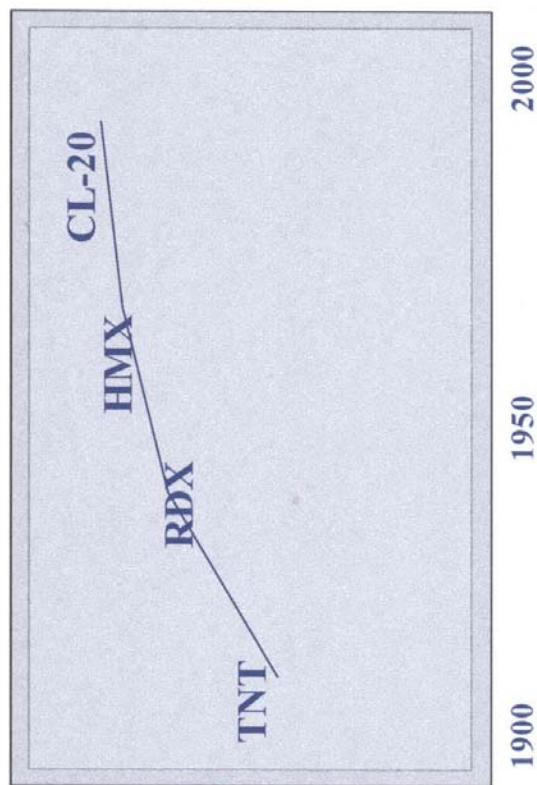
Overview



- **BACKGROUND**
- **GOALS**
- **POTENTIAL ADVANTAGES**
- **CHALLENGES**
- **NANO-ENERGETIC EXPLOSIVE MATERIALS**
- **COATED NANO-ENERGETIC MATERIALS**



Performance Enhancement: Developmental Trend



In the last 50 years, the average power of military high explosives has increased by only about 40%. It has taken a full hundred years to increase power by a factor of two.

The limits of conventional CHNO chemistry are in sight

3



Energy Calculations H.E. vs. Reactive Systems



| Composition | KJ/mole | KJ/gram | KJ/cc |
|---|---------|---------|-------|
| RDX | 1404 | 6.32 | 11.5 |
| TNT | 1036 | 4.56 | 7.55 |
| PETN | 1998 | 6.32 | 11.1 |
| Al/MnO ₂ | 442 | 4.80 | 19.2 |
| Al/MoO ₃ | 439 | 4.46 | 17.1 |
| Al/Teflon | 348 | 3.41 | 12.2 |
| Al/Ni* | 236 | 2.75 | 14.0 |
| *used 1:1 ratio of aluminum : nickel; other stoichiometries exist | | | |
| Al+O ₂ ** | 838 | 31.06 | 83.9 |
| **based on starting aluminum only | | | |



Nanometric Fuels



- **Scale Differences...**
 - Very High Specific Surface Area
 - 4- 6 Orders of Magnitude Increase
 - Short Diffusion Path-Length
- **... Can Lead to Important Performance Enhancements**
 - Tailorable Energy Release Rates
 - Complete Burning of Fuel Particles
 - Significant Surface-Energy
 - Accelerated Burn Rates
 - Enhanced I_{sp}
 - Ideal Detonation in Fueled H.E.
 - Higher Detonation Velocity
 - Higher Detonation Pressure
- **....Can Lead to Overall Performance Gains**
 - Higher Energy Release Rates
 - Improved Energy-Release Efficiency
 - Higher Energy-Content Formulations
- **...But Scale Differences Also Lead to Some Problems**
 - Fundamental Understanding of Chemistry and Physics of these Materials and Mixtures
 - High Percentage of “Dead Weight”
 - Inert Passivation Layer
 - Very High Specific Surface Area
 - Very High Viscosity of PBX Mix
 - Handling, Processing Difficulties



Nanoscale Energetic Materials - Fundamental Issue



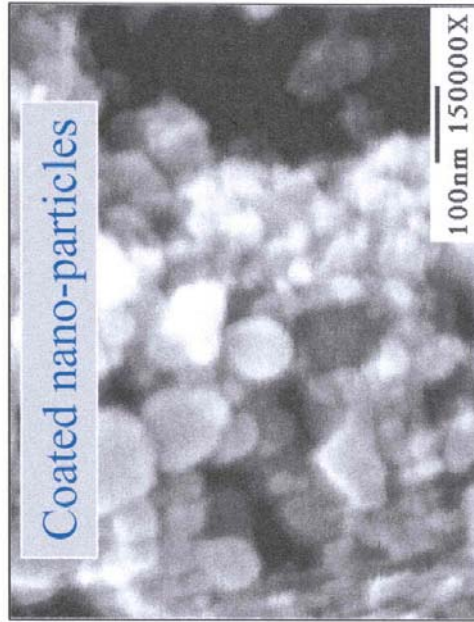
- **Fundamental Issue:** A Comprehensive Model of Reaction Processes in Heterogeneous Nanoscale Energetic Materials Is Needed
 - Initiation Processes
 - Reaction Growth, Kinetics, Propagation
 - Reaction Parameters, Dependencies (T, P)
 - Activation Energy, Energy Release
 - Solid State, Gas Phase or Solid-Liquid Mechanisms?
 - Surface vs. Bulk Electronic Description, Effects on Reaction
- **Current Status:** Nanoparticles are midway between molecular, micron scales. Little is known about local or bulk reaction behavior at this scale; do surface molecular reactions play a significant role?



ADVANCED ENERGETICS Current Materials

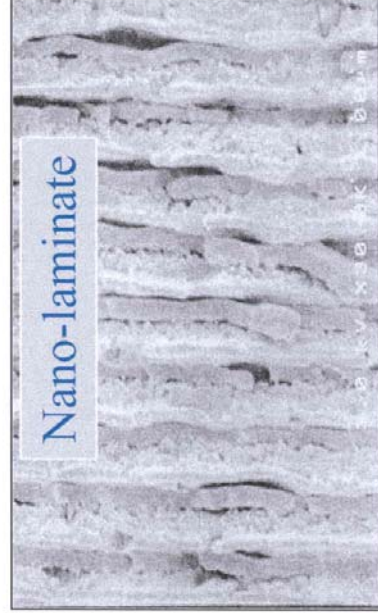


Coated nano-particles



- Powder-based systems
 - Mixed micro-powders
 - Mixed nano-powders
 - Nano-scale Stoichiometric Energetic Particles (StEPs)

Nano-laminate



- Laminate Systems
 - Micro-laminates
 - Nano-laminates



Nanoscale Explosive Composites

Objectives

- *Use Nanoscale Fuels and/or Oxidizers to Enhance High Explosive Performance, Insensitivity*
- Develop a process for reliably producing sub-micron (nanoscale) energetic particles
- Develop methods for the characterization of these particles
- Perform dynamic tests on formulated nanoscale energetics



Nanoscale Explosive Composites

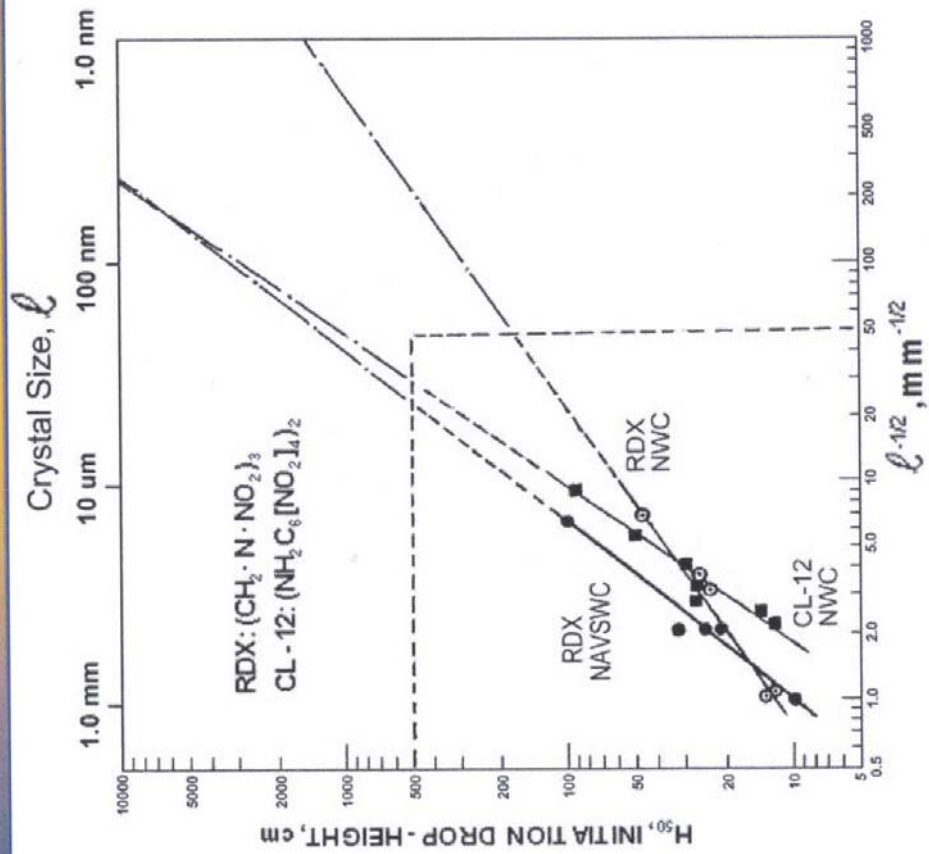
Background



- Milled PETN vs. crash-precipitated PETN has dramatically different sensitivity even though both methods produce ~ 2 micron particle size explosive (milled is much less sensitive)
- Why?
- Could it be fewer hot spots/defects to initiate and propagate reaction; low mobility of dislocations?
- Is it possible to produce a sub-micron particle by crystallization that would have few hot spots or few dislocations and therefore be less sensitive?



Crystal Size - Sensitivity Relationship





Nanoscale Explosive Composites

Approach



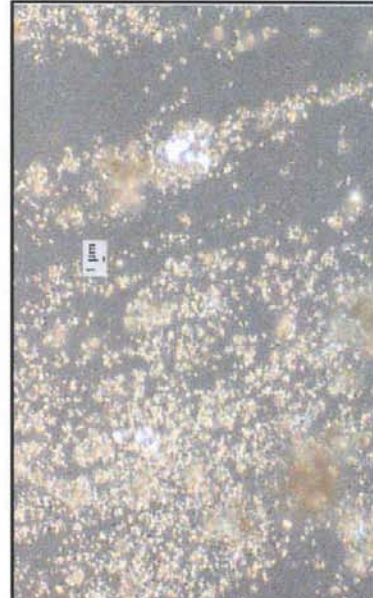
- Initially the idea was to create numerous nucleation sites to cause many small crystals to form and to exhaust the supply of material to limit crystal growth
- First effort was to use nano-aluminum as the nucleation sites
- Second effort focused on coating a nano-thick layer of explosive on the aluminum giving improved, intimate mixing and high surface area



Encapsulated Reactive Materials



Micron Size Coated Aluminum



Submicron Coated Aluminum

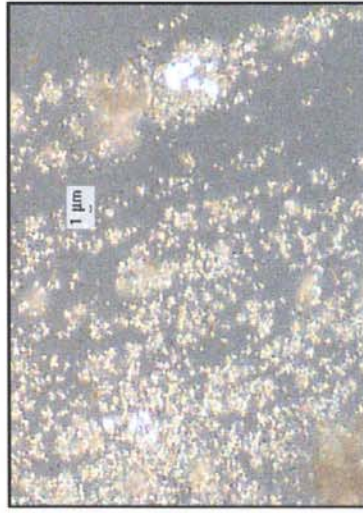
- **Encapsulation/Coating Benefits...**
 - Intimate Contact Between Fuel, Oxidizer
 - No Binder Layer
 - Higher Solids Loading
 - Higher Fuel Ratios
 - Higher Total Energy Content
 - Faster Reaction Rate
 - Larger Composite Particles Reduce Problems with Processing, Handling
 - Material Coating Thickness on Nanofuel Particles Is Nano-scale
 - Fewer Defects, Better Crystals
 - Improved Sensitivity Properties
 - Amorphous Coating Layer?
 - Multiple-Layer Composites of Nano-fuel, Oxidizer, H.E. Materials Possible



Nanoscale Explosive Composites

Results

- Initially attempts with nano-aluminum
 - Alex nano-aluminum
 - Particle size approximately 150-170nm
 - Used RDX explosive
 - Loaded 1:1 by weight and produced submicron size particles based on optical microscope observation
 - No attempt yet made to characterize coverage or homogeneity of material



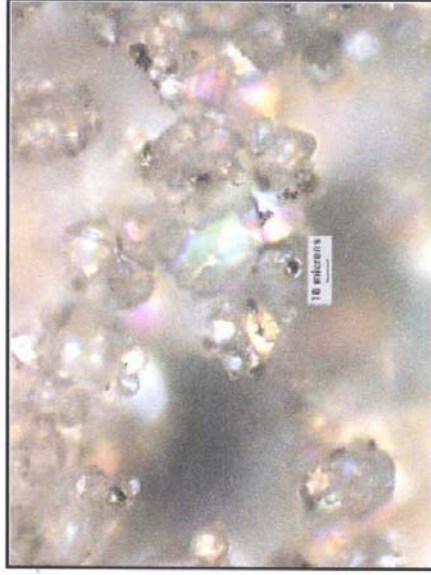


Nanoscale Explosive Composites



Results

- Additional experiments performed with H-2 or H-5 aluminum
 - H-2 or H-5 aluminum
 - RDX explosive
 - Loaded 15% - 50% by weight aluminum; produced many RDX crystals that had Aluminum coated onto the RDX crystal surface
 - Material appeared inhomogeneous in character by optical microscope
 - Used single solvent and solvent/anti-solvent methods of crystallization

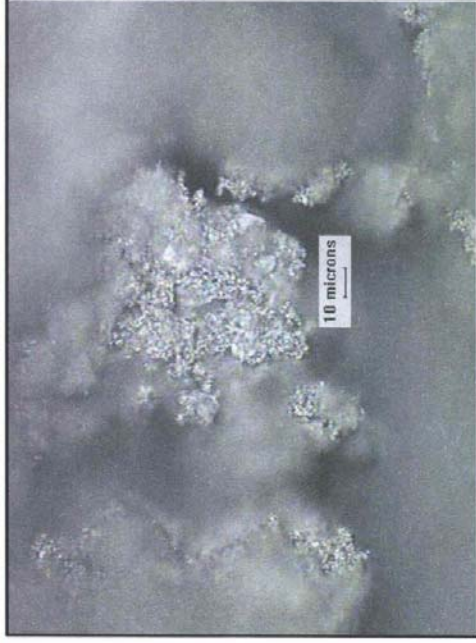




Nanoscale Explosive Composites

Results

- Recently performed several new experiments using 1:1 ratio of RDX to alex aluminum
- Modified solvent removal method; obtained consistent sub-micron sized particles
- Also coated CL-20 on alex aluminum
- Measured surface area of alex aluminum and CL-20 coated alex using BET

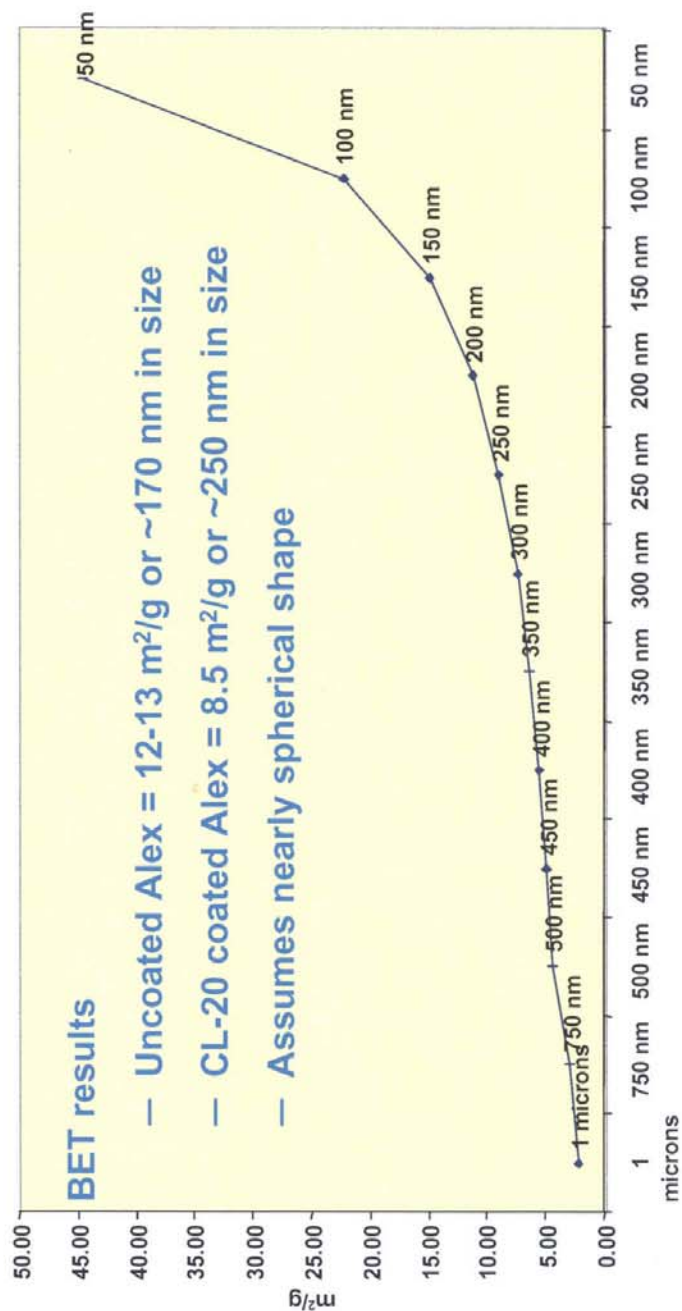




Nanoscale Explosive Composites

Surface Area vs. Size

Surface Area m^2/g





Nanoscale Explosive Composites

Results



- Safety handling data was collected on nano-aluminum coated with explosive and compared to mechanically mixed explosive and nano-aluminum
- Initial safety data appears to support idea that explosive is less sensitive at the nano-scale
- Explosive-coated aluminum was then coated with binder to make molding powder; this material was also tested in small scale safety tests



Nanoscale Explosive Composites

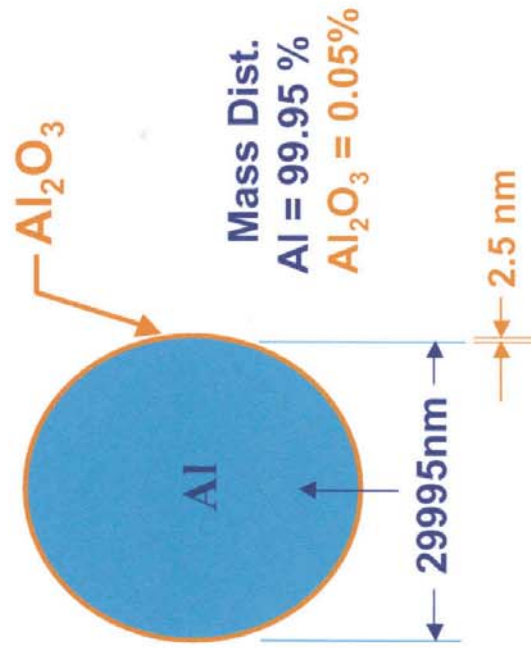
Small Scale Safety Results

| Composition | Impact (cm) | Friction (kg) | ESD | DSC |
|--|-------------------|---------------|-----------------|----------------|
| CL-20 coated on Alex aluminum (50%: 50%) | 20.8 | 8.4 | < 0.0113 J | 248.2°C |
| CL-20 coated on Alex with Elvax binder (5% binder) | 26.2 | 12.8 | 0.595 J | 236°C |
| CL-20 mixed with Alex aluminum (50%: 50%) | 18.5 | < 4.8 | 0.0113 J | 251.9°C |
| CL-20 mixed with Cerac aluminum (50%: 50%) | 29.8 | 6.0 | 0.1288 J | 256.4°C |
| RDX coated on Alex aluminum (50%: 50%) | 33.6 | 12.8 | 0.0113 J | 239.5°C |
| RDX coated on Alex with Elvax binder (5% binder) | 37.5 | 24.0 | 0.0595 J | 237.4°C |
| RDX mixed with Alex aluminum (50%: 50%) | 31.3 | 9.6 | 0.0595 J | 239.9°C |
| RDX mixed with Cerac aluminum (50%: 50%) | 25.3 | 8.4 | 0.0595 J | 242.2°C |
| RDX standard CL-20 | 22.4/25.4 8.62 | 8.4 < 4.8 | 0.0113 J --- | 240°C 251°C |



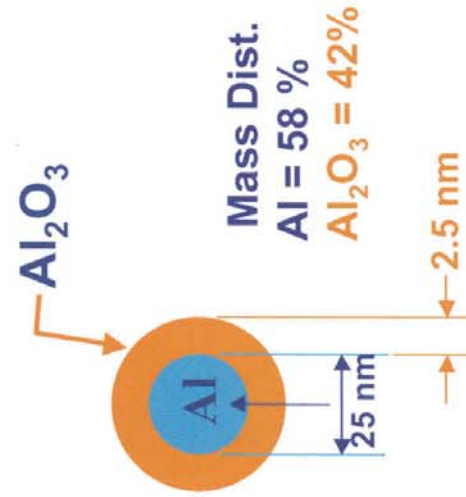
Surface Area Advantages and Challenges

30 micron aluminum particle



Surface area = 0.1 m²/g

30 nm aluminum particle



Surface area = 74 m²/g



Bomb Calorimeter



| material | date | cal/gm(measured) | cal/gm(calculated) | % TME |
|-------------------|---------|------------------|--------------------|--------|
| benzoic acid std. | 8/31/00 | 6327 | 6318 | 100.14 |
| teflon(7a) | 9/11/00 | 1224 | 1596 | 76.69 |
| | | 1250 | 1596 | 78.32 |
| CMC aluminum | 9/13/00 | 4991 | 7424 | 67.23 |
| from ether soln. | | 4995 | 7424 | 67.28 |
| alex aluminum(jr) | 9/5/00 | 6071.7 | 7424 | 81.78 |
| | | 6100 | 7424 | 82.17 |
| H-5 aluminum | 9/1/00 | 7118 | 7424 | 95.88 |
| | 9/1/00 | 7168 | 7424 | 96.55 |
| cerac aluminum | 9/13/00 | 7133 | 7424 | 96.08 |
| | | 7153 | 7424 | 96.35 |
| Aveka/viton | | | | |
| Aveka/PVDF | | | | |



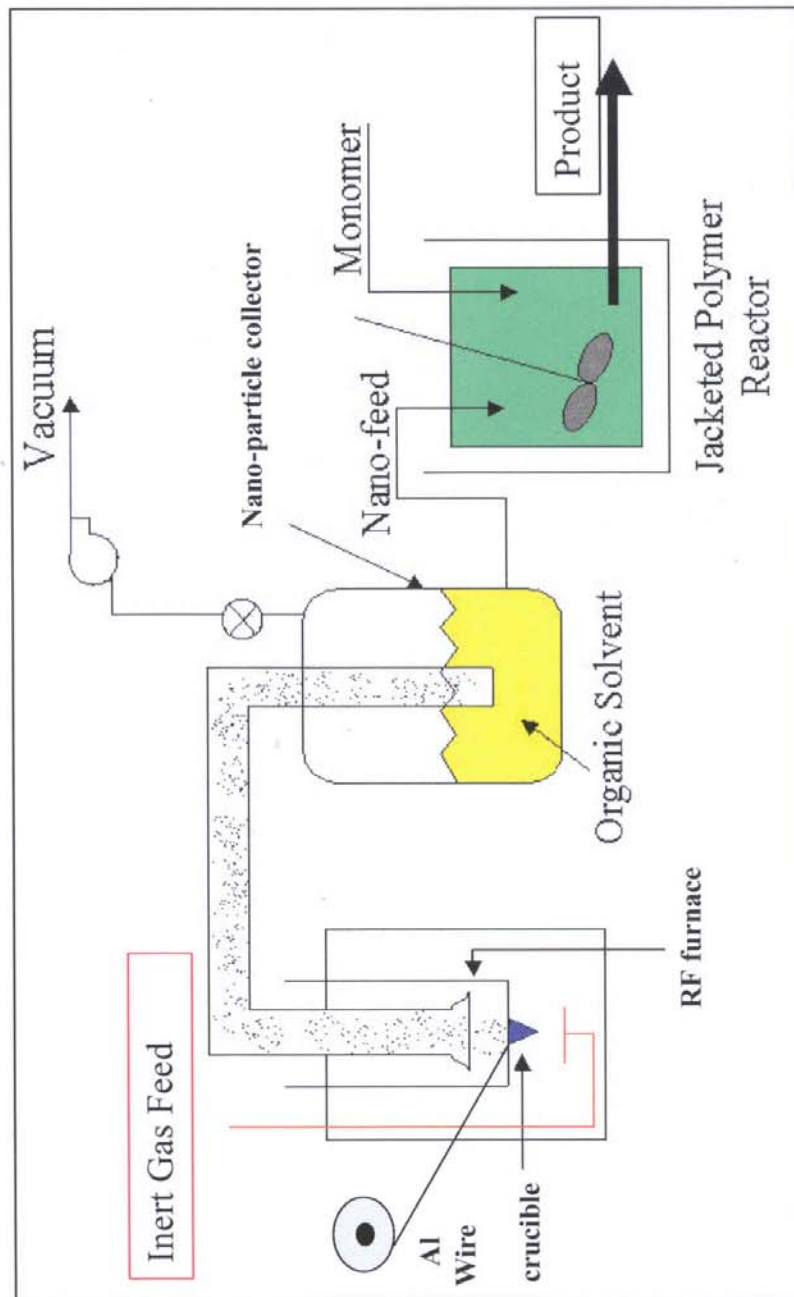
Aveka SBIR Project Tasks



- A. Scale-up to larger production quantities using inductive heating
- B. Optimization of process parameters for the pressure reactors
- C. Drying studies of coated nanoparticles
- D. Crosslinking the fluoropolymer coating
- E. Size characterization of the fluoropolymer coated nanoparticles
- F. Scale-up to 1 kg/hr production rate for coated aluminum nanopowders

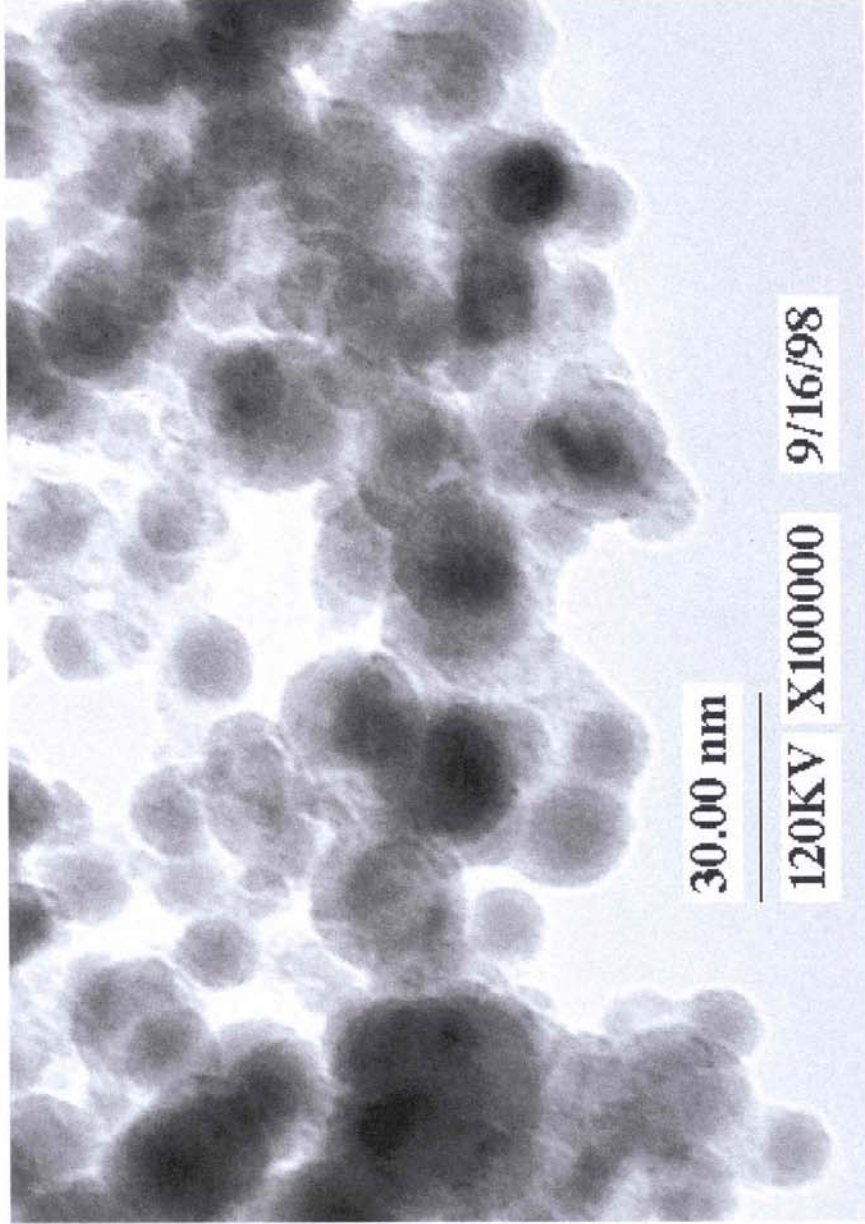


Aveka Coated Nano-Particle Process





AVEKA: Polymer-coated Nano-Aluminum Particles



23



B.E.T. Surface Data



| <u>remarks</u> | | |
|--------------------------|--|---|
| Aveka Viton/Al (50%/50%) | $61.8 \text{ m}^2/\text{g} = 35 \text{ nm}$ $62.5 \text{ m}^2/\text{g}$ | centrifuged and decanted collected in glovebox |
| Aveka uncoated aluminum | $78.1 \text{ m}^2/\text{g} = 30 \text{ nm}$ | exposed to air |



X-ray diffractometer



- Philips X-ray diffractometer: characterization of thin films and fine powders
- Determine amounts of material in different phases
- Determine the crystal size of material, using Scherrer equation
- Aveka nanoaluminum: 32nm
- BET analysis of the same lot of Aveka nanoaluminum implies 30nm particle size, assuming spherical shape
- X-ray will also provide lattice strain in the crystal, an important feature that adds energy

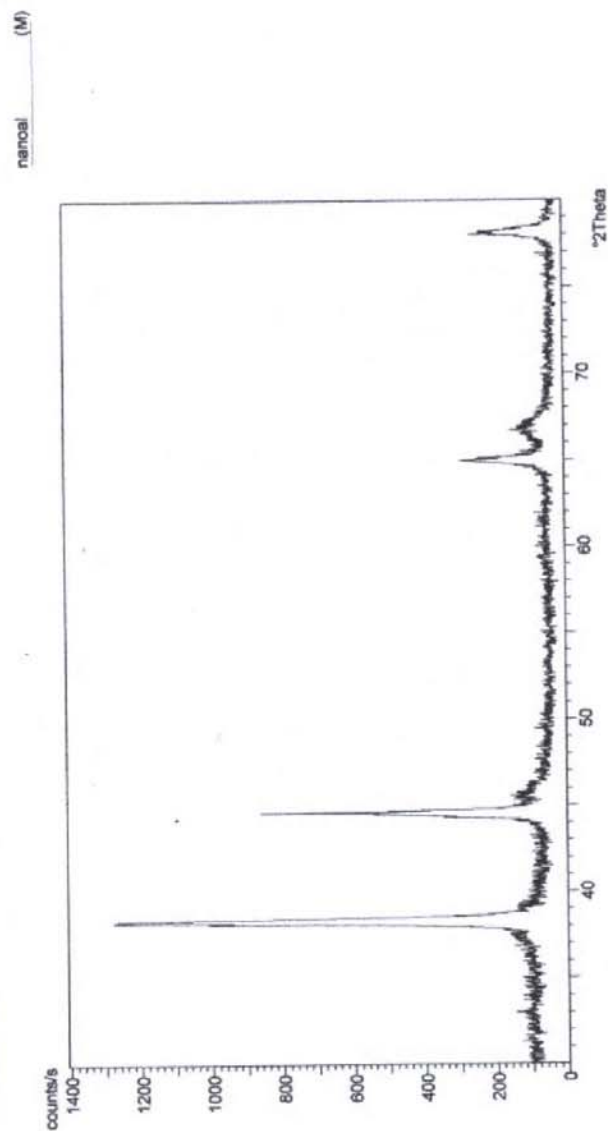




X-ray diffractometer

X'Pert Graphics & Identify
Graph: Avelka NanoAl #3

User-1
02/22/2001 15:01



HERD



Future challenges



- **Good physical characterization of manufactured nano materials**
 - surface areas
 - oxide content
 - coatings properties
- **Processing issues with nano-sized material**
 - high surface areas mean low solids loading/rheology problems
 - effective coatings that still allow fast reactions
 - long term storage/aging of these reactive materials
- **Energy release mechanisms , initiation properties unknown**
 - what are the best experiments to do to characterize output ?
 - how do we measure kinetics ?
 - how do we measure energy partitioning ?
 - What are the initiation and propagation mechanisms ?
- **Combustion efficiencies**
 - do intermolecular reactions lead to complete combustion?
 - Is energy transfer to the working fluid efficient?

NANOSCIENCE MECHANICS OF MATERIALS

AFOSR LRIR 2306/AM (01MN01COR)

Ronald W. Armstrong
AFRL/MNME
2306 Perimeter Road
Eglin AFB, FL 32542-5910

Abstract

Predictive constitutive relations are to be obtained for the deformation and fracturing properties of materials containing nanometric-sized constituents. Such relations are of particular interest for nanoenergetic materials. The approach is to accomplish this goal by extending current understanding, test methods, and dislocation mechanics based models that have been established for predicting the behaviors of counterpart microscale materials.

Introduction

1. Dislocation pile-up based Hall-Petch (H-P) considerations.

The dependence of the plastic yield, flow and fracture stresses of polycrystalline materials on the reciprocal square root of their average grain diameters, as interpreted on a dislocation pile-up (Hall-Petch) basis, was extended to provide a model understanding of localized adiabatic (hot spot) heating when associated with discontinuous load-drop behavior in impacted materials, including energetic materials [1]. In further work, it was proposed that the susceptibility of materials to such localized heating in shear bands was directly proportional to the stress versus inverse square root of grain diameter slope, known as the H-P “k” value, or microstructural stress intensity [2, 3]. The stress intensity label was applied by analogy to the macroscopic fracture mechanics stress intensity in that the mathematical description of a dislocation pile-up has direct connection with the description of a continuum mechanics modeled shear crack [4].

2. Constitutive equation development.

Recent grain size dependent H-P type results and model analyses have been based on structural material properties and extended to consideration of the influence of temperature and strain rate effects that mostly enter into the average friction stress for dislocation movement within the pile-ups [5]. Maximum load condition, dynamic recovery, dynamic strain aging, deformation twinning, and true fracture strain considerations have been described, in the latter case, relating to particle size influences on the ductility of materials. The thermally activated equation analysis for temperature and strain rate effects was combined with the dislocation pile-up model to describe mechanically-induced “hot spot” behavior in energetic material decompositions. An H-P

type prediction was obtained for initiation of explosion of RDX (cyclotrimethylene-trinitramine) crystals in drop-weight impact tests [6].

3. Elastic/plastic/cracking hardness stress-strain analysis.

Conventionally, energetic crystal particles of sub-millimeter to micrometer size are employed in explosive and propellant formulations. The individual crystals are known to be relatively brittle, hence, microindentation hardness testing has been utilized as a convenient, though complicated, quasi-static method of evaluating the material deformation properties, much as employed for ceramic materials. Such energetic crystals are found to be relatively hard in comparison with their relatively weak molecular or hydrogen bonding. The occurrence of cracking at microhardness impressions in RDX crystals has been evaluated on an indentation fracture mechanics basis and compared with parallel measurements on MgO crystals, also including a comparison of dislocation characteristics [7]. More recently, these material hardness properties have been assessed on an indentation hardness stress-strain basis [8] that was utilized for comparing the relative elastic, plastic and cracking behaviors of explosive and related inert crystal materials [9]. Microhardness testing is extended recently to very low load “nanoindentation” testing for which the proposed hardness stress-strain method of analysis appears to be useful in deciphering the meaning of results [10]. Such nanoindentation testing is being qualitatively applied at present to RDX crystals examined at nanoscale dimensions with the Atomic Force Microscope [11].

4. Molecular dislocation/lattice modeling.

An early investigation of comparative dislocation etch pitting at residual microindentation impressions in RDX and LiF crystals established that dislocation generation and movement were particularly difficult in RDX [12]. The results were explained on the basis of a special resistance to shear displacements, even within the dislocation displacement field, because of the interlocked nature of adjacent molecules within the structure of the RDX orthorhombic *Pbca* unit cell [13]. Extension to modeling the deformation of related HMX (cyclotetramethylenetetranitramine) explosive, with a monoclinic unit cell, led to explanation of twinning being preferred in HMX because of the flexibility of the larger molecule [14]. The occurrence of nitroso compounds as an early decomposition product in drop-weight impact, mechanical sensitivity, testing of RDX crystals was shown to be an expectation of forced slip deformation within the corresponding lattice structure [15].

Current research

The preceding research topics are being pursued for application to understanding energetic material properties and the influence of explosive loading on dynamic behaviors of structural materials. The topics are summarized as: (1) dislocation pile-up prediction of crystal and/or polycrystal size dependent mechanical behaviors; (2)

thermally-activated defect rate equation analysis; (3) modeled hardness stress-strain description; and (4) mechanical property interpretation at the atomic/molecular scale.

1. Extension to nanometric-sized energetic materials.

Evaluation of the dislocation self energies in RDX and related energetic crystals, relative to surface energy considerations and by comparison with a dislocation-assisted vapor growth mechanism, gives indication that the dislocation cores might contain included solvent carried over from conventional crystal growth from supersaturated solutions [16]. A fuller review of experimental and modeled dislocation properties in energetic crystals is in progress [17]. Of particular interest is the extension of these considerations to nanoscale crystal sizes where the surface energy plays an increasingly important role in material processing behavior [18]. Also of interest in connection with the generation of thermomechanical stresses are the relative surface energies of energetic crystals and related polymer binder materials that are employed in explosive and propellant formulations [19].

2. Extension to nano-indentation and -impact testing.

Collaboration with J. Sharma and colleagues [11] has involved analysis of very recent results obtained on nanoindentations put into an RDX crystal using an atomic force microscope (AFM) and relating, apparently, to microscale indentation effects described for MgO, RDX [7], and ammonium perchlorate (AP) crystals [20]. At this scale, individual dislocation generation and movements should be able to be evaluated from AFM surface profile measurements that are in progress. Also, the measurements are to be correlated with the hardness stress-strain characteristics modeled on the microscale. In addition, collaboration with R. Clough has been recently undertaken to consider development of a dynamic hardness test method achieved by ball impacts, relating to previous analyses for usefully assessing the influence of deformation rate on material properties [21]. Development of a nanoindentation test facility at AFRL/MNME is planned.

3. Extension to composite explosive/propellant formulations.

As mentioned above, the extension of dislocation pile-up based H-P model considerations to predict a material sensitivity to shear banding behavior shows the consideration to be important for energetic materials. Recent application of the same type of pile-up model consideration has been to predict a positive H-P dependence for the indentation fracture mechanics stress intensity of fine grained alumina materials, that is, grain size refinement provides in general for both strengthening a material and improving its fracture toughness [22]. The question of how far such considerations may be extended in the direction of nanoscale materials continues to be of interest [23] and, also, the extent to which such considerations may be applied to composite materials is being investigated [24]. In this regard encouraging results have been obtained on extending to modeled “flow unit” displacements in polymeric materials the thermal-activation type description employed for temperature and strain rate influences in polycrystalline viscoplastic materials [25].

An interesting comparison between grain size versus particle size strengthening of materials is that grain size reduction potentially contributes to increasing material ductility whereas particle strengthening reduces material ductility [26]. The intention is to connect research activity on this topic with an award that has been received recently for an AFOSR International Research Initiative (IRI) effort in collaboration with the University of Cambridge (UK) on the dynamic deformation properties of composite materials [27].

Acknowledgment/Disclaimer

This work is being sponsored in part by the Air Force Office of Scientific Research, USAF/AFRL, under an LRIR award. The views and conclusions contained herein are those of the author only.

References

1. R.W. Armstrong, C.S. Coffey, and W.L. Elban, Adiabatic Heating at a Dislocation Pile-Up Avalanche, *Acta Metallurgica*, 1982, **30**: 2111.
2. R.W. Armstrong and W.L. Elban, Temperature Rise at a Dislocation Pile-Up Breakthrough, *Materials Science and Engineering*, 1989, **A122**:L1.
3. R.W. Armstrong and F.J. Zerilli, Dislocation Mechanics Aspects of Plastic Instability and Shear Banding, *Mechanics of Materials*, 1994, **17**:319.
4. R.W. Armstrong, Grain Size Effects in Plasticity, *Encyclopedia of Materials Science and Technology*, Elsevier Science Publishers, Oxford, U.K., 2001, in print.
5. F.J. Zerilli and R.W. Armstrong, Dislocation Mechanics/Microstructural Based Descriptions of Strength Properties of Metals and Alloys, International Conference on the Processing and Manufacturing of Advanced Materials, THERMEC 2000, Dec 4-8, 2000, Las Vegas, NV, to be published in the *Journal of Materials Processing Technology*, 2001.
6. R.W. Armstrong, C.S. Coffey, V.F. DeVost and W.L. Elban, Crystal Size Dependence for Impact Initiation of RDX Explosive Crystals, *Journal of Applied Physics*, 1990, **68**:979.
7. R.W. Armstrong and W.L. Elban, Cracking at Hardness Micro-Indentations in RDX Explosive and MgO Single Crystals, *Materials Science and Engineering*, 1989, **A111**:35.
8. B.L. Hammond and R.W. Armstrong, Recovered Elastic and Plastic Strains at Residual Microindentations in an MgO Crystal, *Philosophical Magazine*, 1988, **57**:41.

9. R.W. Armstrong and W.L. Elban, Dislocation Roles in Energetic Crystal Responses, ONR/LANL Workshop on the Fundamental Physics and Chemistry of Combustion, Initiation, and Detonation of Energetic Materials, Chemical Propulsion Information Agency, CPIA Publication 589, March 1992, p. 367.
10. R.W. Armstrong, H.J. Shin and A.W. Ruff, Elastic/Plastic Effects During Very Low Load Testing of Copper, *Acta Metallurgica et Materialia*, 1995, **43**:1037.
11. J. Sharma, C.S. Coffey, R.W. Armstrong and W.L. Elban, Sub-Molecular Fracture Steps in Shock-Shattered RDX Crystals, Amer. Phys. Soc., Shock Compression of Condensed Matter 2001 Meeting, Atlanta, GA, 24-29 June 2001; see Nano-Fractography of Shocked RDX Explosive Crystals with Atomic Force Microscopy, *Applied Physics Letters*, 22 Jan 2001, **78**:457.
12. W.L. Elban and R.W. Armstrong, Microhardness Study of RDX to Assess Localized Deformation and Its Role in Hot Spot Formation, Seventh (International) Symposium on Deformation, U.S. Naval Academy, Annapolis, MD, June 16-19, 1981; Naval Surface Weapons Center, NSWC MP 82-234, 1982, p. 976.
13. R.W. Armstrong and W.L. Elban, Microstructural Origin of Hot Spots in RDX Crystals, ONR Workshop on Energetic Material Initiation Fundamentals, Chemical Propulsion Information Agency, CPIA Publication 475, December 1987, p. 177.
14. R.W. Armstrong, H.L. Ammon, Z.Y. Du and X.J. Zhang, Energetic Crystal Lattice-Dependent Responses, Structure and Properties of Energetic Materials, Materials Research Society, MRS, 1993, **296**:227.
15. R.W. Armstrong, W.L. Elban, A.L. Ramaswamy and C.M. Wu, Thermomechanical Aspects of Energetic Crystal Combustion, Challenges in Propellants and Combustion 100 Years after Nobel, Begell House, Inc., NY, 1997, p. 313.
16. R.W. Armstrong and W.L. Elban, Dislocations Characteristics in Energetic Crystals, Shock Compression of Condensed Matter – 1999, American Institute of Physics, NY, 2000, CP505, Part 2, p. 723.
17. R.W. Armstrong and W.L. Elban, Dislocations in Energetic Crystals, invited article in process of development for Dislocations in Solids, F.R.N. Nabarro, editor, Elsevier Science Publishers.
18. W.H. Wilson, M.P. Kramer and R.W. Armstrong, Air Force Research in Nano-Energetics – Potential Advantages and Challenges, 221st Amer. Chem. Soc. Meeting, San Diego, April 1-5, 2001.
19. W.L. Elban, R.W. Armstrong and T.P. Russell, Plasticity/Interfacial Energy Influences on Combustion-Driven Cracking of RDX Energetic Crystals, *Philosophical Magazine A*, 1998, **78**:907.

20. H.W. Sandusky, B.C. Glancy, D.W. Carlson, W.L. Elban and R.W. Armstrong, Relating Deformation to Hot Spots in Shock-Loaded Crystals of Ammonium Perchlorate, *Journal of Propulsion and Power*, 1991, **7**:518.
21. R.B. Clough, S.C. Webb and R.W. Armstrong, Dynamic Hardness Measurement of 1018 Steel in Dropped Ball Impact Tests, article being developed for submittal to the *Journal of Test and Evaluation*, 2001.
22. R.W. Armstrong, Grain Size Dependent Alumina Fracture Mechanics Stress Intensity, Seventh International Conference on the Science of Hard Materials (ICSHM7), March 5-9, 2001, Ixtapa, Mexico, submitted to the *International Journal of Refractory Metals and Hard Materials*.
23. C.S. Pande, R.A. Masumura and R.W. Armstrong, Pile-Up Based Hall-Petch Relation for Nanoscale Materials, *Nanostructured Materials*, 1993, **2**:323.
24. R.W. Armstrong, Micro-to-Nano-Structural Modeling of Composite Material Deformation Properties, in process of submittal for the Eighth International Conference on Composites Engineering (ICCE/8), Tenerife, SP, August 5-9, 2001.
25. F.J. Zerilli and R.W. Armstrong, Thermal Activation Based Constitutive Equations for Polymers, *Journal de Physique IV France*, 2000, **10**:3.
26. R. W. Armstrong, Strength and Ductility of Metals, *Transactions of the Indian Institute of Metals*, 1997, **50**:521.
27. R.W. Armstrong and R.L. Sierakowski, Dynamic Deformation Properties of Energetic Composite Materials, AFOSR International Research Initiation (IRI) award, 2001, in cooperation with J.E. Field, Physics and Chemistry of Solids Group, Cavendish Laboratory, University of Cambridge, U.K.

The Power of Nano-Energetics*

R.W. Armstrong*, K. Kline**, M.P. Kramer*, W.H. Wilson*

*AFRL/MNME, 2306 Perimeter Road, Eglin AFB, FL 32542.

** University of Florida, Graduate Engineering and Research Center, 1350 N. Poquito Road, Shalimar, FL 32579.

ABSTRACT

Previous description has been given of potential advantages and challenges associated with the development of nano-energetic materials [1]. Such nanometric-scale energetic materials, as well as counterpart combustible metals, and reactive materials, are all of current research interest, for one reason, because surface-control of their decomposition properties provides for the possibility of orders of magnitude increase in energy release rates at ultrafine particle sizes [2]. Recent report of enhanced burn rate results for aluminum particle combustion [3] appears to substantiate the prediction.

The surface energy property is of paramount importance at nanometric particle sizes, as evidenced by nano-particle processing difficulties with agglomeration. Particle coating can alleviate the problem, especially relating to coating energetic materials with polymers that have relatively lower surface energies. Otherwise, the added surface areas of smaller energetic particles provide for energy enhancement and this can be substantial, say, compared to heats of fusion among different materials. At the smallest particle sizes, or at the level of atomic or molecular clusters, issues of strained bonds at the material surfaces and size-dependent surface or interfacial energies are to be considered [4]. The topic lends itself to molecular dynamics (MD) modeling as described for the simulated oxidation of aluminum nano-clusters [5].

Generally, more severe conditions of phase transformation or material deformation are required to produce smaller material particles and, consequently, added internal defects, say, point or line (dislocation) defects, might be expected to be contained within the particles. For energetic materials, the large lattice-structure-determined Burgers vectors of dislocations provide internal strain energies that so outweigh the relative surface energies that hollow dislocation cores of nm dimensions are predicted to be energetically feasible, based on a pioneering model description, particularly, for vapor grown crystals [6].

The mechanical strength and fracturing behaviors of nanometric-scale material particles and structures are challenging areas of research so far as concerns a dearth of material testing methods and also prediction of size-dependent material deformation/decomposition properties. Extrapolations to nm crystal sizes of significantly increased drop-weight height measurements required for mechanical initiation of energetic crystals remain to be confirmed. Recent atomic force microscopy (AFM) observations on RDX (cyclotrimethylenetrinitramine) crystals have indicated the presence of shock-generated nanoscale shear cracks with displacement vectors smaller than the length of individual

molecules [7]. More recent AFM observations have included preliminary examination of nanoindentation deformations.

References

1. W.H. Wilson, M.P. Kramer and R.W. Armstrong, Abstract: "Air Force research in nano-energetics – potential advantages and challenges", 221st American Chemical Society Meeting, San Diego, CA, Apr 1-5, 2001.
2. R.W. Armstrong, "Workshop on the strategic investment for nanoscience & nanotechnology in AFRL", Universal Technology Corporation, May 30,31, 2001, Dayton, OH, CD-ROM.
3. R. Dye, Technanogy, LLC, presentation at AFRL/MNME, Eglin AFB, FL, Jun 5, 2001.
4. Q. Jiang, D.S. Zhao and M. Zhao, "Size-dependent interface energy and related interface stress", *Acta Materialia*, Vol. 49, Issue 16, pp. 3143-3147 (20 Sep 2001).
5. T.J. Campbell, R.K. Kalia, A. Nakano, P. Vashishta, S. Ogata, and S. Rodgers, "Dynamics of oxidation of aluminum nanoclusters using variable charge molecular dynamics simulations on parallel computers", *Physical Review Letters*, Vol. 82, pp. 4866-4969 (1999).
6. R.W. Armstrong and W.L. Elban, "Dislocation characteristics in energetic crystals", *Shock Compression of Condensed Matter – 1999*, American Institute of Physics, NY, 2000, CP505, Part 2, pp. 723-726.
7. J. Sharma, R.W. Armstrong, W.L. Elban, C.S. Coffey and H.W. Sandusky, "Nanofractography of shocked RDX explosive crystals with atomic force microscopy", *Applied Physics Letters*, Vol. 78, No. 4, pp. 457-459 (22 Jan 2001).

Twenty-Ninth International Pyrotechnics Seminar, Westminster, Colorado, July, 2002
F.J. Schelling, editor, (IPSUSA, Inc., 2002), pp. 239-240.

DISLOCATION MECHANICS BASED CONSTITUTIVE RELATIONS FOR DYNAMIC DEFORMATION OF POLYCRYSTALS

R.W. Armstrong, AFRL/MNME



**US-Korea Workshop
on Advances in Metallic Structural Materials
Kihei, Maui, HI
21-23 January 2003**



Computer-Friendly Z-A Equations

The Z-A dislocation mechanics description for the stress-strain dependence as a function of temperature, strain rate and polycrystal grain size.

$$\sigma = \sigma_a + B e^{-\beta T} + B_0 \sqrt{\varepsilon_r (1 - e^{-\varepsilon_r / \varepsilon_r})} e^{-\alpha T}$$

The Peierls stress:

$$\beta = \beta_0 - \beta_1 \ln \dot{\varepsilon}$$

Dislocation intersections:

$$\alpha = \alpha_0 - \alpha_1 \ln \dot{\varepsilon}$$

Dislocation pile-ups:

$$\sigma_a = \sigma_G + k \ell^{-1/2}$$

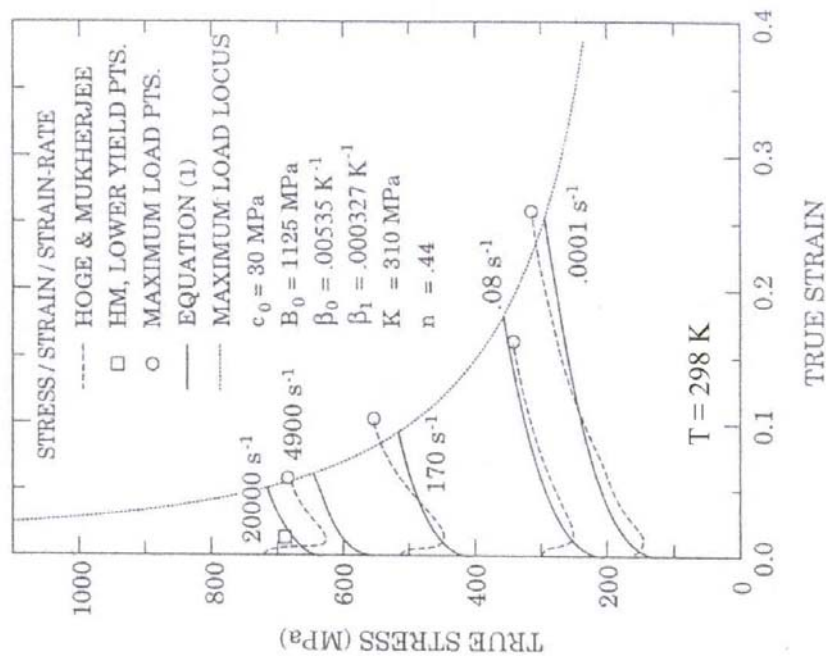
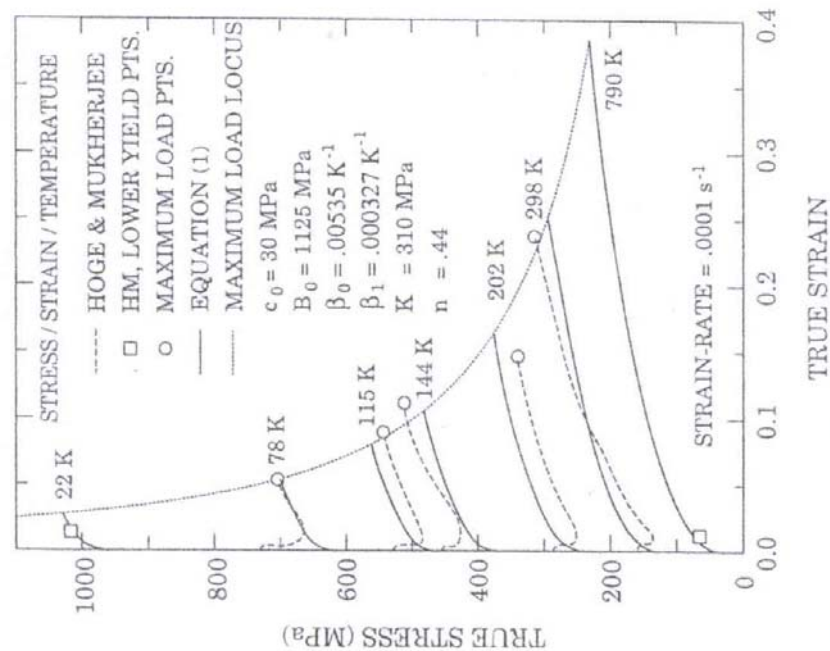
Dynamic recovery:

$$\varepsilon_r = \rho / \left[\frac{1}{b\lambda} - \frac{d\rho}{d\varepsilon} \right]$$

F.J. Zerilli & R.W. Armstrong,
Intern. Conf. on Processing &
Manufacturing of Advanced Materials
THERMEC 2000, CD-ROM, 2001



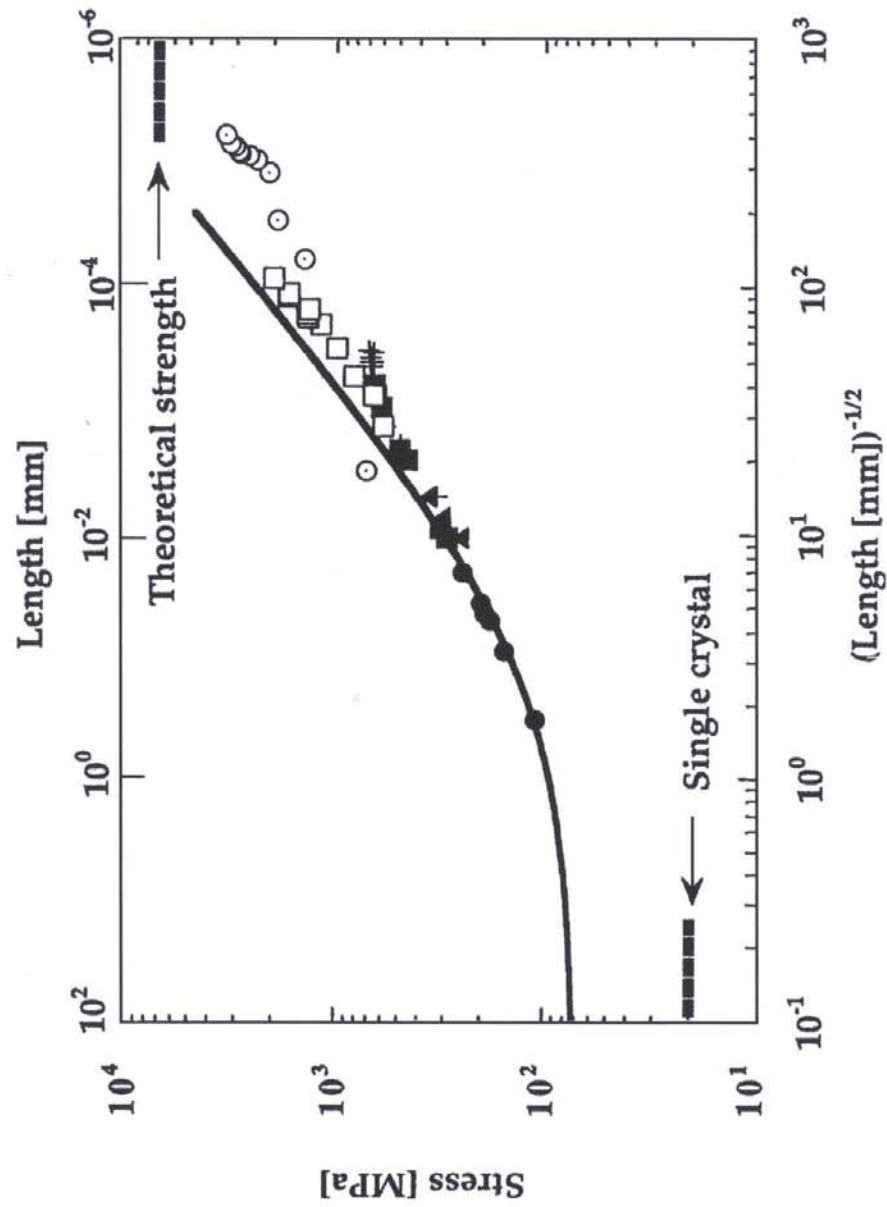
Z-A Reference Description of the Stress/Strain/Temperature and Strain Rate Dependencies of T_a



R.W. Armstrong & F.J. Zerilli,
Chemical Physics (Russian),
Vol. 20 No. 8, 2001, p. 104

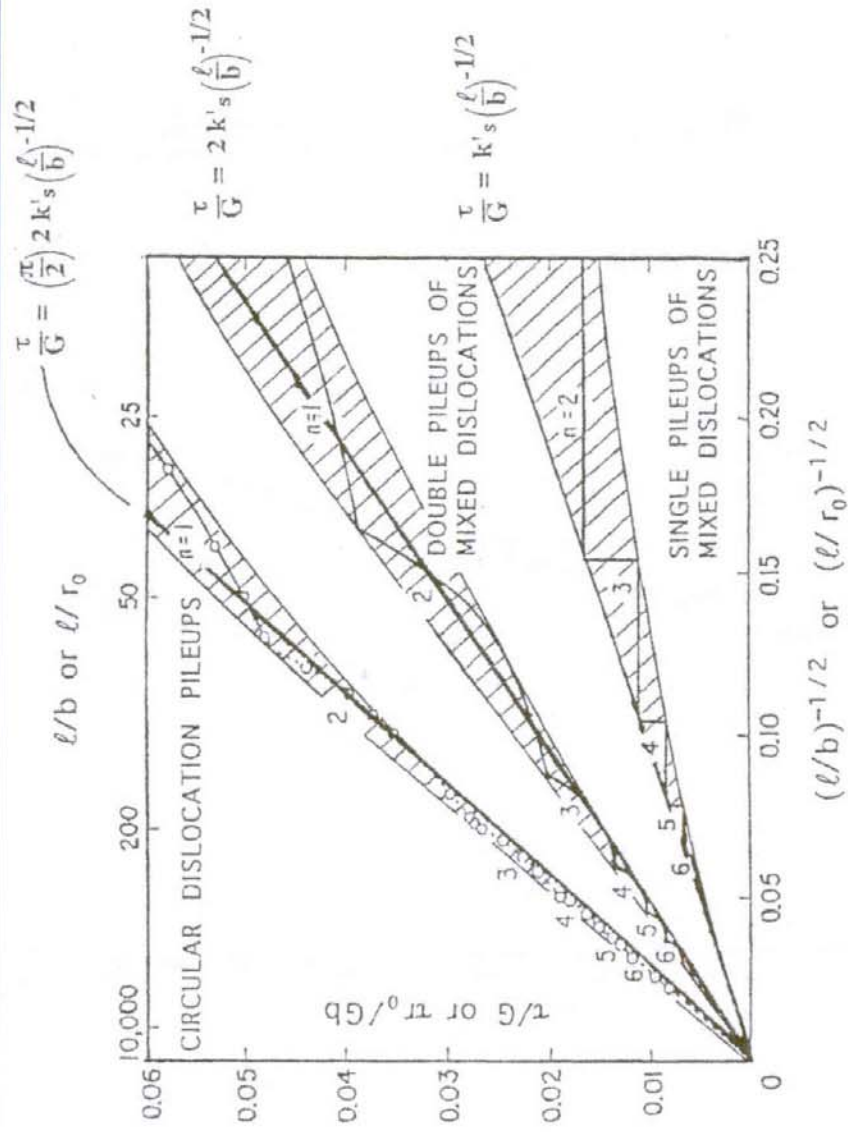


Hall-Petch Dependence for Iron Extended to Nanometric Scale



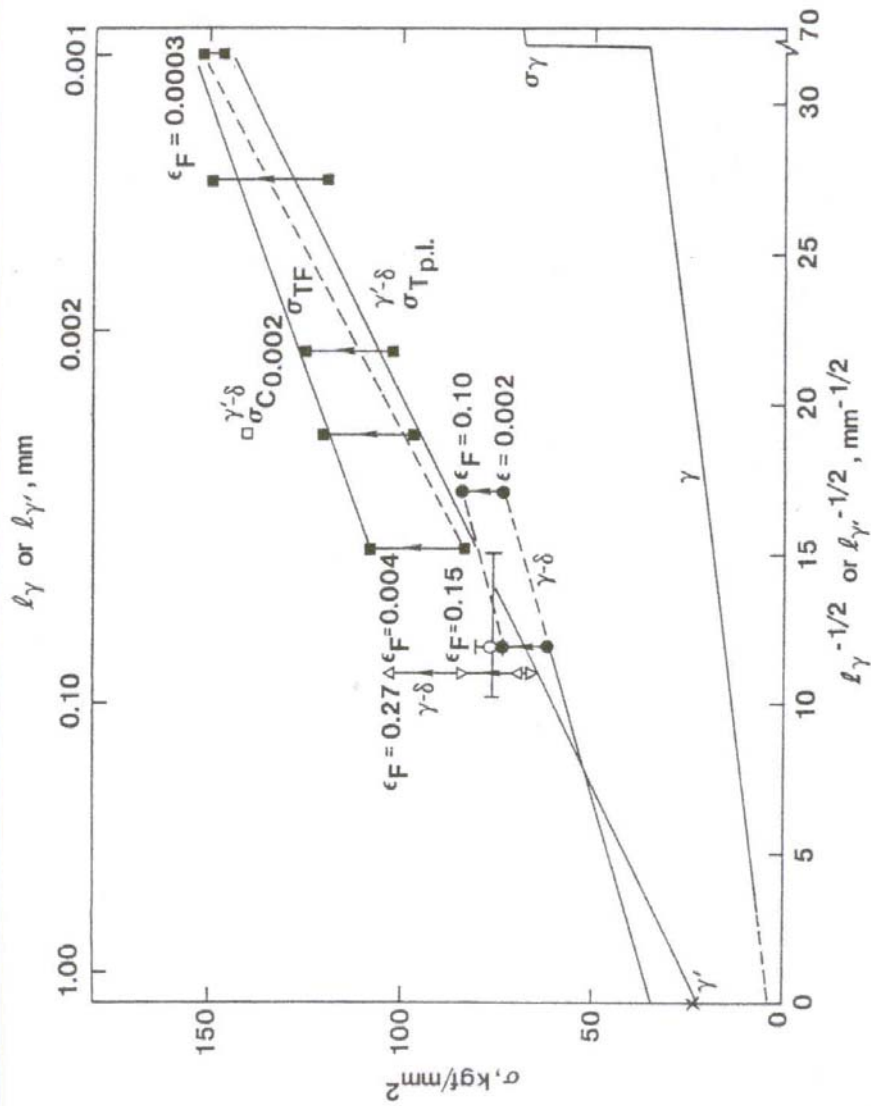


Match of Dislocation Pile-Up and Crack Dependencies





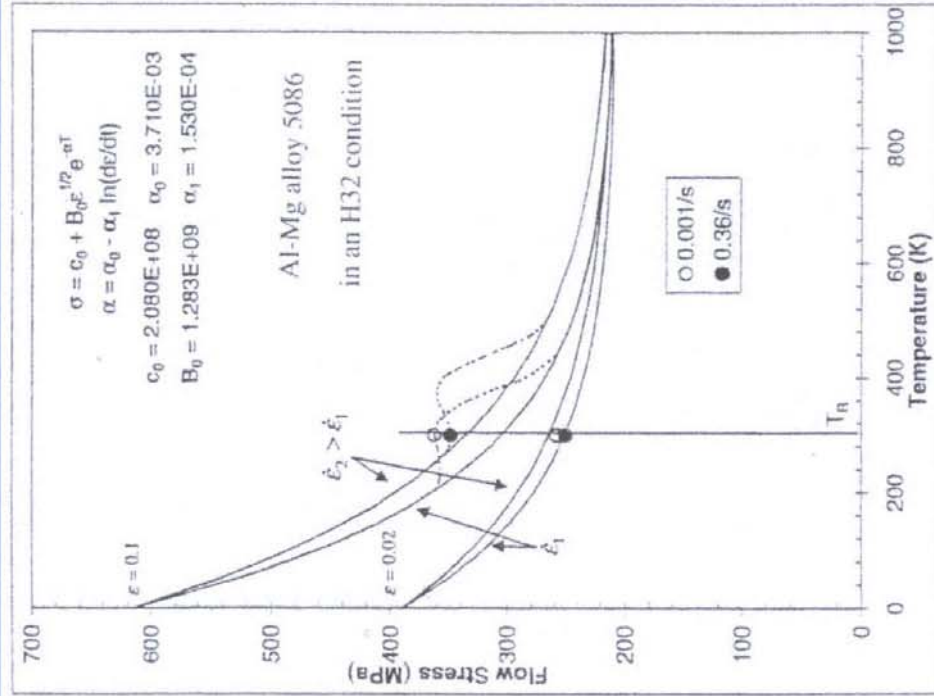
FCC and Ordered or Disordered Single Phase or Unidirectional Solidified Lamellar-Type Nickel Base Eutectic Alloy H-P Behaviors



R.W. Armstrong,
United Technologies Research
Center (UTRC) Report UTRC75-84, 1975



Superposition of Dynamic Strain Aging Influence on Z-A Description for Al/Mg Alloy 5086

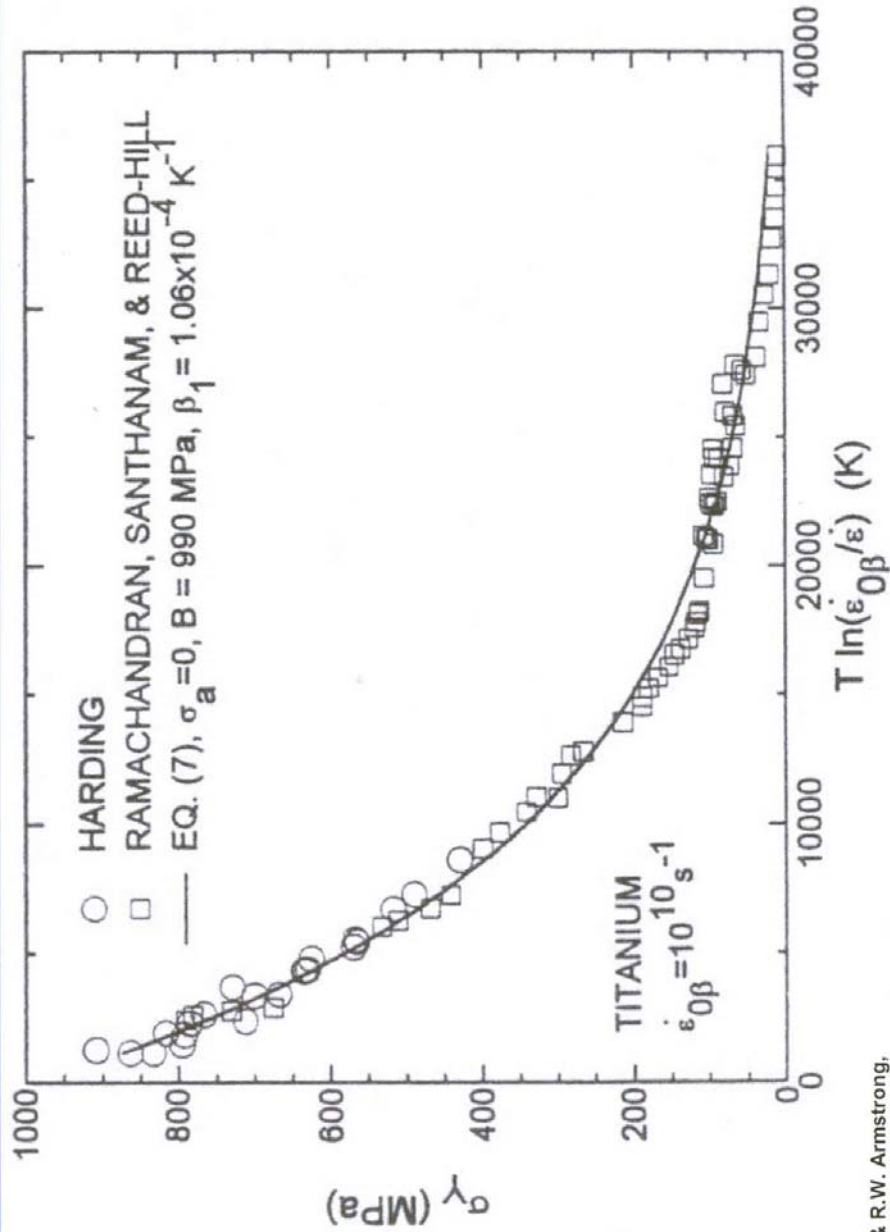


A strain rate reversal
in the region of room
temperature

M. Wagenhofer, M.E. Natishan,
R.W. Armstrong & F.J. Zerilli,
Scripta Materialia, Vol. 41, 1999, p. 1177



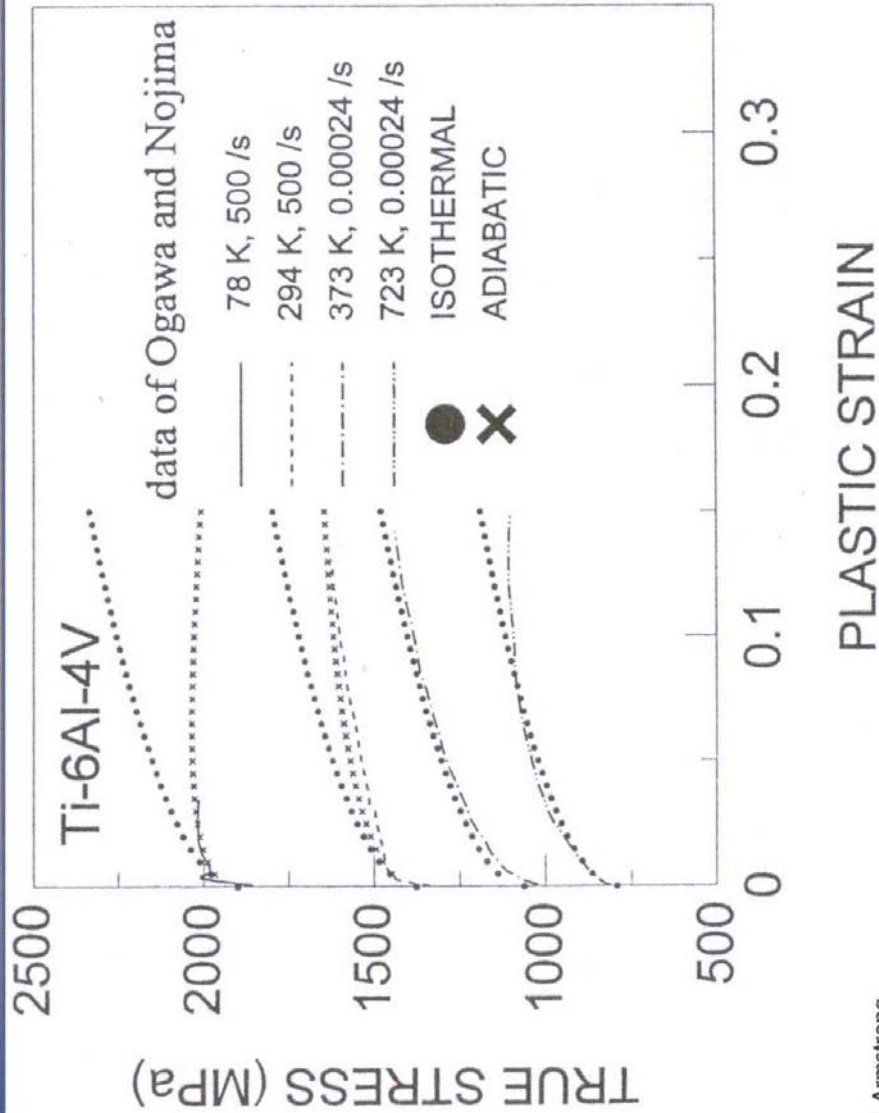
Z-A Description of Yield Stress as a Function of Temperature and Strain Rate for Commercial-Purity Ti



F.J. Zerilli & R.W. Armstrong,
 Shock Compression of Condensed
 Matter – 1995, AIP CP370 Part 1, 1996, p. 315



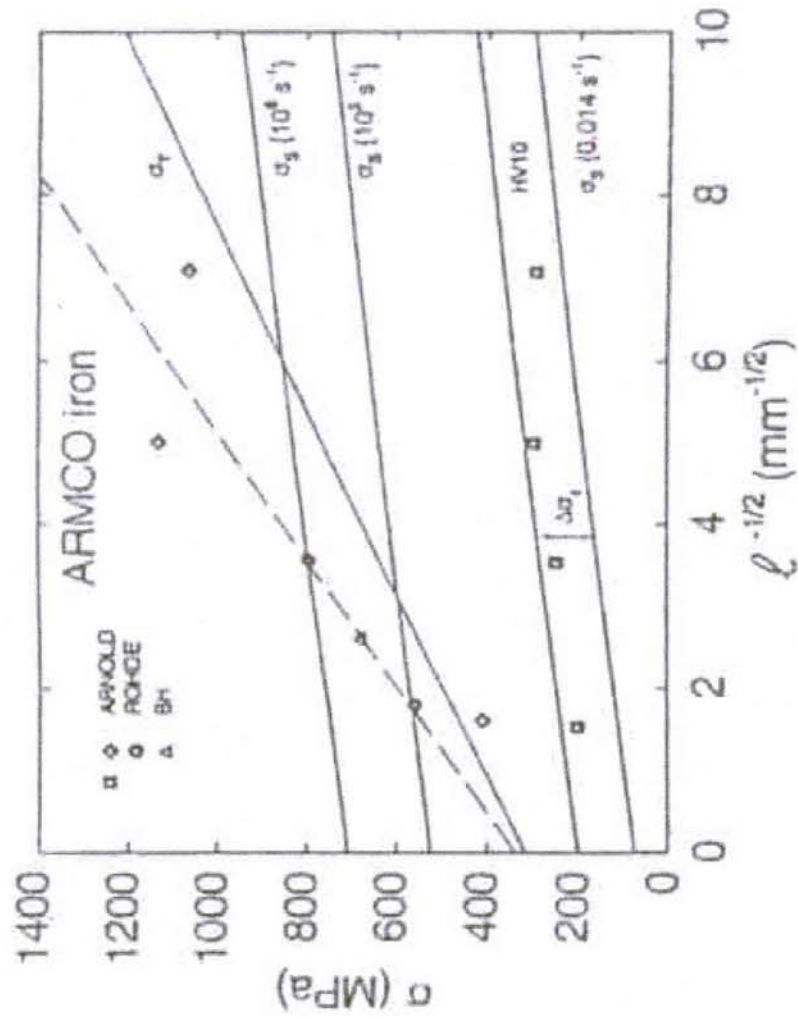
Computed and Experimental Stress/Strain Curves for Alloy Ti-6Al-4V



F.J. Zerilli & R.W. Armstrong,
Shock Compression of Condensed
Matter – 1995, AIP CP370 Part 1, 1996, p. 315



H-P Slip (S) and Twinning (T) Relation to Hugoniot Elastic Limit Measurements

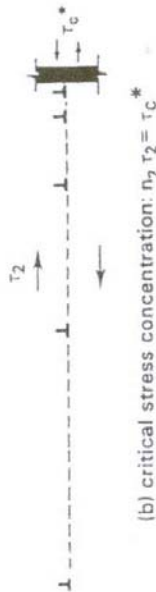




Model of Dislocation Pile-Up Avalanches



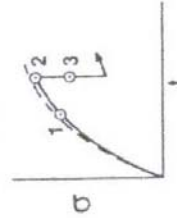
(a) isothermal stress build-up: n_1 dislocations



(b) critical stress concentration: $n_2 \tau_2 = \tau_c^*$



(c) adiabatic collapse-discontinuous load drop



(d) pressure-time curve for τ_1 , τ_2 , and τ_3

$$\Delta T \leq \frac{k_s l^{1/2}}{16\pi} \left(\frac{2v}{c^* b K} \right)^{1/2} \quad \text{if } \left(\frac{2K}{c^* v b} \right) \leq 1.0$$

$$\dot{\gamma} = N b v,$$

$$v = v_0 \exp \left[- \left(G_0 - \int_{\tau_{th}}^{\tau_{th}} b A^* d\tau_{th} \right) / kT \right],$$

$$b A^* = W_0 / \tau_{th},$$

$$\tau_{th} \propto H_{50}^{1/n},$$

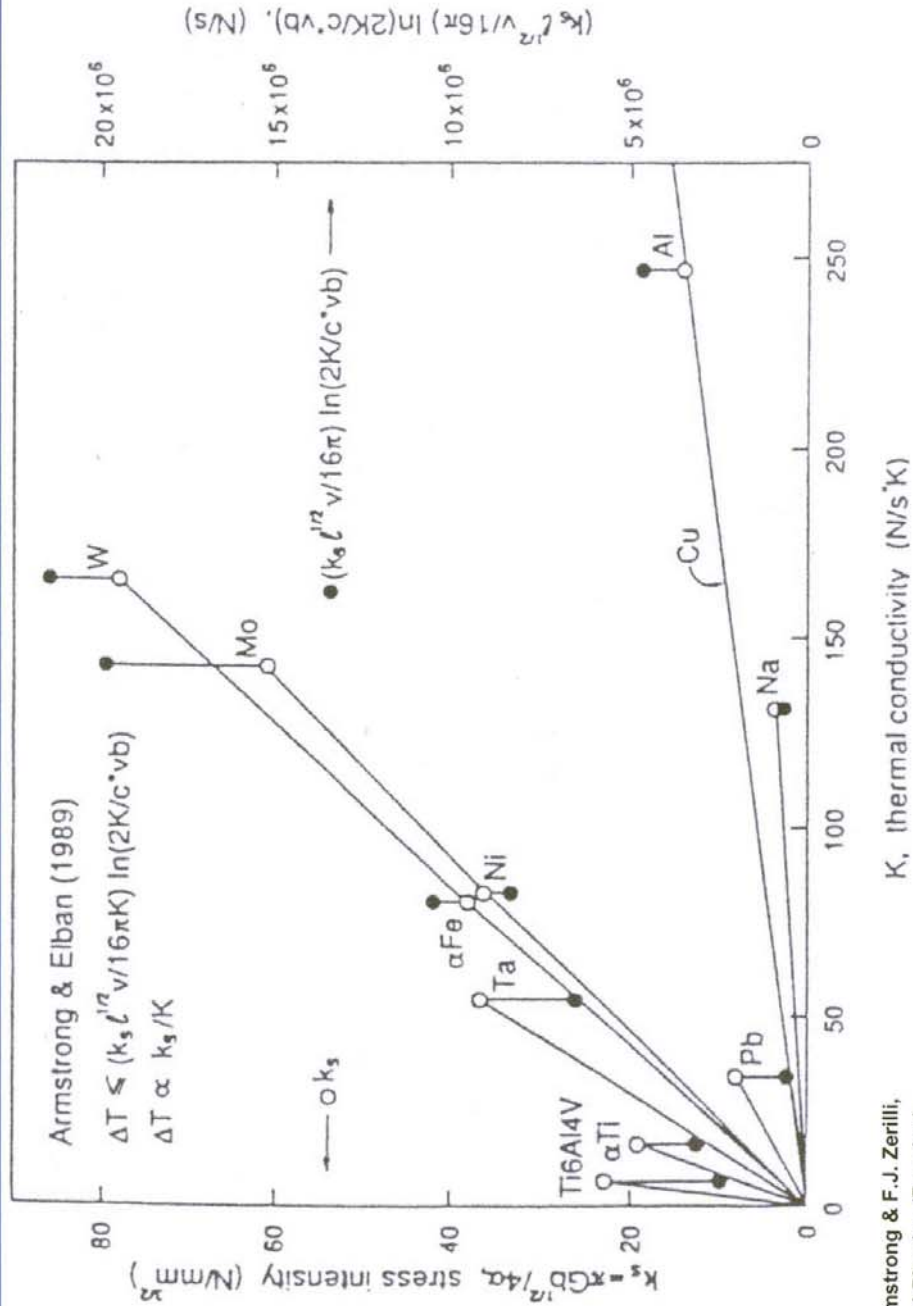
$$v = v_0 (H_{50} / H_{50}^0)^{W_0 / n k T} \exp(-G_0 / kT)$$

$$\begin{aligned} \log H_{50} = & \log H_{50}^* + (n/m^*) \log \{ [8\pi\sqrt{2}\Delta T \\ & \times K^{1/2} c^{*1/2} b^{1/2} / k_s v_0^{1/2} \\ & \times \exp(-G_0 / 2kT)] l^{-1/2} \}. \end{aligned}$$

$$m^* = W_0 / 2kT$$



Susceptibility to Shear Banding on a Dislocation Pile-Up Avalanche Basis



R.W. Armstrong & F.J. Zerilli,
Chemical Physics (Russian),
Vol. 20 No. 8, 2001, p. 104

THE POWER (AND STRENGTH) OF ENERGETIC/REACTIVE NANO MATERIALS

R.W. Armstrong, AFRL/MNME



2003 Nano Materials for Aerospace
Symposium: Expanding the Envelope
Corpus Christi, TX
27-30 January 2003



The Power (and Strength) of Energetic/Reactive Nano Materials

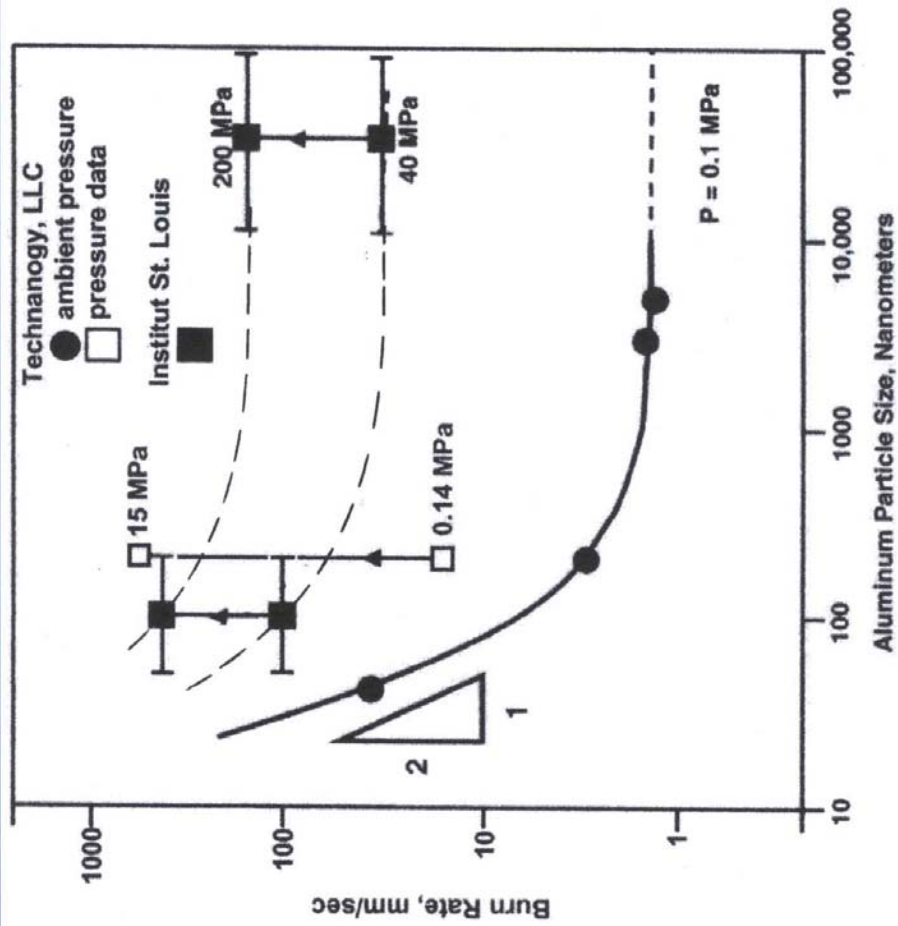


Nanometric-sized energetic materials, as well as counterpart combustible metals, and reactive materials, are all of current research interest, for one reason, because surface-control of their decomposition properties provides for the possibility of orders of magnitude increases in energy release rates at ultrafine particle sizes, as indicated by extrapolation of recent size-dependent burn rate results obtained for aluminum particle combustion properties in both laboratory and gun propellant experiments [1]

1. R.W. Armstrong, B. Baschung, D.W. Booth, and M. Samirant, "Enhanced Propellant Combustion with Nanoparticles", Nano Letters, 2003, in print.



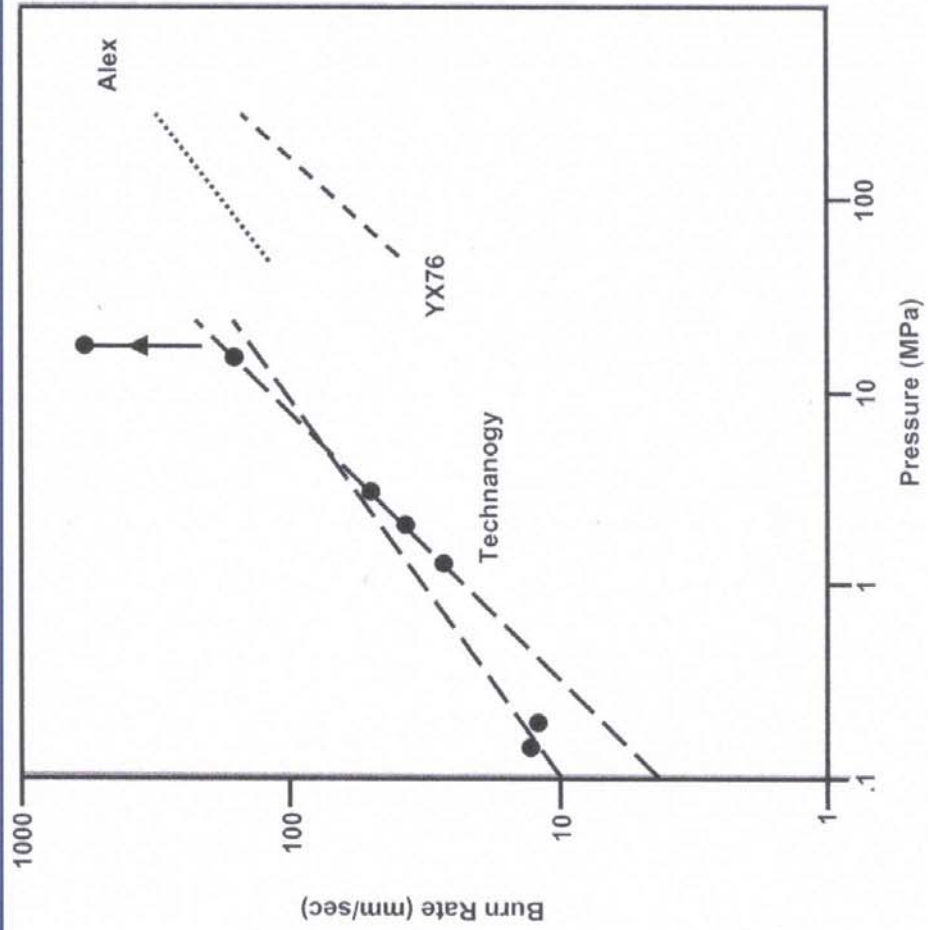
Burn Rate Dependence on Al Particle Size



AAC/PA 02-404



Al Nanoparticle-Containing or YX76 Materials Burn Rate – Pressure Dependence



AAC/PA 02-404



The Power (and Strength) of Energetic/Reactive Nano Materials

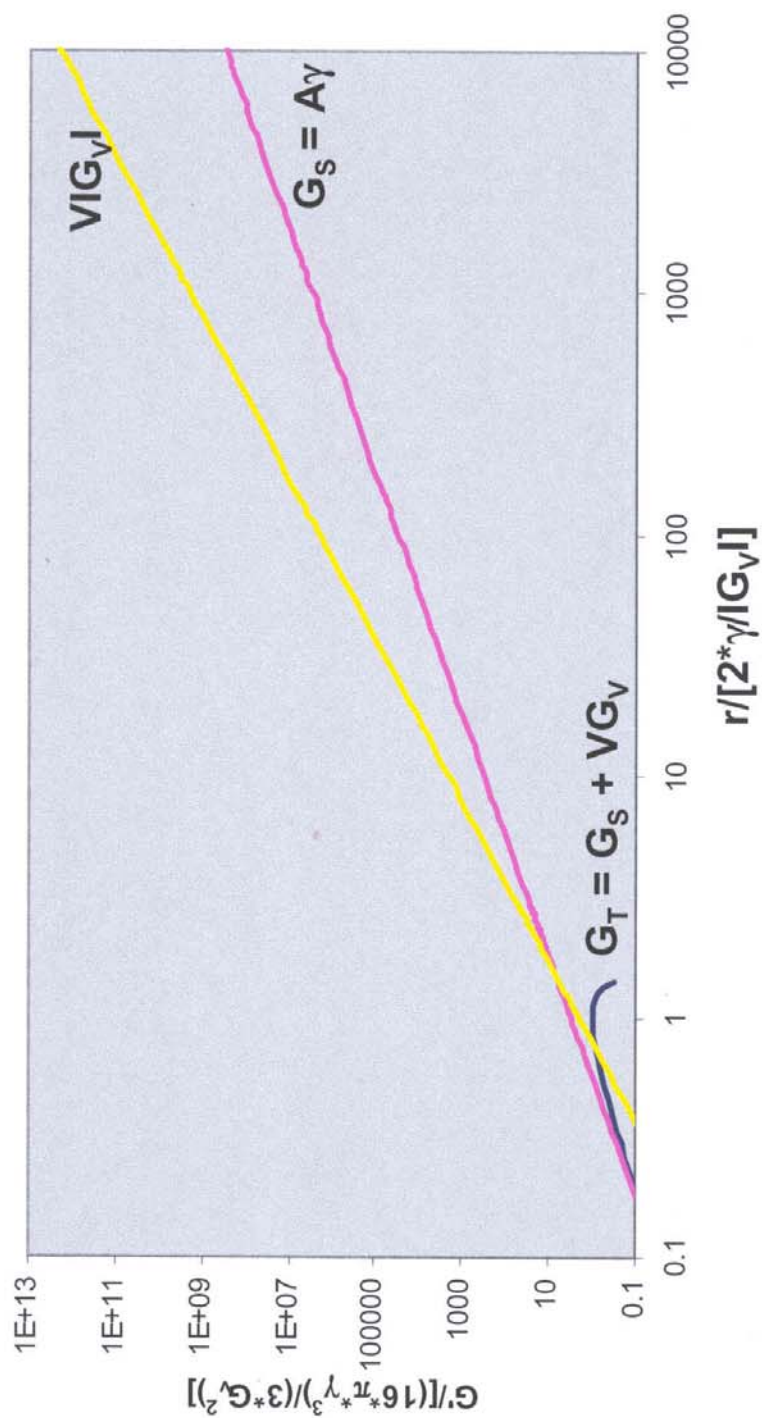


From a research point-of view, the surface energy property is of paramount importance at nanometric particle sizes, as evidenced practically by nano-particle processing difficulties with agglomeration. Particle coating can alleviate the problem, especially relating to coating energetic materials with polymers that have relatively lower surface energies; see reference [2] for representative surface energy values, and physical property consequences.

2. W.L. Elban, R.W. Armstrong, and T.P. Russell, "Plasticity/Interfacial Energy Influences on Combustion-Driven Cracking of RDX Energetic Crystals", Philosophical Magazine A, **78**, 907 (1998).



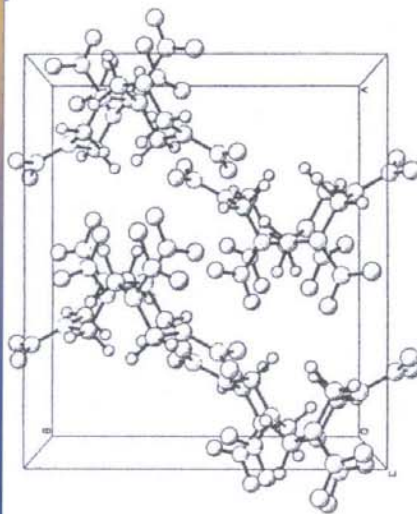
Normalized Free Energy (G) Versus Spherical Particle Radius



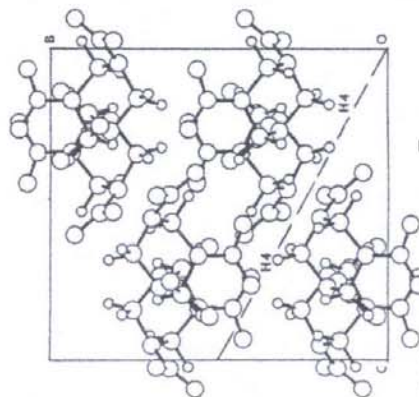
K.L. Kline, MS Thesis, University of Florida, Graduate Engineering and Research Center, 2002



Molecular-Scale Dislocation Shear Interactions



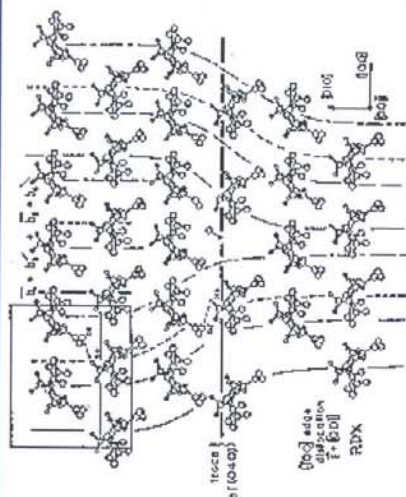
RDX Orthorhombic Unit Cell



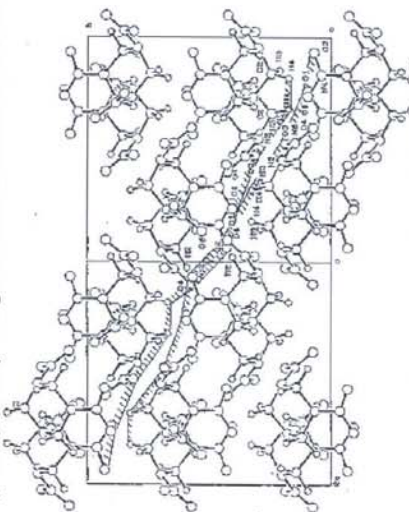
$\pm [012]$ Shear on $(02\bar{1})$ Slip Plane

Ammon, Armstrong, Bodine, Elban, Hoffsommer, & Hughes

AAC/PA 02-287



$\frac{1}{2}[100]$ Edge Dislocation in RDX



Molecule Interactions for $[100] (02\bar{1})$ Slip



AFM Observations on RDX Crystal Surfaces



APPLIED PHYSICS LETTER

VOLUME 78, NUMBER 4

Nanofractography of shocked RDX explosive crystals with atomic force microscopy

J. Sharma^{a)}

Carderock Division, Naval Surface Warfare Center, Bethesda, Maryland 20817

R.W. Armstrong^{b)}

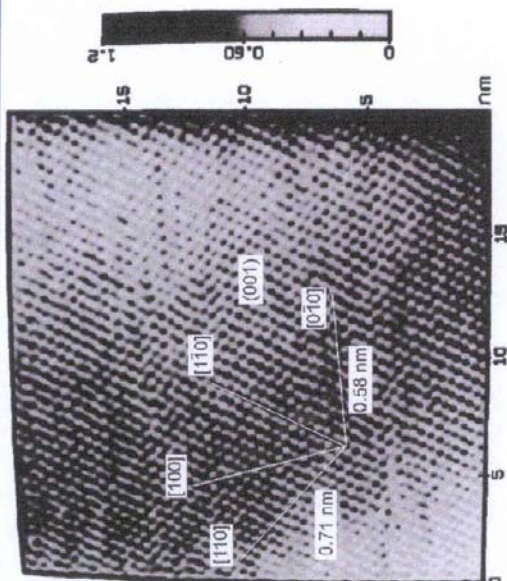
University of Maryland, College Park, Maryland 20742

W.L. Elban

Loyola College, Baltimore, Maryland 21210

C.S. Coffey and H.W. Sandusky

Indian Head Division, Naval Surface Warfare Center, Indian Head, Maryland 20640



Examination with atomic force microscopy has revealed apparent shear-type cleavage steps with heights as small as 0.05 nm, smaller than the size of cyclotrimethylenetrinitramine (RDX) molecules, on the fracture surfaces of crystals that were subjected to aquarium shocks of 61.9 or 129 kbar, both greater than the pressure (38 kbar) required for the alpha-to-gamma phase transformation. The shocked centimeter size, originally transparent crystals became opaque and white from prolific fractures and internal cracks that are associated with their breakup into nanocrystallites of sizes extending from 500 down to 20 nm. The submolecular steps are related geometrically to the macroscale (K_{II}) fracture mechanics mode of shear fracturing that has obvious consequences at the nanoscale level for nonregistry between molecules across the crack surfaces. The results are of interest in relation to lattice trapping of crack fronts and as a contribution to the possibility of deformation-induced chemical decomposition/detonations. © 2001 American Institute of Physics.

[DOI: 10.1063/1.1342046]

a) Corresponding author b) Now at AFRL/MNME, Eglin AFB FL

AAC/PA 01-502



Comparison of Solid-Vapor and Solid-Liquid Interfacial Energies



RDX

$$[\gamma_{sv}] = 0.0432\text{--}0.0503 \text{ J m}^{-2}$$

$$[\gamma_{sl}] = 0.0003\text{--}0.0074 \text{ J m}^{-2}$$

Al

$$[\gamma_{sv}] = \sim 0.84 \text{ J m}^{-2}$$

Al₂O₃

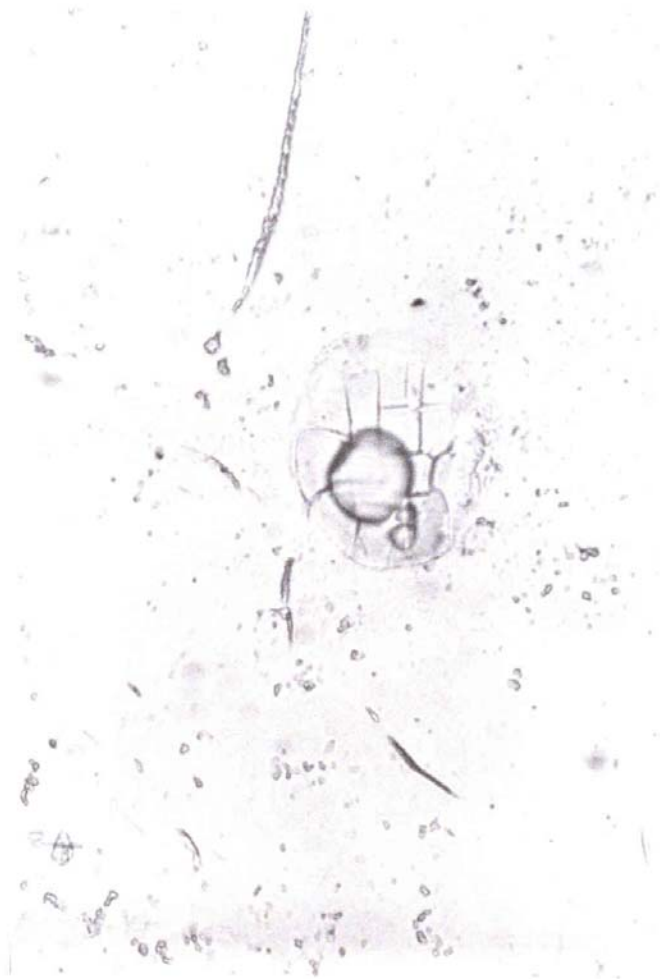
$$[\gamma_{sv}] = 2.15 \text{ J m}^{-2}$$

| Material | $\gamma_{sv}/\text{J m}^{-2}$ | $\gamma_{sl}/\text{J m}^{-2}$ |
|------------------|-------------------------------|-------------------------------|
| Lithium fluoride | 0.340 | 0.181 |
| Sodium chloride | 0.227 | 0.084 |
| Silver | 1.100 1.140 | 0.126 |
| Gold | 1.400 1.410 | 0.132 |
| δ -Iron | 1.950 2.150 | 0.204 |
| Paraffin | 0.0262–0.0263 | 0.0001–0.0019 |
| Polyethylene | 0.0340 | 0.0034 |
| Polystyrene | 0.0433 | 0.0001 |

R.W. Armstrong, C.F. Clark, & W.L. Elban,
Combustion of Energetic Materials
(Begell House, Inc., NY, 2002) p. 354



Liquid-Enhanced Micro-Cracking at a Laser-Melted Spot on an RDX Crystal Surface



AAC/PA 01-502



The Power (and Strength) of Energetic/Reactive Nano Materials

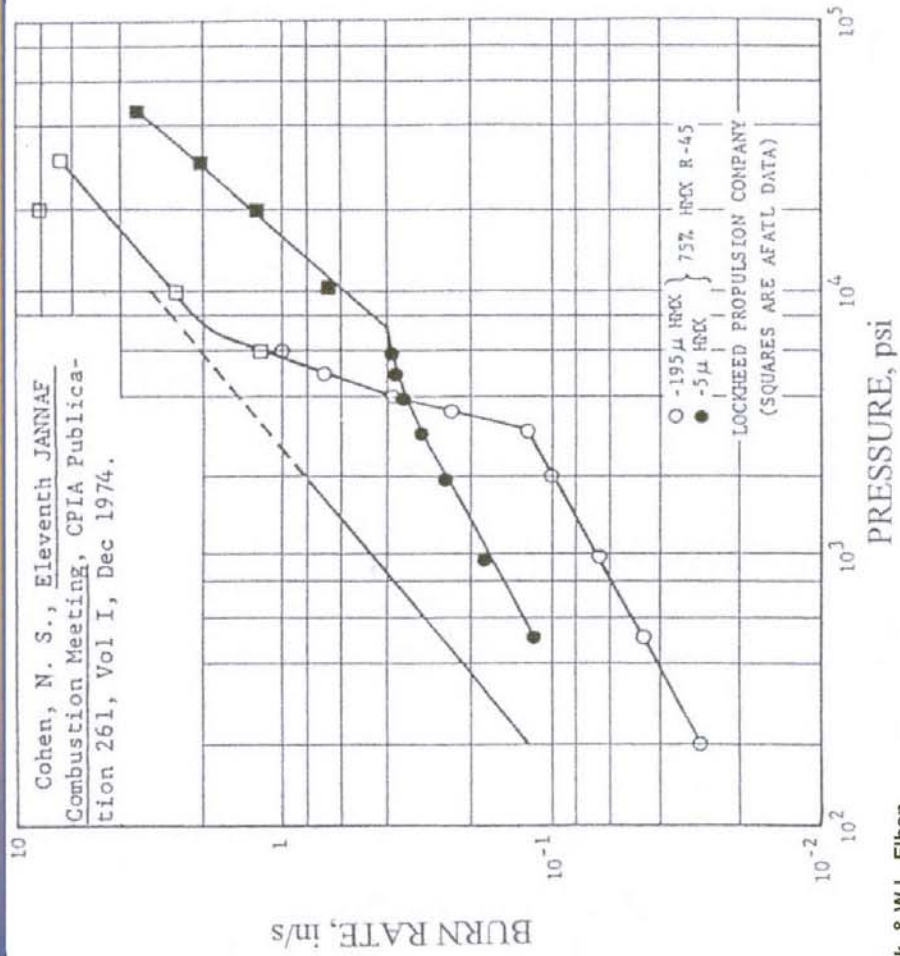


Dislocation defect considerations are presumed to control the mechanical strength and fracturing behaviors, even, of nanometric-scale material particles and structures --- thus presenting challenging areas of research so far as concerns a dearth of material testing methods and also prediction of size-dependent material deformation/decomposition properties. Recent atomic force microscopy (AFM) observations on deformed RDX crystals have indicated the presence of shock-generated nanoscale shear cracks with displacement vectors smaller than the length of individual molecules [3].

3. J. Sharma, C.S. Coffey, R.W. Armstrong, W.L. Elban, and S.M. Hoover, "Sub-Molecular Fracture Steps in Shock-Shattered RDX Crystals and Follow-on Nano-Indentation Evaluation of Early Stage Plasticity", in Shock Compression of Condensed Matter – 2001, M.D. Furnish, N.N. Thadhani and Y. Horie, eds. (AIP Press, N.Y., 2002) Conference Proceedings 620, Part 2, p. 837.



Burn Rate vs Pressure for Two HMX (Cyclotetramethylenetetranitramine) Particle Sizes



R.W. Armstrong, C.F. Clark, & W.L. Elban,
Combustion of Energetic Materials
(Begell House, Inc., NY, 2002) p. 354

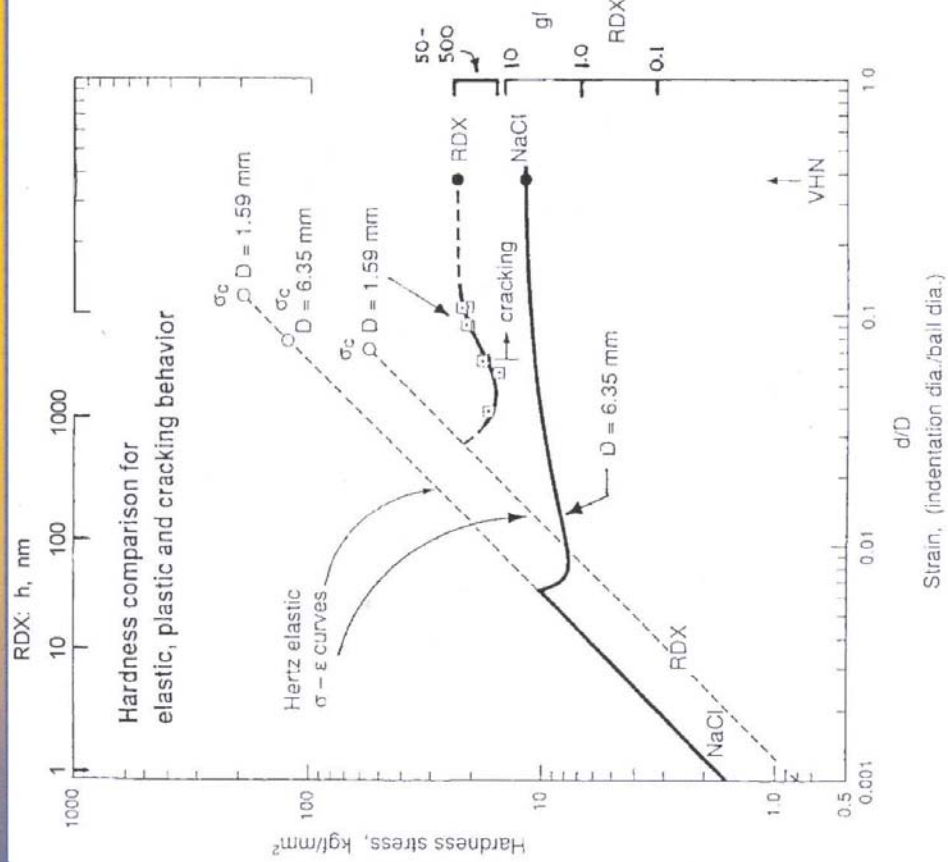


Large Dislocation Self Energies and High Lattice Resistance to Movement in Energetic Crystals

| Material | Dislocation Strain Energy Coefficient ($E_{L/p}$), | $\left(\frac{E_{L/p}}{\Delta H_{f/m}} \right)$ | Peierls-Nabarro Stress, (τ_p), N/mm ² | $\left(\frac{\tau_p}{G} \right)$ |
|----------|--|---|---|-----------------------------------|
| RDX | 6.3×10^{-19} | 12 | 580 | 0.077 |
| LiF | 0.9×10^{-19} | 2.1 | 3100 | 0.050 |
| MgO | 2.4×10^{-19} | 1.9 | 8000 | 0.054 |



RDX is Elastically Softer, Plastically Harder, and More Brittle Than NaCl



W.L. Elban, R.W. Armstrong, &
T.P. Russell, Philosophical
Magazine A, Vol. 78 (1998) p. 907



Model of Dislocation Pile-Up Avalanches



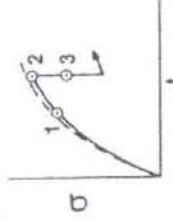
(a) isothermal stress build-up: n_1 dislocations



(b) critical stress concentration: $n_2 \tau_2 = \tau_c^*$



(c) adiabatic collapse-discontinuous load drop



(d) pressure-time curve for τ_1 , τ_2 , and τ_3

$$\Delta T \leq \frac{k_s l^{1/2}}{16\pi} \left(\frac{2v}{c^* b K} \right)^{1/2} \quad \text{if } \left(\frac{2K}{c^* v b} \right) \leq 1.0$$

$$\dot{\gamma} = Nbv,$$

$$v = v_0 \exp \left[- \left(G_0 - \int_{\tau_{th}^0}^{\tau_{th}} bA^* d\tau_{th} \right) / kT \right],$$

$$bA^* = W_0 / \tau_{th},$$

$$\tau_{th} \propto H_{50}^{1/n},$$

$$v = v_0 (H_{50}^0 / H_{50}^0)^{W_0 / nkT} \exp(-G_0 / kT)$$

$$\begin{aligned} \log H_{50} = & \log H_{50}^* + (n/m^*) \log \{ [8\pi\sqrt{2}\Delta T \\ & \times K^{1/2} c^{*1/2} b^{1/2} / k_s v_0^{1/2} \\ & \times \exp(-G_0 / 2kT)] l^{-1/2} \}. \end{aligned}$$

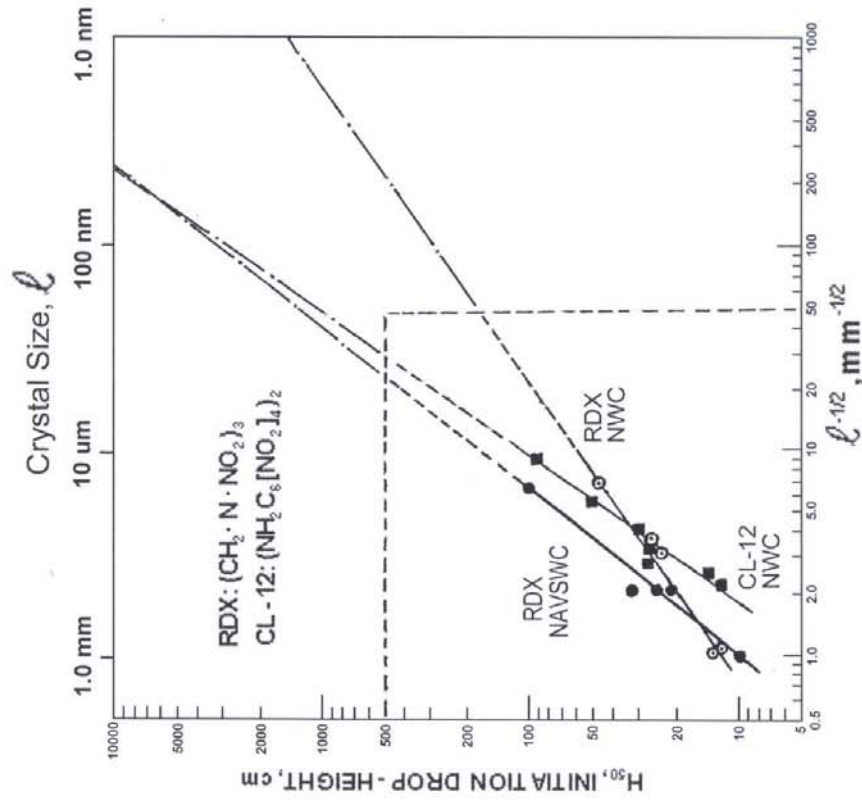
$$m^* = W_0 / 2kT$$



Crystal Size - Sensitivity Relationship



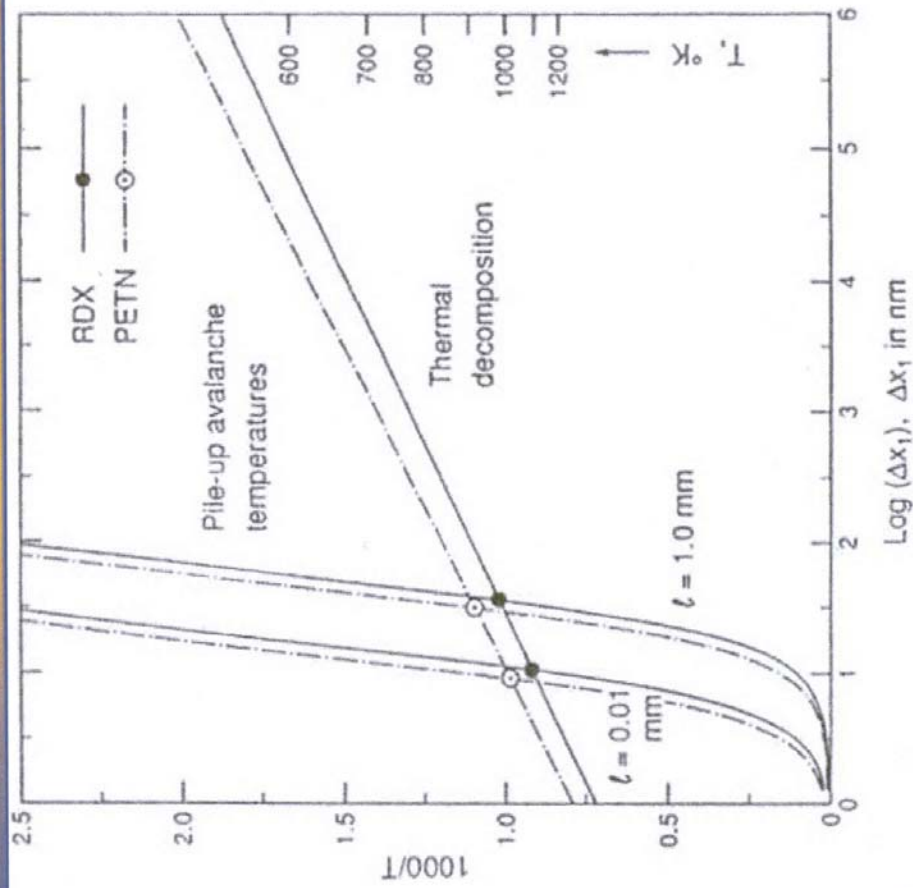
- For conventional explosives, generally initiation sensitivity decreases as crystal size decreases
- Does this trend of sensitivity decrease apply if crystal size is reduced to nano-scale?
- Tests of our nano/explosive composites indicate that it does!
 - Impact & friction sensitivities of nano-CL 20 and nano-RDX better than standards for micron-sized CL-20 and RDX
 - When the coated materials are again coated with binder materials, sensitivities are then better than RDX standards



AAC/PA 02-301



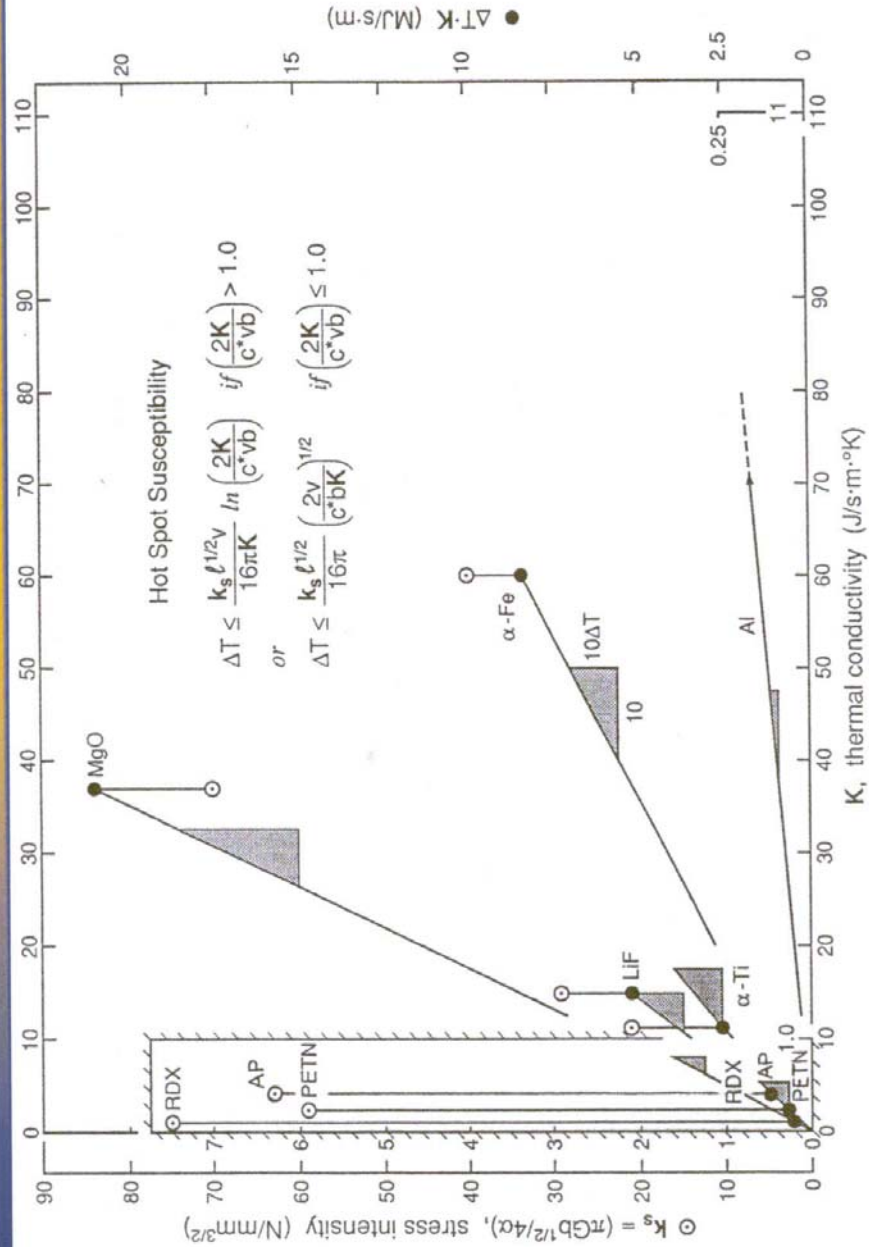
Comparison of Deformation-Induced Hot Spots with Thermal Explosion Predictions for RDX and PETN (Pentaerythritol Tetranitrate) Crystals of Two Sizes



R.W. Armstrong, Journal de
Physique IV, 1995, Colloque C4-89



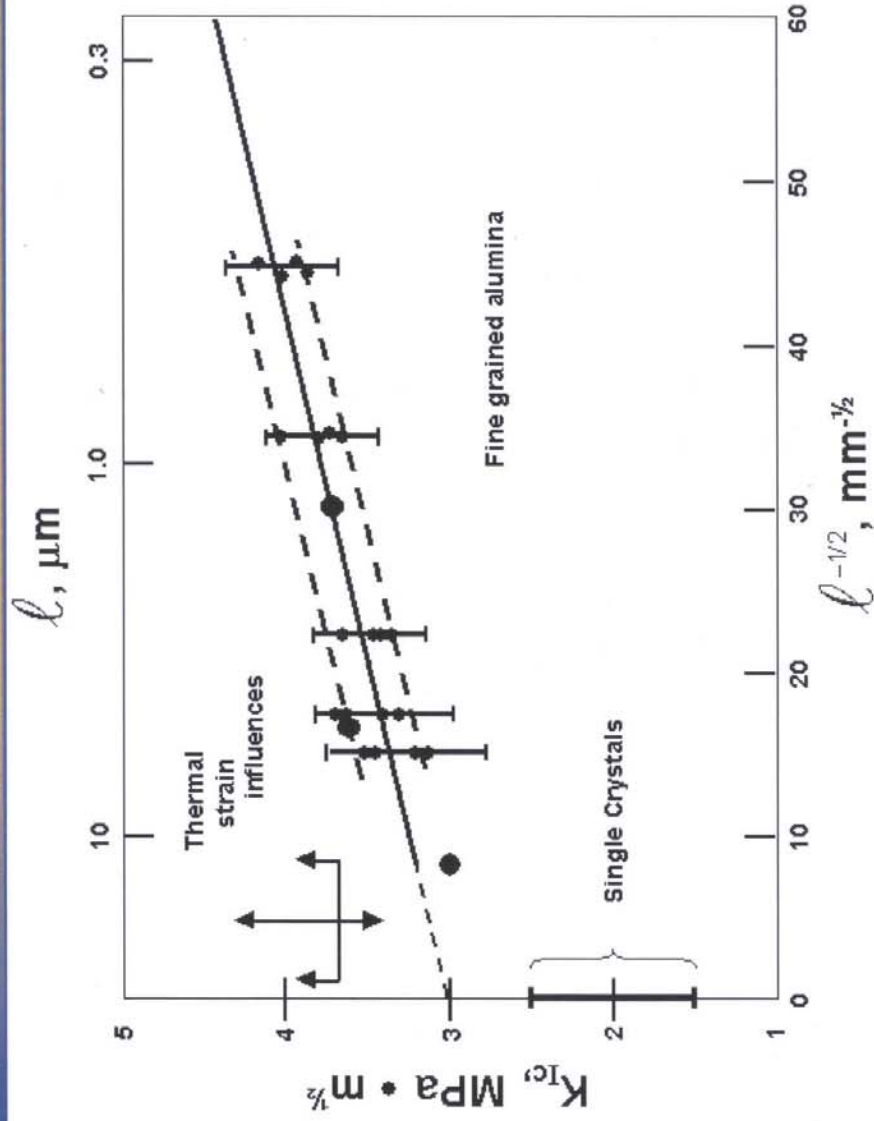
Theoretical Shear Banding/Hot Spot Susceptibility for Energetic & Structural Materials



AAC/PA 01-502

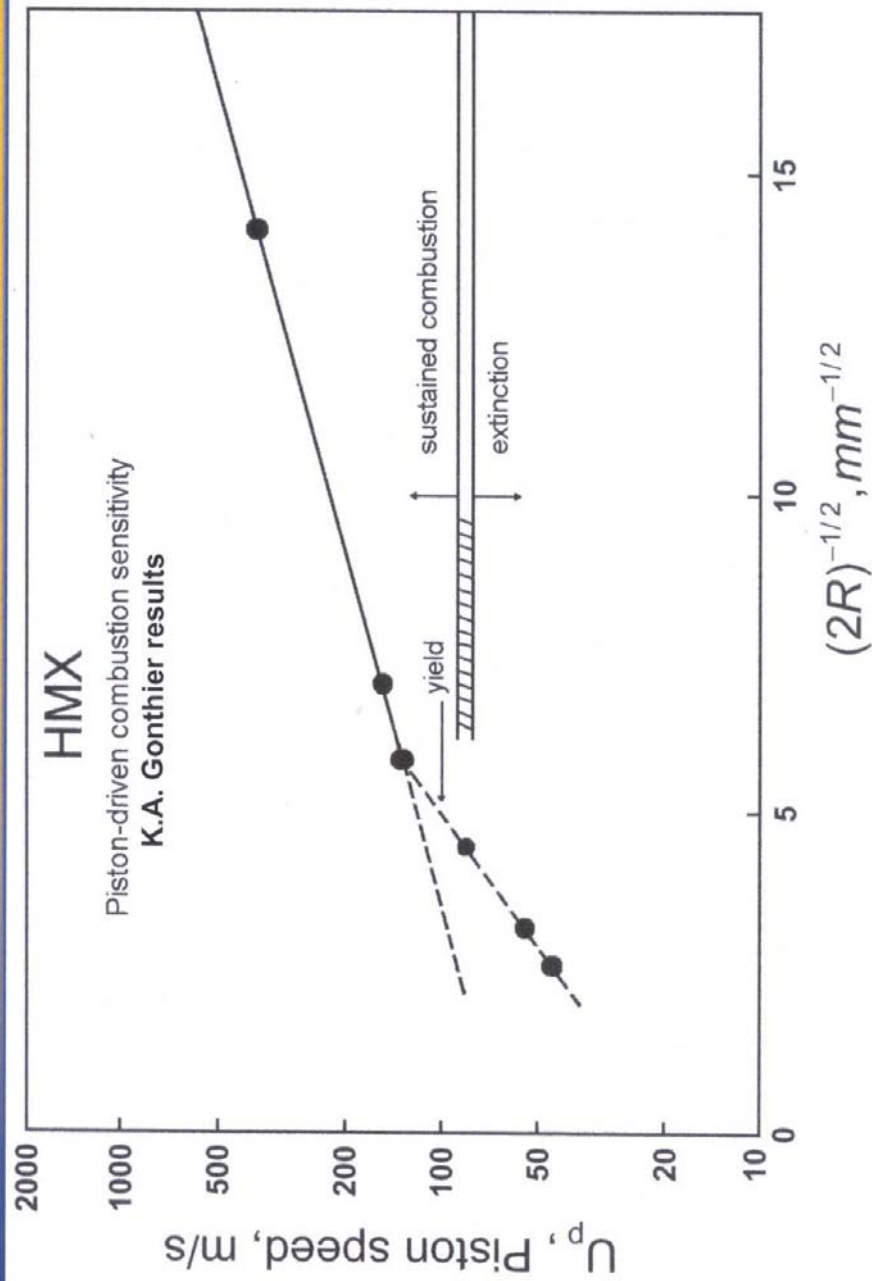


Greater Indentation Stress Intensity (Toughness) for Finer Grained Alumina





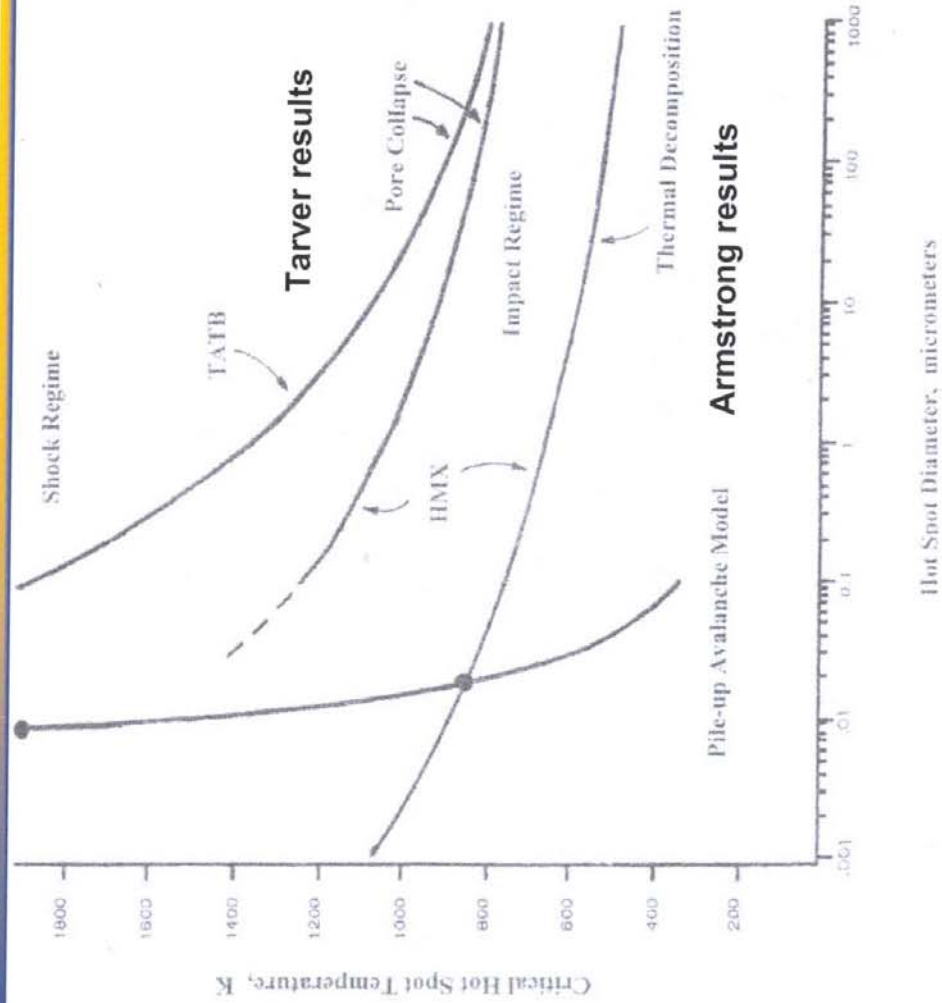
Model Particle Size Influence on Piston-Forced Combustion During Compaction of HMX Particles



AAC/PA 02-291



Comparison of Critical Hot Spot Temperatures for Dislocation Pile-Ups Versus Pore Collapses



AAC/PA 02-291



The Power (and Strength) Of Energetic/Reactive Nano Materials



Summary

SMALL is better

**in the Energetic/Reactive
Nano Materials Future**

Enhanced Propellant Combustion with Nanoparticles

R. W. Armstrong,^{*,†} B. Baschung,[‡] D. W. Booth,[§] and M. Samirant[‡]

AFRL/MNME, Eglin AFB, Florida 32542, ISL, French-German Research Institute of Saint Louis, BP 34, F-68301 Saint-Louis, FR, and Technanogy, LLC, 1601 Alton Parkway, Irvine, California 92606

Received November 22, 2002; Revised Manuscript Received December 19, 2002

ABSTRACT

Enhanced burn rate results are presented for ammonium perchlorate/Al nanoparticle strand burners at atmospheric (and higher) pressure and for the comparative combustion in a high pressure closed vessel of a solid propellant containing 15% of either conventional micrometer-scale Al or nanometric Al. The burn rate at the smallest nanometric Al particle size appears to be asymptotically approaching an inverse particle-diameter-squared dependence.

Surface-Controlled Decomposition. The enhancements at nanometric particle, grain, crystal, or other unit sizes of either structural material strength properties or electronic device/circuit performances appear to be relatively mature research topics compared to the achievement of greater energy release rates at similar ultrafine particle dimensions. Such potential achievement of substantial increases in energy release rates for the chemical decomposition of ultrafine particles might be foreseen, however, because such decompositions are often surface area dependent, as well-demonstrated, for example, in the use of ultrafine particles for catalytic assistance of chemical reactions. Here, we are concerned with the achievement of enhanced propellant (and explosive) energy release rates at nanometric particle sizes, particularly, involving Al particles whose surface-controlled oxidation to alumina is strongly exothermic.¹

Burn Rate Dependence on Al Particle Diameter. Recent early indications of increasing the burn rate of solid rocket propellant materials with addition of Russian-produced "Alex" nanoscale Al powder ingredient has been credited by Baschung et al.² to results reported by Kuo and colleagues.³ Baschung et al. made their own comparison at ISL, France, of the combustion behaviors exhibited by a new double-base gun propellant, at different pressures in a high-pressure closed vessel of 50 cm³ volume. The propellants employed 15% of Alex material substituted for the same amount of conventional micrometer-sized Al in otherwise the same Pechiney YX 76 propellant formulation of 55% nitrocellulose and 30% dioxymethylene dinitrate (DINA). Also recently, Technanogy, LLC has produced another Al nanoparticle material and obtained experimental strand-type

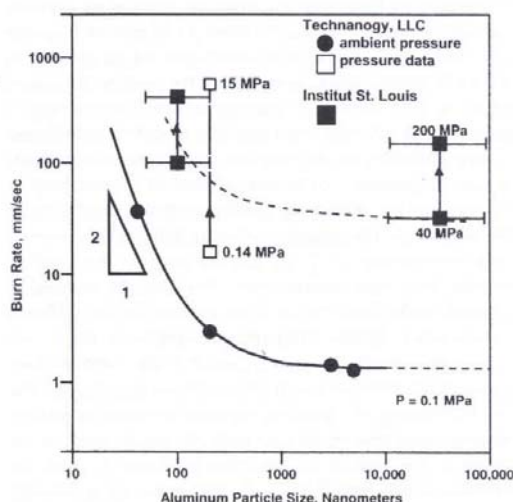


Figure 1. Burn rate as a function of aluminum particle size, also showing indicated pressure ranges for the vertical lines, and providing indication at the smallest particle sizes of an inverse square dependence of burn rate on particle diameter.

burn rate measurements, both as a function of particle diameter at ambient pressure and, separately, for 200 nm particle diameter material burned at different higher pressures.

First, Figure 1 shows a comparison of the combined Alex and Technanogy results in terms of the burn rate dependence on particle diameter. The aluminum material employed in the ISL experiments had a range of particle sizes: for the conventional Al between 10 and 100 micrometers; and, for the Alex Al between 50 and 200 nm. As noted by the vertical

* Corresponding author.

† AFRL/MNME.

‡ French-German Research Institute of Saint Louis

§ Technanogy, LLC

line segments at each particle size, pressures between 40 and 200 MPa were realized in the closed chamber for these burn rates that were monitored in terms of the dynamic vivacity property of the propellants. The dynamic vivacity L is defined as the derivative of the pressure dp/dt divided by the product of the pressure p times the maximum pressure P_{\max} achieved in the experiment, as the expression (STANAG 4115):

$$L = dp/dt \times 1/p \times 1/P_{\max}$$

Monitoring the vivacity during the pressure histories provided an account of the change in burning behavior during consumption of the material mass. For the ISL comparison of the two different sized Al ingredients, emphasis was given to the Alex-containing propellant exhibiting a pressure-dependent steep increase in vivacity at the beginning of combustion. The initial burn rate behavior was found to depend only on pressure and not on loading density, apparently eliminating such mechanical effect as porosity from playing a major role in determining the higher Al nanoparticle burn rate property.²

Also shown in Figure 1 are the Technanogy strand-type burn rate measurements obtained for different Al particle diameter ingredients within a standard ammonium perchlorate formulation. The strands were 3.175 mm in diameter with 88% solids and of 6.35–8.47 mm length pressed to 80–85% density. Here, as indicated, the particle diameters, found by high resolution scanning electron microscopy to be essentially spherical, were carefully sieved to the indicated particle diameters and the burn rate measurements were made at ambient pressure. As shown, substantial enhancement of the burn rate occurred in the particle diameter range between 200 and 40 nm, for example, giving an indicated exponential slope dependence of $\{-2\}$ marked near the smallest particle burn rate measurement. For this Al material a nominal oxide thickness of 2 nm applies for the different particle sizes. Similar burn rate measurements have been made with strands containing greater solids content, even approaching 100%, and with other oxidizer ingredients.⁴ For the Technanogy Al product, separate pressure-dependent measurements were made also with 200 nm Al particles. In Figure 1, the vertical line segment is shown to cover an increase in burn rate from ~12–580 mm/s for a pressure increase from 0.14 to 15 MPa, respectively, and shown at the higher pressure, to give a greater burn rate than achieved with the ISL gun propellant.

Burn Rate/Pressure Dependencies. The pressure, P , dependence of the propellant burn rate, r , is normally of interest for description via a power law dependence, that is, in accordance with the so-called Vieille's law, expressed as²

$$r = \beta P^\alpha$$

in which β and α are experimental constants. The general form of the power law dependence has a theoretical interpretation.⁵ In particular, small values of the pressure exponent, α , are aimed for, in order to avoid transition to unstable burning at high pressures. Figure 2 shows a comparison of

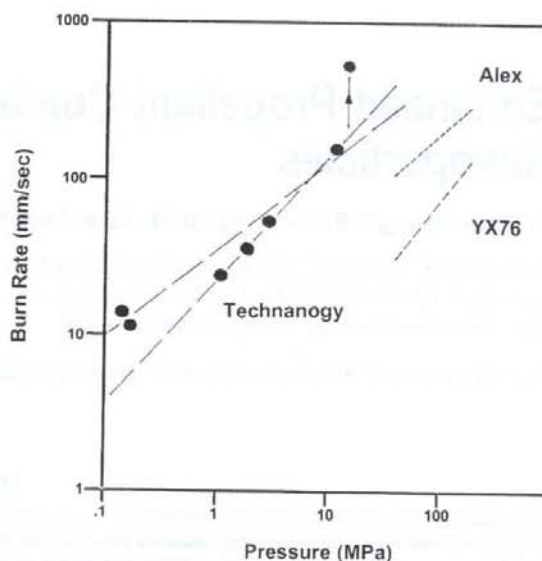


Figure 2. Pressure dependence of the burn rate for 200 nm particle diameter aluminum and for conventional and Alex containing aluminum gun propellant.

the pressure dependent results obtained by Baschung et al. for both gun propellant materials in comparison with results obtained in the Technanogy experiments.

A smaller (exponential) slope, α , for the Alex-containing gun propellant of 0.66 was deduced by Baschung et al., in comparison with α equal to 0.8 for the conventional Al sized propellant, and an enhanced β value of 9.85 mm/s was obtained for the new formulation with Alex material. For the Technanogy product, the power law dependence is obeyed strictly only at the intermediate pressures between 1.1 and 11.3 MPa, giving an α value near to that of the conventional gun propellant along with an appreciably increased β value of 25 mm/s. Otherwise, an average long-dashed line of larger β and smaller α is shown in Figure 2 in order to adjust to the lowest pressure measurements. The lowest pressure measurements, which are high relative to the Vieille law extrapolation, may be compared to the separately determined particle diameter dependence measurements shown in Figure 1. More interestingly, the highest measured burn rate 583 mm/s at 15 MPa in Figure 2 is shown to be significantly above the Vieille dependence for the lower pressure measurements, thus being indicative of unstable burning.

Model Consideration. A burn rate dependent on the inverse square of the Al particle diameter should be expected at very small particle sizes because of the energy release rate being determined by the available amount of particle surface area, say, specified by the number of Al particles per unit surface area. The surface area change with particle diameter is innocuous at large particle diameters where continuation of individual particle burning is controlled more so by further diffusion of Al atoms through the coherent alumina "skin". Such inverse square of the nanoparticle size dependence compares, for example, to a lesser particle-

diameter-determined burn rate controlled by the amount of particle surface area per unit volume (within the burn zone), then corresponding to a reciprocal dependence of the burn rate on particle diameter. A higher burn rate dependence even than the inverse square dependence would be determined for control by the number of particles per unit volume, corresponding to a reciprocal cube dependence on the particle diameter. For any of these proposed bases, the current results give promising indication of order(s) of magnitude enhancement of energy release rates in the new regime of nanometric particle ingredients, and current experiments/analyses are in progress in pursuit of firmer grounding of the potential enhancements.¹

Acknowledgment. Appreciation is expressed to Byron Allmon, at AFRL/MNME, for construction of figures and assistance with the manuscript.

Note Added in Proof: Recent contact with Professor Dana Dlott, University of Illinois, has led to receipt of a proof copy of the coming *Chemical Physics Letters* article "Fast spectroscopy of energy release in nanometric explo-

sives", co-authored by Shufeng Wang, Yanqiang Yang, Zhaoyong Sun, and Dana D. Dlott, in which important laser-induced measurements are described of nanosecond-scale energy release rate characteristics for a dilute 1% Alex/nitrocellulose system.

References

- (1) Wilson, W. H.; Kramer, M. P.; Armstrong, R. W. In *Symposium on Defense Applications of Nanomaterials*; 221st ACS National Meeting, 1–5 April, 2001, San Diego, CA, CD-ROM.
- (2) Baschung, B.; Grune, D.; Licht, H. H.; Samirant, M. In *Combustion of Energetic Materials*; Kuo, K. K., DeLuca, L. T., Eds.; Begell House: NY, 2001; p 219.
- (3) Mench, M. M.; Yeh, C. L.; Kuo, K. K. In *Proceedings of the 29th International Annual Conference of Institut Chemische Technologie (ICT)*; Karlsruhe, Germany, 1998; pp 30/1. Chiaverini, M. J., Serin, N., Johnson, D. K., Lu, Y. C., Kuo, K. K. In *Challenges in Propellants and Combustion 100 Years after Nobel*; Kuo, K. K., Ed.; Begell House: NY, 1997; p 719.
- (4) Booth, D. W. Private communication.
- (5) DeLuca, L. T.; Verri, M.; Cozzi, F.; Jalongo, A.; Columbo, G. In *Challenges in Propellant and Combustion 100 Years after Nobel*; Kuo, K. K., Ed.; Begell House: NY, 1997; p 493.

NL025905K

GRAIN SIZE DEPENDENCE OF SHOCK INDUCED TWINNING STRESSES FOR ARMCO IRON

R.W. Armstrong*, W. Arnold**, and F.J. Zerilli***

*AFRL/MNME, 2306 Perimeter Road, Eglin Air Force Base, FL 32542, U.S.A.

**TDW – Gesellschaft für verteidigungstechnische Wirksysteme mBH,
P.O. Box 1340, D-86523 Schrobenhausen, Germany

***Naval Surface Warfare Center, Indian Head Division, 101 Strauss Avenue, Indian Head, MD 20640, U.S.A.

Measurements fitted to a linear inverse square root of grain size dependence for the deformation-twinning-determined Hugoniot Elastic Limit (HEL) stresses of shocked Armco iron specimens of differing average grain sizes are shown to compare favorably with a Hall-Petch (H-P) dependence established for the combination of split Hopkinson pressure bar (SHPB) and conventional deformation test results known to be controlled by deformation twinning. The comparison of shock test results, in the pressure range of ~0.6 to ~2.0 GPa, are suggested to give a counterpart match of HEL and conventional twinning stress values analogous to the calibration of reference static and shock pressure levels required for the $\alpha - \epsilon$ phase transition, in the latter case, corresponding to a volumetrically-better-specified pressure of 13.5 GPa. A further comparison of the essentially athermal twinning stresses with those computed for plastic flow on a dislocation mechanics model basis provides for a grain size dependent transition between twinning- or slip-determined plastic flow stresses.

INTRODUCTION

At higher strain rates and larger polycrystal grain diameters, deformation twinning is an increasingly likely deformation mechanism in structural metals, particularly, body centered cubic (bcc) metals and alloys (1). Current interest centers on the role of twinning under shock loading conditions (2). In the present report, pioneering laboratory test results (3-5) and more recent shock test results (6,7) obtained on deformation twinning in low carbon and Armco iron are brought together on a Hall-Petch (H-P) stress versus inverse square root of average grain diameter basis to give a rational explanation of shock-induced deformation twinning and its relationship to alternative deformation by dislocation mechanics based viscoplastic slip. The compared deformation behaviors relate also to particular solid cylinder impact (Taylor) test results where essentially athermal twinning occurs on first impact and is followed, on a microsecond time scale, by later initiation of dislocation slip within the twin-hardened material (8).

TWINNING VS. SLIP

Figure 1 shows, first, addition of shock-related strength measurements for specimens of different average grain diameters (7) to a previous Hall-Petch (H-P) based compilation (8) of experimental and theoretical slip and twinning stresses collected for

annealed Armco iron materials and, in one case, annealed SAE 1010 steel material, as obtained too on test specimens with different polycrystal grain sizes. In the Figure, the Armco iron twinning stress points listed for the five different temperatures in the range between 88 and 248 K [3], were reported separately at each temperature in the original work as proportional limit (p.l.) stresses, as measured in split-Hopkinson pressure bar tests at a strain rate of $1.1 \times 10^3 \text{ s}^{-1}$.

On a combined data basis, the different temperature dependent twinning results show that preference for twinning over slip was restricted to lower temperatures for smaller polycrystal grain sizes. That is, the temperature-dependent transition from an athermal twinning-controlled yield stress to a thermally-activated slip-controlled one moves to lower temperatures for smaller grain size materials. In Figure 1, the relatively high stress, cross-within-circle, datum at large grain size, was obtained by Rohde (4) in a shock-loading test where extensive twinning occurred. The 1010 steel measurement in the Figure, designated MWA (5) and spanning a vertical range in stress between proportional limit (p.l.) and load drop (l.d.) stresses, was obtained by compression testing at a conventional laboratory strain rate of $2.8 \times 10^{-4} \text{ s}^{-1}$ and at liquid helium temperature, 4.2 K. The higher (l.d.) stress value was determined for pronounced, twin-produced, load drops that accompanied yielding after further stress loading past the lower p.l. stress. This higher raised stress for general yielding, after the p.l., was employed in relation

to all of the p.l. data then for designation of the H-P linear stress dependence shown for the twinning yield stress and expressed in the H-P relation:

$$\sigma_T = \sigma_{T0} + k_T \ell^{-1/2} \quad (1)$$

where $\sigma_{T0} = 330$ MPa and $k_T = 90$ MPa.mm^{1/2}. Equation (1), with these constants, was employed in model calculations that predicted satisfactorily the involvement of twinning in cylinder impact (Taylor) test results (8).

Also shown in Figure 1 are several computed H-P dependencies for dislocation mechanics based model

computations of the so-called Z-A slip-controlled plastic yield stress at different strain rates, expressed as

$$\sigma_y = \sigma_0 + k \ell^{-1/2} \quad (2)$$

where the slope, k , though being smaller than k_T , is also athermal, and σ_0 is given by

$$\sigma_0 = \sigma_G + B e^{-\beta T} \quad (3)$$

where

$$\beta = \beta_0 - \beta_1 \ln(\dot{\epsilon}) \quad (4)$$

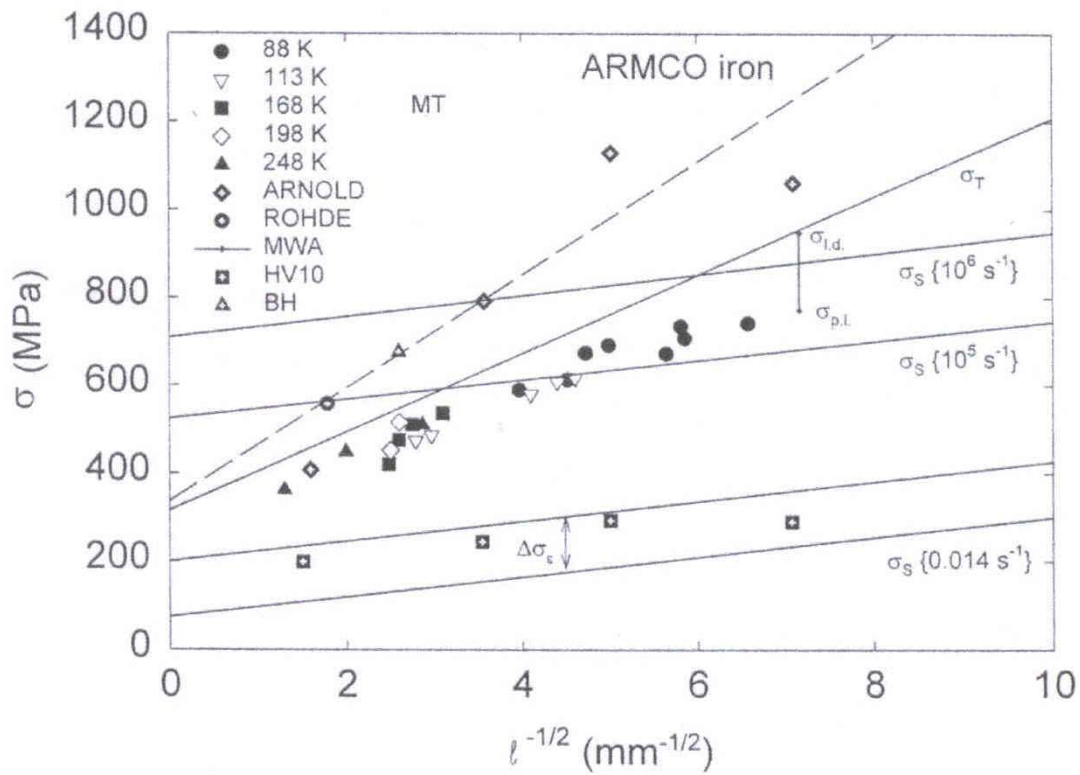


Figure 1. Comparison of experimental shock test results with previous high strain rate or low temperature laboratory test measurements, including computed viscoplastic slip-controlled yield stress results at different strain rates and, also, converted reference hardness flow stress values.

with material constants previously reported for Armco iron (9) as $\sigma_G \sim 0$, $B = 1033$ MPa, $\beta_0 = 0.00698$ K⁻¹, and $\beta_1 = 0.000415$ K⁻¹. The cross-within-circle yield stress point (4), mentioned earlier in Figure 1, for example, applies for twinning detected in the shock wave test at an estimated strain rate of 10^5 s⁻¹, that is in agreement otherwise with the somewhat higher stress

predicted for slip-controlled yielding at that same strain rate.

The slip-controlled yield stress H-P lines at different strain rates in Figure 1, with $k = 22$ MPa.mm^{1/2}, give increasing yield stresses that are raised non-linearly from the lowest conventional laboratory strain rate of

0.014 s⁻¹ to the indicated higher strain rates, all in accordance with the thermal dependence in σ_0 in eqs. 3 and 4.

The second lowest H-P line in Figure 1, however, was computed for the conversion of Vickers HV10 hardness measurements that were made initially on the annealed Armco iron material prior to shocking (7). In this case, with multiplication of the hardness pressure by a factor of (1/3), the measurements, made at 10 kgf load, are converted to estimated compressive flow stress values corresponding to a true strain of 0.075.

The predicted increase in flow stress shown for the second-lowest hardness-determined H-P line in Figure 1 was obtained by accounting for the strain hardening at 0.075 strain past yielding with the stress increment

$$\Delta\sigma = K\varepsilon^n \quad (5)$$

where, for Armco iron (9), the experimental constants are obtained as $K = 266$ MPa and $n = 0.289$. As indicated in the Figure, a computed increase in stress value of 126 MPa is predicted for the raised H-P flow stress line, that is somewhat above the converted hardness points but otherwise provides a reasonable basis for relating the conventionally assessed plastic flow measurements for the pre-shocked material and those results to be described now for shock testing.

Relatively higher, twin-controlled, both cross-within-circle-, -within-triangle-, and four -within-diamond-identified yield stress values are shown in Figure 1, as determined from Hugoniot elastic limit (HEL) measurements obtained in shock-type, plate impact, tests (6,7,10). The HEL measurements have been transformed to unidirectional yield stress measurements according to the relationship

$$\sigma = [(1-2\nu)/(1-\nu)] \sigma_{\text{HEL}} \quad (6)$$

with $\nu = 0.28$, being Poisson's ratio.

Despite the observation being made that there is significant scatter from the linear dashed H-P dependence shown for the six converted HEL-type measurements in Figure 1, the measurements are taken anyway to give the suggested greater H-P line dependence that is indicated. There are reasons for expected test variations. The HEL is not easily determined experimentally, say, relative to the better volumetrically-determined $\alpha - \varepsilon$ phase transformation in iron, also, occurring at a greater pressure of 13.5 GPa. And, in Figure 1, for example, the largest grain size converted HEL measurement, that is shown to fall

below the dashed H-P twinning line for this set of data, is very probably accounted for by stress lowering associated with a reduced number of grains in the specimen cross-section (7) and, therefore, a reduction in true polycrystalline constraint associated with restricted accommodation of the twinning strain (1).

THE TWINNING k_T

The H-P dependencies shown in Figure 1 for the slip and twinning stresses are fully consistent with a model dislocation pile-up explanation for the relation, including explanation of the slope, k_T , being a microstructural stress intensity that is greater for nucleation of twinning at grain boundaries as compared with the smaller k for the propagation of slip (1). A dislocation pile-up based model description was given earlier for the nucleation of twinning (11), with parametric evaluation of k_T being logarithmically dependent on the strain rate raised to a small power. And numerical estimates were given previously also for k_T depending only weakly on temperature and even more weakly on the strain rate.

Arnold reported elastic strain rate values in the range of 10^5 -to- 10^6 s⁻¹ for his HEL test results, except for the one lower measurement for the largest grain size test (7). According to the weak twinning dependence derived from (11), mentioned above, an increase in k_T between 9 and 14% of the conventionally-determined value is estimated. The predicted increase at the shock-type strain rates for k_T , although large enough to be experimentally measured, is smaller than that indicated by the dashed line for $k_T = 130$ MPa.mm^{1/2} from the shock wave measurements.

Such consideration of the k_T value leads to an available alternative upper limit for such H-P k values, say, by comparison with theoretical and experimental upper-limiting k values for cleavage. The tensile cleavage value, k_C , is estimated in one way by the circular pile-up stress intensity for dislocation coalescence (12) as

$$k_C = (m\pi/4\alpha) Gb^{1/2} \quad (7)$$

where m is an orientation factor, $\alpha = 2(1-\nu)/(2-\nu)$, G is the shear modulus and b is the dislocation Burgers vector. With $m = 2$, a value of $k_C \sim 80$ MPa.mm^{1/2} is obtained (12) that compares with the k_T value of 90 MPa.mm^{1/2} from Figure 1 and with experimental cleavage values (13,14) between 90 and 120 MPa.mm^{1/2}. No cracking was found in the shock-loaded specimens of Arnold at the HEL and so the

drawn dashed estimation of k_T in Figure 1 is very probably an overestimate of the true k_T value.

CYLINDER IMPACT RESULTS

A major application of the separate constitutive equations (1) and (2), for twinning versus slip in Armco iron, has been to prediction of solid cylinder (Taylor) impact test results, for example, reported by Johnson and Cook (15), and modeled with their Lagrangian (Elastic Plastic Impact Computation) EPIC material dynamics code (8,9). With the deformation twinning

stress in eqn (1) taken as essentially athermal, then twinning should definitely occur on first impact, if the stress is high enough, and should be followed then by viscoplastic slip in the "new" twin hardened structure. McKirgan (16) has verified the sequential nature of the overall deformation process by step-wise model assessment of the Taylor-type deformation state.

More recently, Taylor test results have been reported for the same shock-tested Armco iron material as

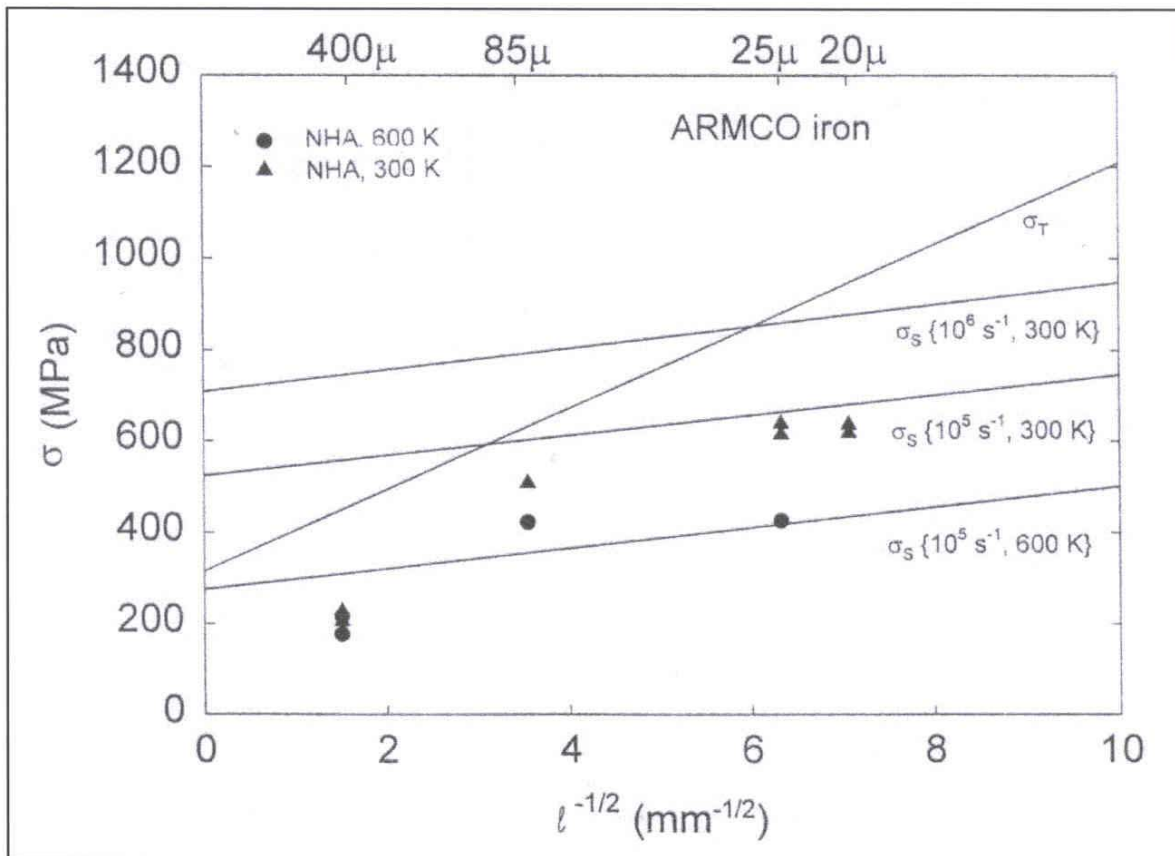


Figure 2. Cylinder impact (Taylor) test results obtained at 300 or 600 K, in comparison with twin- or slip-controlled yield stress relations.

employed for the multiple HEL measurements shown in Figure 1. The Armco iron material has now been tested at the two temperatures of 300 and 600 K as shown by the measured points labeled NHA (17) and

plotted in Figure 2. In this case, comparison is also made at 300 K with the twinning and high strain rate slip determined H-P dependencies taken from Figure 1. An additional computed H-P line has been put onto the

Figure for 600 K and a strain rate of 10^5 s^{-1} , that is appropriate also to such Taylor test results (9).

An apparent curvature in an H-P dependence is indicated in Figure 2 for the total VISAR-determined yield stress points. However, the superposition of the separate H-P dependencies for twinning and slip indicates that the curvature is more likely a consequence of twinning being the controlling mechanism for yielding at the largest grain size and slip, at the smallest grain sizes. Such interpretation is in line with metallographic observations made on the impacted specimens (17). Again, the large grain points, although showing the yield stress to be essentially athermal, are relatively low because of the lack of full polycrystal constraint associated with few grains being present in the specimen cross-section. Further support for this interpretation comes from the reported remark that the deformation of individual grains showed up in the velocity curve records of the large grained specimens, thus connecting with the earlier explanation of the large grain HEL result in Figure 1. An important metallographic observation on the deformed specimens led to the conclusion that deformation twinning had preceded follow-on slip deformation on the basis of the distorted shapes of the otherwise expected straight deformation twin boundaries.

Finally, such consideration as described here of added twinning complication to deciphering the shock-induced deformation properties of structural materials is but one of several challenges necessarily involved with the special regime of shock-induced deformations. For example, the very substantial displacements occurring at nanometric dimensions at all points along the shock front are not, in general, capable of being relaxed by remote displacement of the more widely-spread, initially present, resident dislocation population. Instead, even without twinning, a nano-scale dislocation structure is produced sequentially at the propagating shock front, and left behind for interaction with the lagging movement of the originally resident dislocation structure (18,19). Thus, another additional consideration of a "changed material" to be dealt with in describing subsequent viscoplastic flow obtains. An interesting consequence of such consideration is the description of simultaneous increases in both strength and ductility under particular high strain rate conditions (20).

SUMMARY

A Hall-Petch dependence is indicated for the shock wave determined HEL yield stress of Armco iron material whose shock response is controlled by deformation twinning. Under such high strain rates, in the range of 10^5 to 10^6 s^{-1} , as occur in shock loading compared to conventional and split Hopkinson pressure bar (SHPB) tests, the further indication is that a somewhat greater H-P microstructural twinning stress intensity, k_T , value is obtained.

The relatively different H-P dependence for twinning as compared with slip, when applied in constitutive equation descriptions of the two behaviors, demonstrates that twinning is favored at larger grain sizes in both shock loading and cylinder impact (Taylor) tests. During impact in a Taylor test, twinning occurs before slip, if the stress level is sufficiently high, and then further deformation is achieved by viscoplastic slip in the newly twinned (and hardened) material.

ACKNOWLEDGEMENTS

Joined support received earlier for this research at the University of Maryland College Park (UMCP) and at the Indian Head Division of the Naval Surface Warfare Center (IHD, NSWC) was provided both by the UMCP/NSWC Center for Energetic Concepts Development and the IHD, NSWC Independent Research Program. The shock test and hardness results reported in reference 7 were obtained as part of the doctoral thesis research of W. Arnold at the Technical University of Munich. Ms. Thelma Miller (UMCP) and Mark Grimmonpre and Byron Allmon (AFRL/MNME) are thanked for help with formatting the article and incorporation of Figures.

REFERENCES

1. Armstrong RW, Zerilli FJ. *Advances in Twinning*, eds. S Ankem, CS Pande. Warrendale PA: The Minerals, Metals and Materials Society (TMS), 1999:67.
2. Murr LE, Meyers MA, Niou C-S, Chen YJ, Pappu S, Kennedy C. *Acta Mater.* 1997; 45:157.

3. Moiseev VF, Trefilov VI. *Phys. Stat. Sol.* 1966;18:881.
4. Rohde RW. *Acta Metall.* 1969;17:353.
5. Madhava NM, Worthington PJ, Armstrong RW. *Philos. Mag.* 1972;25:519.
6. Arnold W. *Shock Compression of Condensed Matter - 1991*, eds. SC Schmidt, RD Dick, JW Forbes, DG Tasker. Amsterdam: Elsevier Sci. Publ. B.V., 1992:539.
7. Arnold W. *Dynamisches Werkstoffverhalten von Armco-Eisen bei Stosswellenbelastung*, Dusseldorf: Fortschr.-Ber. VDI Reihe 5 Nr. 247 VDI-Verlag, 1992.
8. Armstrong RW, Zerilli FJ. *J. Phys.-Coll.* 1988;49:C3-529.
9. Zerilli FJ, Armstrong RW. *J. Appl. Phys.* 1987;61:1816.
10. Barker LM, Hollenbach RE. *J. Appl. Phys.* 1974;45:4872.
11. Armstrong RW, Worthington PJ. *Metallurgical Effects at High Strain Rates*, eds. RW Rohde, BM Butcher, JR Holland, CH Karnes. New York NY: Plenum Publ., 1974:401.
12. Armstrong RW, Elban WL. *Mater. Sci. Eng. A*, 1989;122:L1.
13. Madhava NM. *Stress-Grain Size Analysis of the Yield and Fracture Behavior of Steel and Titanium at 4.2 K*, Ph.D. Thesis, University of Maryland, 1975.
14. Armstrong RW. *Eng. Fract. Mech.* 1987;28:529.
15. Johnson GR, Cook WH. *Proceedings of the Seventh International Symposium on Ballistics*. The Hague, The Netherlands, 1983:541.
16. McKirgan JB. *Microstructurally-Based EPIC Simulations of Taylor Impact Tests*, M.Sc. Thesis, University of Maryland, 1990.
17. Nahme H, Hiltl M, Arnold W. *Shock Compression of Condensed Matter - 1995*, eds. SC Schmidt, WC Tao. New York NY: Amer. Inst. Phys., Conf. Proc. 370, Part 1, 1996:619.
18. Bandak FA, Armstrong RW, Douglas AS. *Phys. Rev. B* 1992-II;46:3228.
19. Bandak FA, Tsai DH, Armstrong RW, Douglas AS. *Phys. Rev. B* 1993-II;47:11681.
20. Armstrong RW, Zerilli FJ. *Fundamental Issues and Applications of Shock-Wave and High-Strain-Rate Phenomena*, eds. KP Staudhammer, LE Murr, MA Meyers. New York NY: Elsevier Science Ltd, 2001:115.

DISLOCATION MECHANICS ASPECTS OF IMPACT/SHOCK INITIATION OF DETONATION

R.W. Armstrong

AFRL/MNME
2306 Perimeter Road
Eglin Air Force Base, FL 32542

Deformation shear influences, rather than hydrostatic pressure considerations, are described for impact/shock initiation behaviors of energetic crystals in terms of differentiating between discrete dislocation and continuum mechanics descriptions of shear banding properties. The dislocation mechanics view extends downward to inter-molecular interactions at the crystal lattice scale and includes the proposed creation of nanometer-scale dislocation structures at sufficiently strong shock fronts. An initial comparison is given between dislocation pile-up avalanche and pore collapse models for impact/shock initiations.

INTRODUCTION

Modern research study has been directed to assessing the relative importance of shear stress/strain behaviors of solid energetic material formulations as compared with hydrostatic pressure influences on initiation behaviors. Not so long ago, Eyring (1) pointed out in discussion, presumably on an hydrostatic pressure basis, that initiation in the solid state must involve an effective space associated with holes, dislocations, or the

separations of grains where the breaking up of a(n energetic) molecule can occur with respect to the same strong bond in the gas phase. In this same vein, Gilman and Armstrong (2) gave emphasis in developing model results for the shear-induced polymerization of benzene to the pioneering “mechanochemistry” experiments of Bridgman demonstrating that shear stresses combined with compression enhanced the onset of chemical reaction.

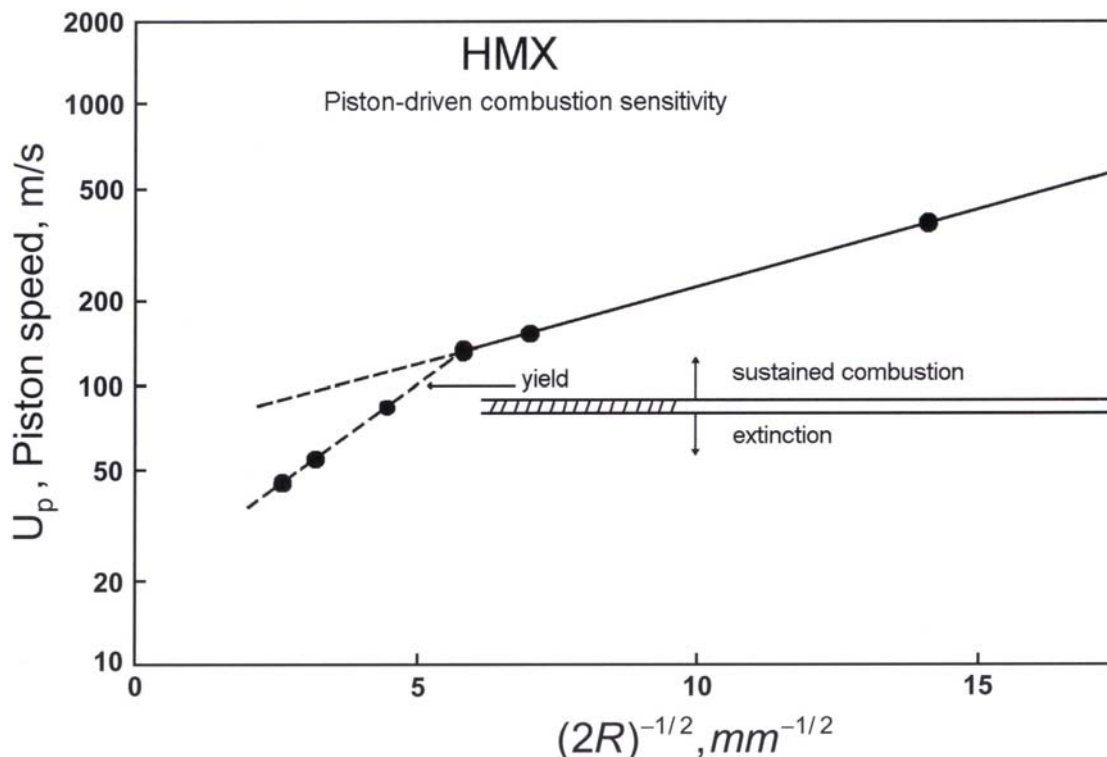


Figure 1. Particle size dependence of model piston-driven impacted beds of HMX particles, after computed results presented by Gonthier (5).

In the current report, the mechanism of hot spot development accomplished via internal stress concentrations leading even to crystal fracture associated release of a dislocation pile-up avalanche (3) is considered in further detail, including certain comparisons with a continuum mechanics model view of shear banding. Connection of the dislocation mechanics model with crystal-lattice-scale considerations of molecular stability and bond breaking is described. And, lastly, preliminary comparison is made between the shear-based dislocation avalanche mechanism and a pressure-based pore collapse mechanism for hot spot generation.

MODEL RESULTS

Particle Size Influences

The dislocation pile-up avalanche model has been characterized by a parametric inverse square root of crystal or grain size dependence for the drop-weight impact sensitivity property. Supporting drop-weight impact sensitivity results were presented (4) for RDX (cyclotrimethylenetrinitramine). Additional crystal size dependent results for RDX and a related energetic crystal structure, CL-12, were similarly presented later (5).

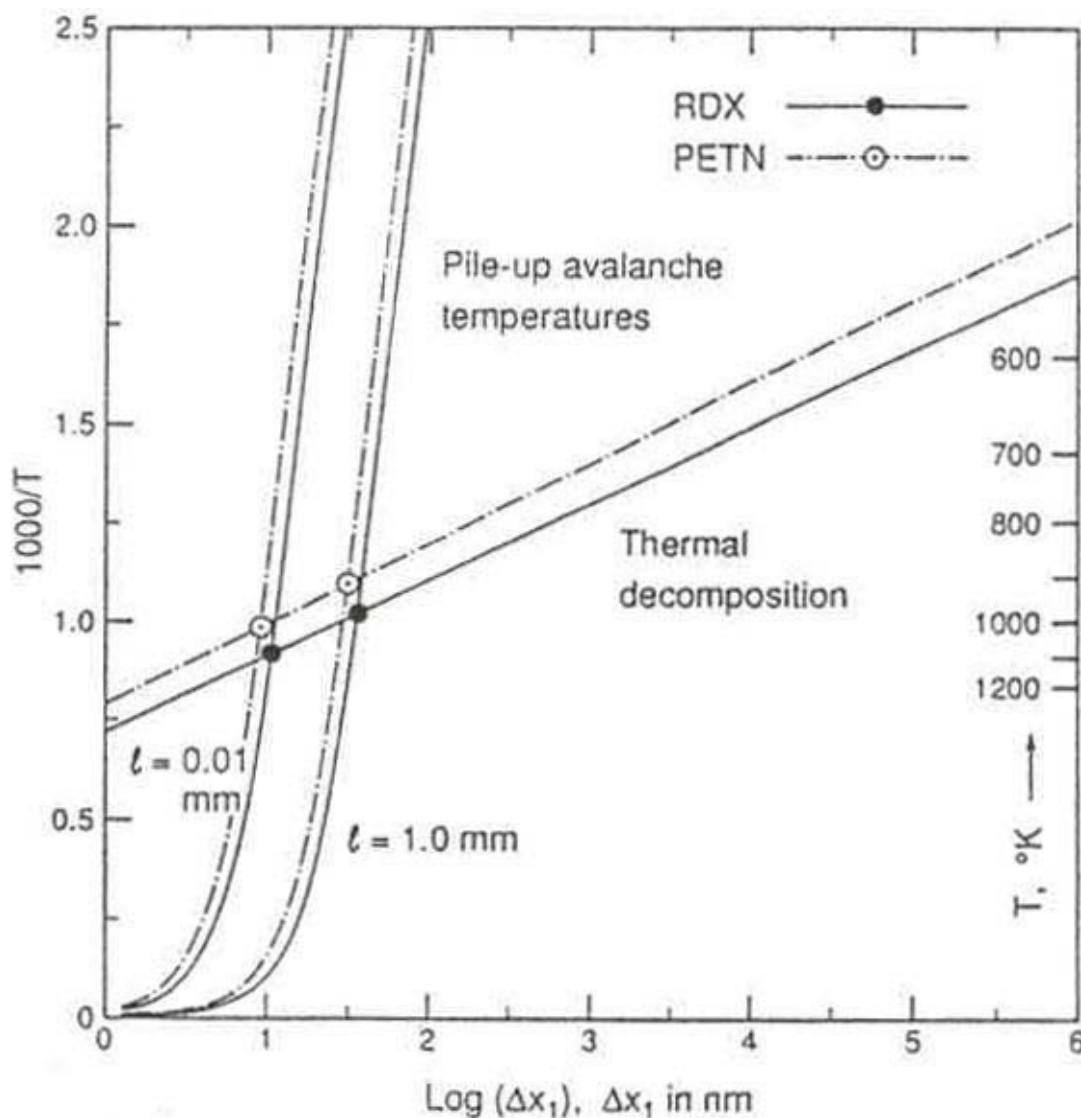


Figure 2. Theoretical pile-up avalanche temperatures, at two crystal sizes for RDX and PETN, in comparison with their previously computed thermal explosion temperatures.

In Figure 1, a similar model interpretation to that mentioned for (4,5), is given for somewhat distantly related test results analyzed more recently by Gonthier (6). In the Figure are plotted computed results for impacting piston velocity versus reciprocal square root of particle diameter for different compacts of HMX (cyclotetramethylenetetranitramine) particle beds and with demarcation indicating that the beds with larger particle diameters were being impacted at lesser velocity than needed to sustain combustion within the bed. The computations were based on earlier reported experimental results obtained by Jacobs, Sandusky and Elban (7).

Figure 1 has been constructed on the following basis: (1) the Hertzian-type contact stresses between spherical particles in the bed correspond to those required for full yielding of the particles and thus follow an inverse square root of particle size dependence, as for the impact sensitivity prediction mentioned above; and (2) at high impacting velocity (relating to the material strain rate), the material flow stress depends simply on the logarithm of the strain rate. Consequently, the graph is proposed to represent, at small particle sizes, an effective yield stress dependence on the reciprocal square root of particle diameter. At the largest particle diameters in Figure 1, the condition of general yield has not been obtained and combustion is not sustained.

Lattice/Molecule Stabilities

Comparison is made in Figure 2 between the predicted pile-up avalanche initiated hot spot properties of RDX and PETN (pentaerythritol tetranitrate) crystals, relating also to previous model calculations given by Boddington (8) for thermal explosion.

The pile-up avalanche temperatures are computed on an upper limiting temperature basis (3) stemming from previous difficulty in accounting quantitatively for any significant temperature rise on a continuum mechanics model description of shear banding behavior. The discrete dislocation pile-up versus continuum mechanics comparison of

such behaviors is accounted for by neglect, normally, of any crack-like stress-concentrating behavior in the continuum mechanics modeled shear band. The consideration enters into the comparison of such continuum and discrete (or smeared) dislocation model computations in two ways: (1) the continuum-type average strain within a shear band is assumed generally to be uniform; and, (2) the non-uniformly-spaced dislocations in a pile-up produce a locally magnified stress that is enhanced at the pile-up tip in direct proportion to the number of dislocations.

In Figure 2, the difference in elastic constant parameters involved in determining the dislocation pile-up avalanche temperatures for RDX and PETN is not so great, even producing predicted hot spot temperatures lower for PETN than RDX at the same hot spot size. This is opposite to PETN being known generally to be more impact sensitive than RDX. However, intersection of the computed avalanche temperature curves with their respective explosion temperatures shows that PETN is predicted, anyway, to be more sensitive than RDX, that is, PETN undergoes initiation at a lower temperature than RDX because of the lesser stability of the PETN molecule on a thermal explosion basis!

Consideration in Figure 2 of the fundamental stabilities of the different energetic molecules is not unrelated to the discrete dislocation model application to evaluation of shear displacements associated with dislocation movement at the inter-molecular-scale in the crystal lattice structures (9). The case for the orthorhombic Pbc_a crystal structure of RDX has been considered in detail. For example, identified [100](021) slip in RDX has been connected on a model crystal lattice basis with reported nitroso-compound formations identified in both drop-weight impact and combustion test specimens.

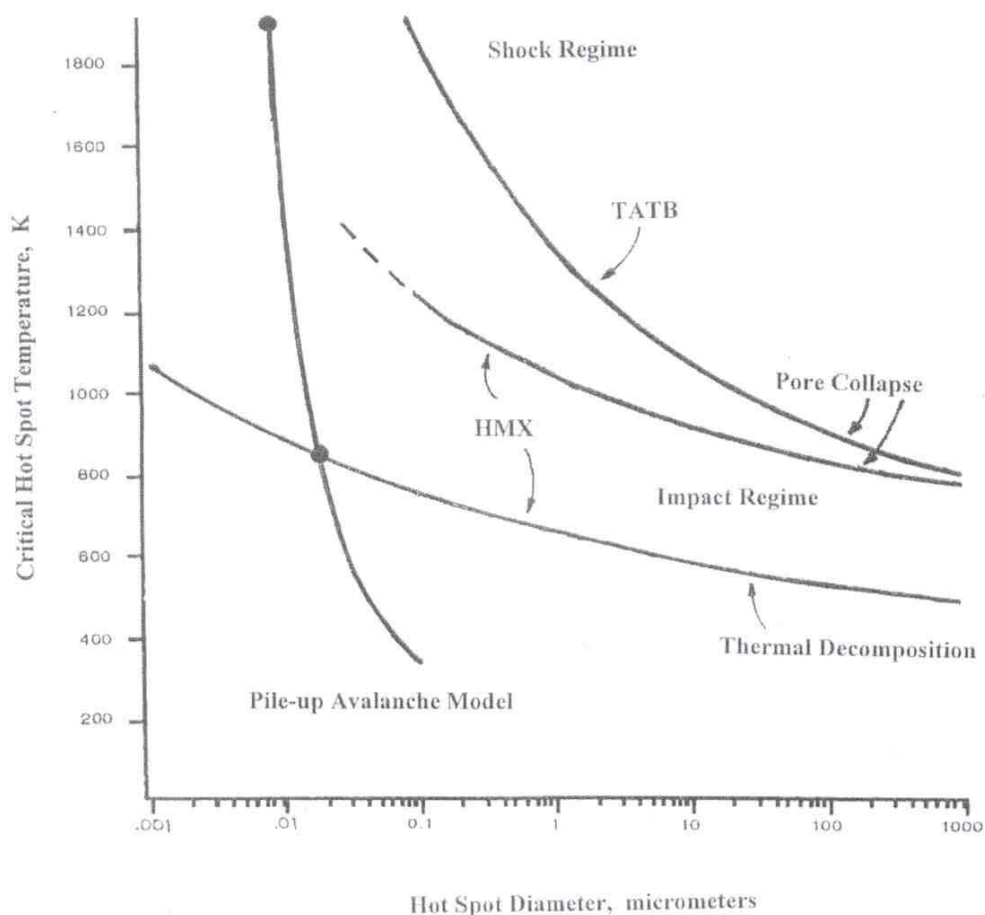


Figure 3. Comparison of model hot spot temperatures for dislocation pile-up avalanches and pore collapses, spanning estimated hot spot dimensions appropriate to impact and shock regimes.

The point here, relative to the earlier description of Eyring's comment (1), is that dislocation (shearing) movement in the relatively dense crystal lattices of these energetic crystals is quite capable of bringing out-cropping appendages of adjacent molecules into critical reaction coordinate distances (5).

A further crystal-lattice-scale consideration involves application of the discrete dislocation model to analysis of proposed nano-scale events transpiring in shock initiation (10). Here, the issue raised is complication for shocks of sufficient amplitude that are considered to generate a nano-scale dislocation structure at the shock front. Shock hardening of metallic materials is well-known, even to the degree of recent description being reported of three-dimensional dislocation dynamics modeling of unstable dislocation "channeling" that occurs in neutron-irradiated metals (11). The same type of

model had been proposed earlier for immediate occurrence in shocked energetic materials in that nano-scale dislocation loops were proposed to form at the propagating shock front, then to be swept through by subsequent lagging movement of the original dislocation network within the material (12). The key aspect of such mechanistic consideration is that the very localized subsequent channeling behavior of the originally resident dislocation population through the nano-scale network promotes shear banding development, and, hence, is an additional factor to be considered in evaluating localization of the dislocation work leading to enhancement of any temperature rise.

Dislocation shear comparison with pressured pore collapse

Recent advances in dislocation model descriptions, as have been described in the modern literature, and, likewise, recent quantitative assessment of hot spot temperature rises to be expected from the pressure-induced collapse of pores has led to the suggestion of making comparison between the two model considerations (13). Such comparison is made possible, at least on a preliminary basis, by recent quantitative assessment made by Tarver and colleagues for the case of pore collapse (14).

Figure 3 shows a first attempt at comparison between dislocation pile-up avalanche and pore collapse models. The dislocation basis of applying such computation to HMX is the same as made for RDX and PETN in Figure 2. The pile-up avalanche dependence has been superposed onto the graphical results developed by Tarver and colleagues for initiation of HMX and TATB (triaminotrinitrobenzene), taken to be caused in these cases by pressure-induced pore collapses. The critical conditions for the upper pore-size-equivalent hot spot temperatures shown in the Figure for HMX were reportedly determined on the basis of “multistep Arrhenius kinetic chemical decomposition models derived from thermal explosion and kinetic experiments”.

The indicated attempt at comparing the two-type hot spot model mechanisms in Figure 3 must be assessed with the thought in mind that “apples and oranges” are possibly being compared. Whereas the hot spot diameter for the pore collapse mechanism in Figure 3 is taken as the pore diameter for the collapse mechanism, the same abscissa diameter in the Figure is taken as the much smaller estimated hot spot diameter produced for a pile-up avalanche initiated within a 1.0 mm diameter crystal.

Consider, as Tarver has mentioned, that the pore sizes may be comparable to the crystal sizes. Then collapse of a 1.0 mm pore in an HMX compact would initiate at a temperature of ~800K. From the same Figure results, a much smaller hot spot diameter would lead to explosion at a somewhat lower temperature marked by the lower filled circle at the intersection of the mechanical work and thermal explosion curves. Such pile-up release at the greater stress intensity associated with cracking would be capable of generating the highest

temperature, extending to the upper filled circle point on the vertically-extended pile-up avalanche model curve. Thus, the preliminary indication is that dislocation pile-up avalanches produced by a shear component of the applied stress tensor may be capable of generating hot spot initiations quite comparable to, and perhaps even higher than, those associated with similar sized pore collapses.

Finally, the reminding comment should be stated that such comparison as has been described suffers additionally from the pile-up collapse mechanism being evaluated until now by overestimating the degree of hot spot heating. Recently, more realistic model calculations are being pursued for the pile-up release mechanism (15), as monitored by the same type of computationally intensive 3-dimensional parametric dislocation mechanics approach mentioned for reference 11.

ACKNOWLEDGEMENT

Byron Allmon, AFRL/MNME, is thanked for help with Figures and formatting.

REFERENCES

1. Eyring, H., *Fast Reactions in Energetic Systems*, C. Capellos and R.D. Walker, eds., D. Riedel Publishing Company, Boston, MA, 1980, p. 711.
2. Gilman, J.J. and Armstrong, R.W., *High-Pressure Science and Technology-1993*, S.C. Schmidt, J.W. Shaner, G.A. Samara, and M. Ross, eds., AIP Conference Proceedings 309, Colorado Springs, CO, 1993, p. 199.
3. Armstrong, R.W., Coffey, C.S., and Elban, W.L., *Acta Metallurgica*, **30**, 2111 (1982).
4. Armstrong, R.W., Coffey, C.S., DeVost, V.F., and Elban, W.L., *J. Appl. Phys.*, **68**, 979 (1990).
5. Armstrong, R.W., *Approches Microscopique et Macroscopique des Detonations*, S. Odier, ed., *Journal de Physique IV*, **5**, Colloque C4-89 (1995).
6. Gonthier, K.A., “Modeling and Analysis of Reactive Compaction for Granular Energetic Solids”, Technical Report AFRL-MN-EG-TR-2001-7091, Eglin AFB, FL (August, 2001).

7. Jacobs, S.J., Sandusky, H.W., and Elban, W.L., *Powder Technology*, 89, 209 (1996)
8. Boddington, T. , *Ninth Symposium (International) on Combustion*, Academic Press, N.Y., 1963, p. 287.
9. Armstrong, R.W. and Elban, W.L., “Dislocations in Energetic Crystals”, submitted for *Dislocations in Solids*, Vol. 12, F.R.N. Nabarro, ed., Elsevier Science Publishers, 2003, in print.
10. Armstrong, R.W., *Revue Scientifique et Technique de la Defense* (Traduction: J. Boileau), 16, [2], 162 (1992).
11. Rubia, de la, T.D., Zbib, H.M., Khraishi, T.A., Wirth, B.D., Victoria, M., and Caturia, M.J., *Nature*, 406, 871 (2000).
12. Bandak, F.A., Armstrong, R.W., Douglas, A.S. and Tsai, D.H., *Physical Review B*, 47, [18], 11681 (1 May 1993-II)
13. Klimenko, V., private communication, *International Workshop on New Models and Predictive Methods for Shock Wave/Dynamic Processes in Energetic Materials and Related Solids*, University of Maryland, (1999).
14. Tarver, C. *Shock Compression of Condensed Matter – 1999*, M.D. Furnish, L.C. Chhabildas, and R.S. Hixson, eds., AIP Conference Proceedings, 505, 2000, p. 873.
15. Grise, W.R., “3-D Parametric Dislocation Dynamics Applied to the Formation and Release of Dislocation Pile-Ups and Localized Heating”, submitted for The Minerals, Metals, and Materials Society (TMS) *Symposium on Dynamic Deformation: Constitutive Modeling, Grain Size, and Other Effects*, San Diego, CA (March 2003).

Dislocations in Energetic Crystals

R.W. Armstrong* and W.L. Elban**

*Emeritus Professor, Department of Mechanical Engineering, University of Maryland, College Park, MD 20742; Senior Scientist, Air Force Research Laboratory, Munitions Directorate, Eglin AFB, FL 32542.

**Professor, Department of Electrical Engineering and Engineering Science, Loyola College, Baltimore, MD 21210.

Abstract

Dislocations in molecularly bonded energetic crystal lattices are associated with an interesting contrast in mechanical properties: the crystals are elastically soft, plastically hard, and brittle. The combination of properties is shown here to relate to the important consideration of mechanically enhanced chemical decomposition possibly leading to explosive detonation. A variety of dislocation Burgers vectors and line vectors occur in individual crystals because of the characteristically weak intermolecular bonding among oddly-shaped molecules that are packed into otherwise low-symmetry crystal structures. Large Burgers vector dimensions occur as a result of the weak molecular bonding and outweigh the low magnitude of elastic stiffnesses to give relatively large dislocation self-energies, consonant with low dislocation densities being observed in such crystals.

Despite the weak bonding, dislocation movement is reasoned to be intrinsically hindered in the lattice structures because of cross-blockages among the intertwined, oddly-shaped molecules. An important consequence is that the crystals exhibit limited operation of restricted slip or twinning systems. Models of the molecular displacements occurring for identified slip systems show molecular interactions in agreement with detected chemical decompositions. Alternatively, energetic crystals have relatively low (anisotropic) values of surface energies that lead to low values of theoretical cleavage stresses. Thus, energetic crystals are elastically compliant, relatively hard, and brittle.

The relatively high crystal yield stresses and low cleavage stresses provide only a narrow range in stress level for dynamic dislocation behavior. In this range, localized hot spot heating from the dislocation work, though involving only small numbers of dislocations in pile-up avalanches, is significantly enhanced because of characteristically low material thermal conductivities. In shock wave studies, hindrance to dislocation movement at, and behind, the shock wave front is an important consideration, as is the generation of nanoscale dislocation clusters at large shock pressures and the role of anharmonic lattice strains at the dislocation cores in allowing either "in situ" hot spot heating or direct electronic excitations.

1. Crystal dislocation characteristics

The combination of large Burgers vectors and low elastic stiffnesses for energetic crystal lattices leads to large dislocation self-energies and consequently low dislocation densities in crystals that are mostly grown from solution. The low symmetry of the crystal lattice structures leads also to a variety of dislocation Burgers vectors and line vectors; however, the intertwined packing of oddly-shaped molecules produces strong intrinsic resistance to dislocation movement that allows only few slip or twinning systems to operate. The crystal surface energies are low and, with restricted plastic flow, cleavage is relatively easy.

1.1. Large Burgers vectors

The large Burgers vector dimensions in molecularly bonded lattice structures, and in related crystal structures characterized by large interatomic or intermolecular lattice parameters, provided an opportunity in the early days of dislocation studies of optically detecting dislocation end points at intermolecular-scale ledge heights on otherwise flat crystal surfaces exposed during growth from the vapor [1]. Very fine striated ledge structures had been observed with the optical microscope on the surfaces of vapor-grown crystals subjected to supersaturations less than the theoretical value required for growth on a perfectly flat surface. Cabrera and Burton showed that such ledges had to be a non-equilibrium phenomenon [2]. Frank [3] gave a model explanation for the generation of such ledges spiraling outward from emergence sites of

screw dislocations and thus explained the growth of crystals at low vapor supersaturations through the continuous availability of such ledges for attachment of atoms or molecules.

Griffin [4] first reported from the Royal Holloway College (RHC) a screw dislocation-type spiral marking on the surface of a beryl crystal. Verma [1] followed shortly thereafter, also while at the RHC, with optical phase contrast microscopy observations of spiral ledges terminating at presumed dislocation positions threading otherwise molecularly flat surfaces of silicon carbide crystals brought from India. With supervision from S. Tolansky, the optical microscope technique was pushed to provide quantitative measurement using multiple beam interferometry of a 1.5 nm step height along the [0001] growth surface normal, equivalent to a c-axis unit cell length for a dislocation Burgers vector in a 6H (hexagonal) crystal [5]. Figure 1 shows an example.

It is interesting to note the important consequence of there being relatively few dislocations with such [0001] Burgers vectors in these silicon carbide or related hexagonal crystals because the optical microscope observations and measurements were facilitated by the low areal density of dislocations. Such growth spirals were observed on silicon carbide crystals also by Amelinckx [6], and on the (0001) surfaces of n-paraffin crystals by Dawson and Vand [7], and on the surface of an n-nonatriacontane crystal by Anderson and Dawson [8]. Not long after report of these optical microscope observations, Menter [9] obtained electron microscope pictures of dislocations in copper and platinum phthalocyanine crystals by imaging the Burgers vector displacements along 1.2 nm separations of (201) lattice planes.

The preceding observations were made before dislocations were directly observed in the transmission electron microscope (TEM) via strain field imaging of the defects in thin metal foils [10,11]. The TEM technique allowed high magnification observations of dislocations to be made through strain-induced changes in the local diffracted intensity, say, over regions extending radially tens of nms from the dislocation cores, even with the much smaller Burgers vectors of dislocations in metals and alloys. Whereas a low dislocation density is generally required to make successful dislocation step height measurements on crystal growth surfaces with an optical microscope, much higher dislocation densities are conveniently studied with the higher magnifications employed in the TEM. Unfortunately, electron beam damage often interferes with molecular crystal defect observations in the TEM.

The same low dislocation density requirement of optical step height measurements applies for the observation of dislocations by the two techniques of chemical etch pitting or x-ray diffraction topography. X-ray topography involves optical microscope enlargement of strain-induced contrast in the diffracted x-ray intensity, thus occurring at dislocations for the same reason as in the TEM technique, but here in Laue or Bragg diffraction images recorded on fine grained nuclear emulsions. Reference [12] gives a description of dislocation observations by optical, x-ray, electron and field ion microscopy. The chemical etch pitting and x-ray topography techniques have been applied very successfully to observing dislocations in energetic crystals. Connick and May [13] first reported etch pitting observations of dislocations in cyclotrimethylenetrinitramine (RDX) crystals and Lang [14] first reported that dislocations had been observed in RDX crystals by transmission x-ray topography. RDX has an orthorhombic crystal structure with space group $Pbca$ [15].

1.2. Chemical effects

Nabarro [16] points out that Faraday [17] reported the observation of efflorescence occurring at mechanical scratches put into, for example, surfaces of otherwise perfectly stable crystal surfaces of sodium sulfate decahydrate. Reference to the original article shows that the same observation was made on other related decahydrate crystals. Faraday described the effects "as a curious illustration of the influence of mechanical forces over chemical affinity". Nabarro suggested, because efflorescence involves only a change in part of the molecular unit cell structure, that imperfect dislocations might be involved in the scratching deformation as compared with perfect dislocations participating in the crystal growth process, and thereby being relatively inert. He also pointed out that etch pits and dehydration points were reported to be uncorrelated in gypsum.

The segregation of solute atoms or molecules at the cores of dislocations in crystals of any type is a natural consideration because of the severe state of strain at the dislocation centers, and occurs frequently enough to have led to coining of the term "dislocation decoration". This influence is well known in atomic diffusion studies and, also, in deformation studies of discontinuous yielding and follow-on plastic flow. For the case of large Burgers vector dislocations, however, the strain state is relatively so severe as to allow dislocation cores in vapor grown crystals to be hollow. The condition for this occurring was theoretically predicted by Frank [18]. Also, for crystals grown from solution, as is the main method of production of energetic crystals, the dislocation cores may contain a residual amount of solvent. Thomas [19], while commenting also on Faraday's observations with decahydrate crystals, pointed out that sufficient water occurred in the channels of dislocation cores in sucrose crystals to appreciably affect their electrical conductivities.

Figure 2 shows a modern x-ray section topograph that reveals the strain field of a screw dislocation in a 6H silicon carbide crystal plate [20]. The dislocation core is demarcated by a hollow "micropipe". Scanning electron microscope (SEM) images were obtained of the emergent holes at the micropipe intersections with the crystal surface. Different micropipe diameter measurements were shown to be proportional to the square of the x-ray derived dislocation Burgers vectors, as predicted by Frank [18]. In fact, the micropipes were only observed at double Burgers vector or larger dislocation centers; and, the largest micropipes took on an hexagonal cross-section. Hirth [21] has recently extended the Frank model consideration to include the case of a micropipe being represented by an elliptical hole.

1.3. Self-energies

Beyond the dislocation core structure and its associated energy, there is the important far reaching linear elastic strain energy component of the total self-energy. The well-known formula for the elastic strain energy per unit length of the dislocation line is expressed in terms of the product of a strain energy coefficient, involving the material shear modulus and square of the Burgers vector, and the logarithmic ratio of outer and inner cut-off radii. The inner cut-off radius is determined by the dislocation core property; however, the logarithmic term is generally thought to be a minor variable in determining the dislocation energy.

Table 1, from Armstrong and Elban [22], gives in column 2 computed values of the strain energy coefficient, multiplied by unit intermolecular length along the dislocation line, for a [100](040) edge dislocation in RDX compared to 110 edge dislocations in LiF and MgO. The elastic strain energy is seen to be greater for RDX. In column 3, the elastic strain energy coefficient is divided by the heat of formation per molecule for each of the materials to show that the dislocation strain energy is greater for RDX. Thus, the lower shear modulus of RDX is more than compensated by the larger Burgers vector influence and, also, the larger reference length along the dislocation line. Also in Table 1, computed values are given for the conventional Peierls-Nabarro (P-N) stress that depends linearly on the shear modulus and exponentially on the ratio of interplanar spacing and Burgers vector [23]. Although RDX has a lower computed P-N stress, it is shown to be a larger fraction of the shear modulus. Of course, such estimate is vitiated by the cross-blockage between adjacent molecules consideration and, so, an even higher dislocation movement stress should be expected.

2. Crystal morphologies and perfections

Energetic crystals form a subgroup of the broader class of molecular organic crystals that are mostly grown in solution from supersaturated liquids. Gem-like crystals with flat, nearly specular, external habit planes are produced in the growth process. Dislocation bundles, as occur even in the natural production of diamonds, pierce the individual planar facets and facilitate growth by producing molecular scale step heights in accordance with the Frank [3] model of crystal growth. Internally, the crystals are built up of striated growth bands, parallel to the planar facets, that meet at impurity-associated growth sector boundaries.

Connick and May [13], in a study of RDX crystal growth, provided an example of the variety of external crystal morphologies that can be produced from different supersaturated solvents. Thus, tabular crystals with dominant (001) habit planes were produced by growth from cyclohexanone solution while prismatic

crystals with prominent $\langle 001 \rangle$ axes were grown from solution in acetone or dimethyl formamide. Armstrong and Elban [24] reported crystals having both the morphology described by Connick and May and a new crystal morphology with prominently exposed $\{210\}$ surfaces when grown by slow evaporation of reagent-grade acetone with Holston RDX Class D (specifying 1-2 mm size crystals) put into solution. The relatively large crystals were several mm in size. Klapper [25] has produced beautiful color pictures of the natural appearances of such inorganic and organic crystals as cesium-alum, benzil, salol, and benzophenone.

Figure 3 shows, from Klapper [26], a schematic vapor- or solution-growth representation of the relation between external growth planes and an internal microstructure, first, of growth sectors with growth banding parallel to the external crystal facets, secondly, of growth sector boundaries defining the intersection of growth sectors, and, lastly, separate “sprays” of straight dislocation bundles spreading through individual crystal growth sectors. As indicated, the dislocation bundles are oriented roughly perpendicular to the external crystal facets. Figure 4 shows a sectioned (001) surface of an RDX crystal that has been etched to reveal its internal growth sector pattern [27]. The planar (Miller-index type) surfaces of the growth bands are identified in the Figure from the trace intersections based on a stereographic projection method of analysis [28]. Such internal growth structures are particularly well-documented by x-ray topography studies of both solution-grown and vapor-grown crystals [26,29], including silicon carbide and sapphire crystals.

The straight line dislocation bundles, that are very often impurity decorated, are those generally associated with the type of ledge structure described by Frank [3] to participate fundamentally in the crystal growth process. These dislocations have been shown to either propagate from a crystal seed, to nucleate at the seed interface, particularly at inclusion particles, or to arise from perturbations in the crystal growth conditions. In the latter case, the observation of incorporated liquid inclusions has been attributed to local variations of supersaturation and solvent flow at the liquid–crystal interface [26]. Gross [30] reported the observation of solvent inclusions in RDX crystals. Klapper accounts for the straight line character of the dislocation bundles on a minimum energy basis, thus favoring the identification of screw dislocation growth, as described by Frank [3]. However, bundled dislocations with edge and mixed screw plus edge characters have been identified also to participate in the crystal growth process.

Both the dislocation core energy and the anisotropic character of elastic constants that determine the coefficient for the elastic self-energy [31], as mentioned for Table 1, enter into the determination of the dislocation growth line orientations. The striated growth bands themselves are caused by local variations in the impurity content grown into the crystals through the ledge structures. The growth sector boundaries appear to mark small localized impurity-dependent mismatches in lattice parameter or slight planar misorientations. Van Enkevort and Klapper [32] report a modern example of matching x-ray topography measurements with highly sensitive differential interference contrast optical microscopy showing 0.9 and 1.8 nm (unit cell and half-unit cell, respectively) steps on the growth faces of nickel sulfate hexahydrate crystals, relating to the observations mentioned above from Faraday [17] and Verma [1]. In this case, pure screw dislocation out-crops were responsible for the growth features.

McDermott and Phakey [33] showed by x-ray topography and etch pitting a one-to-one match of a small dislocation bundle with etch pits of the individual dislocations on the crystal growth surface of an RDX crystal, as shown in Figure 5. An opposite case of out-cropping pill boxes at dislocation line end points was identified also on the surfaces of the same batch of RDX crystals studied in cross-section by van der Steen and Duvalois, as shown with identified plane indices in Figure 6 [27,28]. Rather detailed x-ray topography results were reported for dislocation Burgers vectors and line vectors in laboratory-grown RDX crystals by Halfpenny et al. [34]. A large variation in both dislocation Burgers vectors and line vectors was determined. The variety of dislocation line shapes in carefully grown crystals of cm scale dimensions, including the observation of dislocation helices, was interpreted to indicate that significant post-growth dislocation movement had occurred. A combination of x-ray topography and etch pitting results were reported also to lead to expectation of a variety of dislocation types in energetic pentaerythritol tetranitrate (PETN) crystals [35].

3. Mechanical properties

Despite the large variety of dislocation Burgers vectors and line vectors in energetic crystals, the crystals are hard and easily cracked. The behavior has been traced to the difficulty of mechanically-forced dislocation movement. Such movement, whose dynamic characteristics are narrowly limited between relatively high yield and low cleavage stresses, is capable of conveying outcropping appendages of adjacent molecules into critical reaction coordinate distances. Chemical reaction is enhanced by the localized "hot spot" heating produced by the dislocation work.

3.1. Early mechanical testing of anthracene/naphthalene.

Kochendorfer [36] did early work on the deformation of naphthalene as an example of determining slip systems for a molecular crystal, in this case, having a monoclinic crystal structure and nm scale lattice parameters ($a = 0.86$ nm, $b = 0.60$ nm and $c = 1.12$ nm). Robinson and Scott [37] followed later with tensile stress-strain measurements of the critical shear stress for structurally similar anthracene crystals as a function of temperature and strain rate. Although the ends of the melt-grown crystal rods were cleaved along (001) surfaces to provide shorter tensile specimens, the thus tested crystals were quite ductile with single slip occurring on the (001) [010] system or, with greater strain hardening, the (001)[110] system. Robinson and Scott pointed out that the same slip systems were known then to occur in pure naphthalene crystals.

Despite lack of knowledge of the thirteen elastic constants for the anthracene crystal structure, the P-N stress was reasoned by Robinson and Scott to be an important factor in determining the crystal strength properties. Of greater importance in this study was the schematic demonstration on a lattice model basis, as indicated by identified plane projections and directions in Figure 7a,b, that slip should occur relatively easily across (001) along [010] but should occur with greater difficulty along [110]. Although arranged in a layered herring-bone lined-up array of uniaxial molecules, the crystal model nevertheless shows reasonably unobstructed pathways for the proposed [010] shear displacements between the rows of molecules.

Perhaps more closely related to results to be described for an energetic crystal, di Persio and Escaig [38] reported "in-situ" x-ray topographic observations made during mechanical testing of a reasonably simple body-centered cubic structure obtained for hexamethylene tetramine crystals. Deformation in constant strain rate compression tests and in tensile creep tests was monitored. The crystals were free of growth bands and contained very low dislocation densities. Cracking occurred often in the compression tests, even at the lowest machine testing speed. From the compression tests and tensile creep observations, it was concluded that the dislocations must have a large P-N stress, also reasoned to occur because of molecular misfit difficulties associated with displacements in the dislocation cores. Difficulties proposed for adjacent intermolecular nitrogen - hydrogen interactions during dislocation movement in a $\langle 111 \rangle$ slip direction were briefly discussed.

3.2. Micro-indentation hardness testing.

The brittleness of most energetic crystals and, also, interest in testing small material samples for personal safety led to micro-indentation hardness testing providing an excellent means of obtaining information on crystal plasticity and cracking mechanisms in these materials. Elban and Armstrong [24] first reported etch pitting evidence of highly localized plastic flow surrounding Knoop micro-indentation hardness impressions in RDX crystals. Figure 8 provides an example of etch pits surrounding various Knoop and diamond pyramid indentations put into the (210) surface of an RDX crystal [24,39,40]. The areas covered by the hardness-produced dislocation pits in RDX were approximately eleven times greater than the residual impression sizes, as compared with an area about ninety times larger for the x-ray determined plastic strain field of an indentation in LiF. Previous measurements on MgO crystals showed etch pit and x-ray contrast zones were roughly comparable [41]. Halfpenny et al. [35] also reported etch pitting evidence of restricted plastic flow at indentations in RDX crystals and, in PETN crystals, somewhat larger areas of very directionally distributed dislocation pits were observed at indentations. In a subsequent study, Gallagher et al. [42] investigated the orientation dependence of Knoop microhardness measurements in both RDX and PETN crystals and correlated the results with a model of the hardness anisotropy being

determined by the orientation dependence associated with achieving the critical resolved shear stress for dislocation slip.

Well-defined crystallographic cracking was observed at the micro-indentation sites in each of the preceding studies [24,35,40]. Earlier, Hagan and Chaudhri [43] measured the crack size dependence of diametral cracking at diamond pyramid micro-indentations in RDX and PETN crystals and, in line with a model of the predicted crack size dependence on load [44], determined fracture surface energies for such cracking. These experiments led Elban [45] to make a comparison of the mechanically determined surface energies and those determined separately from contact angle measurements in wettability studies. The fracture surface energies were found to be larger by less than a factor of two for RDX and less than a factor of three for PETN. Possible explanations for the differences in the energies were given of plastic work being associated with the cracking process or significant anisotropy in energy being associated with different surfaces. Hagan and Chaudhri commented that substantial plastic flow had occurred in association with the cracking in PETN. Also, they found a higher fracture surface energy in RDX for (100) cracking than (001) cracking, in agreement with the qualitative observation by Connick and May [13] that (001) cracking was easiest.

There are two dislocation flow considerations that bear on affecting mechanically-induced fracture surface energy measurements: cracks are formed or small cracks made larger because of dislocation flow; and, dislocation generation and movement can occur at crack tips to blunt or otherwise restrict crack growth. The role of dislocation flow in forming a crack is well-illustrated by the case of $\{110\}\langle 110\rangle$ slip on adjacent slip planes in MgO crystals combining to form cleavage cracks on the relatively unfavorable $\{110\}$ cleavage planes [46]. Figure 9 shows a comparison of residual diamond pyramid diagonal lengths and tip-to-tip diagonal crack extensions measured for indentations on (001) MgO and (210) RDX crystal surfaces [22,40,47,48]. The cm-size RDX crystal on which the major (triangular point) measurements had been made was supplied by H.H. Cady, Los Alamos National Laboratory. Note the reasonable agreement with Hagen and Chaudhri's reported crack size measurements [43] on RDX, although the lowest load datum measured by them is shown in the Figure to deviate from the theoretical indentation exponential (3/2) dependence predicted on an indentation fracture mechanics basis [44]. This low indentation load datum plus the low load measurements shown for MgO are in the regime where visible cracking first occurs.

In Figure 9, the force dependencies of the indentation diagonal lengths and diagonal tip-to-tip crack sizes of $\{110\}$ cracks in MgO and (001) cracks in RDX present an interesting comparison. The (left-side) line of slope 2 in the Figure applies for a constant hardness. For MgO, the dependence of the indentation force on indentation size follows the same indentation-fracture-mechanics-based (3/2) dependence as shown for the crack size measurements. The cracking-controlled decrease in hardness at larger indentation sizes was attributed to the positive influence of cracking on dissipating the pent-up dislocation pile-up strain energies. X-ray topography evidence was obtained on MgO showing reduced strain fields associated with such cracking in larger ball indentation tests [47]. By contrast, RDX shows in Figure 9 an apparently negligible influence of cracking on the material hardness, that is seen to be essentially constant at all crack sizes. The combined indentation and crack size measurements for RDX are controlled by the dislocation flow, consistent with the proposed intermolecular-mechanism-based difficulty of dislocation movement.

Another hardness-based method for comparison of plastic flow or cracking behavior that is informative of the position of RDX and related energetic materials among a wider range of materials is shown in Figure 10, as developed by Hammond and Armstrong [49]. Here, a hardness stress, defined as the mean pressure on a ball indenter of diameter, D , is plotted versus a measure of the hardness strain, defined by the ratio of the circular contact diameter, d , divided by D . For elastic loading behavior, a linear hardness stress dependence on (d/D) can be computed from the elastic constants of the ball and test material in accordance with the theory of Hertz [50]. In Figure 10, all of the linear dependencies are computed for a steel ball indenting the various materials that are identified: AP is ammonium perchlorate; and, anthracene, as discussed above, is shown on the left side of the Figure to have the lowest elastic loading curve, that is to be compared, on the right-side Figure location, with indication of a low value for the conventional diamond pyramid, or Vickers hardness number, VHN. The elastic loading lines are raised in order of increasing material elastic stiffnesses. Also, at the end points of the elastic loading lines for a number of materials are

the theoretical hardness stresses for cracking, σ_c , as computed on an indentation fracture mechanics basis for different ball sizes [51,52]. The Hertzian cracking stress is seen to be lower at larger ball sizes.

Experimental ball indentation test results are shown in Figure 10 (as open square points) for an RDX (210) crystal surface indented with a steel ball of 1.59 mm D value and d values determined from optical measurements of the residual indentation sizes. As noted, several smaller indents were free of cracking. The hardness values with associated cracks are lower than the theoretical Hertzian stress for cracking, shown at the terminus of the elastic loading line, because of the role of dislocations on promoting cracking. However, the plastically-cracked material measurements are not very far below the theoretical elastic cracking stress, and so Figure 10 gives indication of only a relatively limited range in stress level for dynamic dislocation behavior preceding cracking in RDX, say, compared to the much larger range shown for NaCl.

Diamond pyramid, or Vickers, hardness test results are supposed to give a plastic hardness stress equivalent to that obtained in a ball indentation test with $(d/D) = 0.375$ [53], and so, on the right side of Figure 10, representative diamond pyramid hardness, or VHN, values are shown for a variety of materials. Consider the comparative hardness curves shown for MgO, RDX, and NaCl crystals, in the latter case, where a continuous hardness stress-strain determination produced excellent agreement with the measured value of the conventional hardness [50,49]. MgO is at the top of the vertically distributed conventional hardness values with an indicated hardness of approximately 7 GPa ($1 \text{ GPa} = 98.1 \text{ kgf/mm}^2$), falling below a theoretical Hertzian stress value, for the same hardness-determined ball size, in excess of 20 GPa. The lower hardness is obtained because of the dislocation promoted cracking that has been described. NaCl has a lower elastic stiffness than MgO, of course, but greater elastic stiffness than RDX. However, RDX has a greater plastic hardness than NaCl and lower theoretical cracking stress. The comparison establishes a quantitative basis for concluding that RDX is elastically compliant, plastically hard, and relatively brittle.

3.3. Drop-weight impact testing for crystal sensitivity.

Early work on the initiation of explosives by mechanical loading, particularly, by drop-weight impact testing, led to an explanation of localized hot spot heating being responsible for the effect [54,55]. Field et al. [56] set out the main mechanisms for the generation of hot spots as: (1) adiabatic compression of gas pores; (2) viscous heating of extruded material between grains or at external surfaces; (3) frictional heating between contacting surfaces; and, (4) localized adiabatic shear during mechanical failure. Modern demonstration of such hot spots was produced by Coffey and Jacobs in drop-weight impact tests of explosive particles placed onto heat sensitive film [57].

Important evidence for discontinuous load drop behavior, analogous to yield point behavior, being associated with the hot spot heating and chemical decomposition was provided by Heavens and Field [58] who monitored the transmitted pressure wave in impact tests on thin layers of powder particles. The results are summarized in Table 2 in columns under schematically-drawn impact stress-time responses shown for an assortment of energetic and inert materials that were tested. Explosive initiations were obtained for the “sharp drop” type curves characteristic of the energetic materials shown in the right hand column of Table 2, and for ammonium perchlorate (NH_4ClO_4 , AP) in the second-from-right hand column. Other evidence for the need of the deformation to be concentrated in narrow shear bands associated with the sharp load drop behavior and, also, with adiabatic heating, was obtained in a companion study by Winter and Field [59], who investigated the reverse situation of small particles impacting onto larger explosive crystal surfaces. Such adiabatic shear bands are associated with discontinuous load drops.

Armstrong et al. [60] pointed out that achievement of appreciable hot spot temperatures at the slip band level required the non-uniformly distributed dislocations to be blocked by strong obstacles and, also, that the pile-up energy had to be dissipated by an avalanche-type of collapse of the obstacles. Theoretical description of the dynamic release of a pile-up had been described on a dislocation group basis by Head for the case where there is a linear dislocation velocity dependence on the shear stress [61]. Figure 11 gives an example of sequential steps of spreading (to the left) of an initial pile-up, viewed on a continuous distribution of infinitesimal dislocations basis, after the pile-up block was removed suddenly. The local dislocation density, compared to the average value in the normalized initial slip length, is shown to spread

rapidly on initial release of the pile-up. At one hundredth of the time it would take for a single dislocation to travel the length of the pile-up when driven by the external stress, and with a linear stress-velocity law, about one-fifth of the released dislocations have raced ahead to a distance of about one tenth of the unit pile-up length. Thus, the consideration obtains that an initial build-up of strain energy might proceed isothermally until, at critical microstructural stress intensity, breakthrough occurs and the stored energy is released adiabatically [60]. Other related model descriptions of dynamic dislocation pile-up properties have been given by Gerstle and Dvorak [62] and Ockendon and Ockendon [63]. Such pile-ups are now known to be an integral part of slip band propagation against planar boundary obstacles in all materials including, for example, ice polycrystals [64].

An important feature of significant dislocation pile-up activity coming into play in determining the mechanical properties of a material is that crystal size or, within a polycrystal, the grain size influence becomes very recognizable [65]. For polycrystalline metals, the onset of yield point behavior for plastic yielding [66,67] and subsequent plastic flow stress [68] both follow a Hall-Petch dependence on the reciprocal square root of the polycrystal grain diameter. An increased slope for the grain size dependence, now termed the microstructural stress intensity after fracture mechanics connection, is associated with greater pile-up activity [65]. Somewhat analogous pile-up formation, and sudden release, at slip band intersections is directly observable via birefringent transmitted light experiments during tensile deformation of MgO crystals. Also, the subject of crystal size influence on initiation and explosion of energetic crystals has been of scientific interest since early impact deformation results were reported by Bowden and Singh [69].

Application of the pile-up model to drop-weight impact test results obtained on RDX crystals led to prediction of greater drop-weight heights being required to initiate smaller size crystals on a logarithmic basis of drop-weight height versus reciprocal square root of crystal size [70]. Figure 12 shows experimental measurements demonstrating the effect for RDX crystals. A strongest obstacle of cleavage cracking was assumed to release the pile-up avalanche for hot spot generation. Bowden et al. [71] had proposed that the speed of cracking itself, with an associated plastic zone at its tip, could be responsible for chemical decomposition. Fox and Soria-Ruiz [72] produced evidence for the consideration from experiments on several carbonate and azide crystals. In the latter study, an interesting association of crystal hardness and estimated crack tip temperature was described.

Connection of the pile-up avalanche model for deformation-induced crystal initiation was made, also, with theoretical work of Boddington [73] who derived a relationship between the hot spot size and temperature required for direct initiation of thermal explosion. Reasonable estimations were determined from the pile-up model of deformation-induced temperature rises [74] and of hot spot sizes and lifetimes [70]. Comparison of calculated RDX and PETN crystal deformation-induced hot spot temperatures, relative to their thermal explosion temperatures, led to the conclusion of PETN being more sensitive because of the lesser stability of its molecular structure. For more ductile metallic materials, the dislocation pile-up avalanche model has been suggested to provide the fundamental mechanism for adiabatic shear banding at small plastic strains [75]. Based on the model, Figure 13 shows a derived graphical basis for comparison of the shear banding susceptibilities of a number of metallic, ionic and energetic materials [76]. In the Figure, a greater slope to the material point is indicative of greater shear band susceptibility.

The two dependencies shown in Figure 13 for the theoretical avalanche-induced temperature rise apply for different material property combinations, among which the microstructural stress intensity, k_s , and thermal conductivity, K , show the greatest material variations [60]. For metals and ionic solids, then, lines of greater slope to the different (open circle) material points in the Figure establish a greater shear band susceptibility, that reasonably agree with the (closed circle) upper limiting temperature rise predictions shown using the right-hand ordinate scale of the Figure. In the Figure, RDX, PETN and AP follow the second inequality and are seen, at the necessarily reduced scale dimensions, to be relatively shear band prone even compared, for example, to α -iron whose low temperature shear banding behavior is very well-known.

3.4. Shock loading.

Shock wave phenomena, modeled hydrodynamically to involve discontinuities in pressure, temperature, and density, across an idealized shock “front”, are associated with explosive decompositions of energetic materials and their formulations [76]. A one-dimensional state of strain obtains in the shock propagation direction. For the real case, the shock front is taken to be a narrow zone of nanometric-scale dimensions experiencing shear stresses comparable to the theoretical strength.

Dislocation model aspects of shock wave loading began with a pioneering description by Smith of the creation of dislocations at the shock wave front in metals [77]. Meyers [78] has extended the model in a modern account. Figure 14 shows another model description of distributed nanometer-scale dislocation loops proposed to produce a residual state of one-dimensional strain in the shock propagation direction across a presumed non-planar shock front [79]. An analysis has been given of the dislocation structure [80]. The shear stress state across the compressional front is shown in the top left corner of the Figure near to the indicated sectioned crystal edge. Assumed nanometer-scale dislocation shear loops are distributed so as to give, at the curved arrow positions, reacted dislocations with Burgers vectors parallel to the shock propagation direction, hence, the residual, essentially one-dimensional, strain-state.

The presence of such a nanometer-scale structure should promote shear banding, also, for subsequent plastic flow from the originally resident dislocation structure whose thermally-activated movement lags behind the shock front that travels at a velocity elastically-determined for one-dimensional strain [81]. The situation is proposed to be analogous to dislocation channeling that occurs in post-deformation of neutron-irradiated metals, where follow-on dislocation movement is made easier through slip band channels cleared by first dislocation movements sweeping-out the neutron-induced dislocation loops. Otherwise, considerable research has been performed by Gupta and colleagues [82, 83] on the shock wave deformation of LiF crystals, for example, as described in a later paper on investigating details of stress relaxation at shocked crystal surface layers previously hardened by solute diffusion [84].

Special challenges occur for dislocation mechanics in the regime of shock wave loading both because of the nanometric size of events at the shock front and its speed of passage that requires dislocation-connected reaction times from picoseconds to nanoseconds [85]. Results in the low shock regime are presumed to connect with normal high strain rate deformation results, for example, as achieved in split Hopkinson pressure bar tests and Taylor cylinder impact tests [81]. At these strain rates, deformation twinning is favored over dislocation slip for a number of metals and alloy systems [86]. Follow-on thermally-activated slip trails behind the shock front. For larger amplitude shocks, creation of a dislocation nanostructure occurs at the shock front and, then interaction of the trailing viscoplastic flow with the newly created nanoscale dislocation clusters is an important consideration. At the highest shock amplitudes, “in situ” initiation is envisioned to occur within the strain fields of dislocation cores [85,81]. At the most fundamental level, the mechanism of vibrational energy (up pumping) enhancement should be favored at dislocation cores because of the importance of anharmonic coupling to the process [87-89].

An early experiment on the shock initiation of individual cm-size RDX crystals, measured on a microsecond time scale, was reported by Adams and colleagues [90]. The crystals were found to be less sensitive to shock initiation than powdered material; however, once shocked the crystals were significantly more sensitive to a second shock. The result was explained on the basis that the first shock produced internal damage that provided sources of hot spots. Sandusky et al. [91] obtained sub-microsecond optical observations of luminous slip and cracking systems trailing behind the shock front of AP crystals supplied by T.L. Boggs, Naval Air Warfare Center, China Lake, CA. Significant light generation occurred from the shock interaction with microhardness impressions put into the crystal surface before shocking. X-ray photoelectron spectroscopy (XPS) measurements made on the shocked AP crystals demonstrated that perchlorate decomposition occurred at the shocked indentation sites [92]. Higher shock pressures applied to RDX crystals were also shown to produce deformation-associated luminosity in RDX and cyclotetramethylenetetranitramine (HMX) crystals [93].

The importance of crystal orientation on the shock initiation sensitivity of cm-size body-centered tetragonal PETN crystals was established in a series of papers by Dick and colleagues [94-96]. The experiments built onto very complete information being known about the linear and volume compression of shocked PETN crystals [97], their elastic-plastic properties [98] and elastic constants [99]. The times and shock

propagation distances from the impacted crystal surface for “run-to-detonation” were very different for different crystal orientations. Match with the dislocation Burgers vectors and slip systems led to correlation of this measure of crystal sensitivity for $\langle 110 \rangle$ directed shocks with difficult shearing across $\{100\}$ planes of interleaved molecules, where it was reasoned significant “steric hindrance” should oppose molecular displacements.

For $\langle 100 \rangle$ directed shocks that should produce shearing across the primary $\{110\}$ slip planes, having essentially no interleaved molecules, relatively easy slip occurred and the crystals did not detonate. Intermolecular distances between outcropping arms of adjacent molecules were computed for different shear displacements across the crystal planes to demonstrate the occurrence of steric hindrance. In [96], the PETN results were connected with a similar dislocation model analysis for RDX of intermolecular interactions proposed to explain the formation of nitroso compounds [100]. In a follow-on analysis, Dick suggests that, because of the low stiffness coefficients of PETN compared to metallic, ionic and covalent crystals, the theoretical perfect crystal strength might have been reached in his crystals so as to produce homogeneous slip and thus explain equally well the experimental results [101]. The model of steric hindrance was also applied by Dick [102] to explain the explosive behavior reported for nitromethane crystals when rapidly loaded in a diamond anvil, high pressure cell [103].

3.5. Laser damage experiments.

The use of a laser beam to probe damage processes within individual energetic crystals or powder compacts is also of interest to the energetic materials community [104]. For dislocation-based interest in the present report, brief descriptions are given here of very low power ignition of melt spots on an RDX crystal surface, in order to investigate thermal stress influences on the combustion process [105], and, at the opposite extreme, high energy input for initiation of detonation [106,107]. Figure 15 shows, from the thermomechanically-based combustion study, a re-solidified melt spot produced with an impinging laser beam directed onto an RDX crystal surface at a grazing angle of about ten degrees. A micrometer-scale network of cracking is observed underneath the circumferentially-enclosed melt spot-crystal interface. Cracking was reasoned to occur more easily inside the melt spot because only the liquid-solid interfacial energy had to be supplied [108].

A very different appreciably laser-damaged situation is shown in Figure 16a,b, where heavy damage is shown at a hole (in 16b) drilled into an AP crystal surface from a straight-on focused, nanosecond pulsed, laser beam [109]. In this case, the crystal was laser-heated through the low-temperature orthorhombic-to rocksalt cubic phase transformation and cracking occurred sequentially in both crystal phases. The initial macro-scale cracking on the ambient temperature $\{010\}$ cleavage plane of the orthorhombic structure is observed in Figure 16a, for a magnified region of 16b, while residual microscopic cracking is observed in Figure 16a on the previous $\{010\}$ planes of the laser-heating-induced transformed cubic (rocksalt) structure. Figure 17 gives a dislocation reaction description of the compressive stress-state leading to the $\{010\}$ cubic cracking, based on the complementary crystal axes shown in both Figures. The hydrostatic tensile stress state of the reacted $\langle 100 \rangle$ dislocations was reasoned to contribute to sub-surface hollow decomposition sites observed with the scanning electron microscope. X-ray photoelectron spectroscopy (XPS) measurements gave evidence of decomposition to ammonium chlorate and atomic force microscopy images gave indication of transformation product [109].

4. Chemical reactivity

4.1. Cleavage-induced chemical reaction

As mentioned earlier, the concept of chemical decomposition of thermally unstable solids resulting from elastic strain energy released during crack propagation breaking intramolecular bonds was introduced by Bowden et al. [71]. The amount of decomposition gas generated during fracture within a closed chamber was measured for β -lead azide, sodium azide, PETN, and several inert solids, as given in Table 3. The results and their interpretation were presented subsequently in more detail [72]. Particularly noteworthy was the obtainment of estimates of the effective temperature at the various crack tips, calculated assuming that the mechanism occurring is the same as for conventional thermal decomposition.

In a separate study, Fox and Soria-Ruiz [110,111] associated differences in decomposition kinetics of calcite as a function of temperature with the movement (rather than mere presence) of dislocations on several different slip planes. Easy decomposition occurred on those planes in which the carbonate (CO_3^{2-}) ion was favorably oriented, being essentially perpendicular to the plane. As such, this provided an early indication that solid-state chemical reactivity involved particular crystallographic arrangements of ions (or molecular species, more generally), rather than being just a bulk phenomena.

More recent fracture-induced decomposition results for PETN were obtained by Hauser et al. [112]. Using mass spectroscopy distinctly different decomposition products were obtained depending on the rate of crack propagation. Slow, low energy cracks, achieved by a machine-driven chisel, caused the cleavage of the outer molecule CH_2O -to- NO_2 bonds, such as occurs in conventional thermal decomposition. Rapid, high energy cracks, resulting from an explosively-driven chisel, caused the breaking of the inner and stronger C-C bonds at the center of the molecule. Thus, it was concluded that the reaction pathway for decomposition was influenced by the amount of energy transmitted to the crack tip.

4.2. Polymerization related to sucrose decomposition.

Enhanced reactivity at dislocations in inert (non-energetic) solids has been extensively reviewed by Thomas [113,114]. The emphasis has been primarily on inorganic materials, but photomicrographs were presented [19] that indicate common aspects [115] exist between the initial stages of solid-state polymerization and the beginning stages of decomposition of molecular crystal sucrose, also associated with the presence of dislocations.

4.3. AP decomposition

The most extensive work on an energetic (oxidizer) solid to connect chemical decomposition with the presence of dislocations has been reported for single crystal ammonium perchlorate, AP. Pioneering results were obtained by Galwey and Jacobs [116], showing that decomposition of as-grown orthorhombic (stable room temperature phase) AP crystals is initiated by defects and occurs primarily at mosaic crystal boundaries. Decomposition then proceeds in a three-dimensional manner, consuming the boundary regions. Subsequently, Herley and Jacobs [117] investigated the effect of exposing similar crystals to γ -ray irradiation before thermal decomposition occurred. Assuming the same decomposition mechanism, the authors concluded that irradiation shortened the induction period for initial decomposition while the reaction rate constant was found to be enhanced for the acceleratory period of decomposition. The change in rate constant was attributed to an increase in the number of decomposition nuclei (presumably associated with dislocations) that were produced by the irradiation.

Much more detailed thermal decomposition results were reported by Herley and Jacobs [118,119] for millimeter size and powdered AP crystals unirradiated and exposed to x- or γ -ray irradiation. Previous observations concerning the effect that irradiation has on induction period and acceleratory period decomposition rate were confirmed. Separate microscopic examination of partially decomposed crystals revealed that the number of decomposition nuclei increased in the irradiated crystals. Irradiation also increased the rate that potential decomposition sites became active. The combined kinetic and microstructural results show that the same decomposition processes take place in both unirradiated and irradiated AP, but that irradiation increases the rate constants.

The most direct evidence relating thermal decomposition sites in laboratory-grown single crystals of AP to dislocations was obtained by Herley et al. [120]. Initial nucleation processes involved in establishing thermal decomposition sites were investigated using both light and (transmission and scanning) electron microscopies. Both unstrained and plastically deformed (i.e., from pre-compression) crystals were heated at relatively mild elevated temperatures (170-210° C) in order to study the initial stages of decomposition by surface nucleation. On the (001) surface of unstrained crystals, isolated, circular nucleation sites appear to occur at random. This was also observed for some sites on the (210) surface, but other sites were aligned crystallographically.

For the strained crystals, the nucleation sites were well aligned in both surfaces and were mostly in the same crystallographic directions as pits that formed in chemical etch pitting studies on separate crystals. The close correspondence in the two sets of observations led to the conclusion that the decomposition nuclei form preferentially at dislocations that intersect the surfaces. The initial decomposition nuclei stop growing when a critical size is reached, and new nuclei (originating a little below the surface) form and grow until the top surface layer has completely reacted. Nucleation of deeper interior decomposition sites is also reasoned to be associated with dislocations based on observations that relate to the activity of known slip systems.

The effects that x- and γ -ray irradiation have directly on the chemical decomposition of AP was also investigated by Herley and Levy [121]. As with thermal decomposition, circular decomposition nuclei (resembling etch pits) formed having approximately the same size and surface density ($2\text{--}40 \times 10^6/\text{cm}^2$). Many of the nuclei formed by irradiation were aligned in the same crystallographic directions observed in the thermal decomposition studies of pre-irradiated and pre-stressed crystals. Thus, it was concluded that dislocations are also involved in this type of decomposition. Irradiation-induced decomposition sites form initially throughout the exposed volume, in a roughly uniform distribution, while thermal decomposition sites appear on the surface initially and grow inward subsequently.

Having established the direct involvement that dislocations have in the radiation-induced decomposition of AP, Herley and Levy [122,123] reported measurements of dislocation density as a function of radiation level. Figure 18 shows etch pit observations on matching crystal surfaces indicating dislocation movement caused by the irradiation. The threshold for dislocation generation was found to be about 10^5 rad. Between 10^5 and 10^6 rad, the dislocation density increased linearly with irradiation, and above 10^6 rad, the density was too high to measure reliably. It was concluded that the observed accelerated decomposition rates occurred because additional decomposition nuclei formed at dislocations generated during irradiation. Further, it was proposed that interior gaseous decomposition products created stress levels in the lattice high enough for Frank-Read sources to operate, thus providing an explanation for radiation-induced dislocation generation. The interesting results are, no doubt, very particular to the stability of the AP molecule, its lattice energy, and the gaseous decomposition products.

4.4. Spectroscopy

Tang et al. [124] have reported mass spectrographic results for the decomposition of RDX, PETN, silver azide and lead azide crystal surfaces impacted with a focused laser beam. The work followed on from interest at the University of Cambridge Cavendish Laboratory [125] in detecting molecular fragments via time-of-flight mass spectroscopy after fracturing crystals of PETN and lead azotetrazole. The work relates as well to the results reported by Fox and Soria-Ruiz [110]. Although significant damage sites were shown by scanning electron microscope observations of cratering and cracking on the various crystal surfaces, no dislocation connection via slip traces or other crystallographic markings were reported. Rather, the results were interpreted in terms of the reaction pathways taken by the different molecules in the decomposition process. In this regard, such measurements relate as well to the important consideration of the decomposition of energetic crystals in combustion studies of propellant formulations. Brill [126] has given a description of surface chemistry considerations employing Fourier infrared (FTIR) spectrometry to identify the chemical reaction steps for decomposition of AP, RDX, HMX and other energetic compounds for different burn rate conditions. Behrens and Bulusu [127] have detected early nitroso compound formation via mass spectroscopy observations made during thermal decomposition and pointed out that the measurements were consistent with decomposition in the solid phase as reported also from mechanical test results [128].

4.5. X-radiation induced decomposition

Synchrotron x-ray topography was used by Bhat et al. [129] to investigate beam-induced low-level decomposition (about 1%) in large AP single crystals. Significant structural damage was observed in the outer layers of the crystal causing bending to occur by slip on previously reported systems. An enhancement in the decomposition rate was reported with dislocations serving as the decomposition nuclei. The precipitation of decomposition products at the nuclei causes crystals (initially transparent) to become

opaque in a process that resembles the formation of a colloidal suspension. Importantly, the synchrotron white beam is able to image the resultant defect structure at higher levels of decomposition than was possible in conventional laboratory experiments using monochromatic radiation.

The use of x-ray topography to examine sub-structural changes occurring during chemical reactions in several crystalline solids, including single crystal AP, was reported by Sheen and Sherwood [130]. The suitability of using laboratory and synchrotron sources to study solid-state decomposition was characterized in more detail. Using white beam synchrotron, transmission Laue diffraction topographs of AP were obtained as a function of absorbed doses. Graded absorption of the available wavelengths across the crystal thickness caused the crystal to bend initially with the development of a large amount of dislocation structure. Eventually, the strain equalized and flexure of the crystal was eliminated, followed by detection of chemical decomposition based on image broadening and subsequent formation of product powder rings.

4.6. Shock reactivity

The roles that deformation, fracture, and material microstructure have on the shock reactivity of single crystal AP were investigated by Sandusky et al. [91]. Experiments were conducted in a mineral-oil bath with the shock being provided by a small explosive donor. This arrangement allowed samples to be recovered for subsequent chemical analysis and microstructural characterization. Particularly noteworthy experiments involved shocking crystals possessing a large surface strain center created by a Vickers indenter. High-speed photographic coverage revealed distinct diagonal lines immediately behind the shock front corresponding to (010)[001] slip, a moving luminous band believed associated with a propagating crack, and light near to the hardness impression that was conjectured to be due to chemical reaction. A subsequent experiment was conducted [131] on an AP crystal containing several Vickers impressions and shocked at the reaction threshold. High-speed photographs again showed luminosity near impressions. The recovered crystal was cleaved through two of the impressions, allowing spatial chemical analysis to be performed in the crystal interior by using the XPS technique to scan 1.0 x 1.0 mm areas. The line widths of XPS spectra were correlated [92] with dislocation densities that were measured directly using a chemical etch pit technique and related to somewhat analogous irradiation results obtained by Herley and Levy [121-123] that were discussed earlier. The linewidth of the $\text{Cl}(2p_{3/2})$ spectra ranged from 1.70 eV for the region of greatest visible damage to 1.22 eV for the region with no visible damage or for an as-grown (control) crystal.

The broadening of the photoelectron lines was attributed to the lattice distortion present in the immediate vicinity of the dislocations. On the same freshly cleaved surfaces, the largest amounts of chemical decomposition were associated with the hardness impressions. However, the highest levels were not detected in the areas immediately adjacent to the impressions where dislocation densities were found (based on line-width measurements) to be highest. Rather, the highest decomposition levels were found in areas where the dislocation densities had intermediate values and appeared to be associated with a prominent (001) crack or irregular cleavage steps emanating from an impression. It was concluded that the observed luminosity resulted from chemical reaction occurring either at the tip of the (001) crack or in its plastic zone.

5. Molecular modeling

The various methods of molecular modeling have been applied mainly to prediction of crystal structures and densities, determination of the P-N stress, dislocation displacements relating to intermolecular interactions, and shock wave properties, including electronic or vibrational excitations and shear wave characteristics.

5.1. Crystal densities

Prediction of energetic crystal densities is important because, in addition to interest in greatest energy density for explosiveness, both the detonation pressure and velocity increase with density [132]. The topic relates to x-ray and neutron diffraction methods employed in crystal structure determinations. Computer assisted modeling and graphics programs are employed with energy minimization techniques. Stine [133] has summarized empirical methods for predicting densities and heats of formation of proposed high explosives. Gilardi [134]

has given a crystal structure-based description of interest in polycyclic energetic compounds for enhancing performance and/or safety. An interesting connection with such modeling efforts is provided by the description given by Armstrong et al. [135] for deformation twinning in the monoclinic beta-HMX crystal structure where the crystal structure derived potential energy was followed in identifying a type II $\{101\}<101>$ twinning mechanism; see Figure 19. Twinning was concluded to be favorable over slip in the beta-HMX structure because of the flexibility of the HMX molecule. Density considerations have been investigated on a molecular fragmentation basis also so as to understand proposed explosive versus non-explosive behaviors of related molecular structures [136].

5.2. The P-N stress for anthracene

The computer simulation of an $[010](001)$ edge dislocation in anthracene has been reported [137]. The structure relates to that described by Robinson and Scott [37] for Figure 7. Figure 20 shows equipotential contours in the (001) . A dislocation width of 6.2 times the Burgers vector was obtained, indicative of a relatively low P-N stress for the material. The hardness stress-strain result indicated for anthracene in Figure 10 is consistent with a low shear strength being observed for the material, presumably because of only minor intermolecular blockages occurring in the slip process. An interesting consideration in regard to the intermolecular blockage of adjacent molecules is the suggestion of Nabarro that taking account of the displacement normal to the slip plane in evaluating the P-N stress should give a more accurate value. Lee and Dundurs [138] found in evaluating the suggestion on a conventional basis that the stress was lowered.

5.3. Model dislocation displacements

A schematic picture is shown in Figure 21 for a $[100]$ Burgers vector dislocation with line direction along $[001]$ one half-cell deep in an RDX crystal. The dislocation has been reasoned to slip on (040) because of the minimized intermolecular interferences for shear displacements during movement [100]. The indicated molecular positions at the dislocation core are clearly far out of order relative to normal nearest neighbor associations. Based on the consideration that dislocation cores in such molecular crystals might be hollow, as predicted by Frank [18], see section 1.2, the hollow core radius computed for RDX is greater than 7 nm, that is about 6 unit cell distances, thus relating as well to the relatively large values of the dislocation self-energies.

The issue of molecular interferences associated with dislocation movement is demonstrated as well for the RDX lattice structure by examination of slip across the (021) slip plane that was identified at hardness micro-indentation sites by Elban et al. [139]. Figure 22 gives a (100) view of the molecular blockages occurring for shearing across the (021) slip plane, in and out of the projected plane of observation, along $[100]$. The nitrogen-oxygen interactions indicated by the cross-hatched areas of overlapping molecules when displaced along $[100]$ are just those favoring the creation of nitroso compounds detected in "go/no-go" drop-weight impact tests [128] and in thermal decomposition experiments [127].

Dick and Ritchie [140] followed up also on the earlier work by Dick and colleagues [94-96], and in extension of individual reports of their own [141,142], to evaluate the importance of molecular interferences, or steric hindrances, in causing shorter run-to-detonation distances in PETN crystals shocked along different directions, that is, the distance along a crystal rod traversed by a shock wave before detonation is initiated. Also, elastic precursor stress levels specifying different shock strengths were measured along the different directions using a light gas gun facility. Unhindered $[100]$ and $[101]$ directions were tested along with hindered $[110]$ and $[001]$ tests. The elastic precursor strength increased in that same order. The results are in agreement with the reasoning for dislocation passage being blocked by interfering-close intermolecular distances. Intermolecular interactions were evaluated with a molecular mechanics program AMBER developed for biochemical systems. Snapshots of the differently sheared lattice were presented. The computations were stated to support the elastic precursor measurements; and, intramolecular bond rotations and angular strains were found to be relatively important as compared with little changes occurring in bond lengths.

5.4. Hot Spots in MD simulations

Molecular dynamics (MD) methods lend themselves to shock wave modeling considerations because of the nm-scale sharpness of the shock front and presumed femtosecond-to-picosecond time scale of fundamental

events. Karo and colleagues performed pioneering computations relating to energy partitioning and transfer processes, thermal versus athermal characteristics, bond rupturing, and defect influences [143]. Tsai [144,145] has described the influence of a cluster of vacancies on enhancing hot spot development through structural relaxation at the clustered defect site. During such relaxation, apparent slip bands developed at the cluster site and spread across the specimen. Bandak et al. [146] elaborated on the model. Figure 23 shows an (001) body-centered cubic lattice cell of Morse-potential-type atoms, also containing a ten-vacancy cluster that relaxed under the MD process of rapid compression to form a pair of dislocation dipoles. The stress-strain behavior of the system was followed to show apparent yielding during relaxation of the vacancy cluster. In a follow-up study of a simple molecular lattice containing vacant molecules, Tsai and Armstrong emphasized that such permanent relaxation was associated with conversion of the higher potential energy of molecules adjacent to the defect structure to thermal hot spot energy [147]. The important point is that significant hot spot heating is always associated with mechanical relaxation and so a hot spot influence is always present at such sites. The same conclusion was obtained for adaptation of the MD method to a lattice of eight-membered molecular units [148].

The issue of an MD description being appropriate for the comprehensive description of the generation and propagation of shock waves, covering the gamut from match with the continuum theory of planar detonation to connection with local defect properties, as described above, was taken up by C.T. White and colleagues [149]. The associated hot spot mechanism of void collapse was confirmed for a model diatomic lattice [150]. Other MD aspects have been reported for shock compressions and hot spot properties, as follows: model assessment of the multi-phonon up-pumping time scale [151], vibrational heating of naphthalene molecules [152], and picosecond MD resolution of events behind a modeled shock front in polymethylmethacrylate to compare with dye-monitored experimental measurements [153].

5.5. Shock mechanochemistry and atomic force microscopy

Gilman [154] has pointed to historical evidence, stemming from Bridgman's experiments, for the importance of shear deformations in promoting chemical reactions. Based on an analysis of detonation front velocity, Gilman argues that the front propagation is too fast for thermally-activated chemical reactions to occur [155] and homogeneous shear-induced electronic excitations akin to metallization then provide the mechanism for chemical decomposition. The issue relates to earlier discussion [85,76] of the various stages: dislocation movement behind a shock front contributing to initiation of decomposition for weak shocks; that dislocation structure moving behind the shock front, for stronger shocks, and interacting with nanoscale dislocation clusters formed at the front; and, to "in-situ" dislocation core enhancement of decomposition for even stronger shocks. In principle, the importance of anharmonic coupling to the mechanism of vibrational up pumping so as to provide chemistry in the shock front is enhanced within the strain field of the dislocation cores [89]. The Frank hollow core consideration [18] that appears to apply at the nm-scale for energetic crystals should be involved.

Recent results on energetic crystal surfaces obtained with atomic force microscopy (AFM) by Sharma, and analyzed with colleagues, may help to further quantify deformation and thermal influences on energetic material decompositions, for example, relating to recent description of post-shock examination of RDX crystals having undergone an allotropic phase transformation [156]. Sub-molecular-sized shear crack displacements were detected within nanometric-sized crystals formed by multiple fracturing of the initial bulk crystal specimen [157]. Recent measurements have included examination of nanoindentations made within the AFM [158]. Figure 24 shows an AFM picture of the RDX crystal lattice at nm-scale resolution of individual molecule "spots" [159]. Other AFM examinations of laboratory-grown RDX crystals, in an as-cleaved condition and after various deformations and/or heat treatments, have shown differently oriented surface step structures and clustered zones of disordered molecules.

6. Summary

The enhanced visibility of steps associated with the large Burgers vectors of dislocations in energetic/molecular crystals is aided indirectly by the occurrence of low dislocation densities also associated with the large Burgers vectors that lead to relatively high self-energies. A significant variation in dislocation Burgers and line vectors occurs during crystal growth because of the low symmetry of the

molecular crystal structures, conformational requirements of positioning oddly-shaped, relatively large, molecules, and their relatively weak intermolecular bonding.

Dislocation movement, whether in static indentation tests, under drop-weight impact, or in shock wave loading, is relatively hindered by intermolecular cross-blockages of adjacent juxtaposed molecules, thus giving plastic flow stress values near to the theoretical limit for cleavage cracking. The high self-energies of the dislocations make dislocation nucleation prohibitive while, once present, their strain fields can assist chemical decomposition under suitable thermal and environmental circumstances.

Local concentration of strain energy within the relatively more stable energetic crystals is required to induce intramolecular decomposition, relating to (intermolecular-type) hydrogen and (intramolecular) nitrogen/oxygen bond breakages, for example, as indicated in Figures 19, 21, and 22. Dislocation pile-ups provide an explanation of crystal size effects in energetic crystal decompositions. Such molecular crystals give relative enhancement of local heating from plastic work because of their insulating character.

An interesting recent connection is with the thermomechanical aspect of energetic crystal combustion when serving as an ingredient of a propellant motor. Such combustion occurs over a melt layer formed on the individual crystal surfaces. Micro-cracking, as indicated in Figure 15, is enhanced at the liquid-solid interface because of need to supply only the lower liquid-solid interfacial energy of cracks, as compared with the far larger solid-vapor value [108]. Recent model fracture mechanics estimates of the pressures required to propagate such micro-crack networks, relating to the indentation fracture mechanics measurements in Figure 9, give indication of possible crystal shattering instabilities for combustion under high pressure conditions [160].

The role of dislocations in shock wave initiation of detonations is not resolved. Possible mechanisms begin with dislocation activity following behind the shock front for low shocks, shock front generation of dislocations for greater shocks also connecting with follow-on movement of the previously-resident dislocation structure, and, finally, “in-situ” initiation at dislocation cores for high shocks.

Acknowledgements

The authors express appreciation to the many colleagues who have contributed valuable help with our research activities on this topic. Research support has been received with appreciation from the Office of Naval Research, the Naval Surface Warfare Center, both White Oak Laboratory and Indian Head Division, and, most recently, the Air Force Office of Scientific Research. Byron Allmon is thanked for help with compiling the article tables and figures. And, lastly, appreciation is expressed to Michael Duesbery for suggesting that the article be written, and, especially, to Frank Nabarro for many helpful and guiding comments received during his review.

References

1. A.R. Verma, "Crystal Growth and Lattice Imperfections - Interferometric and X-ray Diffraction Studies: Reminiscences", in International School on Synthesis, Crystal Growth and Characterization of Materials for Energy Conversion and Storage (National Physical Laboratory, New Delhi, 1981) p. 1.
2. N. Cabrera and W.K. Burton, "Crystal Growth and Surface Structure, Part II", in Crystal Growth, Discussions of the Faraday Society, No. 5, (Gurney and Jackson, London, 1949) p. 40.
3. F.C. Frank, "The Influence of Dislocations on Crystal Growth", in Crystal Growth, Discussions of the Faraday Society, No. 5 (Gurney and Jackson, London, 1949) p.48, General Discussion, Ibid., p. 67; Philos. Mag. 41, (1950).
4. L.J. Griffin, "Observation of Unimolecular Growth Steps on Crystal Surfaces", Philos. Mag. 41, 196 (1950).
5. A.R. Verma, "Spiral Growth on Carborundum Crystal Faces", Nature 167, 939 (1951).

6. S. Amelinckx, "Spiral Growth on Carborundum Crystal Faces", *Nature* 167, 939 (1951).
7. I.M. Dawson and V. Vand, "The Observation of Spiral Growth-Steps in n-Paraffin Single Crystals in the Electron Microscope", *Proc. Roy. Soc. London*, A206, 555 (1951).
8. N.G. Anderson and I.M. Dawson, "The Study of Crystal Growth with the Electron Microscope: III. Growth-step Patterns and the Relationship of Growth-step Height to Molecular Structure in n-nonatriacontane and in Steric Acid", *Proc. Roy. Soc. London*, A218, 255 (1953); see J.P. Hirth and J. Lothe, "Theory of Dislocations (McGraw-Hill Book Co., N.Y., 1968) p. 10.
9. J.W. Menter, "The direct study by electron microscopy of crystal lattices and their imperfections", *Proc. Roy. Soc. London*, A236, 119 (1956).
10. P.B. Hirsch, R.W. Horne and M.J. Whelan, "Direct Observations of the Arrangement and Motion of Dislocations in Aluminum", *Philos. Mag.* 1, 677 (1956).
11. W. Bollmann, "Interference Effects in the Electron Microscopy of Thin Crystal Foils", *Phys. Rev.* 103, 1588 (1956).
12. J.B. Newkirk and J.H. Wernick, Eds., "Direct Observations of Imperfections in Crystals" (Interscience Publishers, N.Y., 1961).
13. W. Connick and F.G.J. May, "Dislocation Etching of Cyclotrimethylene Trinitramine Crystals", *J. Cryst. Growth* 5, 65 (1969).
14. A.R. Lang, quoted in "Diffraction and Imaging Techniques in Materials Science", S. Amelinckx, R. Gevers and J. Van Landuyt, Editors, Vol. II (North-Holland Publishers, Amsterdam, 1978) p. 678.
15. C.S. Choi and E. Prince, "The Crystal Structure of Cyclotrimethylene-trinitramine", *Acta Cryst.* B28, 2857 (1972).
16. F.R.N. Nabarro, "Theory of Crystal Dislocations" (Dover Publications, N.Y., 1967) p. 302.
17. M. Faraday, "Experimental Researches in Electricity - Sixth Series", *Philos. Trans. Roy. Soc. London*, 55 (1834).
18. F.C. Frank, "Capillary Equilibria of Dislocated Crystals", *Acta Cryst.* 4, 497 (1951).
19. J.M. Thomas, "The chemistry of deformed and imperfect crystals", *Endeavor*, 29, 149 (1970).
20. M. Dudley, W. Si, S. Wang, C. Carter, Jr., R. Glass and V. Tsvetkov, "Quantitative analysis of screw dislocations in 6H-SiC single crystals", *Il Nuovo Cimento* 19D, 153 (1997).
21. J.P. Hirth, "Dislocations Within Elliptical Holes", *Acta mater.* 47, 1 (1999).
22. R.W. Armstrong and W.L. Elban, "Cracking at Hardness Micro-indentations in RDX Explosive and MgO Single Crystals", *Mater. Sci. Eng.* A111, 35 (1989).
23. J.P. Hirth and J. Lothe, "Theory of Dislocations" (McGraw-Hill Book Company, N.Y., 1968) p. 216.
24. W.L. Elban and R.W. Armstrong, "Microhardness Study of RDX to Assess Localized Deformation and Its Role in Hot Spot Formation", Seventh Symposium (International) on Detonation, (Naval Surface Weapons Center, Silver Spring, MD, 1982), NSWC MP 82-334, p. 771.
25. H. Klapper, "Kristalle, die geerntet werden", *die waage*, 33, [1], 28 (1994).

26. H. Klapper, "Defects in Non-Metal Crystals", in *Characterization of Crystal Growth Defects by X-ray Methods*, B.K. Tanner and D.K. Bowen, Editors (Plenum Press, N.Y., 1980) p. 133; R.W. Armstrong, "Characterization of Materials by X-ray Diffraction Topography", in *Crystal Properties and Preparation*, (Trans Tech Publications, Switzerland, 1988), 16, p. 1; also, *Advanced Techniques for Microstructural Evaluation*, R. Krishnan, T.R. Anantharaman, C.S. Pande, and O.P. Arora, Editors, Proceedings of Indo-U.S. Workshop, DST/ONR, 1988, p. 1.
27. A.C. van der Steen and W. Duvalois, "What Do Explosive Particles Look Like?", in *ONR/TNO Workshop on Desensitization of Explosives and Propellants*, A.C. van der Steen, Editor, (TNO Prins Maurits Laboratory, Rijswijk, The Netherlands, 1991), 3, p. 1.
28. R.W. Armstrong, "Dislocation Mechanisms for Shock-Induced Hot Spots", *J. de Phys. IV - Coll. 5*, C4-89 (1995).
29. H. Klapper, "X-ray Topography of Organic Crystals", in *Crystals 13* (Springer-Verlag, Berlin, 1991) p. 109.
30. K.A. Gross, "Liquid Inclusions in RDX", *J. Crystal Growth* 6, 210 (1970).
31. J.D. Eshelby, W.T. Read and W. Shockley, "Anisotropic Elasticity with Applications to Dislocation Theory", *Acta metall.* 1, 251 (1953).
32. W.J.P. van Enkevort and H. Klapper, "Observation of Growth Steps with Full and Half Unit Cell Heights on the {001} Faces of Nickel Sulfate Hexahydrate in Relation to the Defect Structure", *J. Cryst. Growth* 80, 91 (1987).
33. I.T. McDermott and P.P. Phakey, "A Method of Correlating Dislocations and Etch Pits: Application to Cyclotrimethylene Trinitramine", *J. Appl. Cryst.* 4, 479 (1971); *An X-ray Topographic Study of Defect Structures*", *Phys. Stat. Sol. (a)* 8, 505 (1971).
34. P.J. Halfpenny, K.J. Roberts and J.N. Sherwood, "Dislocations in energetic materials: Dislocation characterization and post-growth motion in single crystals of cyclotrimethylene trinitramine", *Philos. Mag.*, 53, 531 (1986).
35. P.J. Halfpenny, K.J. Roberts and J.N. Sherwood, "Dislocations in energetic materials: Part 3. Etching and microhardness studies of pentaerythritol tetranitrate and cyclotrimethylene trinitramine", *J. Mater. Sci.* 19, 1629 (1984).
36. A. Kochendorfer, "Dynamics of Plastic Deformation: Naphthalene Crystals", *Zeits. Kristallogr.* 97, 263 (1937).
37. P.M. Robinson and H.G. Scott, "Plastic Deformation of Anthracene Single Crystals", *Acta metall.* 15, 1581 (1967).
38. J. di Persio and B. Escaig, "Initiation of Dislocation Slip in the B.C.C. Lattice; The case of the van der Waals B.C.C. Hexamine", *Phys. Stat. Sol. (a)* 40, 393 (1977).
39. R.W. Armstrong and W.L. Elban, "Dislocation Aspects of Plastic Flow and Cracking at Indentations in Magnesium Oxide and Cyclotrimethylenetrinitramine Explosive Crystals", in *Microindentation Techniques in Materials Science and Engineering*, P.J. Blau and B.R. Lawn, Editors (Amer. Soc. Test. Mater., Phila., PA, 1986) p. 109.
40. W.L. Elban, R.W. Armstrong, K.-C. Yoo, R.G. Rosemeier and R.Y. Yee, "X-ray reflection topographic study of growth defect and microindentation strain fields in an RDX explosive crystal", *J. Mater. Sci.* 24, 1273 (1989).

41. R.W. Armstrong and A.C. Raghuram, "Anisotropy of Micro-hardness in Crystals", in *The Science of Hardness Testing and Its Research Applications*, J.H. Westbrook and H. Conrad, Editors (Amer. Soc. Metals, Metals Park, OH, 1973) p. 174.
42. H.G. Gallagher, P.J. Halfpenny, J.C. Miller and J.N. Sherwood, "Dislocation slip systems in pentaerythritol tetranitrate (PETN) and cyclotrimethylene trinitramine (RDX)", *Philos. Trans. Roy. Soc. Lond.*, A339, 293 (1992).
43. J.T. Hagan and M.M. Chaudhri, "Fracture surface energies of high explosives PETN and RDX", *J. Mater. Sci.* 12, 1055 (1977).
44. B.R. Lawn and E.R. Fuller, "Equilibrium Penny-Like Cracks in Indentation Fracture", *J. Mater. Sci.* 10, 2016 (1975).
45. W.L. Elban, "Surface energies of high explosives PETN and RDX from contact angle measurements", *J. Mater. Sci.* 14, 1008 (1979).
46. R.W. Armstrong and C.Cm. Wu, "Lattice Misorientation and Displaced Volume for Microhardness Indentations in MgO Crystals", *J. Amer. Ceram. Soc.* 61, 102 (1978); M.M. Chaudhri, "The displacement of material and the formation of {110} cracks around spherical indentations in MgO crystals", *Phil. Mag. Letters*, 53, L55 (1986).
47. K.-C. Yoo, R.G. Rosemeier, W.L. Elban, and R.W. Armstrong, "X-ray Topography Evidence for Energy Dissipation at Indentation Cracks in MgO Crystals", *J. Mater. Sci. Lett.*, 3, 560 (1984).
48. W.L. Elban, J.C. Hoffsommer, D.J. Glover, C.S. Coffey and R.W. Armstrong, "Summary Report: Microstructural Origins of Hot Spots in RDX Explosive and Several Reference Inert Materials", (Naval Surface Weapons Center, White Oak, MD, 1984) NSWC MP 84-358.
49. B.L. Hammond and R.W. Armstrong, "Recovered elastic and plastic strains at residual micro-indentations in an MgO crystal", *Philos. Mag. Lett.* 57, 41 (1988).
50. R.W. Armstrong and W.H. Robinson, "Combined elastic and plastic deformation behavior from a continuous indentation hardness test", *New Zealand J. Sci.* 17, 429 (1974).
51. F.C. Frank and B.R. Lawn, "On the Theory of Hertzian Fracture", *Proc. Roy. Soc. London*, A299, 291 (1967).
52. B.R. Lawn, "Hertzian Fracture in Single Crystals with the Diamond Structure", *J. Appl. Phys.* 39, 4828 (1968).
53. D. Tabor, *The Hardness of Metals* (Oxford, Clarendon Press, 1951).
54. F.P. Bowden and A.D. Yoffe, "Initiation and growth of explosion in liquids and solids", (Cambridge University Press, London, 1952); "Fast reactions in solids", (Buttersworths Scientific Publications, London, 1958).
55. G.T. Afanas'ev and V.K. Bobolev, "Initiation of solid explosives by impact", (Israel Program for Sci. Transl., Jerusalem, 1971).
56. J.E. Field, G.M Swallowe and S.N. Heavens, "Ignition mechanisms of explosives during mechanical deformation", *Proc. Roy. Soc.* A382, 231 (1982).
57. C.S. Coffey and S.J. Jacobs, "Detection of Local Heating in Impact or Shock Experiments with Thermally Sensitive Films", *J. Appl. Phys.* 52, 6991 (1981).

58. S.N. Heavens and J.E. Field, "The Ignition of a Thin Layer of Explosive by Impact", *Proc. Roy. Soc. London* A338, 77 (1974); G.M. Swallowe and J.E. Field, "The Ignition of a Thin Layer of Explosive by Impact; The Effect of Polymer Particles", *Ibid.*, A379, 389 (1982).
59. R.E. Winter and J.E. Field, "The role of localized plastic flow in the impact initiation of explosives", *Proc. Roy. Soc.* A343, 399 (1975)
60. R.W. Armstrong, C.S. Coffey and W.L. Elban, "Adiabatic Heating at a Dislocation Pile-up Avalanche", *Acta. Metall.* 30, 2111 (1982).
61. A.K. Head, "Dislocation Group Dynamics. VI. The Release of a Pile-up", *Philos. Mag.* 27, 531 (1973).
62. F.P. Gerstle and G.J. Dvorak, "Dynamic formation and release of a dislocation pile-up against a viscous obstacle", *Philos. Mag.* 29, 1337 (1974); A dislocation pile-up model of dynamic yielding and flow in steel", *Ibid.*, 1347 (1974).
63. H. Ockendon and J.R. Ockendon, "Dynamic dislocation pile-ups", *Philos. Mag.* A47, 707 (1983).
64. F. Liu, I. Baker and M. Dudley, "Dislocation-grain boundary interactions in ice crystals", *Philos. Mag.* 71, 15 (1995).
65. R.W. Armstrong, "The Yield and Flow Stress Dependence on Polycrystal Grain Size", in *Yield, Flow and Fracture of Polycrystals*, T.N. Baker, Editor (Applied Science Publ., Barking, U.K., 1983) p. 1.
66. E.O. Hall, "The Deformation and Aging of Mild Steel: III. Discussion of Results", *Proc. Phys. Soc. London*, B64, 747 (1951).
67. N.J. Petch, "The Cleavage Strength of Polycrystals", *J. Iron Steel Inst.* 174, 25 (1953).
68. R.W. Armstrong, I. Codd, R.M. Douthwaite and N.J. Petch, "The plastic deformation of polycrystalline aggregates", *Philos. Mag.* 7, 45 (1962).
69. F.P. Bowden and K. Singh, "Size effects in the initiation and growth of explosion", *Nature* 172, 378 (1953).
70. R.W. Armstrong, C.S. Coffey, V.F. DeVost and W.L. Elban, "Crystal size dependence for impact initiation of cyclotrimethylene trinitramine explosive", *J. Appl. Phys.* 68, 979 (1990).
71. F.P. Bowden, P.G. Fox and J. Soria-Ruiz, "Direct Observation of Thermal Decomposition Produced by Fracture in Brittle Crystalline Solids", *Nature* 220, 778 (1968).
72. P.G. Fox and J. Soria-Ruiz, "Fracture-induced thermal decomposition in brittle crystalline solids", *Proc. Roy. Soc.*, A317, 79 (1970).
73. T. Boddington, "The Growth and Decay of Hot Spots and the Relation between Structure and Stability", Ninth Symposium (International) on Combustion, The Combustion Inst. (Academic Press, N.Y., 1963) p. 287.
74. R.W. Armstrong and W.L. Elban, "Temperature rise at a dislocation pile-up avalanche", *Mater. Sci. Eng.* A122, L1 (1989).
75. R.W. Armstrong and F.J. Zerilli, "Dislocation mechanics aspects of plastic instability and shear banding", *Mech. Mater.* 17, 319 (1994).

76. R.W. Armstrong, "Dislocation Mechanisms for Shock-Induced Hot Spots", *J. de Phys.* IV-Coll., 5, C4-89 (1995).
77. C.S. Smith, "Metallographic Studies of Metals After Explosive Shock", *Trans. The Metall. Soc., Amer. Inst. Min. Metall. Eng.* 212, 574 (1958).
78. M.A. Meyers, "A Mechanism for Dislocation Generation in Shock-Wave Deformation", *Scripta Metall.* 12, 21 (1978).
79. R.W. Armstrong, R.S. Miller and H.W. Sandusky, in R.W. Armstrong, "Indentation Hardness Testing, Defect Structure and Shock Model for RDX Explosive Crystals", in *ONR Workshop on Dynamic Deformation, Fracture and Transient Combustion*, Chemical Propulsion Information Agency, CPIA Publication 474, p. 77 (1987).
80. F.A. Bandak, R.W. Armstrong and A.S. Douglas, "Dislocation structure for one-dimensional strain in a shocked crystal", *Phys. Rev.* 46, 3228 (1992).
81. R.W. Armstrong and F.J. Zerilli, "Dislocation mechanics aspects of shock-wave and high-strain-rate phenomena", in *EXPLOMET 2000, Fundamental Issues and Applications of Shock-Wave and High-Strain-Rate Phenomena*, K.P. Staudhammer, L.E. Murr, and M.A. Meyers, Editors (Elsevier Science Ltd, N.Y., 2001) Chapter 15, p. 115.
82. Y.M. Gupta and G.R. Fowles, "Shock-Induced Dynamic Yielding in LiF Single Crystals", in *Metallurgical Effects at High Strain Rates*, R.W. Rohde, B.M. Butcher, J.R. Holland and C.H. Karnes, Editors (Plenum Press, N.Y., 1973) p. 367.
83. Y.M. Gupta, G.E. Duvall and G.R. Fowles, "Dislocation Mechanisms for Stress Relaxation in Shocked Lithium Fluoride", *J. Appl. Phys.* 46, 532 (1975).
84. K.S. Tunison and Y.M. Gupta, "Elastic Precursor Decay in Shocked Pure LiF Crystals: Role of Surface Damage", in *Shock Waves in Condensed Matter 1987*, S.C. Schmidt and N.C. Holmes, Editors (Elsevier Science Publ. B.V., N.Y., 1988) p. 277.
85. R.W. Armstrong, "Roles Possibles des Dislocations dans les Detonations par Choc dans les Cristaux Energetique", *Traduction: J. Boileau, Revue Scientifique et Technique de la Defense*, 16, [2], 161 (1992).
86. W.C. Leslie, "Microstructural Effects at High Strain Rate Deformation", in *Metallurgical Effects at High Strain Rates*, R.W. Rohde, B.M. Butcher, J.R. Holland and C.H. Karnes, Editors (Plenum press, N.Y., 1973) p. 571.
87. D.D. Dlott, "Optical Phonon Dynamics in Molecular Crystals", *Ann. Rev. Phys. Chem.* 37, 157 (1986).
88. D.D. Dlott and M.D. Fayer, "Shocked molecular solids: Vibrational up pumping, defect hot spot formation, and the onset of chemistry", *J. Chem. Phys.* 92, 3798 (1990).
89. A. Tokmakoff, M.D. Fayer and D.D. Dlott, "Chemical Reaction Initiation and Hot-Spot Formation in Shocked Energetic Molecular Materials", *J. Phys. Chem.* 97, 1901 (1993).
90. G.K. Adams, J. Holden and E.G. Whitbread, "The Explosive Initiation of a Single Crystal of Cyclotrimethylenetrinitramine", *Extrait du Compte-rendu du XXXIe Congres International de Chimie Industrielle* (Imprimerie Mercurius - anvers, Fr, 1958) p. 1.
91. H.W. Sandusky, B.C. Glancy, D.W. Carlson, W.L. Elban and R.W. Armstrong, "Relating Deformation to Hot Spot in Shock-Loaded Crystals of Ammonium Perchlorate", *J. Propulsion and Power* 7, 518 (1991).

92. B.C. Beard, H.W. Sandusky, B.C. Glancy, and W.L. Elban, "Defect density measurements in shocked single crystal ammonium perchlorate by x-ray photoelectron spectroscopy", *J. Mater. Res.* 7, 3266 (1992).
93. J.W. Forbes, D.G. Tasker, R.H. Granholm and P.K. Gustavson, "Direct Observation of Shocked Explosive Crystals Immersed in Liquids", in *Shock Compression of Condensed Matter – 1989*, S.C. Schmidt, J.N. Johnson, and L.W. Davison, Editors (Elsevier Publ. B.V., N.Y., 1990) p. 709.
94. J.J. Dick, "Effect of crystal orientation on shock initiation sensitivity of pentaerythritol tetranitrate explosive", *Appl. Phys. Lett.* 44, 859 (1984).
95. J.J. Dick, E. Garcia and D.C. Shaw, "Shock Initiation of Pentaerythritol Tetranitrate Crystals: Steric Effects Due to Plastic Flow", in *Shock Compression of Condensed Matter – 1991*, S.C. Schmidt, R.D. Dick, J.W. Forbes and D.G. Tasker, Editors (North Holland Publ., Amsterdam, 1992) p.
96. J.J. Dick, R.N. Mulford, W.J. Spencer, D.R. Pettit, E. Garcia and D.C. Shaw, "Shock response of pentaerythritol tetranitrate single crystals", *J. Appl. Phys.* 70, 3572 (1991).
97. B. Olinger, P.M. Halleck and H.H. Cady, "The isothermal linear and volume compression of pentaerythritol tetranitrate (PETN) to 10 GPa (100 kbar) and the calculated shock compression", *J. Chem. Phys.* 62, 4480 (1975).
98. P.M. Halleck and J. Wackerle, "Dynamic elastic-plastic properties of single-crystal pentaerythritol tetranitrate", *J. Appl. Phys.* 47, 976 (1976).
99. C.E. Morris, "Adiabatic Elastic Moduli of Single Crystal Pentaerythritol Tetranitrate (PETN)", in *Proc. Sixth Symposium (International) on Detonation* (Office of Naval Research, Arlington, VA, 1976) ACR-221, p. 396.
100. R.W. Armstrong and W.L. Elban, "Microstructural Origin of Hot Spots in RDX Crystals", in *ONR Workshop on Energetic Material Initiation Fundamentals*, Chemical Propulsion Information Agency, CPIA Publ. 475, 171 (1987).
101. J.J. Dick, "Supercritical shear in shocked pentaerythritol tetranitrate", *Appl. Phys. Lett.* 60, 2494 (1992).
102. J.J. Dick, "Orientation-Dependent Explosion Sensitivity of Solid Methane", *J. Phys. Chem.* 97, 6193 (1993).
103. G.J. Piermarini, S. Block, R. Damavarapu and S. Iyer, *Propellants, Explosives and Pyrotechnics*, 16, 188 (1991).
104. A.L. Ramaswamy, "Laser Ignition of Secondary Explosives", Ph.D. thesis, Cambridge University, 1993.
105. R.W. Armstrong, A.L. Ramaswamy and J.E. Field, "Thermomechanical Influences on the Combustion of RDX Crystals", in *ONR/SNPE/ONERA Workshop on Combustion Mechanisms*, R.W. Armstrong, Editor, (ONR London, U.K. 1991) p. 168.
106. A.L. Ramaswamy and J.E. Field, "Laser-induced ignition of single crystals of the secondary explosive cyclotrimethylene trinitramine", *J. Appl. Phys.* 79, 3842 (1996).
107. A.L. Ramaswamy, J.E. Field and R.W. Armstrong, "The Laser Initiation of Energetic Materials", in *Pyrotechnics : Basic Principles, Technology and Applications*, (Fraunhofer Institut Chemische Technologie, Karlsruhe, 1995) p. 18-1.

108. W.L. Elban, R.W. Armstrong and T.P. Russell, "Plasticity/interfacial energy influences on combustion-driven cracking of RDX energetic crystals", *Philos. Mag.* A78, 907 (1998).
109. A.L. Ramaswamy, H. Shin, R.W. Armstrong, C.H. Lee and J. Sharma, "Nanosecond and picosecond laser-induced cracking and ignition of single crystals of ammonium perchlorate", *J. Mater. Sci.* 31, 6035 (1996).
110. P.G. Fox and J. Soria-Ruiz, "Fracture-Induced Thermal Decomposition in Brittle Crystalline Solids", *Proc. Roy. Soc. London*, A314, 79 (1970).
111. P.G. Fox, "Some Chemical Consequences of Plasticity", in *Physics of Materials*, D.W. Borland, L.M. Clarebrough and A.J.W. Moore, Editors, (Commonwealth Scientific and Industrial Research Organization, Australia, and University of Melbourne, 1979) p. 73.
112. H.M. Hauser, J.E. Field and V.K. Mohan, "Fracture-Induced Decomposition of a Brittle High Explosive: Pentaerythritol Tetranitrate", *Chem. Phys. Lett.* 99, 66 (1983).
113. J.M. Thomas, "Enhanced Reactivity at Dislocations in Solids", in *Advances in Catalysis and Related Subjects*, Vol. 19, D.D. Eley, H. Pines and P.W. Weisz, Editors (Academic Press, N.Y., 1969) p. 293.
114. J.M. Thomas, "Review Lecture: Topography and Topology in Solid State Chemistry", *Philos. Trans. Roy. Soc. London*, A277, 31 (1974).
115. C.H. Bamford and G.C. Eastmond, "Solid-phase Addition Polymerization", *Rev. Chem. Soc.*, 23, 271 (1969).
116. A.K. Galwey and P.W.M. Jacobs, "The thermal decomposition of ammonium perchlorate at low temperatures", *Proc. Roy. Soc. London*, A254, 455 (1960).
117. P.J. Herley and P.W. Levy, "Thermal Decomposition of Irradiated Orthorhombic Ammonium Perchlorate", *Nature*, 211, 1287 (1966).
118. P.J. Herley and P.W. Levy, "Effects of X- and Gamma-Ray Radiation on the Thermal Decomposition of Solid Orthorhombic Ammonium Perchlorate. I. Experimental and Results", *J. Chem. Phys.*, 49, 1493 (1968).
119. P.J. Herley and P.W. Levy, "Effects of X- and Gamma-Ray Radiation on the Thermal Decomposition of Solid Orthorhombic Ammonium Perchlorate. II. Kinetics and Discussion", *J. Chem. Phys.*, 49, 1500 (1968).
120. P.J. Herley, P.W.M. Jacobs and P.W. Levy, "A photomicrographic and electron microscopy study of nucleation in ammonium perchlorate", *Proc. Roy. Soc. London*, A318, 197 (1970); "Dislocations in Ammonium Perchlorate", *J. Chem. Soc. (A)*, 434 (1971); see also J.O. Williams, J.M. Thomas, Y.P. Savintsev, and V.V. Boldyrev, "Dislocations in Orthorhombic Ammonium Perchlorate", *J. Chem. Soc. (A)*, 1757 (1971).
121. P.J. Herley and P.W. Levy, "Microscopic Observation of X-ray and Gamma-ray Induced Decomposition of Ammonium Perchlorate Crystals", in *Proc. Amer. Nucl. Soc., AIAA Conference on Natural and Man-made Radiation in Space* (NASA Technical Memorandum X-2440, 1972) p. 584.
122. P.J. Herley, and P.W. Levy, "Radiation-induced Dislocations in Ammonium Perchlorate Crystals", *Nature Physical Science*, 232, 66 (1971).
123. P.J. Herley and P.W. Levy, "Quantitative Studies on Radiation Induced Dislocations and the Decomposition Kinetics of ammonium Perchlorate", in *Reactivity of Solids: Proceedings of the Seventh International Symposium on the Reactivity of Solids* (Chapman and Hall, London, 1972) p. 387; "New

Insights on the Thermal Decomposition of Ammonium Perchlorate from Studies on Very Large Single Crystals”, in *Reactivity of Solids* (Plenum Press, London, 1977) p. 355.

124. T.B. Tang, M.M. Chaudhri, C.S. Rees and S.J. Mullock, "Decomposition of solid explosives by laser irradiation: a mass spectrographic study", *J. Mater. Sci.* 22, 1037 (1987).

125. R.W. Armstrong, "Breaking Molecules in Solid Explosives", *European Scientific Notes* (ONR London, 1983) ESN 37-7, p. 290.

126. T.B. Brill, "Surface Chemical Characterization Methods Applied to Energetic Materials", in *Structure and Properties of Energetic Materials*, D.H. Liebenberg, R.W. Armstrong and J.J. Gilman, Editors (Materials research Society, Pittsburgh, PA, 1993) Vol. 296, p. 269.

127. R. Behrens, Jr., and S. Bulusu, "Thermal Decomposition of Energetic Materials. 3. Temporal Behaviors of the Rates of Formation of the Gaseous Pyrolysis Products from Condensed Phase Decomposition of 1,3,5-Trinitrohexahydro-s-triazine (RDX)", *J. Phys. Chem.* 96, 8877 (1992).

128. J.C. Hoffsommer, D.J. Glover and W.L. Elban, "Quantitative Evidence for Nitroso Compound Formation in Drop-Weight Impacted RDX Crystals", *J. Energetic Mater.* 3, 149 (1985).

129. H.L. Bhat, P.J. Herley, D.B. Sheen and J.N. Sherwood, "An X-ray Topographic Study of Beam Induced Decomposition in Ammonium Perchlorate Single Crystals", in *Applications of X-Ray Topographic Methods to Materials Science*, S. Weissmann, F. Balibar and J.-F. Petroff, Editors (Plenum Press, N.Y., 1984) p. 401.

130. D.B. Sheen and J.N. Sherwood, "X-ray Topographic Studies of the Role of Substructure in the Progress of Reactions in Solids", in *Reactivity of Solids: Proceedings of the Tenth International Symposium on the Reactivity of Solids*, P. Barret and L.-C. Dufour, Editors (Elsevier Publ. B.V., N.Y., 1985) p. 93.

131. W.L. Elban, H.W. Sandusky, B.C. Beard and B.C. Glancy, "Microstructural Basis for Enhanced Shock-Induced Chemistry in Single Crystal Ammonium Perchlorate", *J. Propulsion and Power* 11, 24 (1995).

132. D.T. Cromer, H.L. Ammon and J.R. Holden, "A Procedure for Estimating the Crystal Densities of Organic Explosives", *Los Alamos National Laboratory Report LA-11142-MS, UC-45* (1987).

133. J.R. Stine, "Molecular Structure and Performance of High Explosives", in *Structure and Properties of Energetic Materials*, D.H. Liebenberg, R.W. Armstrong and J.J. Gilman, Editors (Mater. Res. Soc., Pittsburgh, PA, 1993), Vol 296, p. 3.

134 R. Gilardi, "The Molecular and Crystal Structures of Polycyclic Energetic Materials", in *Structure and Properties of Energetic Materials*, D.H. Liebenberg, R.W. Armstrong and J.J. Gilman, Editors (Mater. Res. Soc., Pittsburgh, PA, 1993), Vol. 296, p. 233.

135. R.W. Armstrong, H.L. Ammon, Z.Y. Du, W.L. Elban and X.J. Zhang, "Energetic Crystal-Lattice-Dependent Responses", in *Structure and Properties of Energetic Materials*, D.H. Liebenberg, R.W. Armstrong and J.J. Gilman, Editors (Mater. Res. Soc., Pittsburgh, PA, 1993) Vol. 296, p. 227.

136. P. Rudel, S. Odiet, J.C. Mutin and M. Peyard, "Structure cristalline et caractere detonique des cristaux moleculaires nitres", *J. Chim. Phys.* 87, 1307 (1990).

137. N. Ide, I. Okada and K. Kojima, "Computer simulation of an edge dislocation in anthracene crystals", *J. Phys.: Condens. Matter* 2, 5489 (1990).

138. M.-S. Lee and J. Dundurs, "On the Peierls Force", *Philos. Mag.* 26, 929 (1972).

139. W.L. Elban, J.C. Hoffsommer and R.W. Armstrong, "X-ray orientation and hardness experiments on RDX explosive crystals", *J. Mater. Sci.* 19, 552 (1984).
140. J.J. Dick and J.P. Ritchie, "Molecular mechanics modeling of shear and the crystal orientation dependence of the elastic precursor shock strength in pentaerythritol tetranitrate", *J. Appl. Phys.* 76, 2726 (1994).
141. J.J. Dick, "The Importance of Sterically Hindered Shear in Determining the Sensitivity of Explosive Crystals", in *The Structure and Properties of Energetic Materials*, D.H. Liebenberg, R.W. Armstrong and J.J. Gilman, Editors (Mater. Res. Soc., Pittsburgh, PA, 1993), Vol. 296, p. 75.
142. J.P. Ritchie, "Molecular Modeling of Slip Supposed to Occur in the Shock Initiation of Crystalline PETN", in *Structure and Properties of Energetic Materials*, D.H. Liebenberg, R.W. Armstrong and J.J. Gilman, Editors (Mater. Res. Soc., Pittsburgh, PA, 1993), Vol. 296, p. 99.
143. J.R. Hardy, A.M. Karo and F.E. Walker, "The Molecular Dynamics of Shock and Detonation Phenomena in Condensed Matter", in *Progress in Aeronautics and Astronautics*, J.R. Bowen et al., Editors (AIAA, 1981), Vol. 75, p. 209.
144. D.H. Tsai, "Structural defects and "hot spot" formation in a crystalline solid under rapid compression. 1. Vacancy clusters and slip bands", *J. Chem. Phys.* 95, 7497 (1991).
145. D.H. Tsai, "Hot Spot Heating from Impurities and Vacancies in a Crystalline Solid Under Rapid Compression", in *Structure and Properties of Energetic Materials*, D.H. Liebenberg, R.W. Armstrong and J.J. Gilman, Editors (Mater. Res. Soc., Pittsburgh, PA, 1993, 1993) Vol. 296, p. 113.
146. F.A. Bandak, D.H. Tsai, R.W. Armstrong and A.S. Douglas, "Formation of nanodislocation dipoles in shock-compressed crystals", *Phys. Rev. B* 47, 11681 (1993).
147. D.H. Tsai and R.W. Armstrong, "Defect-Enhanced Structural Relaxation Mechanism for the Evolution of Hot Spots in Rapidly Compressed Crystals", *J. Phys. Chem.* 98, 10997 (1994).
148. R.W. Armstrong, H.L. Ammon, W.L. Elban, and D.H. Tsai, "Investigation of Hot Spot Characteristics in Energetic Crystals", in *Energetic Materials*, *Thermochimica Acta*, 2001, in print.
149. C.T. White, D.H. Robertson, M.L. Elert, J.W. Mintmire and D.W. Brenner, "Dissociative Phase Transitions, Split Shock Waves, Rarefaction Shocks, and Detonations", in *Structure and Properties of Energetic Materials*, D.H. Liebenberg, R.W. Armstrong and J.J. Gilman, Editors (Mater. Res. Soc., Pittsburgh, PA, 1993) Vol. 296, p. 123.
150. J.W. Mintmire, D.H. Robertson, and C.T. White, "Molecular-dynamics simulations of void collapse in shocked model-molecular solids", *Phys. Rev. B* 49, 14859 (1994).
151. J. Belak, "Computer Simulation of Molecular Response at a Shock Front", in *High-Pressure Science and Technology - 1993*, S.C. Schmidt, J.W. Shaner, G.A. Samara and M. Ross, Editors (Amer. Inst. Phys., N.Y., 1994) AIP Conf. Proc. 309, Part 2, p. 1063.
152. H. Kim and Y. Won, "Molecular Dynamics Simulations of Vibrational Energy Distribution in Vibrational Cooling and Heating", *J. Phys. Chem.* 100, 9495 (1996).
153. I.-Y.S. Lee, J.R. Hill, H. Suzuki, D.D. Dlott, B.J. Baer and E.L. Chronister, "Molecular dynamics observed 60 ps behind a solid-state shock front", *J. Chem. Phys.* 103, 8313 (1995).
154. J.J. Gilman, "Mechanochemistry", *Science* 274, 65 (1996).

155. J.J. Gilman, "Shear-induced metallization", *Philos. Mag. B*, 67, 207 (1993); "Chemical reactions at detonation fronts in solids", *Philos. Mag.* 71, 1057 (1995).
156. J. Sharma, S.M. Hoover, C.S. Coffey, A.S. Tompa, H.W. Sandusky, R.W. Armstrong and W.L. Elban, "Structure of Crystal Defects in Damaged RDX as Revealed by an AFM", in *Shock Compression of Condensed Matter - 1997*, S.C. Schmidt, D.D. Dandekar and J.W. Forbes, Editors (Amer. Inst Phys., N.Y., 1998) Vol. CP429, p. 563.
157. J. Sharma, R.W. Armstrong, W.L. Elban, C.S. Coffey and H.W. Sandusky, "Nanofractography of shocked RDX explosive crystals with atomic force microscopy", *Appl. Phys. Letters* 78, 457 (22 Jan 2001).
158. J. Sharma, C.S. Coffey, R.W. Armstrong, W.L. Elban, and S.M. Hoover, "Sub-Molecular Fracture Steps in Shock-Shattered RDX Crystals and Follow-On Nano-Indentation Evaluation of Early Stage Plasticity", in *Shock Compression of Condensed Matter – 2001*, (Amer. Inst. Phys., N.Y., 2002) in print.
159. J. Sharma, R.W. Armstrong, W.L. Elban, and C.S. Coffey, "Nanostructure of Defects and Hot Spots of Explosives as Revealed by an Atomic Force Microscope", *Proceedings of the Eleventh Symposium (International) on Detonation*, (Omnipress, Omnipress-CD, 2000) p. 443.
160. R.W. Armstrong, C.F. Clark and W.L. Elban, "Influence of Micro-cracking on Pressure-Dependent Energetic Crystal Combustion", in *Combustion of Energetic Materials*, K.K. Kuo and L. De Luca, Editors (Begell House, Inc., N.Y., 2001) in print.

Dislocations in Energetic Crystals

R.W. Armstrong and W.L. Elban

List of Tables

Table 1. Comparison of dislocation strain energies and Peierls-Nabarro Stresses for RDX, LiF, and MgO, after Armstrong and Elban [22].

Table 2. The types of pressure – time curves shown by various materials subjected to impact, after Heavens and Field [58].

Table 3. Fracture-induced cleavage surface chemical decompositions, after Bowden, Fox, and Soria-Ruiz [71] and Fox and Soria-Ruiz [72].

List of Figures

Figure 1. A phase contrast micrograph of the (0001) face on a 6H SiC crystal showing the growth pattern due to three dislocations of like sign close together and giving rise to three cooperating growth spirals. The central or the last part of the growth is circular while the rest is hexagonal. (X500). After Verma [1].

Figure 2. An (0006) section x-ray transmission topograph showing an image of a screw dislocation micropipe, M; after Dudley, Si, Wang, Carter, Glass, and Tsvetkov [20].

Figure 3. Schematic illustration of (a) division of a crystal into growth sectors according to different growth directions including indication of (dashed) contours at different stages of growth; and (b) typical geometry of grown-in dislocation lines initiated at inclusion particles. After Klapper [26].

Figure 4. Growth sector structure within a sectioned RDX crystal, after van der Steen and Duvalois [27], with growth band (planar) trace identifications, after Armstrong [28].

Figure 5. A {210} x-ray transmission topograph of an RDX crystal showing dislocation bundles spreading from a central seed position to the external crystal growth surfaces; after McDermott and Phakey [33].

Figure 6. A scanning electron micrograph of an RDX crystal, after van der Steen and Duvalois [27], with crystallographically-identified planar growth surfaces, also with A to D locations marked for growth protuberances at positions of dislocation bundle emergence, after Armstrong [28].

Figure 7. Schematic plane sections of the crystal structure of anthracene: (a) (010) projection of the unit cell, with a and c axes identified, and showing carbon atoms and carbon-carbon bonds; (b) (001) projection, with a and b axes marked, and showing carbon-carbon bonds, with the light lines applying for molecules at height c above the dark line molecules; (c) a faulted (001) structure relating to (b). After Robinson and Scott [37].

Figure 8. Dislocation etch pits centered on microindentations in the (210) plane growth surface of RDX: (top) Knoop indentation with long axis parallel to [001]; and (bottom) identified Vickers diamond pyramid indentation with one equiaxed diagonal length parallel to [001]. The long black lines in the figures are cracks. After Elban and Armstrong [24].

Figure 9. Logarithmic dependence, according to constant hardness or constant indentation fracture stress intensity, of applied indenter force on diagonal indentation and crack lengths for RDX and MgO crystals; after Armstrong and Elban [22].

Figure 10. Hardness stress–strain basis for comparing the elastic, plastic and cracking behaviors of crystal materials, including calculation of the terminal elastic cracking stresses for different ball sizes; after Hammond and Armstrong [49].

Figure 11. Release of a dislocation pile-up from its blocking obstacle, showing the shape of the dislocation distribution as it moves from right to left, at sequential (dimensionless) time steps, $t = 0, 0.01, 0.03, 0.10$ and 0.30 , after Head [61].

Figure 12. Drop-weight impact height for 50% probability of initiation as it depends on crystal size, including, for 0.25 mm size crystals, an indication of influence of variation of crystal quality in different batches, after Armstrong, Coffey, DeVost and Elban [70].

Figure 13. Graphical basis for illustrating hot spot susceptibility of materials on a dislocation pile-up avalanche model description, including different hot spot temperature expressions for metallic and ionic materials as compared with energetic RDX and PETN, after Armstrong, Coffey and Elban [60].

Figure 14. Shock model for nanometer-scale dislocation loops that produce a residual deformation state of one-dimensional compression, after Armstrong, Miller, and Sandusky [79], as elaborated by Bandak, Armstrong, and Douglas [80].

Figure 15. Combustion residue and microcracking at an RDX (210) crystal surface burn spot after laser irradiation; the vertical separation of parallel microcracks is ~ 5 micrometers. After Armstrong, Ramaswamy, and Field [105], as further analyzed by Elban, Armstrong, and Russell [108].

Figure 16. Laser-impacted (001)AP crystal surface (a) at high magnification to show the sequential macroscopic (210) cracking in the low temperature orthorhombic phase and higher temperature, finer scale, $\{010\}$ cracking retained from the rocksalt-type cubic phase; and (b) lower magnification view of the central drilled hole exhibiting a whitish halo of sub-surface (001) cracking. After Ramaswamy, Shin, Armstrong, Lee, and Sharma [109].

Figure 17. Schematic dislocation model for explanation of the $\{010\}$ cracking shown in Figure 16a for the higher temperature rocksalt-type cubic structure of AP; after Ramaswamy et al. [109].

Figure 18. Photomicrographs of matching AP (210) cleavage surfaces showing radiation-induced dislocation movement. Side a was not irradiated but side b received a dose of 10^4 rad gamma-ray exposure. A set of dislocations which have moved during irradiation is labeled M while set S has remained stationary. After Herley and Levy [122,123].

Figure 19. Crystallography of Type II $\{101\}<101>$ twinning in HMX; on a stereographic projection basis at top left, and (010) plane projection of pre-and post-twin positions at top right, with tabulated sequential potential energy evaluations for the indicated lattice point displacements, also involving required N-N bond rotation. After Armstrong, Ammon, Du, Elban and Zhang [135].

Figure 20. A projection in the (100) plane of molecular centers at an edge dislocation core in anthracene after relaxation of the lattice positions and with equipotential curves (in units of eV). The crosses denote corner molecules and circles, center molecules. After Ide, Okada, and Kojima [137].

Figure 21. Schematic view of RDX molecule positions for an $[001]$ edge dislocation on the (040) plane, after Armstrong [28].

Figure 22. For RDX, dinitroso-related interactions from $[100](021)$ slip, in and out of the surface-projected (100); after Armstrong [28] and relating to experimental results both from Hoffsommer, Glover, and Elban [128] and Behrens and Buluso [127].

Figure 23. Molecular dynamics modeling of the collapse of a vacancy cluster into a pair of edge dislocation dipoles, after Bandak, Tsai, Armstrong, and Douglas [146].

Figure 24. Atomic force microscope image of molecule positions on an identified RDX (001) cleavage surface, after Sharma, unpublished; see J. Sharma et al. [159].

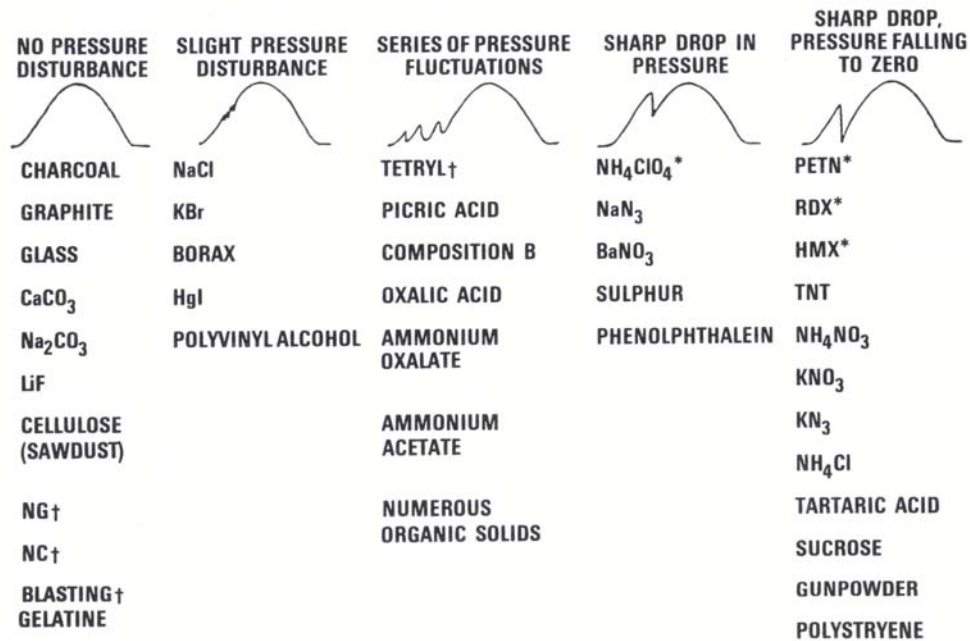
Table 1. Comparison of dislocation strain energies and Peierls-Nabarro Stresses for RDX, LiF, and MgO, after Armstrong and Elban [22].

| Material | Dislocation Strain Energy Coefficient ($E_{\perp/p}$), | $\left(\frac{E_{\perp/p}}{\Delta H_{f/m}}\right)$ | Peierls-Nabarro Stress, (τ_p), N/mm ² | $\left(\frac{\tau_p}{G}\right)$ |
|----------|--|---|---|---------------------------------|
| RDX | 6.3×10^{-19} | 12 | 580 | 0.077 |
| LiF | 0.9×10^{-19} | 2.1 | 3100 | 0.050 |
| MgO | 2.4×10^{-19} | 1.9 | 8000 | 0.054 |

$$E_{\perp/p} = (Gb^2 \Delta \epsilon / 4 \pi \alpha)$$

$$\tau_p (= \tau_{P-N}) = [2G/(1-\nu)] \exp[-2\pi d/(1-\nu)b]$$

Table 2. The types of pressure – time curves shown by various materials subjected to impact, after Heavens and Field [58].



* THESE MATERIALS IGNITED AT THE INSTANT OF THE PRESSURE DROP.

† THESE MATERIALS IGNITED, BUT NOT AT THE INSTANT OF A PRESSURE DROP.

Table 3. Fracture-induced cleavage surface chemical decompositions, after Bowden, Fox, and Soria-Ruiz [71] and Fox and Soria-Ruiz [72].

| Material | No. of expts. | Amount of decomposition (molecules cm ⁻²) | Average No. of monolayers decomposed |
|---------------------------------|---------------|---|--------------------------------------|
| Magnesium oxide | 9 | < 12 ¹³ | < 0.001 |
| Calcium carbonate (calcite) | 14 | 2 × 10 ¹³ | 0.09 |
| Magnesium carbonate (magnesite) | 14 | 1 × 10 ¹⁴ | 0.37 |
| Lead carbonate (cerussite) | 8 | ~ 7 × 10 ¹⁴ | ~ 2 |
| Sodium azide | 5 | 1 × 10 ¹³ | 0.02 |
| β-Lead azide | 10 | ~ 3 × 10 ¹⁵ | ~ 10 |
| PETN | 7 | 2 × 10 ¹⁵ (for mass 28) | ~ 2 |

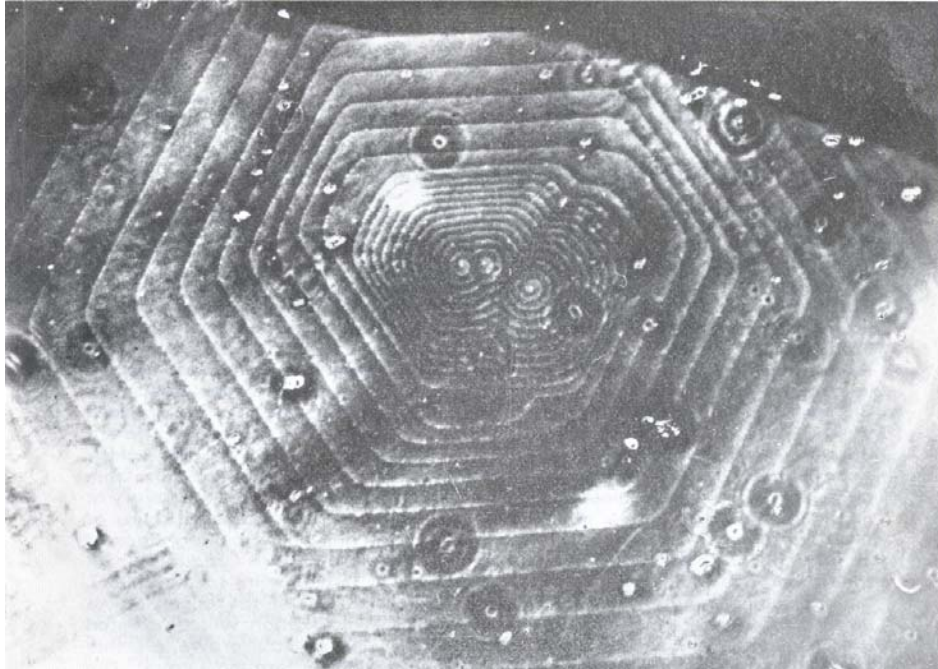


Figure 1. A phase contrast micrograph of the (0001) face on a 6H SiC crystal showing the growth pattern due to three dislocations of like sign close together and giving rise to three cooperating growth spirals. The central or the last part of the growth is circular while the rest is hexagonal. (X500). After Verma [1].

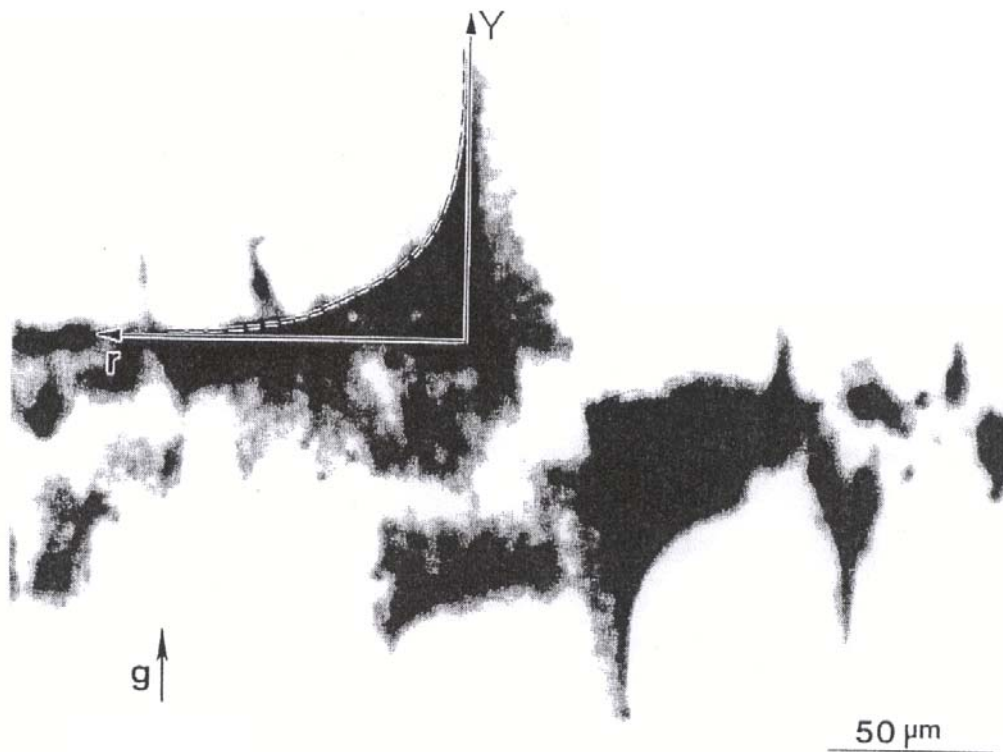


Figure 2. An (0006) section x-ray transmission topograph showing an image of a screw dislocation micropipe, M; after Dudley, Si, Wang, Carter, Glass, and Tsvetkov [20].

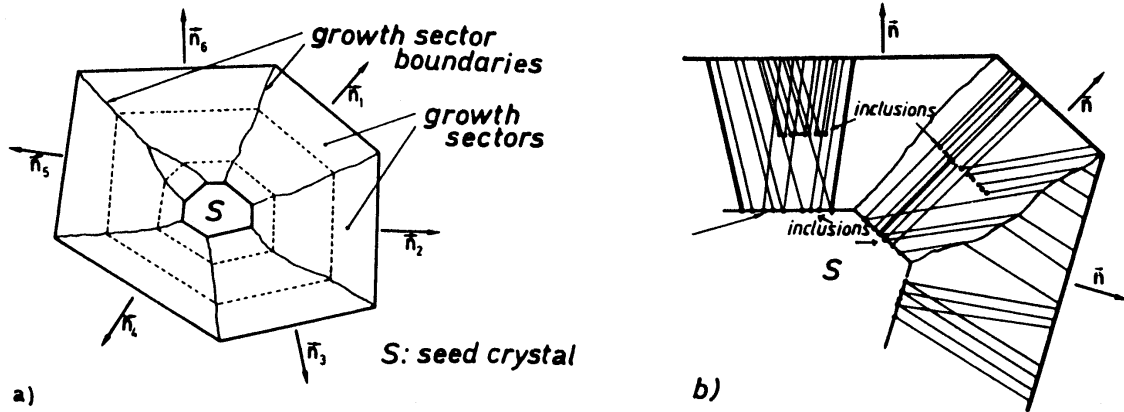


Figure 3. Schematic illustration of (a) division of a crystal into growth sectors according to different growth directions including indication of (dashed) contours at different stages of growth; and (b) typical geometry of grown-in dislocation lines initiated at inclusion particles. After Klapper [26].

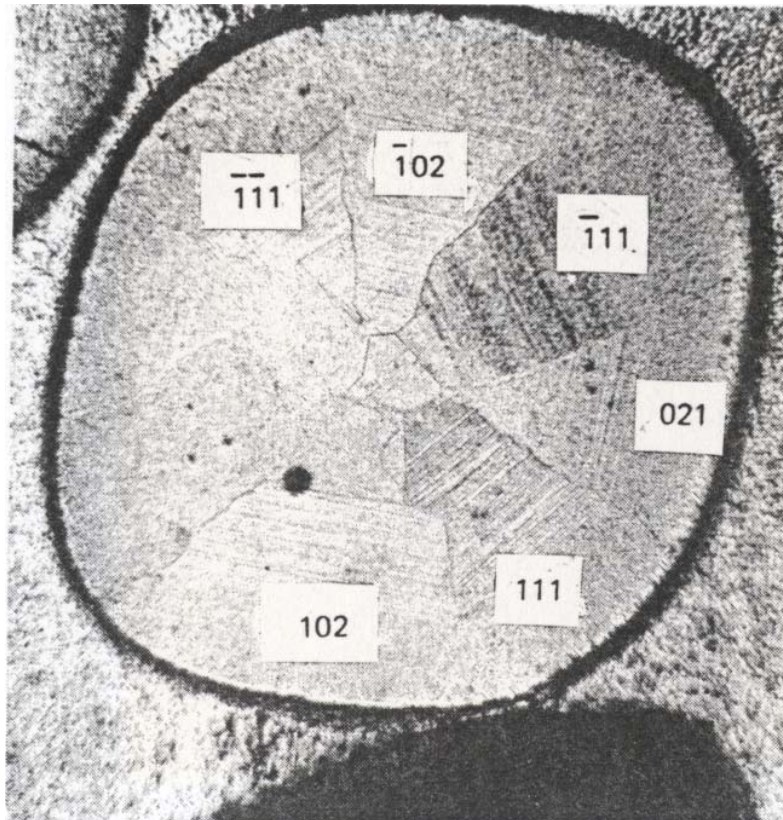


Figure 4. Growth sector structure within a sectioned RDX crystal, after van der Steen and Duvalois [27], with growth band (planar) trace identifications, after Armstrong [28].

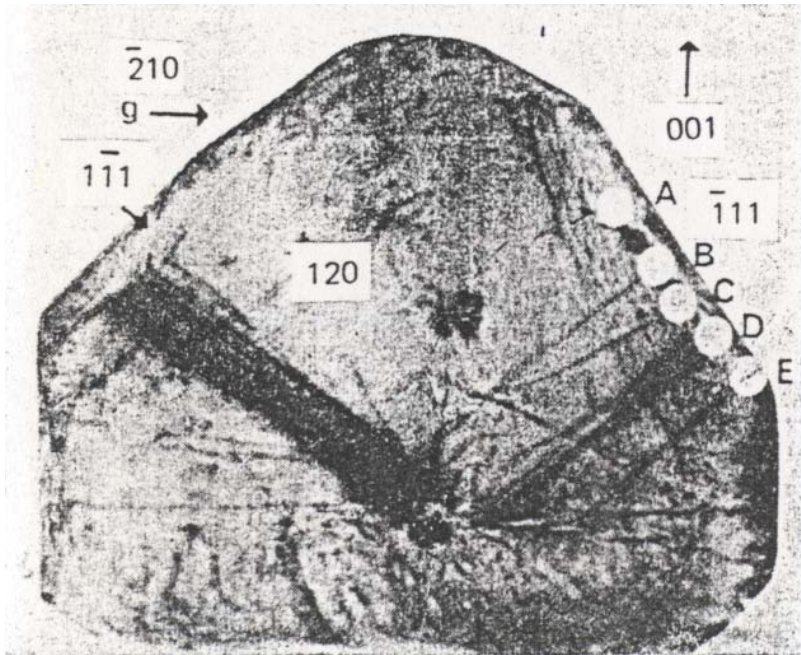


Figure 5. A $\{210\}$ x-ray transmission topograph of an RDX crystal showing dislocation bundles spreading from a central seed position to the external crystal growth surfaces; after McDermott and Phahey [33].

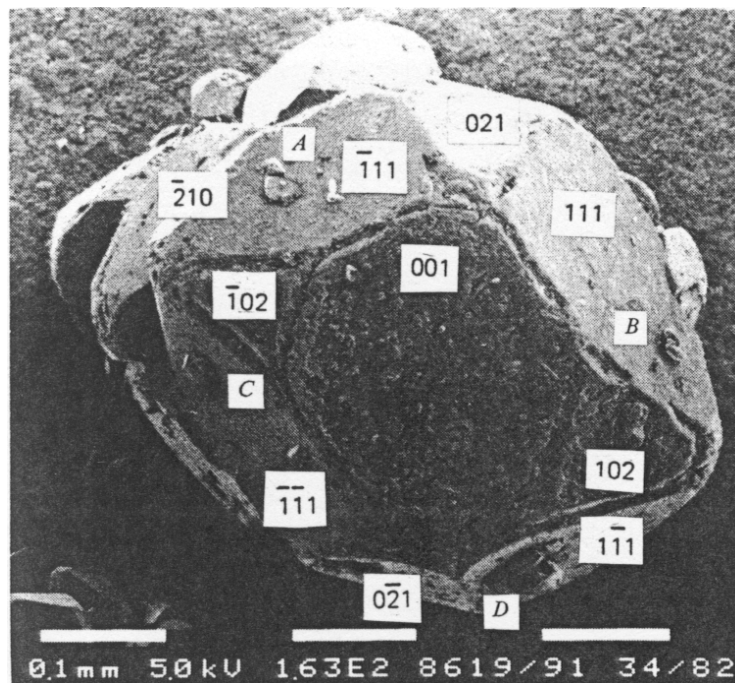


Figure 6. A scanning electron micrograph of an RDX crystal, after van der Steen and Duvalois [27], with crystallographically-identified planar growth surfaces, also with A to D locations marked for growth protuberances at positions of dislocation bundle emergence, after Armstrong [28].

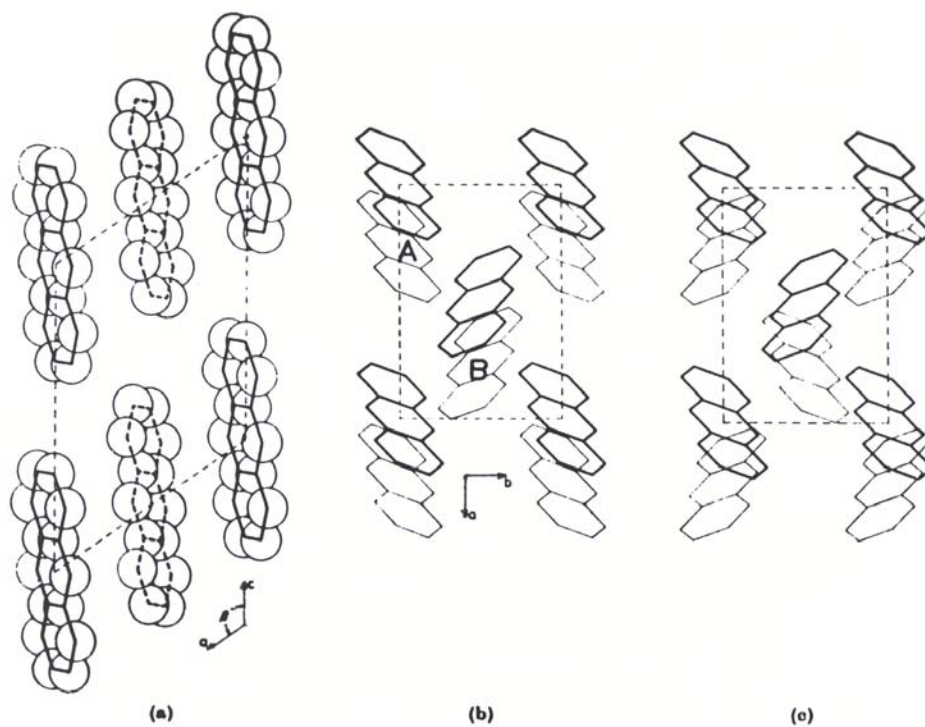


Figure 7. Schematic plane sections of the crystal structure of anthracene: (a) (010) projection of the unit cell, with a and c axes identified, and showing carbon atoms and carbon-carbon bonds; (b) (001) projection, with a and b axes marked, and showing carbon-carbon bonds, with the light lines applying for molecules at height c above the dark line molecules; (c) a faulted (001) structure relating to (b). After Robinson and Scott [37].

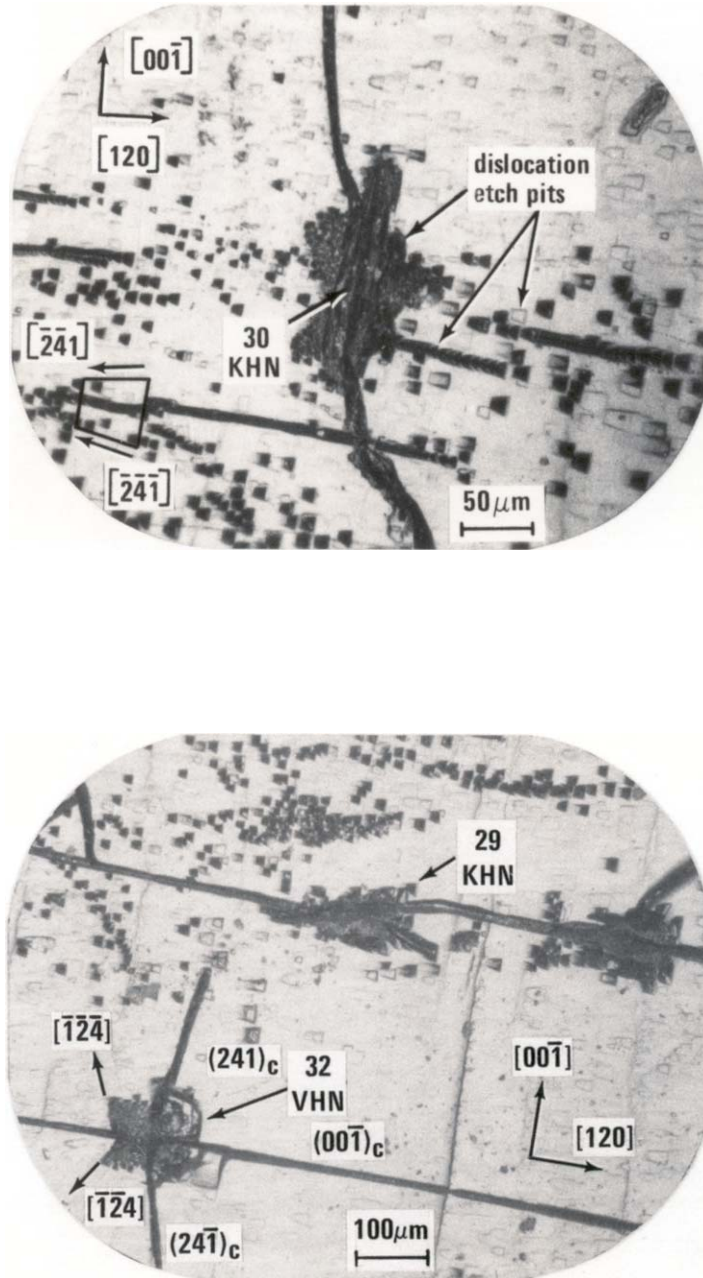


Figure 8. Dislocation etch pits centered on microindentations in the (210) plane growth surface of RDX: (top) Knoop indentation with long axis parallel to $[001]$; and (bottom) identified Vickers diamond pyramid indentation with one equiaxed diagonal length parallel to $[001]$. The long black lines in the figures are cracks. After Elban and Armstrong [24].

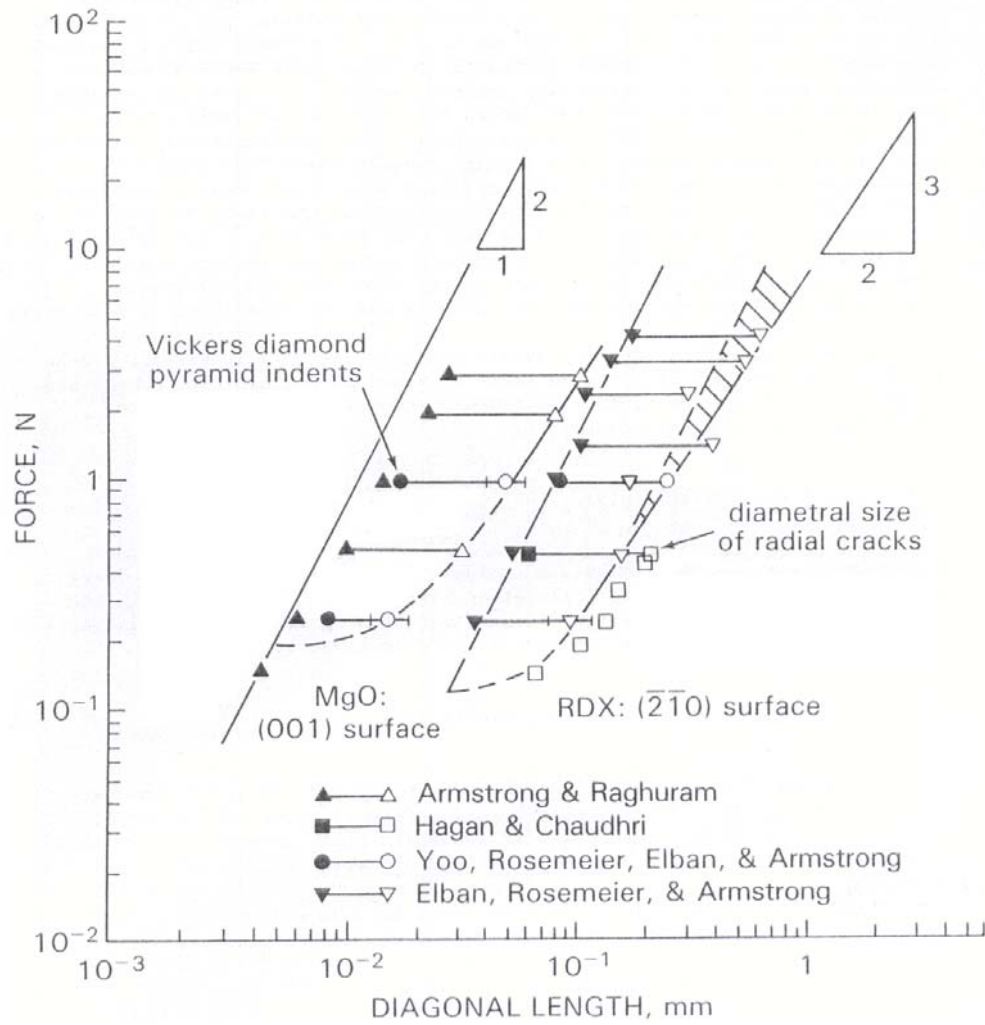


Figure 9. Logarithmic dependence, according to constant hardness or constant indentation fracture stress intensity, of applied indenter force on diagonal indentation and crack lengths for RDX and MgO crystals; after Armstrong and Elban [22].

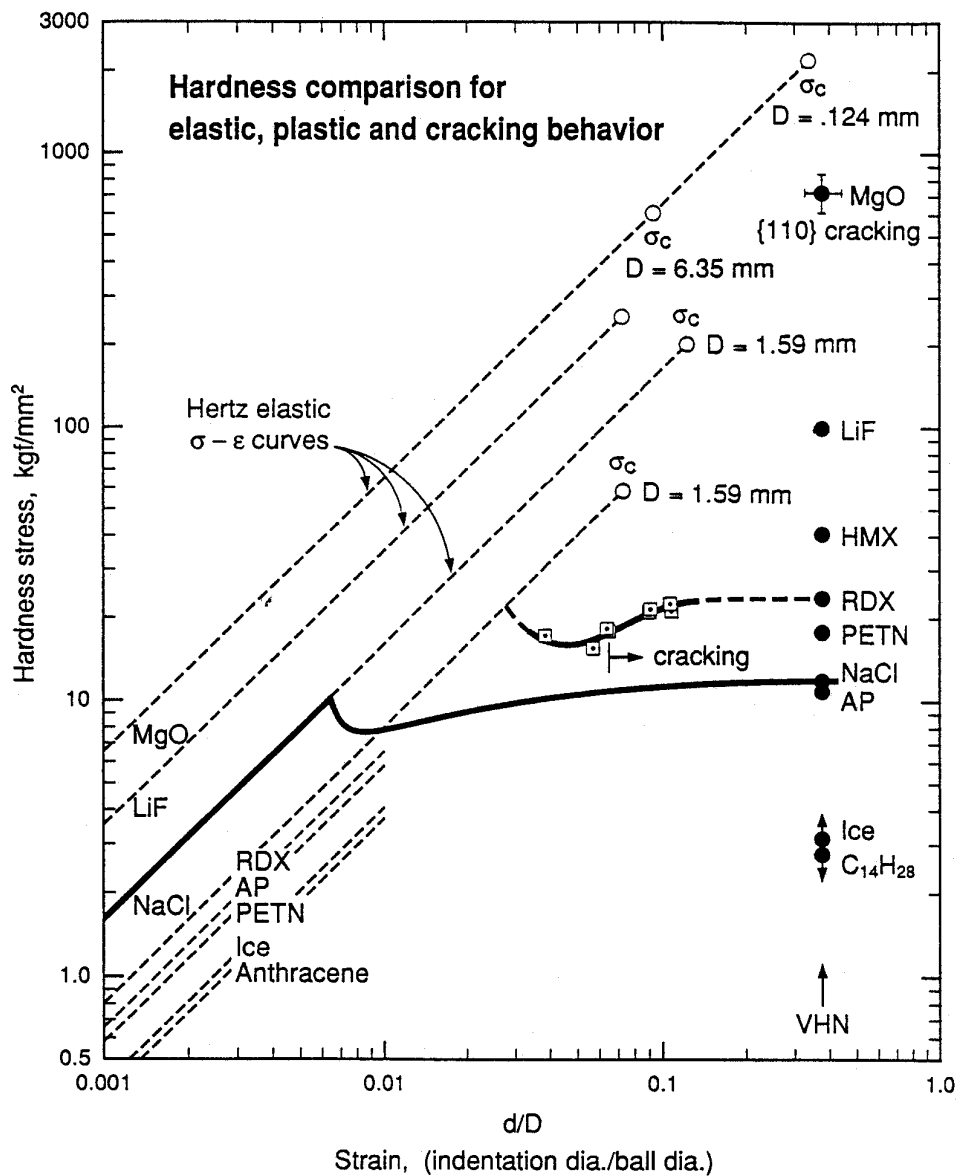


Figure 10. Hardness stress-strain basis for comparing the elastic, plastic and cracking behaviors of crystal materials, including calculation of the terminal elastic cracking stresses for different ball sizes; after Hammond and Armstrong [49].

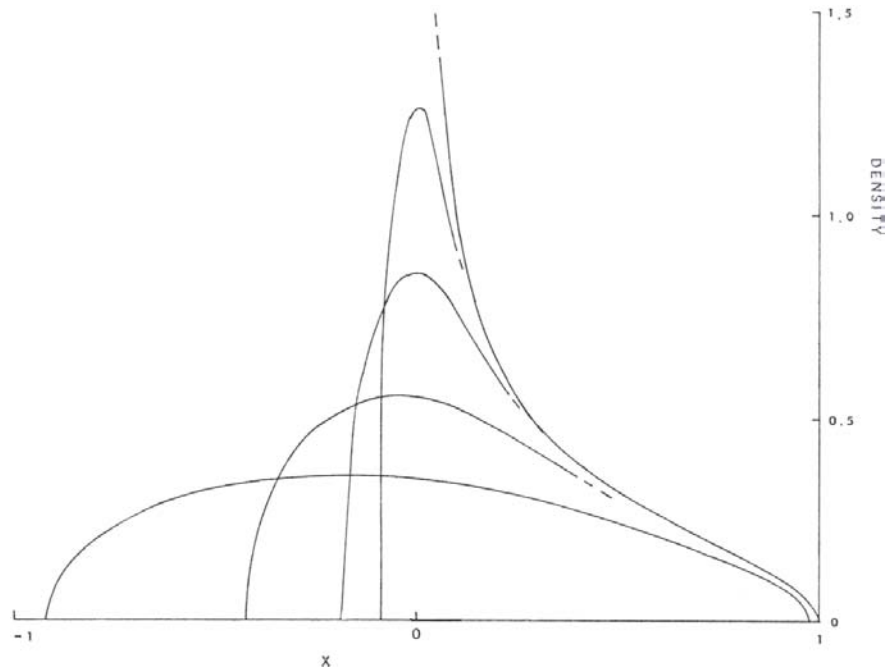


Figure 11. Release of a dislocation pile-up from its blocking obstacle, showing the shape of the dislocation distribution as it moves from right to left, at sequential (dimensionless) time steps, $t = 0, 0.01, 0.03, 0.10$ and 0.30 , after Head [61].

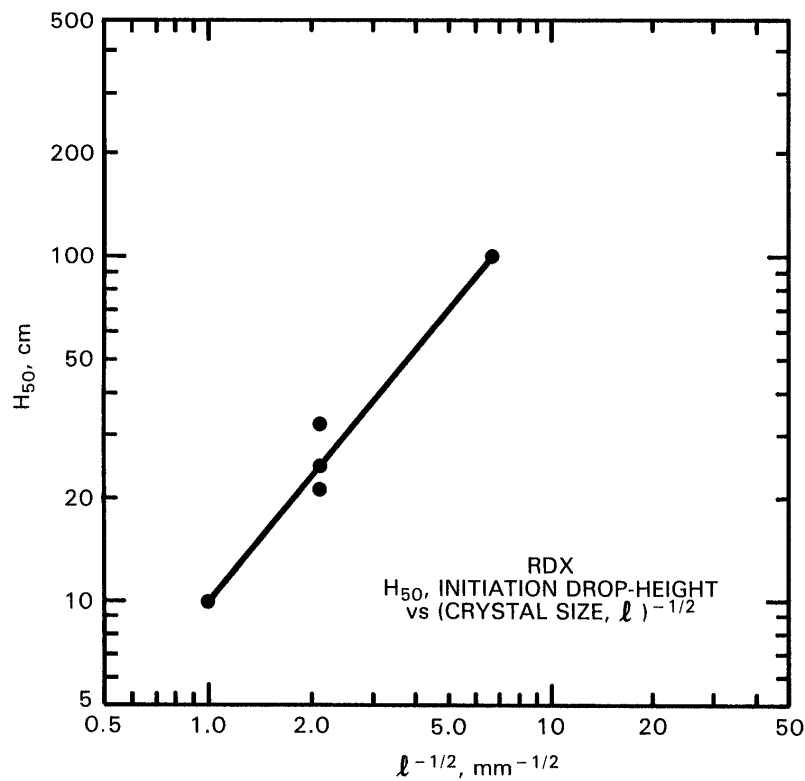


Figure 12. Drop-weight impact height for 50% probability of initiation as it depends on crystal size, including, for 0.25 mm size crystals, an indication of influence of variation of crystal quality in different batches, after Armstrong, Coffey, DeVost and Elban [70].

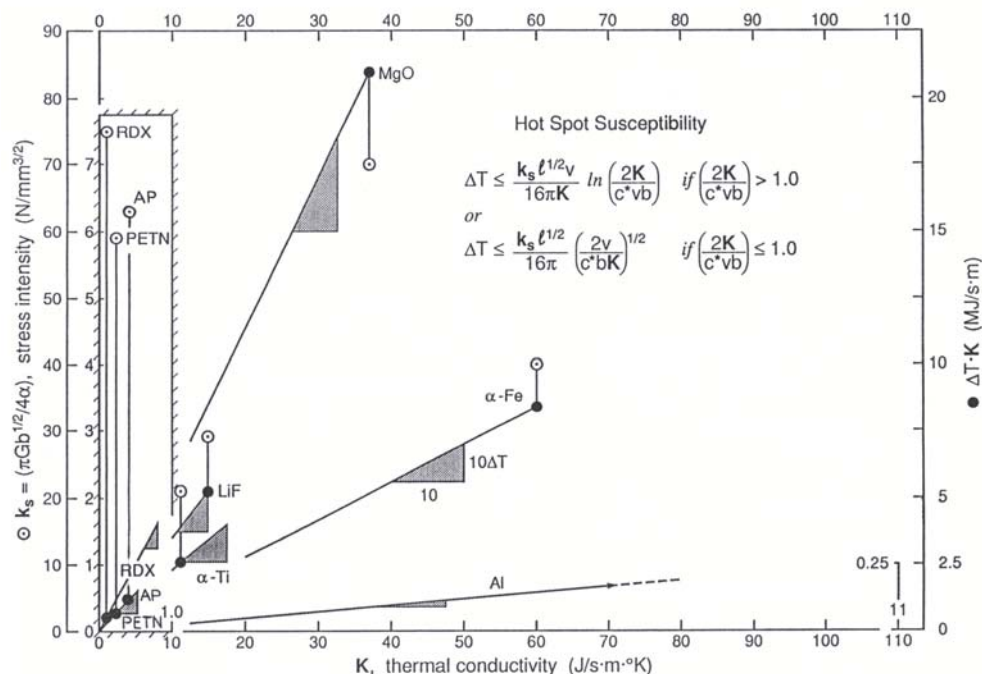


Figure 13. Graphical basis for illustrating hot spot susceptibility of materials on a dislocation pile-up avalanche model description, including different hot spot temperature expressions for metallic and ionic materials as compared with energetic RDX and PETN, after Armstrong, Coffey and Elban [60].

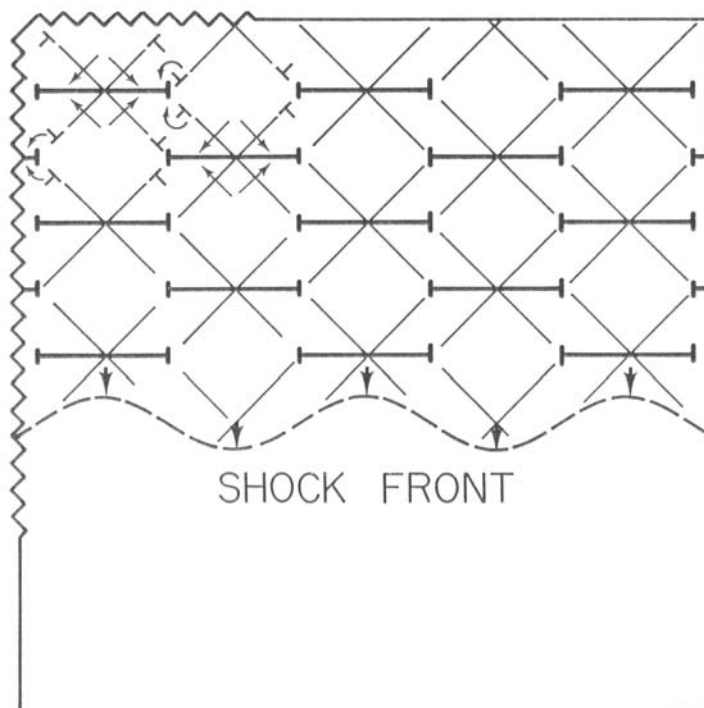


Figure 14. Shock model for nanometer-scale dislocation loops that produce a residual deformation state of one-dimensional compression, after Armstrong, Miller, and Sandusky [79], as elaborated by Bandak, Armstrong, and Douglas [80].



Figure 15. Combustion residue and microcracking at an RDX (210) crystal surface burn spot after laser irradiation; the vertical separation of parallel microcracks is ~ 5 micrometers. After Armstrong, Ramaswamy, and Field [105], as further analyzed by Elban, Armstrong, and Russell [108].

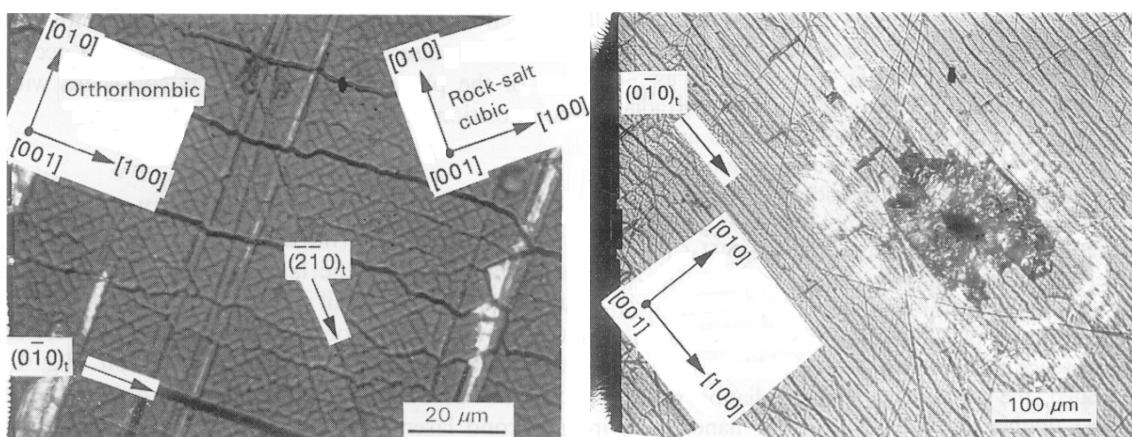


Figure 16. Laser-impacted (001)AP crystal surface (a) at high magnification to show the sequential macroscopic (210) cracking in the low temperature orthorhombic phase and higher temperature, finer scale, {010} cracking retained from the rocksalt-type cubic phase; and (b) lower magnification view of the central drilled hole exhibiting a whitish halo of sub-surface (001) cracking. After Ramaswamy, Shin, Armstrong, Lee, and Sharma [109].

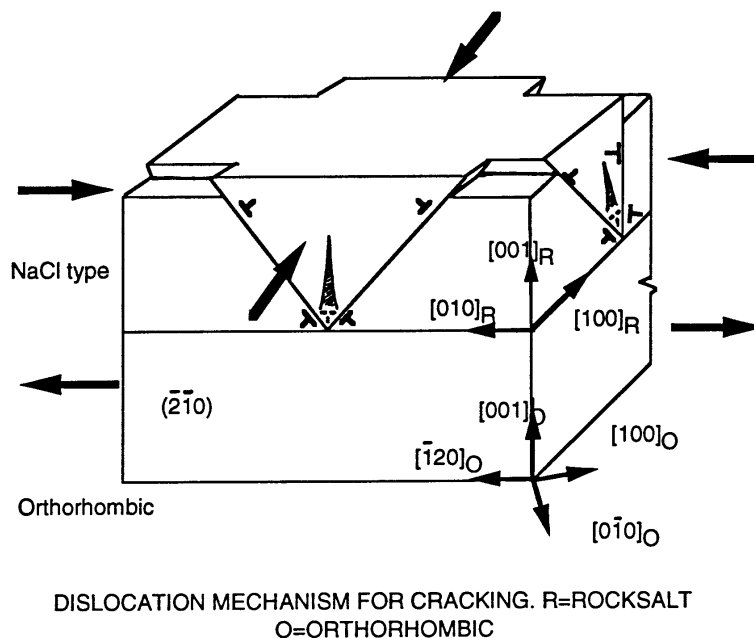


Figure 17. Schematic dislocation model for explanation of the $\{010\}$ cracking shown in Figure 16a for the higher temperature rocksalt-type cubic structure of AP; after Ramaswamy et al. [109].

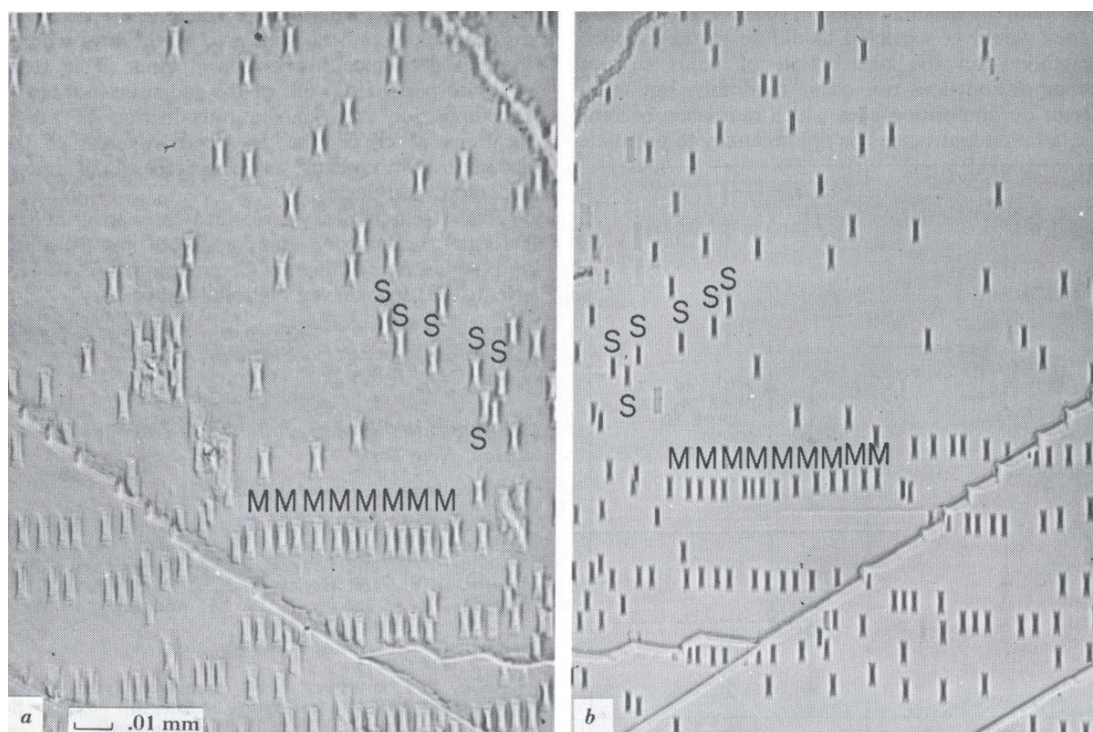
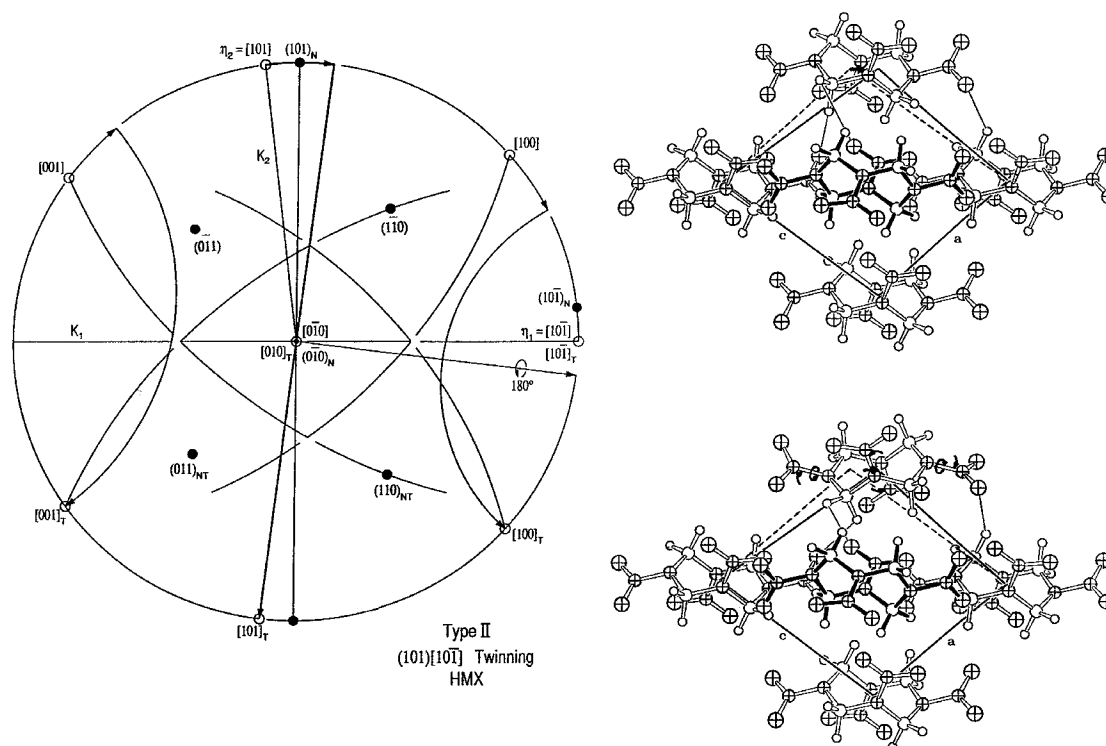


Figure 18. Photomicrographs of matching AP (210) cleavage surfaces showing radiation-induced dislocation movement. Side a was not irradiated but side b received a dose of 10^4 rad gamma-ray exposure. A set of dislocations which have moved during irradiation is labeled M while set S has remained stationary. After Herley and Levy [122,123].



* Type 1 Potential Energy

** Type 2 Potential Energy

‡ Type 2 Potential Energy + 21° rotation of N-N bond

Figure 19. Crystallography of Type II {101}<101> twinning in HMX; on a stereographic projection basis at top left, and (010) plane projection of pre-and post-twin positions at top right, with tabulated sequential potential energy evaluations for the indicated lattice point displacements, also involving required N-N bond rotation. After Armstrong, Ammon, Du, Elban and Zhang [135].

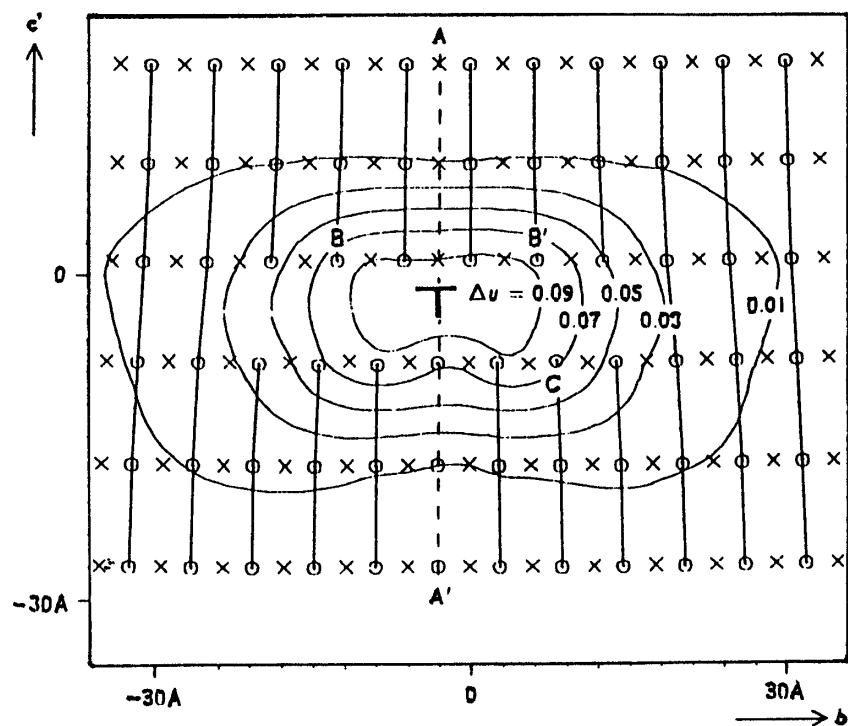


Figure 20. A projection in the (100) plane of molecular centers at an edge dislocation core in anthracene after relaxation of the lattice positions and with equipotential curves (in units of eV). The crosses denote corner molecules and circles, center molecules. After Ide, Okada, and Kojima [137].

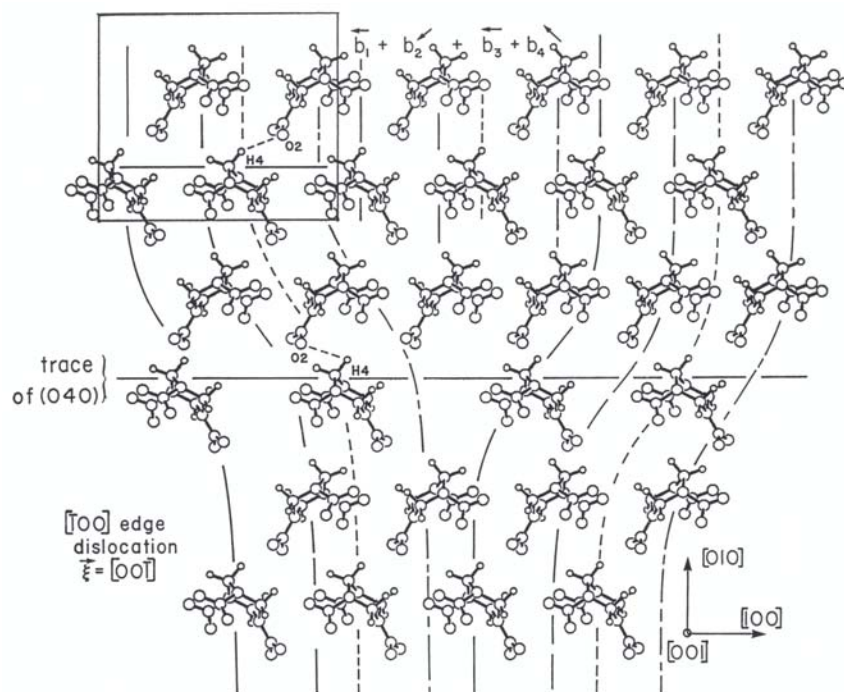


Figure 21. Schematic view of RDX molecule positions for an [001] edge dislocation on the (040) plane, after Armstrong [28].

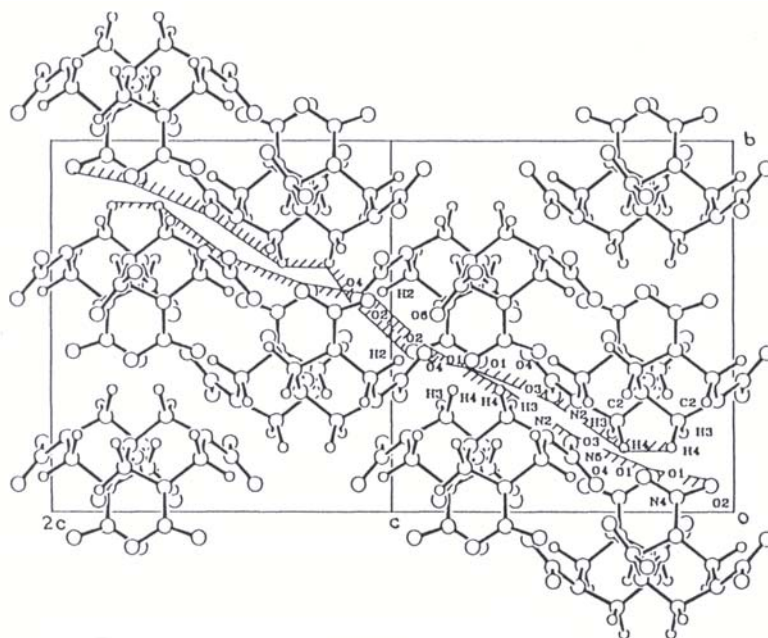


Figure 22. For RDX, dinitroso-related interactions from $[100](021)$ slip, in and out of the surface-projected (100) ; after Armstrong [28] and relating to experimental results both from Hoffsommer, Glover, and Elban [128] and Behrens and Buluso [127].

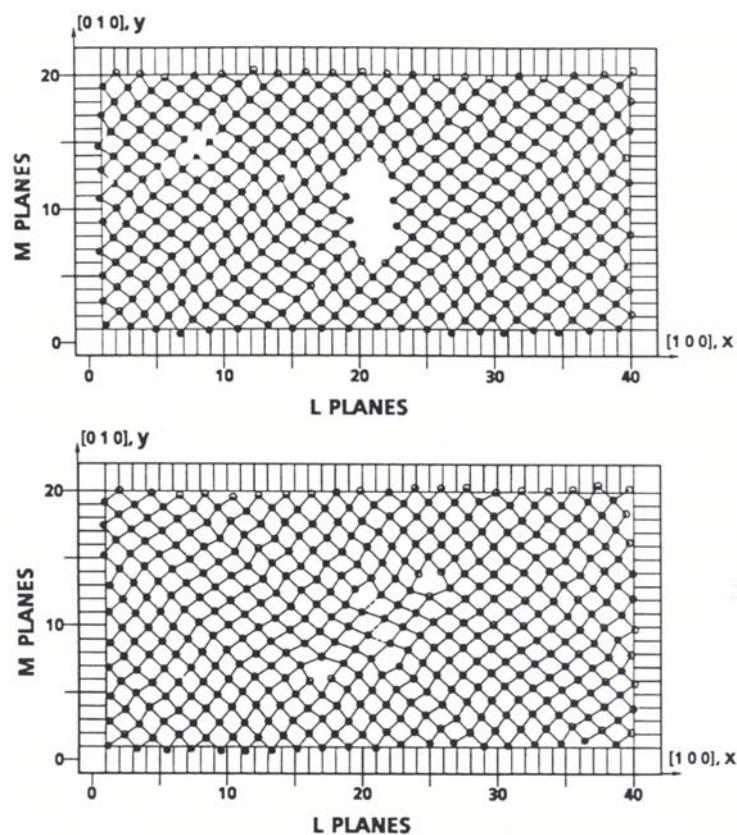


Figure 23. Molecular dynamics modeling of the collapse of a vacancy cluster into a pair of edge dislocation dipoles, after Bandak, Tsai, Armstrong, and Douglas [146].

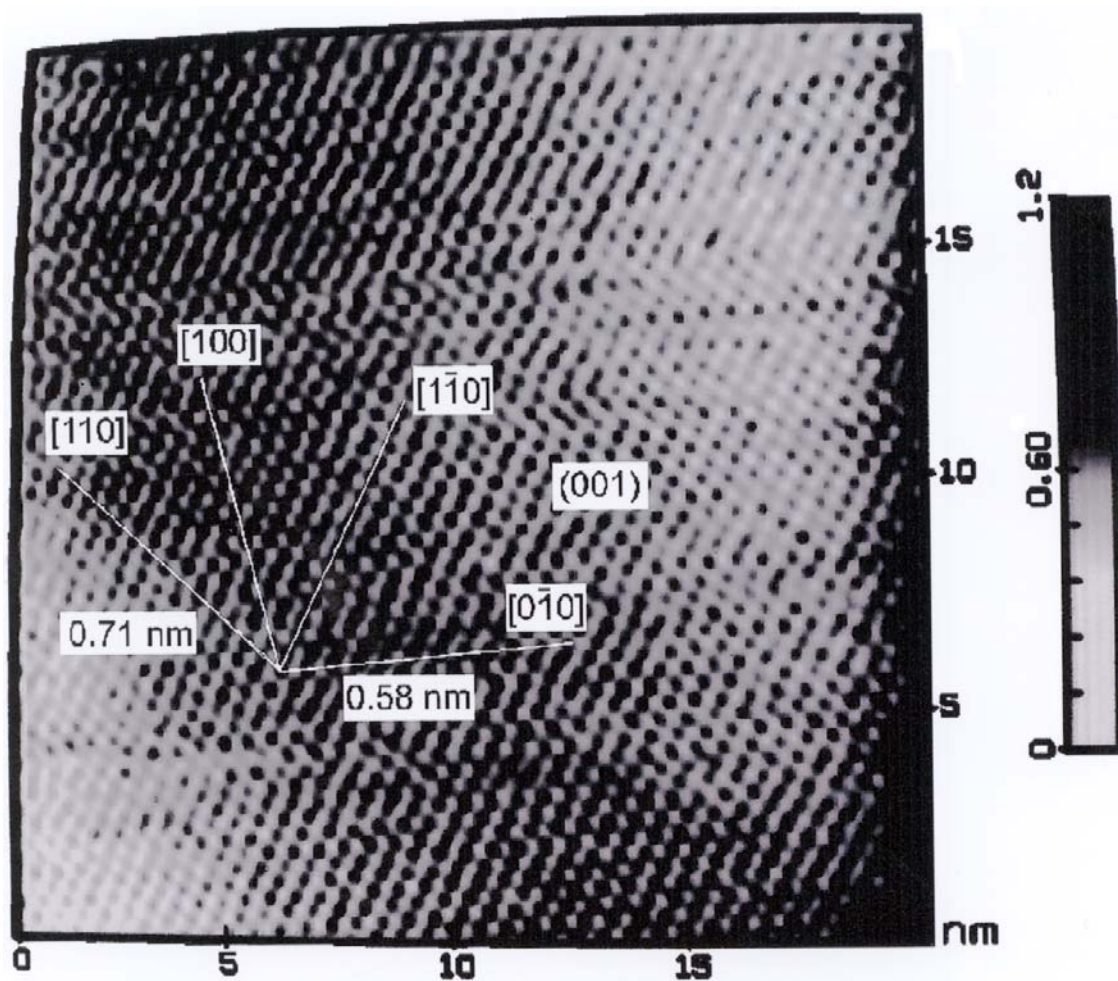


Figure 24. Atomic force microscope image of molecule positions on an identified RDX (001) cleavage surface, after Sharma, unpublished; see J. Sharma et al. [159].

CRYSTAL IMPERFECTIONS SEEN BY X-RAY DIFFRACTION TOPOGRAPHY

R.W. Armstrong

AFRL/MNME, 2306 Perimeter Road, Eglin Air Force Base, FL 32542-5910

Abstract

Internal lattice strains imaged via x-ray diffraction topography (XRDT) methods are presented for relatively low dislocation density, or dislocation-free, crystals, much as investigated for higher dislocation density materials by Professor Gareth Thomas and colleagues and students via transmission electron microscopy (TEM) methods. Relating to the broad range of materials covered today by The Minerals, Metals and Materials Society (TMS), various characterization-type results are shown to be obtainable for millimeter-to-centimeter size crystals exhibiting either metallic, ionic, covalent, or molecular (energetic) type bonding between their respective constituent atoms or molecules.

Introduction

In retrospect, an especially important technical conference was held on the topic: "Direct Observation of Imperfections in Crystals" [1], that was sponsored by the Chemistry and Physics of Metals Committee of, then, The Metallurgical Society (TMS), now, The Minerals, Metals and Materials Society, American Institute of Mining, Metallurgical and Petroleum Engineers, in St. Louis, MO, during March 1-2, 1961. At the time, rather early dislocation observations were being reported, in connection with property measurements, via the several techniques of transmission electron microscopy (TEM), field ion microscopy (FIM), and x-ray diffraction topography (XRDT), as were recently pioneered along with dislocation etch pitting investigations. Professor Gareth Thomas and colleagues reported results on dislocation structures observed in deformed and recovered molybdenum polycrystals, presaging many other observations to come on a wide variety of engineering materials involved in multiple technical uses, as evidenced by the papers delivered in the present meeting by colleagues and students. Also, Professor George Smith, Oxford University, U.K., is reporting in the present TMS symposium on advances made via FIM.

The present paper provides, on the one hand, updated information on characterization-type results obtained via several XRDT techniques, following a number of post-founding reports made in reference [1], for example, for transmission XRDT of sliced silicon wafers by A.E. Jenkinson and A.R. Lang. The technical conference proceedings was co-edited by J.H. Wernick and J.B. Newkirk, who, in the latter case, provided encouragement, because of his research effort with Berg-Barrett (B-B) reflection topography, to the present author and colleague, J.M. Schultz, for inclusion of first results reported for dislocation observations in cleaved zinc crystals. At the conference, G. Borrmann and K. Lehmann presented XRDT results obtained on a very nearly perfect germanium crystal via so-called anomalous transmission of x-rays; and, U. Bonse reported on crystal-monochromated XRDT results obtained on a similar low dislocation content silicon crystal.

NANO AND

*To be submitted for "MICROSTRUCTURAL DESIGN OF ADVANCED MATERIALS: A Commemorative Volume on Professor G. Thomas' Seventieth Birthday, Elsevier Science, 2003.

Here, reflection, transmission, and monochromatic (beam conditioned) topographic observations are presented for characterization of dislocation influences in zinc, sapphire, cyclotrimethylenetrinitramine (RDX), and ammonium perchlorate (AP) crystals, plus layer deposition and diffusion implantation generated strains in otherwise perfect silicon crystals; in the latter case, achieved via line modified asymmetric crystal topography (LM-ACT). In addition, mention is made that the very appreciable advances now achievable via XRDT and related x-ray techniques were reviewed in 1995 in a Special Issue of Physics Today [2], including reference to synchrotron radiation source capabilities such as have been available, for example: CCLRC at Daresbury, U.K.; SSRL at Stanford University; CHESS at Cornell University; NSLS at Brookhaven National Laboratory; LURE at Orsay, FR; HASYLAB at DESY, Hamburg, DE; ESRF at Grenoble, FR; and, the Photon Factory, Japan.

Results

Berg-Barrett (B-B) Observations in Zinc

A stereographic projection description of the B-B reflection XRDT technique, as applied to dislocation observations made through the (0001) cleavage surfaces of zinc crystals, is shown in Figure 1. In the Figure, the inset drawing depicts the physical set-up corresponding to the left-side, zero layer case, of cobalt K α radiation being incident to the crystal (0001) at 6.1° and reflected from the inclined ($\bar{1}013$) at a Bragg angle of 41.6° so as to give a diffracted beam at 77.1° from the (0001) specimen surface, thus traveling a distance as small as possible to the recording nuclear emulsion film. Point-by-point connection between the local diffracted intensity and the real crystal surface region is achieved by enlargement of the developed image in an optical transmission microscope [3].

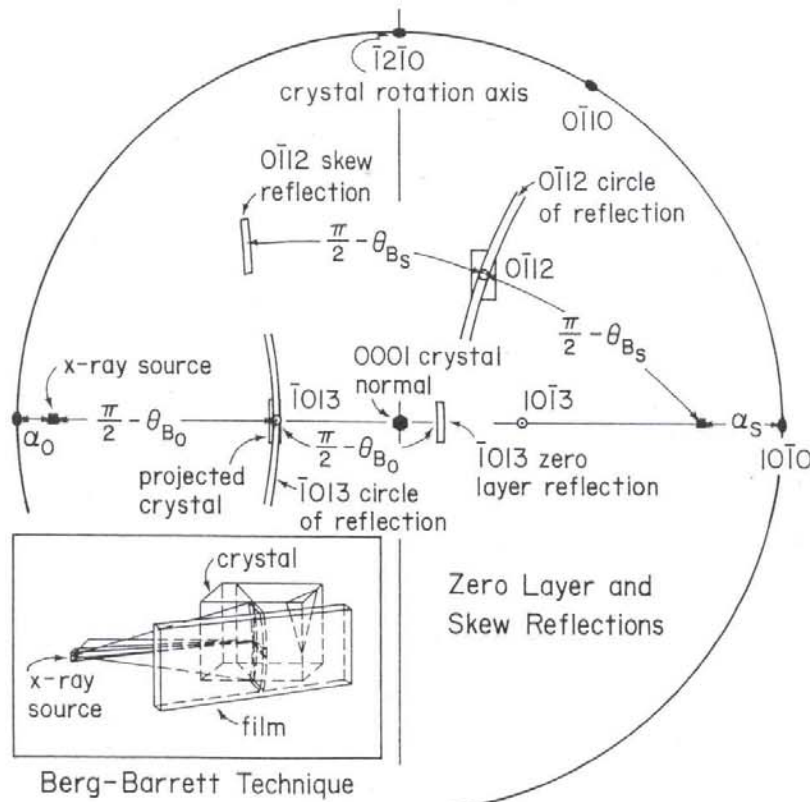


Figure 1: Stereographic standard (0001) projection, with inset physical set-up, for Berg-Barrett reflection x-ray topography of zinc employing characteristic cobalt K α radiation.

Individual dislocations and small angle dislocation subgrain boundaries formed during solidification along the difficult $[0001]$ crystal growth direction for an eight millimeter diameter zinc crystal are shown in Figure 2a, to be compared with the characterized dislocation boundary structure in Figure 2b. The individual dislocation lines within the subgrain volumes are revealed by the (blackened) localized enhancement of the reflected intensity caused by reduction in (the perfect crystal) primary extinction. The occurrence of dislocation loops [4] in such crystals when chemically polished, and occurring also in separate (0001) surface oxidation experiments [5], are observed at, say, smallest ten micrometer diameters, to be comparable to dislocation loop observations made via TEM. The dislocation subgrain boundaries are generally observed to have reduced zones of extinction contrast but are either white (via reduced intensity) or black according to whether the adjacent subgrain reflections are separated or overlapped in the film record. Stereographic [6] and diffracted vector [7] analyses have been given for specification of subgrain misorientations in zinc and nickel crystals, respectively. Different levels of subgrain structures were observed in the nickel crystals, as first reported via Debye-Scherrer x-ray results for nickel polycrystals by Weissmann [8].

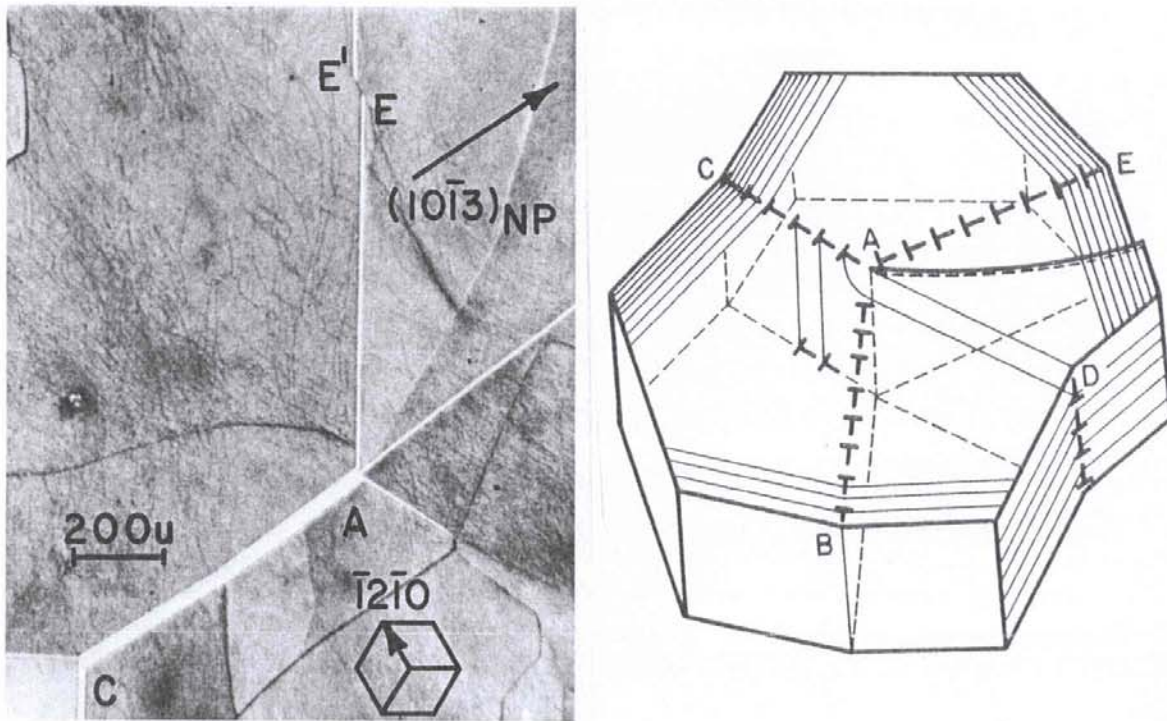


Figure 2: Individual dislocation and subgrain boundary structure within a $(10\bar{1}3)$ B-B image through the (0001) cleavage surface of a zinc crystal solidified along the $[0001]$ crystal growth direction.

Lang Transmission XRDT of (Magnesia and) Sapphire

Employment of the Lang transmission XRDT method [9], as utilized with a micro-focus x-ray generator, is shown via the stereographic projection method for $\{200\}$ diffraction of molybdenum $K\alpha$ radiation directly incident at a small angle to the (001) crystal surface normal in Figure 3, also whereby synchronized traversing of the crystal specimen and recording film occurs on either side of collimating lead screen slits. With this technique, depth perception of the dislocation line structures is achieved via

stereo-pair topographic images indicated to be obtainable in Figure 3 by the inset physical set-up actually applying, relative to the identified diffracting plane normal in the projection, for an opposite (negative) x-ray source direction being positioned on the right equatorial side of the [001] center of the standard projection.

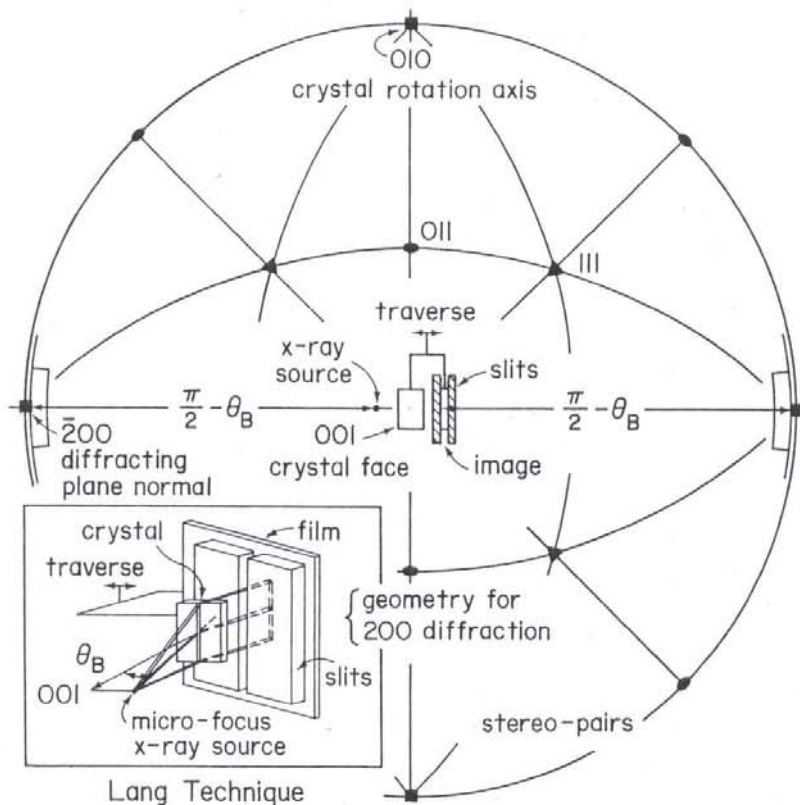


Figure 3: Stereographic standard (001) projection, with conjugate inset physical set-up for Lang transmission x-ray topography of magnesia employing characteristic molybdenum $K\alpha$ radiation.

Figure 4 shows individual dislocation bundles spreading outward from a central seed as accomplished for a sapphire crystal grown by a chemical vapor deposition technique [10]. The crystal growth process was interrupted at certain stages to show the nucleation of additional dislocation bundles then spreading outward also from new points established during the stopped operation, as modeled by Klapper [11], mainly, for organic crystal growth. Comparative B-B and Lang topographs were obtained also on the same crystal slice [12]. By reduction of the Lang-type lead exit slits to smaller width than a reasonably thick sapphire crystal slice, anomalous transmission imaging of a lesser dislocation-induced diffracted intensity was demonstrated in the same image for dislocation lines close to the beam entrance side of the crystal superposed on the enhanced intensity of dislocation lines close to the crystal exit side [13].

Hardness Strains in RDX and AP Crystals

A stereographic projection for $(\bar{1}0\ 00)$ B-B reflection with copper $K\alpha$ radiation of crystal regions surrounding diamond pyramid hardness indentations put at various applied load values into an RDX $(\bar{2}\bar{1}0)$ crystal solution-growth surface is shown in Figure 5a, along with the recorded B-B image in Figure 5b showing very limited spatial extent of the cumulative dislocation strain fields at the indentation sites. Such indentations produced cracking on $\{001\}_c$ and $\{241\}$ cleavage surfaces, as indicated by the filled points, for plane normals, and particular subscripted identifications in Figure 5a.

Assessment of the white-to-black-to-background-gray local diffracted intensities at the indentation sites, along with complementary etch pitting results [14], provided first experimental evidence of very restricted dislocation slip occurring in RDX and related energetic crystals.

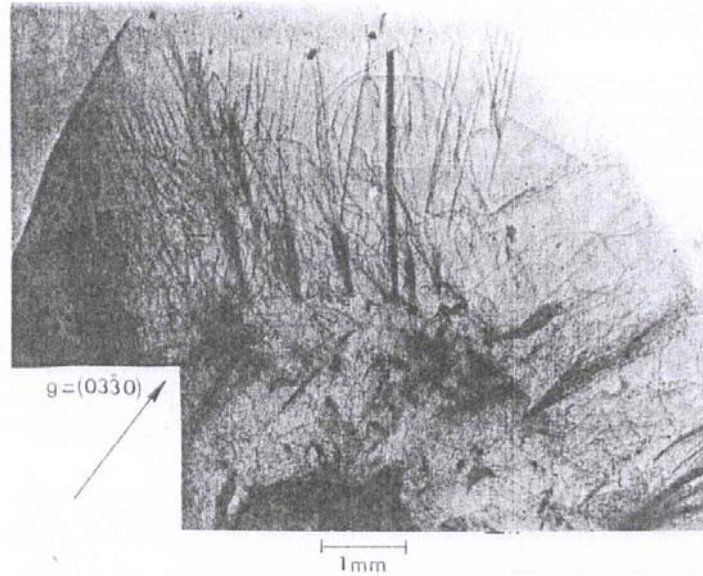


Figure 4: An $(03\bar{3}0)$ Lang transmission topograph of dislocation bundles spreading from nucleation sites induced by growth interruptions for a sapphire crystal produced by chemical vapor decomposition.

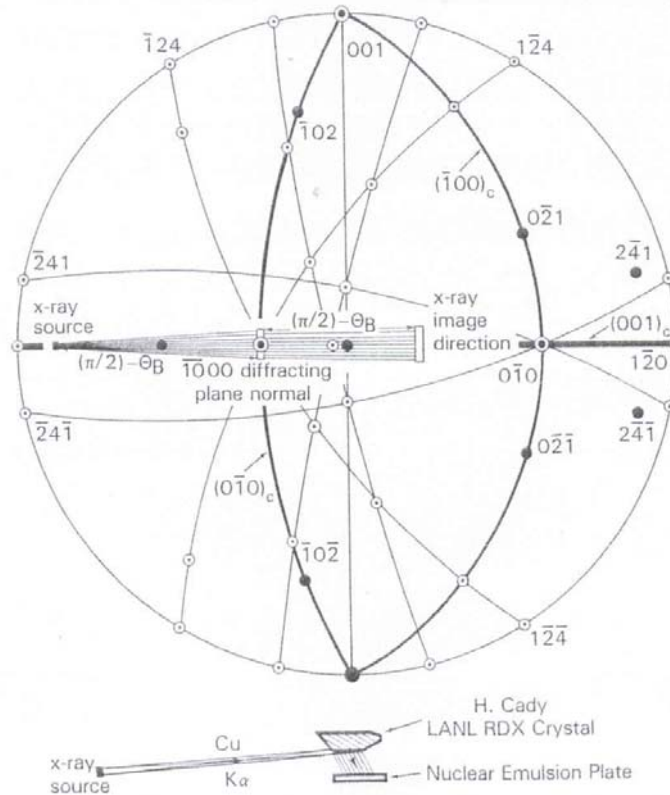


Figure 5a: Stereographic projection for $(\bar{1}0\ 00)$ B-B image of hardness indentations in an RDX crystal.

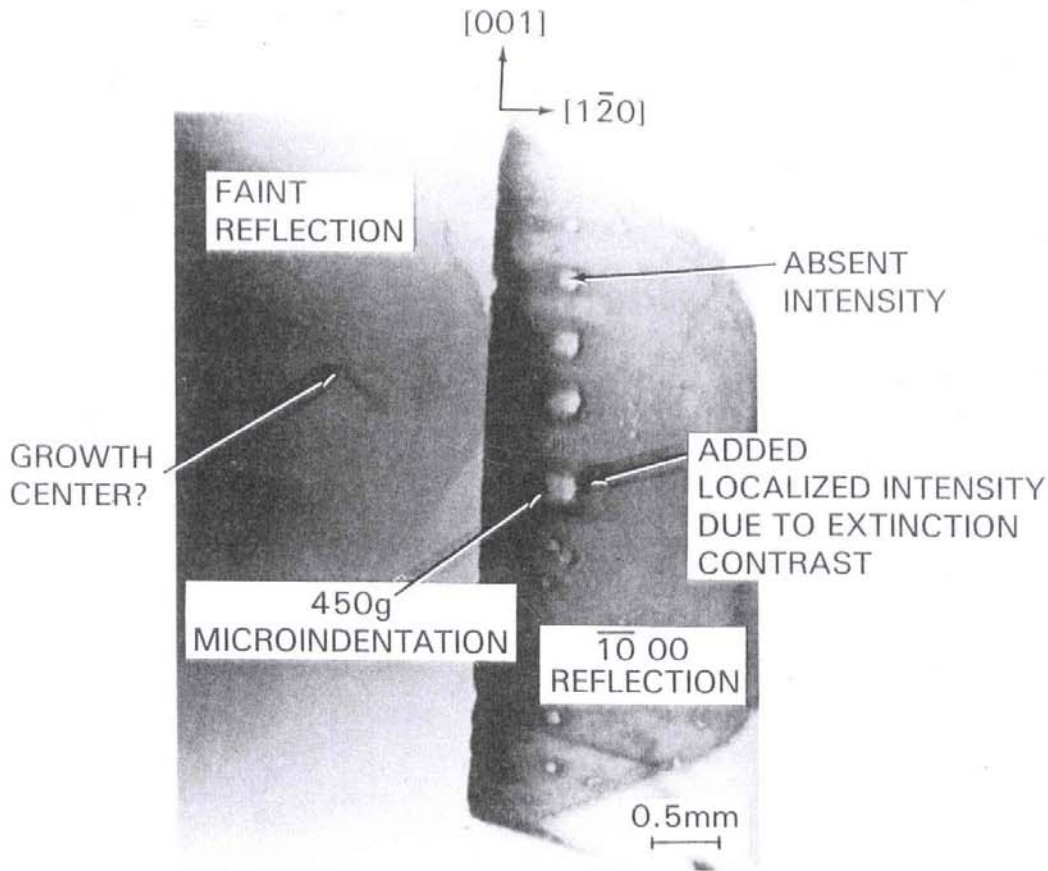


Figure 5b: White-to-black-to-gray diffraction contrast for plasticity/cracking at hardness indentations.

A significantly greater extent of, albeit anisotropic, dislocation slip and cracking behavior is observed for two similar type diamond pyramid indentations put into a clean cleavage facet of an (ionic) AP oxidizer crystal, as shown in the matched optical and $(\bar{5}23)$ B-B images of Figures 6a,b --- with interesting interpreted consequence for the role of dislocation slip being responsible for the observed cleavage cracking [15]! The chosen orientation of the indenter diagonals for the pair of indentations put into the $(\bar{2}10)$ surface has produced (001) cleavage cracks emanating only from one side of the diagonal edges because of favorable dislocation slip on inclined intersecting systems occurring only on that one side, as clearly evidenced also by the larger size of the same half of the residual indentations. Thus, otherwise brittle-type cleavage cracking has occurred in the indentation strain field where greater dislocation strain is evidenced in the x-ray topograph and is associated with the stress concentration of dislocation pile-ups against reacted dislocation obstacles at the slip system intersections.

LM-ACT for perfect silicon crystal devices

A different research effort from that of employing reflection XRDT for monitoring dislocation structures came from the consideration that such topographic imaging could be applied, if the resolution were improved, to monitoring elastic strains accompanying layer depositions and/or implantation strains in electronic devices fabricated on essentially perfect silicon crystal surfaces [16]. For the purpose, advantageous use was made both of: (1) the dynamical theory prediction for reducing the angular spread for the total reflection of x-rays, as originally proposed to play an important role in observing dislocation strain fields [17]; and, (2) further reduction of adverse geometrical vertical divergence determined at the x-ray source by employing a horizontal line geometry in a so-called line modified - asymmetric crystal

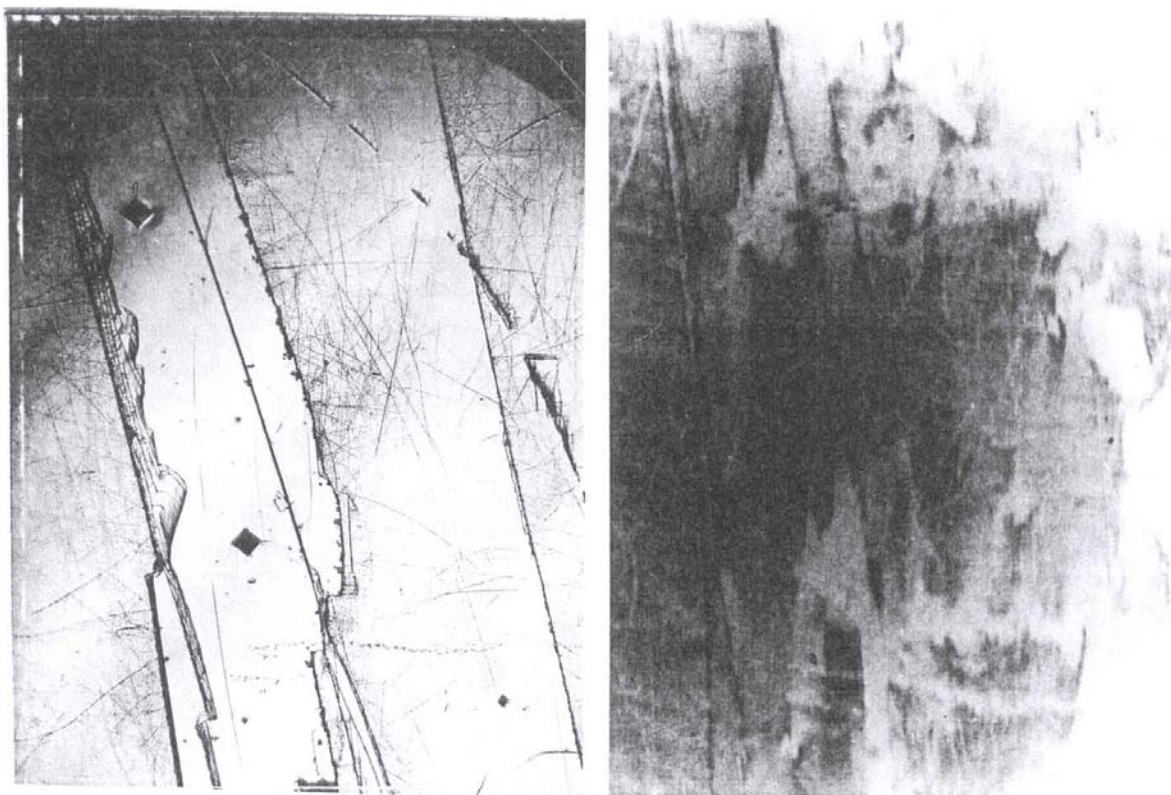


Figure 6a: Optical micrograph of two microindentations on a clean $(\bar{2}10)$ AP crystal surface; and, **6b:** $(\bar{5}23)$ B-B topograph of dislocation strains producing cleavage cracking at slip system intersections.

topography (LM-ACT) design [18]. Predictions from such dynamical theory parameters account for reduction of oblique “rocking curve widths” in synchrotron radiation applications [19] and are being carried forward currently for evaluation of energetic crystal powder diffraction experiments [20].

Figure 7 shows, on top and bottom, the physical experiment and combined dispersion surface construction, respectively, employed for application to investigating diffraction contrast within, and above, the substrate of an otherwise perfect silicon crystal parametric test chip [18]. The asymmetrically-cut silicon crystal beam conditioner, in reconstruction of the beam probe, serves the purpose of reducing the spatial width of the incident horizontal beam while maintaining a small vertical divergence sighted at the x-ray source. The theoretical angular reflecting width exiting the beam conditioner is just greater than the angular range of acceptance for total reflection from the perfect silicon crystal substrate device, now with a further dynamical theory based reduction of the perfect crystal reflected beam width directed onto the emulsion film record.

The described LM-ACT set-up has produced an image resolution at ~ 1 -2 micrometers involving $\sim 500\times$ magnification of exposed emulsion images in an optical transmission microscope [21]. An example is shown in Figure 8a,b of a fine line structure resolved near to the edge of a deposited silica graticule marking enlarged in part in 8b with two 10 micrometer scale marker separations. The graticule markers are revealed because of elastic strains produced within the silicon crystal substrate. The incident x-ray

beam direction in the Figure is from left-to-right along the horizontal lengths of the fine line structure. The imaged line structure extends past the true vertical edge of the line pattern because of the beam probe having traveled at a small angle through a depth of ~ 2 micrometers in the silicon crystal substrate. The graininess in the Figure corresponds to the developed grain size of the nuclear emulsion. Other demonstrated application of the high resolution LM-ACT method has been to monitor sequential implantation deposition steps for fabrication of such parametric [22] and related devices [23].

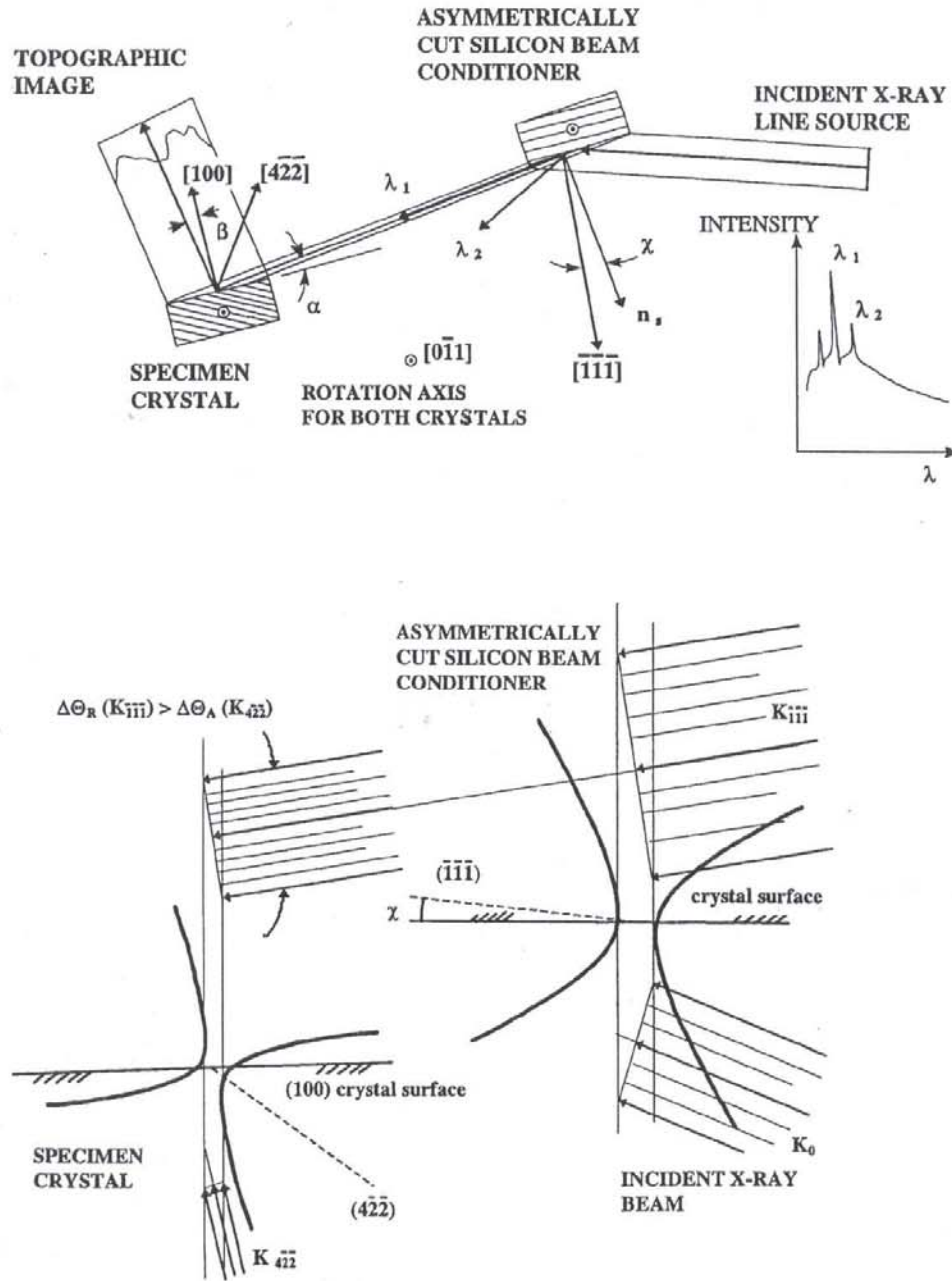


Figure 7: The LM-ACT system applied, via favorable dispersion surface geometries, to reducing the angular width for total reflection of x-rays so as to obtain improved imaging of a parametric test chip.

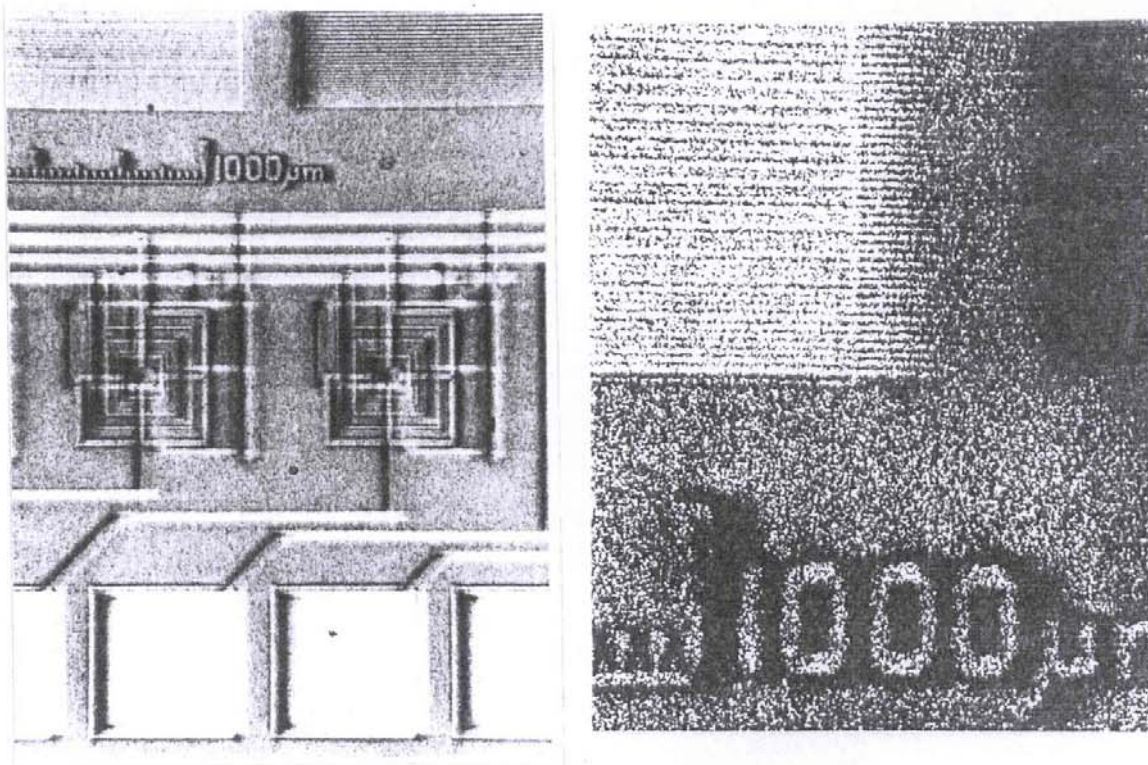


Figure 8a,b: High resolution LM-ACT images obtained of detailed structure in a parametric test chip.

Summary

With relation to pioneering XRDT, FIM, and, especially, TEM defect observations, such as reported in the latter case by Professor Gareth Thomas and colleagues and students, a number of experimental/model XRDT results are reported here for a variety of relatively perfect crystals of quite different materials. The presented results cover observations made on: (1) individual dislocation strain fields; (2) dislocation subgrain boundary geometries/misorientations; (3) cumulative dislocation interactions/cracking at residual hardness indentations; and, (4) elastic strains in an electronic device fabricated on an essentially dislocation-free silicon crystal.

Acknowledgements

Appreciation for helpful discussion is expressed to Ms. Kinnan L. Kline during her M.Sc. thesis research at the University of Florida, Graduate Engineering and Research Center (UFGERC), and to Mr. D. Wayne Richards, among other colleagues, at the High Explosives Research and Development (HERD) Facility, Eglin Air Force Base, FL.

References

1. Newkirk, J.B. and Wernick, J.H. (Eds.) (1961). *Direct Observation of Imperfections in Crystals*. Interscience Publishers, N.Y.
2. Benka, S.G. and Lubkin, G.B. (1995) *Physics Today* **48**, 23.

3. Armstrong, R.W. (1980). In: *The Characterization of Crystal Growth Defects by X-ray Methods*, p. 535. Plenum Press, N.Y.; (1984). In: *Applications of X-ray Topographic Methods to Materials Science*, p. 33. Plenum Press, N.Y.
4. Armstrong, R.W. and Schultz, J.M. (1968) *Surface Science* **12**, 19.
5. Roessler, B. and Burns, S.J. (1974) *Physica Status Solidi (a)* **24**, 285.
6. Wu, C.Cm. and Armstrong, R.W. (1975) *Physica Status Solidi (a)* **29**, 259.
7. Armstrong, R.W., Boettinger, W.J. and Kuriyama, M. (1980) *J. Applied Cryst.* **13**, 417.
8. Weissmann, S. (1956) *J. Applied Phys.* **27**, 389; *Ibid.*, 1335.
9. Lang, A.R. (1978). In: *Diffraction and Imaging Techniques in Materials Science*, **II**, p. 678. North-Holland Publishers, Amsterdam.
10. Farabaugh, E.N. and Wu, C.Cm. (1975). In: *Proc. Third Intern. Conf. Crystal Growth*, ACCG III, p. 116. Stanford, CA.
11. Klapper, H. (1980). In: *The Characterization of Crystal Growth Defects by X-ray Methods*, p. 133. Plenum Press, N.Y.
12. Farabaugh, E.N., Wu, C.Cm. and Armstrong, R.W. (1977). In: *Advances in X-ray Analysis*, **20**, p. 201, Plenum Publishing Corp., N.Y.
13. Armstrong, R.W. (1988). In: *Advanced Techniques for Microstructural Characterization*, p. 1. Trans Tech Publications, Switzerland.
14. Armstrong, R.W. and Elban, W.L. (1989) *Mater. Science Eng.* **A111**, 35.
15. Elban, W.L. and Armstrong, R.W. (1998) *Acta Mater.* **46**, 6041.
16. Beard, W.T. and Armstrong, R.W. (1989). In: *Advances in X-ray Analysis*, **32**, p. 659, Plenum Publishing Corp., N.Y.
17. Roessler, B. and Armstrong, R.W. (1969). In: *Advances in X-ray Analysis*, **12**, p. 139, Denver, CO.
18. Beard, W.T., Lipetzky, K.G. and Armstrong, R.W. (1999). In: *Advances in X-ray Analysis*, **41**, p. 203, JCPDS, CD-ROM.
19. Hart, M., Koga, T. and Takano, Y. (1995) *J. Applied Cryst.* **28**, 568.
20. Kline, K.L. (2002). MSc Thesis, University of Florida, Graduate Engineering and Research Center.
21. Beard, W.T., Lipetzky, K.G., Zhang, X.J. and Armstrong, R.W. (1996) *Applied Phys. Lett.* **69**, 488.
22. Lipetzky, K.G., Beard, W.T., Zhang, X.J., and Armstrong, R.W. (1995). In: *Advances in X-ray Analysis*, **38**, 227.
23. Beard, W.T., Hutchison, W.G., Armstrong, R.W., Zhang, X.J., Fitz, J.L. and Whisnant, J.K. (1993). In: *Physics of Semiconductor Devices*, p. 246, Lal, K. (Ed.). Narosa Publishing House, New Delhi, India.

The seeds of tornado prevention

J. Gregory Glenn and Ronald W. Armstrong

AFRL/MNME, Eglin Air Force Base FL USA

Abstract: The role of electrification in producing tornadoes is assessed in order to present a new inventive "bottom-up" method of fly-ash-like lighter-than-air particle cloud seeding for tornado prevention.

Keywords: Cloud electrification, lightning, ionization, condensation, updraft, vortex development, fly-ash-like nano-particles.

1. Introduction

Tornadoes generally appear after severe frontal thunderstorms involving copious amounts of lightning. Vonnegut (1960) points out the insightful association made in a referenced 1840 comment by Peltier that "Everything proves that the tornado is nothing else than a conductor formed of the clouds, which serves as a passage for a continual discharge of electricity ...". Figure 1 shows the designated oldest known photograph of a tornado (NOAA, 2003) obtained near to one-half century after Peltier's concluding comment. As will be seen in subsequent description given here, Peltier's quoted one sentence elucidation is not quite correct but modern observations do show that tornado development does trail the peak of lightning activity (Goodman 1999; Buechler et al., 2000). And, despite the association of thunderstorm-generated-lightning and tornado occurrences, the fundamental origins/forming conditions of tornadoes are not yet fully deciphered. For example, recent description of electrical features associated with tornadoes (Winn et al., 2000) presumably once developed, allows for conflicting reports of "remarkably intense lightning ..." and the "absence of lightning in the storm".

Recent lightning-tornado association (Goodman 1999, Buechler et al., 2000) is to be compared with previous description (Davies-Jones and Golden, 1975) of rare electrical activity near or within tornadoes. Current emphasis is on the fundamental role of all possible parameters on determining a critical updraft feature even of the thunderstorm origin while leading possibly to any tornadic activity (Dye et al., 1986). Such basic differences in attribution of "on or off" electrification in tornadogenesis accrues, undoubtedly, in part, to the need for coming together in not quite chaotic circumstance of a combination of tornado determining parameters/conditions. The situation bears similarity with the anecdote of defining an elephant from different touches on disparate external parts --- despite one association (Brooks 1951) of the tornado funnel with an elephant's trunk.

Here we first synthesize a series of events, based on previously reported tornadic studies, by which a tornado might be envisioned to originate --- no small feat because of the complexity of involved parameters--- and, then, propose a novel method of defeating such tornadic development at embryonic operation.



Figure 1. Oldest known photograph of a tornado, 28 August 1884, at location 22 miles southwest of Howard SD, as obtained from the NOAA Photo Library: wea00206, Historic NWS Collection.

2. Thunderstorm/tornado elements

Figure 2 illustrates the normal thunderstorm situation of a build-up of positive upper and negative lower charge in the thunderstorm cloud structure. The situation leads eventually to lightning strikes, in this chosen schematic case, being shown to initiate within the cloud (Uman 1994) that, at thunderstorm stage, is in a low-pressure, multi-phase, (ionized) plasma/gaseous/particulate state. The vertical charge separation is thought to involve mostly hydrogen/hydroxyl/nitrous ion-associated water/ice molecule clusters or particles, proposed to generate the charges through strongly-convective ice particle collisions (Dye et al., 1986). In such charge generation process for establishment of the electric field within the thunderstorm cloud, a fundamental role is assigned to existence of a strong intra-cloud updraft, whose collisional charge generation process over-rides, at least, at first, the reverse flow of negative charge to the lower cloud level. In any event, the vertical charge separation is thought to develop in more complicated convective churning of the “vaporious soup” than simply being the result of an eventual gravitationally-determined lower heavier hydroxyl ion attachments as compared to higher lighter hydrogen ion ones. Strong friction forces are proposed to be associated with minute hail nuclei interactions. The buoyant force of the updraft is sufficient to support quite large hailstones or other graupel prior to their release. Cosmic radiation apparently contributes little to the process (Tammet 1994).

Figure 3a is a more detailed elaboration of the charge build-up occurring within a thunderstorm “supercell” structure, also showing the importance of wind shear properties as part of the updraft in contributing to tornado development (Klemp 1999). The build-up of vertically separated charge densities within the potential thunderstorm proceeds until dielectric breakdown of the cloud resistance occurs and lightning strikes are produced, as indicated in Figure 3b. Intra-cloud strikes are of special interest in modern researches that show essentially no correlation with cloud-to-ground strikes (Goodman

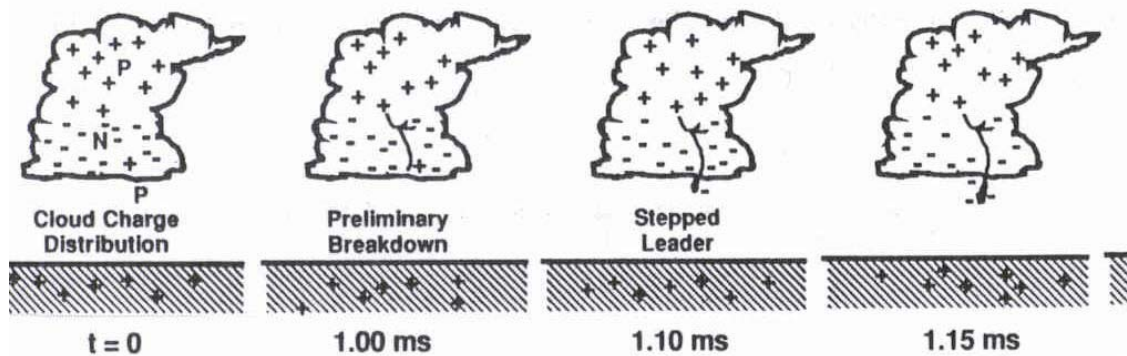


Figure 2. Partial sequence of timed steps in a cloud-to-ground lightning strike, giving emphasis here to intra-cloud initiation of the lightning strike; time is in milliseconds; see Davies-Jones and Golden, 1975.

1999; Buechler et al., 2000). Here, we focus on the intra-cloud strikes for the additional reason that such strikes produce localized cylinders of ionized particles, particularly, of hydrogen and hydroxyl ions, which then are accelerated as charge carriers within the otherwise global electric field of the thundercloud structure.

A role for consideration of the smaller, “unseen” population of molecular elements has been attributed to Rathbun in a later comprehensive analysis of electrical influences on tornadic behavior (Wilkins 1964). The hydrogen ions are accelerated downward and the hydroxyl ions, up, even if attached to water or other molecular clusters. The easier flow of hydrogen ions downward produces re-combination to H_2O molecules and, thence, to ice or water, with an approximately twenty times greater exothermicity for the ionic re-combination as compared with the molecular condensation. The liberated heat at the lower cloud level should contribute significantly to added strengthening of the updraft, otherwise found reasonably difficult to account for, temperature-wise, only on a condensation basis (Vonnegut 1960; Wilkins 1964). Greater influence on the mixed vapor flow, molecular-collision-wise, is produced by the heavier hydroxyl ions that are driven upwards to effect their re-combination at the upper cloud level in the global electric field. Thus, an electrically-driven addition to the updraft is produced with important temperature and pressure components. The encompassing cloud and charge carriers operate as an electrostatic motor (Watkins et al., 1978).

An essentially vertical lightning strike produces a radial distribution of ions traveling upwards and downwards on the cylinder circumferential surface surrounding the post-strike “centerline”, very probably, having peak distribution within a particular radius increment. Perhaps there is a vortex-type screw character to the lightning strike, though as yet only referenced (Wilkins 1964) to an electrodynamic theory proposed by Rathbun. Subsequent pioneering laboratory experiments to study tornado characteristics have been performed by way of demonstrating the character of electric discharges occurring inside of vortex-stabilized vertical arcs (Wilkins 1964; Watkins et al., 1978) that have provided indication of updraft enhancement of lightning strikes. We would term these

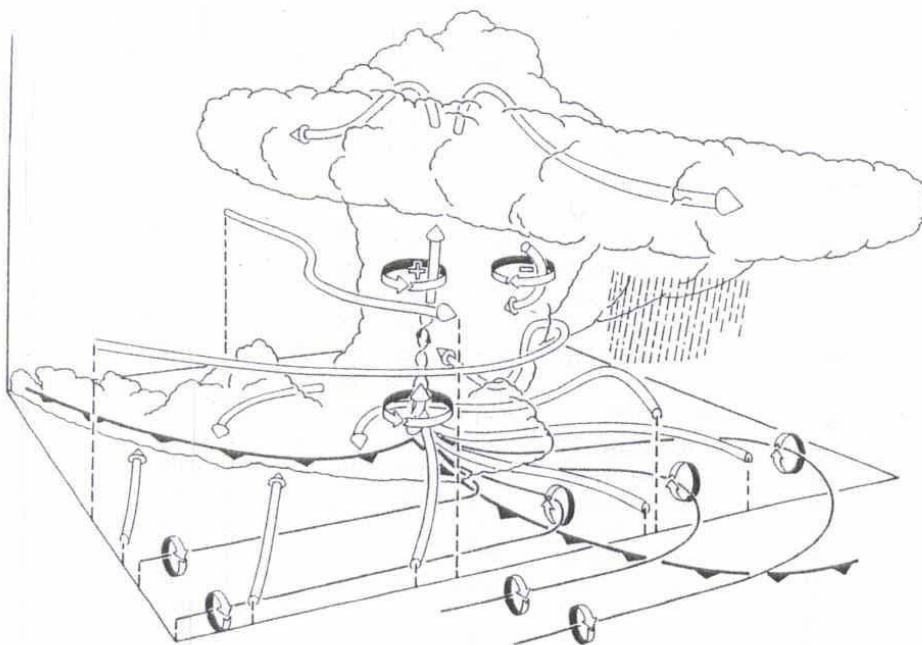


Figure 3.a. J. Klemp three-dimensional schematic illustration of horizontal wind velocity influence on tornado development, including charge separation, as utilized by H.B. Bluestein (1999).

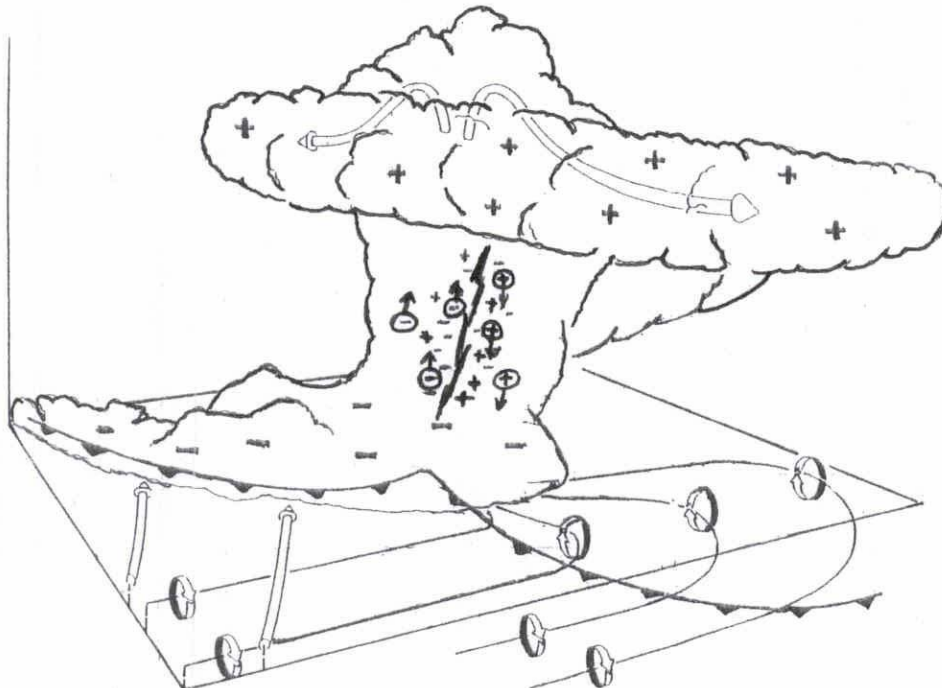


Figure 3.b. Adaptation of Figure 3.a. to show an intra-cloud lightning flash producing charge carriers to activate the thunderstorm "motor" in pre-tornadic development.

experiments, along with most of the referenced information obtained until the present time, as post-tornado characterization. Aircraft measurements of lower cloud positive charges have been attributed to the “deposition of positive charge by lightning” (Mo et al., 2002).

Now, the description given above applies only for a single intra-cloud lightning strike among an increasing number associated with greater thunderstorm strength. The single vertical “motor cell” is among many distributed side-by-side in the super-sized thundercloud --- and these vortex-type cells repel each other with a force proportional to whatever vortex component of strength may have been acquired. Again, because of previous interest in lightning-associated tornadic activity, research study of the association has indicated no reason for repeated strikes to occur within a once struck vortex (Wilkins and McConnell, 1968). However, the mechanism that is being proposed here for an individual cell to achieve tornado status is one of repeated lightning strikes having to occur within the same cellular zone of an earlier strike. Such improbability relates to the observation of tornado development being particularly associated with extensively repeated lightning activity within a given region (Goodman 1999; Buechler et al., 2000). And, along the way towards tornado development is the tell-tale beginning of intensification of localized updraft experienced at the lower cloud surface of the thunderstorm, thermally-assisted by the (downward) arrival of hydrogen ions for re-combination/condensation.

Thus, in summary, intra-cloud lightning is a necessary but not sufficient requirement for tornado initiation. The need for multiple strike activity within an individual pre-tornadic cell relates to the relative rarity of tornado occurrences. Tornado generation is attributed to: [1] sufficient charge separation in the thunderstorm, with accompanying internal atmosphere, to generate copious lightning strikes; [2] repeated intra-cloud strikes within a developing tornadic cylinder for thermally-assisted build-up of vortex strength; and, [3] re-combination of deposited positive charge at the lower cloud surface for temperature rise plus heavier negative ion collisional flow upwards to contribute vertical pressure --- all aided by lateral wind considerations (Klemp 1999).

3. Charge recombination/condensation

A tornado, however formed, contains much less energy than the thunderstorm that produces it. Modern evidence for tornado occurrence following significant lightning activity (Goodman 1999; Buechler et al., 2000) is shown in Figure 4. The strong correlation has led to suggested orbital lightning monitoring as a possible tornado warning system. However, while elimination of the global-type charge separation that occurs in thunderstorm development is “out-of-the-question”, there is opportunity of interfering with tornado initiation caused by lightning “charging” of potential vortices. The basic idea is to effect both lightning suppression and/or recombination of lightning-initiated charges by supplied nanometric fly-ash-like particles (Akeson et al., 2002) put into the embryonic updraft zone, located just below the negatively charged lower cloud level. As a start, the insulating character of the ceramic constituents of fly-ash particles

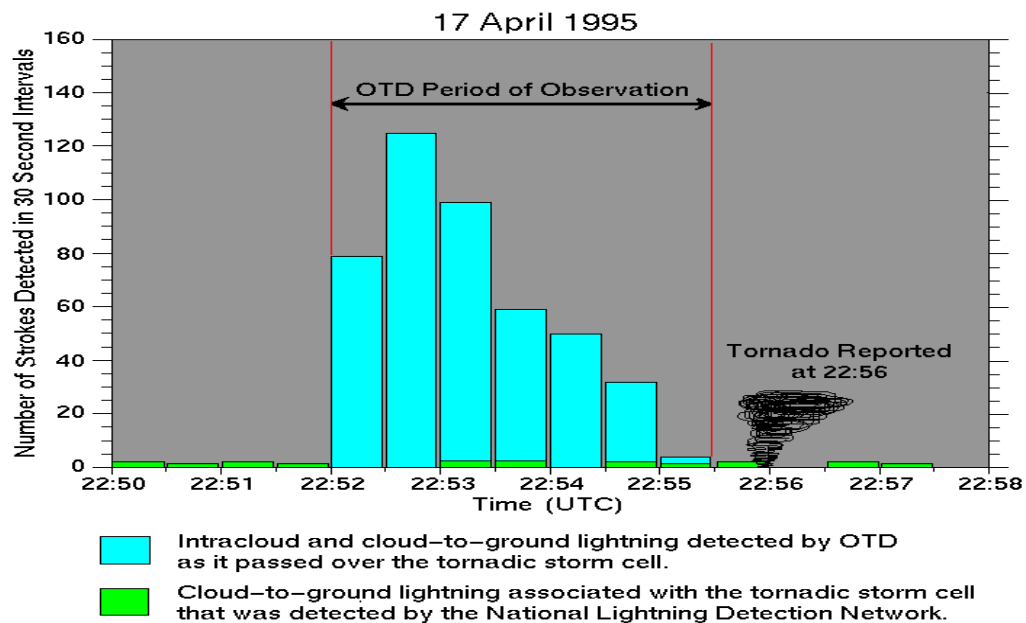


Figure 4. Optical transient detector (OTD) plot reported by NASA Space Science News, as obtained from orbital observations made over a storm in Oklahoma. "OTD registered a sharp increase in lightning flashes as the storm system built, and as clouds rose, then a sudden drop as the system collapsed and spawned a tornado." (Goodman 1999; Buechler et al., 2000).

should contribute to increase of the dielectric breakdown strength of the intra-cloud atmosphere. Also, the low density and small size of the suggested particles should promote their having an important significant lifetime in the intra-cloud chamber, as presumed useful to effecting ion recombination and subsequent phase transformation.

The proposed method of tornado prevention by a cloud seeding procedure is novel for several reasons: [1] essentially lighter-than-air nanometrically-sized particles are involved; and [2] the particles are to be injected into the early updraft development of the lower cloud level. Of course, it has been known for the last ten years that cloud seeding has been accomplished quite effectively for hail suppression (Sheremata 2001). Hail is known to be a by-product of the storm systems that produce tornadoes and such seeding has been utilized to effectively reduce ground level damage through reduction of hail stone sizes. Such alteration of hail characteristics that has been achieved on a large scale, effectively altering cloud energetics even at a scale near to tornado spawning thunderstorms, provides encouragement for the current proposal. In contrast to other rain-making cloud seeding activities, both hail suppression, as referenced here, and the proposed charge recombination/condensation mechanism involves super-saturated atmospheric conditions that need only relatively much smaller particles, even suggested nanometrically-dimensioned ones, to effect charge re-combination and thence molecular condensation. The smaller particle sizes relate to the important consideration of being able to disperse a sufficient number of particles to influence the properties of a sizeable

cloud structure. Under such severe atmospheric conditions, the finer aspects of effective advantage through top-down cloud seeding also to involve epitaxial aspects of utilizing (heavier) silver iodide particles seem relatively unimportant, although such consideration is not discounted among potential low-density candidate particle materials.

The basic idea is to foster recombination of separated ionized hydrogen and hydroxyl constituents from water, along with gaseous water molecules, into water/ice particles in the heavily supersaturated cloud formations presaging possible full tornadic activity, thus, producing significant energy dissipation in the formation of condensed products and consequent, undoubtedly heavy rain or hail, instead of lightning strikes and destructive wind power. The main consideration for accomplishing the task involves a form of "cloud seeding" --- done in a new way with new particle considerations, as follow:

(i) To make important contact, first, with the particular constituent of a heavy concentration of hydroxyl ions at the lowest cloud surfaces, the cloud seeding is to be initiated by liberation of appropriate nanometric, or near-nanometric, sized particles below the lower cloud levels.

(ii) Something-like nanometric-sized fly-ash particles (that are hollow ceramic cenospheres, that unfortunately are normally of larger 30-300 micrometer size) would seem to be ideal from a desired "lighter-than-air" property in that an important concept in this proposed consideration is that, if tornadic development is imminent, the particles would be dragged or pulled upwards, in the convectively-stirred up-draft presaging tornado occurrence, thus going through the clouds from the bottom-up while serving as particle nucleation/growth sites, first, for hydroxyl ion absorption and then, further up in altitude, hydrogen ion reaction/nucleation to form hail or rain.

(iii) Perhaps, a weak positive charge state could be added to such particles, first, to help prevent their own agglomeration and then, when appropriately dispersed, to help in promotion of first stage hydroxyl ion adsorption. As an aside, if only positively charged particles, near to being lighter than air, were liberated simply to combine with the hydroxyl ions, the advantage of gaining dissipation of the very appreciable ionization potential energy in forming water or hail particles would be lost.

(iv) The proposal of employing nanometric particles in order to accomplish tornado defeat is important for at least two size-dependent reasons: (a) such small size is in the presumed smaller, or smallest, particle regime theoretically capable of nucleating water droplets under large supersaturation conditions; and, (b) there is the more practical consideration of being able to carry/disperse "billions and billions" of particles during conveying flight.

Acknowledgements

This work has been funded by Entrepreneurial Research Funds after internal lab competition under the guidance of Dr. Sierakowski, Chief Scientist, Munitions Directorate, Air Force Research Laboratory, Eglin Air Force Base FL. Helpful interaction has been provided by Professor Kelvin K. Droegemeier, School of Meteorology, and Director, Center for Analysis and Prediction of Storms, University of Oklahoma, Norman OK, and, his colleague, Dr. Ming Xue. Additional helpful

communications have been received from Professor William P. Winn, Department of Physics, and Chairman, Langmuir Laboratory, New Mexico Tech, Socorro NM; and, Dr. Steven J. Goodman, Global Hydrology and Climate Center, NASA Marshall Space Flight Center, Huntsville Alabama. Such acknowledgements are not intended to imply agreement with the tenets of the present text.

References

Akesson, J., Seal, S., Shukla, S. and Rahman, Z., February, 2002. Copper plating processing control by SEM, *Adv. Mater. Proc.*, p. 33.

Altschuler, M.D., 2002. Atmospheric electricity and plasma interpretations of UFO's, Condon Report, Sec. VI, Chap 7: Atmospheric electricity and plasma, p. 5, <http://912a-87.umd.edu/condon/test/s6chap07.htm>.

Brooks, E.M., 1951. Tornadoes and related phenomena, Compendium on Meteorology, (Amer. Meteor. Soc., Boston MA) p. 673.

Buechler, D.E., Driscoll, T.E., Goodman, S.J., and Christian, H.J., 2000, Lightning activity within a tornadic thunderstorm observed by the optical transient detector (OTD), *Geophys. Res. Letts.* **27**, 2257.

Davies-Jones, R.P. and Golden, J.H., 1975. On the relation of electrical activity to tornadoes, *J. Geophys. Res.* **80**, 1614

Dye, J.E., *et al.*, 1986. Early electrification and precipitation development in a small, isolated Montana cumulonimbus, *J. Geophys. Res.* **91**, 1231.

Goodman, S.J., 1999. Lightning detectors watch storms that spawned tornadoes, http://science.msfc.nasa.gov/newhome/headlines/essd03apr98_1.htm.

Klemp, J., in Bluestein, H.B., 1999. Tornado alley: Monster storms of the great plains, (Oxford University Press, Oxford UK) p. 74.

Mo, Q., Helsdon, Jr., J.H., and Winn, W.P., 2002. Aircraft observations of the creation of lower positive charges in thunderstorms, *J. Geophys. Res.* **107**.

NOAA Photo Library/Historic NWS Collection/Monsters/Tornadoes/wea00206, 2003. <http://www.photolib.noaa.gov/historic/nws/wea00206.htm>.

Sheremata, D., 2001, Cloud seeding: Shooting for the clouds, <http://www.cangeo.ca/JA98/Clouds.html>.

Tammet, H., 1993/4. Atmospheric Electricity: II. Air Ions, CRC Handbook of Chemistry and Physics, 74th Edition, D.R. Lide, Ed. (CRC Press, London UK), p. 14-25.

Uman, M.A., 1993/4. Atmospheric electricity: IV. Lightning, CRC Handbook of Chemistry and Physics, 74th Edition, Ed. Lide, D.R. (CRC Press, London UK), p. 14-27.

Vonnegut, B., 1960. Electrical theory of tornadoes, *J. Geophys Res.* **65**, 203.

Watkins, D.C., Cobine, J.D., and Vonnegut, B., 1978. Electric discharges inside tornadoes, *Science* **165**, 171.

Wilkins, E.M., 1964. The role of electrical phenomena associated with tornadoes, *J. Geophys. Res.* **69**, 2435.

Wilkins, E.M. and McConnell, L.T., 1968. Threshold conditions for vortex-stabilized electrical discharges in the atmosphere, *J. Geophys. Res.* **73**, 2559.

Winn, W.P., Hunyady, S.J., Aulich, G.D., 2000. Electric field at the ground in a large tornado, *J. Geophys. Res.* **105**, 20,145.

COMPARATIVE MODEL X-RAY DIFFRACTION CHARACTERISTICS OF RDX AND ALUMINUM

Kinnan L. Kline

University of Florida Graduate Engineering and Research Center, Shalimar, FL 32579

Ronald W. Armstrong, Michael P. Kramer, David W. Richards

AFRL/MNME, Munitions Directorate, Eglin Air Force base, FL 32542

Abstract. The involvement of the combined constituents RDX (cyclotrimethylenetrinitramine) and aluminum particles in energetic material formulations provides a reason for comparing the theoretical x-ray diffraction properties of the two very different materials, as determined, for example, in powder diffraction or topographical imaging experiments. Also, of interest is x-ray determination of the internal dislocation strain fields in the two materials because of their very different deformation and fracturing behaviors. Thus, a comparison is made: (1) of the limiting theoretical perfect and imperfect crystal integrated x-ray intensities computed for symmetrical diffraction, on a primary and secondary extinction basis, respectively; and, (2) of the modeled dislocation strain field “widths” affecting the x-ray intensities for the two materials. Beyond the complications presented both by the lower diffracting power of the complex orthorhombic RDX crystal lattice and its larger cell dimensions, the advantage of lower energetic crystal dislocation densities is offset by the greater extent, and influence, of the dislocation strain fields.

INTRODUCTION

Compared on a mechanical properties basis, RDX is elastically compliant, plastically hard, and brittle (1), whereas aluminum is elastically stiffer, plastically softer, and considerably more ductile.

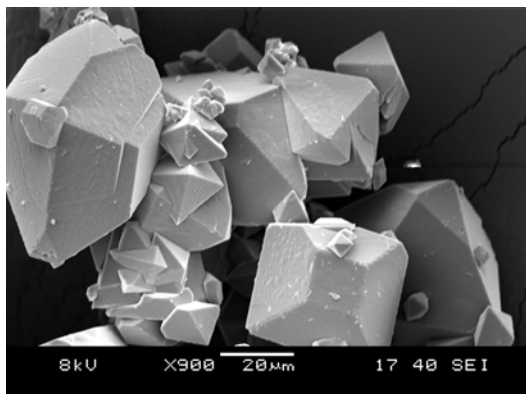


Figure 1. An RDX scanning electron micrograph

The difference in properties of RDX and aluminum can be traced to the bonding of molecules and atoms in the respective lattice structures and, particularly, traced to the properties of dislocations in the two materials. Also, the deformation properties of RDX are relatively complicated (1) whereas the mechanical properties of aluminum are relatively simple, especially, in terms of relating those deformation properties of aluminum to its consequent dislocation behavior.

X-RAY DIFFRACTION

The role of x-ray diffraction in characterizing the internal perfection of metallic, ionic, covalent, and molecular lattice structures is well-established, even spanning early powder diffraction peak profile analyses and more recent lattice imaging of dislocation strain fields akin to

the technique of transmission electron microscopy (2). For the x-ray case, the theoretical (relative) intensity associated with reflection of x-rays from an ideally perfect crystal is expressed as (3)

$$\rho_P = (8/3\pi)(\lambda^2/\sin[2\theta_B])(|F_{hkl}|/V)(e^2/mc^2) \{|\sin[\theta_B - \chi]|/|\sin[\theta_B + \chi]|\}^{1/2} \zeta\{P\},$$

in which λ is the x-ray wave length, θ_B is the Bragg angle, F_{hkl} is the cell structure factor, V is the cell volume, $(e^2/mc^2) = 2.82 \times 10^{-13}$ cm, χ is the (negative) angle between the Bragg plane and crystal surface normal directions, and $\zeta\{P\} = \{(1+\cos[2\theta_B])/2\}$ is the (average) polarization factor. ρ_P is small because of the influence of the phase interference between multiply-reflected rays in the perfect crystal lattice.

The opposite limiting theoretical diffracted intensity, defined x-ray-wise for an ideally imperfect crystal, ρ_S , applies for the model of the rays satisfying the Bragg condition for a single-time reflection only, as given by (3)

$$\rho_S = (1/2\mu)(\lambda^3/\sin[2\theta_B])(F_{hkl}/V)^2(e^2/mc^2)^2 (1 - \cot[\theta_B]\tan[\chi]) \cdot \zeta\{P\}^2,$$

where μ is the normal x-ray absorption coefficient and all other symbols have their same value as for ρ_P . The greater penetration of x-rays associated with ρ_S is compared, generally

with a very much reduced penetration depth, ξ , known as the x-ray extinction depth, corresponding to the primary extinction of x-rays undergoing interference through multiple reflections.

The computed values of the two limiting x-ray intensities are shown in Figure 2 for both RDX and aluminum symmetrical plane reflections obtained with copper K α radiation (4). Richard Gilardi (5) supplied the values of F_{hkl} for RDX. The (111) lowest angle aluminum reflection occurs at $2\theta_B \sim 38.5$ degrees. Comparable values of $\{hkl\}$ occur for RDX at much smaller values of $2\theta_B$. For the individual materials, of course, $\rho_S > \rho_P$, although more so for aluminum, and its intensities are greater than those of RDX, for either case, principally because of the larger values of F_{hkl} . For RDX, the ratio ρ_S/ρ_P shows the particularly complex dependence on $2\theta_B$ that is indicated because of the complicated form of F_{hkl} . Alternatively, the substantial range in intensity between ρ_P and ρ_S for aluminum, particularly for the (111) reflection, provides ample room for characterization of its (mosaic) dislocation structure.

The indicated situation for RDX of smaller Bragg angles, greater x-ray penetration depths, lower diffracted intensities, and multiple reflections, all combine to make more complicated its x-ray diffraction characteristics.

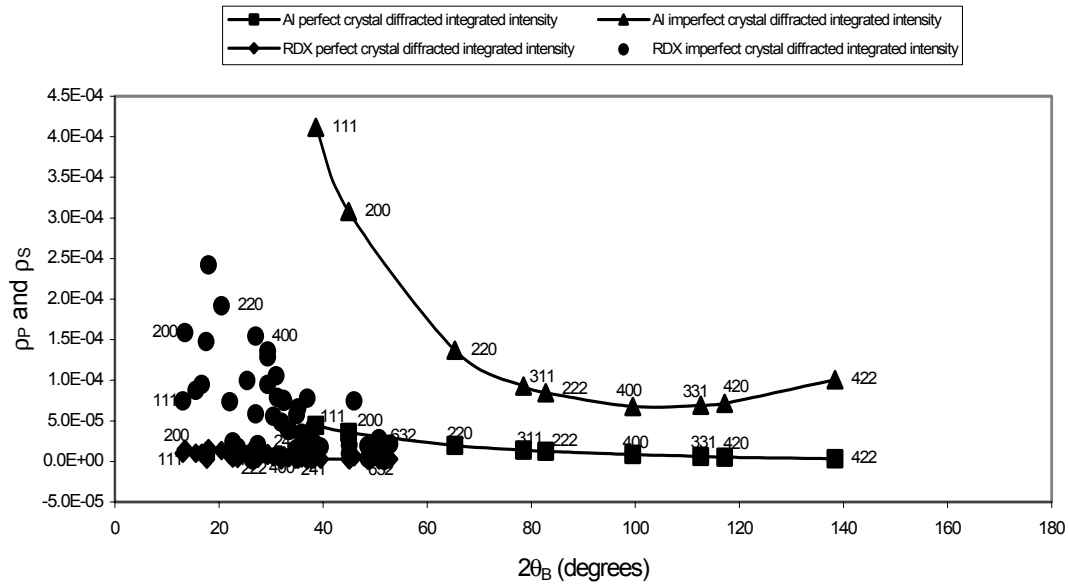


Figure 2. Integrated x-ray intensities, ρ_P and ρ_S , for RDX and aluminum, versus their diffracting angles $2\theta_B$

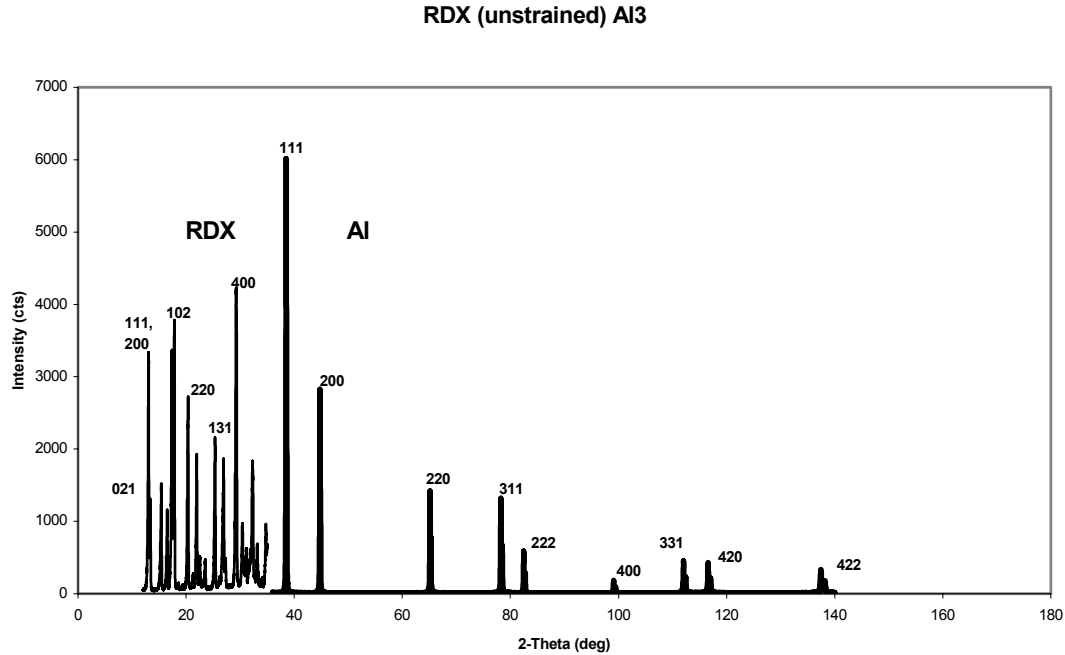


Figure 3. Combined diffraction traces for RDX and aluminum taken under otherwise identical conditions

An example of combined RDX and aluminum powder diffraction traces obtained in separate experiments accomplished under otherwise very similar conditions is shown in Figure 3. The ordinate intensity counts should be considered an arbitrary scale but, for relative, order-of-magnitude, comparison basis, the results may be

reasonably compared with those in Figure 2; see, for example, the comparison of the RDX (102) and the aluminum (111).

DISLOCATION INFLUENCES

The influence of crystal straining, further to whatever level of mosaic imperfection already exists in the crystals being examined by x-ray diffraction, is to lower the diffracted peak intensities for particular reflections and to broaden the peak widths. Thus, Figure 4 shows the lowered intensities, at closed circle positions, put onto a number of RDX peak intensities recorded before the powder specimen was subjected to a gentle “crushing” deformation. The result is similar to that obtained in a prior experiment (6) where the focus was on the lowering of the recorded intensity, and spread, of the otherwise prominent (400) diffraction peak -- because of identification of the (040) slip plane and $b = a[100]$ Burgers vector dislocation in the orthorhombic RDX crystal lattice.

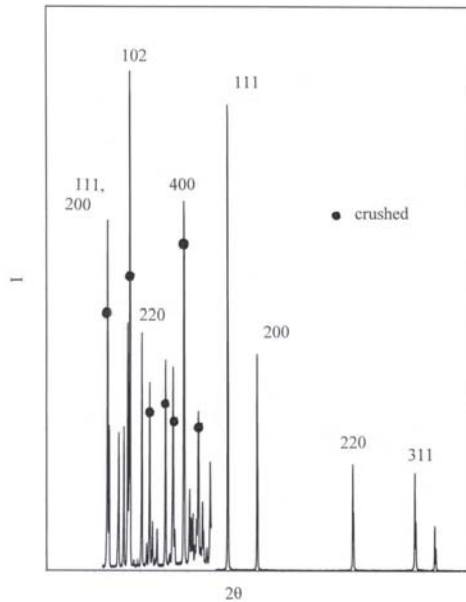


Figure 4. Not-crushed/crushed RDX intensities.

In x-ray imaging, or topographical, experiments, whether at low Bragg angles in transmission or large angles, $\theta_B \sim 45$ degrees, in reflection, the emphasis is on spatially resolving dislocations through their strain field influences on locally

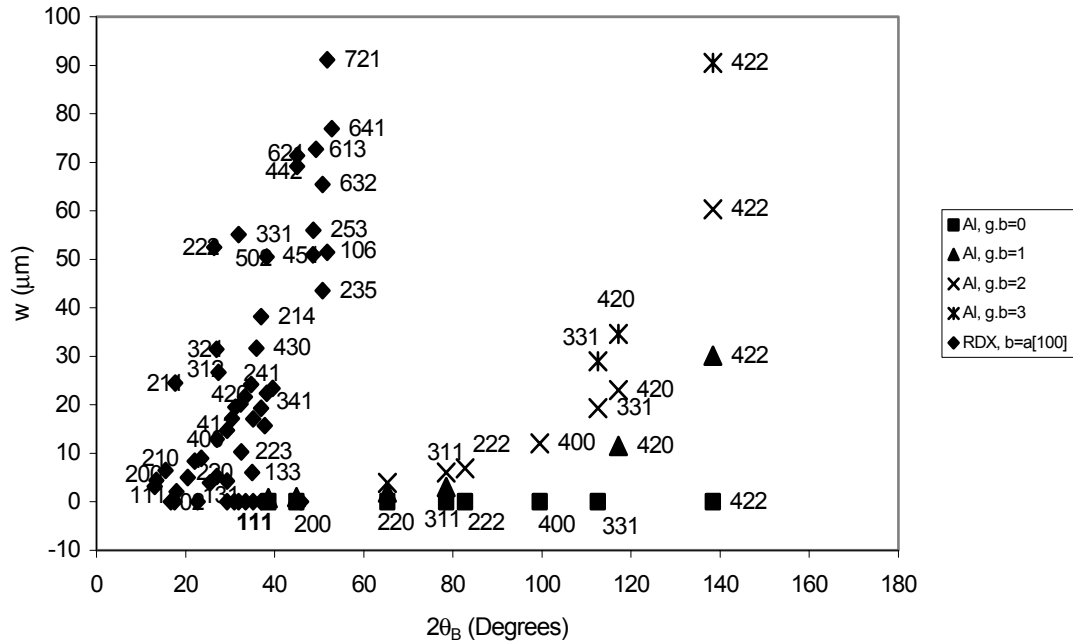


Figure 5. Theoretical dislocation image widths in x-ray diffraction topographs of RDX and aluminum

enhancing the diffracted x-ray intensity in the surrounding vicinity of the dislocation line positions. In transmission x-ray topography experiments, such reflections as the (200), (102), and (220) ones shown in Figures 3 and 4 have been favorably employed (7) whereas in surface reflection, at larger Bragg angles, the (632) and (10 00) have been necessarily employed (8).

The theoretical dislocation widths seen in x-ray topographical images have been associated (9) with the primary extinction distance, ξ , specified on a dynamical theory basis as for $\rho\rho$:

$$\xi = (mc^2/e^2)(\pi V/\lambda|\zeta\{P\}||F_{hkl}|) / [|\sin(\theta_B - \chi)|][\sin(\theta + \chi)],$$

where all parameters have been previously identified. The dislocation image width has been given by

$$w \sim (\xi/2\pi) \mathbf{g}_{hkl} \cdot \mathbf{b}$$

with \mathbf{g}_{hkl} being the reciprocal lattice vector for the (hkl) plane.

Figure 5 shows the computed images obtained for $\langle 110 \rangle$ type dislocations in aluminum as compared with the $a[100]$ dislocation in RDX. In general, at the relevant small angles shown for

aluminum, the image widths are much smaller than those shown for the various prominent reflections of RDX. The results are interpreted to reflect the condition of the dislocation strain field extending to relatively larger distances in RDX, and to relatively greater purpose in connection with the limited deformation and cracking-prone behavior of RDX.

REFERENCES

1. Armstrong, R.W., and Elban, W.L., *Dislocations in Solids*, edited by F.R.N. Nabarro and J.P. Hirth, Elsevier Science Publishers, N.Y., 2003, **12**, in print.
2. Armstrong, R.W., *Nano and Microstructural Design of Advanced Materials*, edited by M.A. Meyers, R.O. Ritchie, and M. Sarikaya, Elsevier Science Publishers, N.Y., 2003, in print.
3. Armstrong, R.W., *The Characterization of Crystal Growth Defects by X-ray Methods*, edited by B.K. Tanner and D.K. Bowen, Plenum Press, Oxford, 1979, p. 349.
4. Kline, K.L., *Comparative Model Powder X-ray Diffraction Characteristics of Aluminum and RDX*, M.S. Thesis, University of Florida, 2002.
5. Gilardi, R., U.S. Naval Research Laboratory, 2001, private communication.
6. Elban, W.L., Hoffsommer, J.C. and Armstrong, R.W., CPIA Publication 482, p. 75, (1988).
7. Halfpenny, P.J., Roberts, K.J., and Sherwood, J.N., *Philos. Mag.* **53**, 534 (1986).
8. Elban, W.L., Armstrong, R.W., Yoo, K.C., Rosemeier, R.G., Yee, R.Y., *J. Mater. Sci.* **24**, 1273 (1989).
9. Lang, A.R., *Modern Diffraction Imaging in Materials Science*, edited by S. Amelinckx, R. Gevers, G. Remaut, and J. Van Landuyt, North Holland Publ., p. 407 (1970).

Coating and Recrystallization of Energetic/Reactive Nano-materials

M. P. Kramer^{*}, A.E.D.M. van der Heijden[#], D. W. Richards^{*}, W. H. Wilson^{*},
R. W. Armstrong^{*}, and A. C. van der Steen[#]

^{*} - Air Force Research Lab, Energetic Materials Branch; Eglin AFB, FL 32542, USA

[#] - TNO Prins Maurits Laboratory, Division Munition Technology and Explosion
Safety; P.O. Box 45, 2280 AA Rijswijk, The Netherlands

ABSTRACT:

Nanometric fuel-oxidizer material systems that release energy comparable to that of HCNO explosives are of high current interest as replacements or enhancements for high explosive materials. Reaction and energy release rates in such materials may be accelerated by reducing particle size to nanometric scale. This increases surface area for a given mass, and reduces average diffusion path lengths. One approach is to directly coat nanometric fuel particles with a nanometric-thick layer of an organic oxidizer or explosive material. In this research, coating and crystallization techniques are being developed for direct encapsulation of metal fuel nano-particles. There is also high interest in development of better understanding of the physics controlling the formation and growth of ultrafine (including nanometric) crystals of explosive materials, and of composite nano-structures composed of organic explosives and metal clusters, so that techniques for the direct crystallization of materials as coatings on metal fuel particles can be optimized.

At the Air Force Research Lab, Energetic Materials Branch, two methods are currently being used to recrystallize RDX, CL-20, and other organic materials onto spherical Aluminum particles ranging in size from 30 nm to 1 μ m diameter. In each method, the organic material is first dissolved in a suitable solvent. The Aluminum particles are then added, with continuous agitation. In the first method, a suitable non-solvent is then added. After precipitation of the organic material, the solvent and non-solvent are then removed by vacuum distillation. In the second method, non-solvent is not used; instead, the solvent is slowly removed by distillation with constant agitation. Materials produced in these ways are generally about three times the diameter of the starting nanometric Aluminum powder used. Powder x-ray diffraction data indicates that the materials recovered are of the desired composite configuration rather than a mixture of distinct Aluminum and organic crystal particles.

At TNO Prins Maurits Laboratory, similar results are being pursued, with some differences in the techniques being developed. The crystallization of the energetic material RDX on nanometric aluminium particles is studied by using a drowning-out process. It is based on the addition of an RDX solution in an organic solvent to a non-solvent, in which the aluminium particles are suspended. The results obtained with this technique under different process conditions and the characterization of the obtained products (by means of e.g. scanning electron microscopy and thermal analysis) will be presented in this paper.

The Power and Strength of Energetic/Reactive Nano-Materials

R.W. Armstrong*, M.P. Kramer*, W.H. Wilson*

*AFRL/MNME, 2306 Perimeter Road, Eglin AFB, FL 32542.

ABSTRACT

A number of relatively new energetic/reactive material formulations employing nanometric particle size ingredients might be thought to be somewhat novel because of the consideration of bringing their energy release rate and decomposition times closer together. In addition, there is the advantage of such ultrafine particle solids being stronger generally and, consequently, less sensitive to mechanical forces and deformations, for example, as experienced in drop-weight impact and shock wave tests.

Thus, nanometric-sized energetic materials, as well as counterpart combustible metals, and reactive materials, are all of current research interest, for one reason, relating to surface-control of their decomposition properties providing for the possibility of orders of magnitude increases in energy release rates at ultrafine particle sizes. An indication of this benefit is shown in Figure 1 by extrapolation to nanometric particle sizes of recent burn rate results obtained for aluminum particle combustion properties in both laboratory and gun propellant experiments [1].

From a research point-of view, the surface energy property in the nano-particle regime is of paramount importance, as evidenced practically by nano-particle processing difficulties with agglomeration. Particle coating can alleviate the problem, especially relating to coating particles with materials that have relatively lower surface energies. In this regard, a comparison of solid surface energies (or stresses) of materials with their volume free energies provides interesting insight into the differences between the fundamental material lattice structures and their physical/mechanical property consequences; see reference [2] for a reported listing.

And, then, dislocation defects are presumed to control the mechanical strength and fracturing behaviors, even, of nanometric-scale material particles and structures --- thus presenting challenging areas of research so far as concerns a dearth of material testing methods and also prediction of size-dependent material deformation/decomposition properties. Recent atomic force microscopy (AFM) observations on nano-indented and otherwise deformed RDX crystals have indicated the presence of shock-generated nanoscale shear cracks with displacement vectors smaller than the length of individual molecules [3].

1. R.W. Armstrong, B. Baschung, D.W. Booth, and M. Samirant, "Enhanced Propellant Combustion with Nanoparticles", *Nano Letters*, **3**, 253 (2003)
2. W.L. Elban, R.W. Armstrong, and T.P. Russell, "Plasticity/Interfacial Energy Influences on Combustion-Driven Cracking of RDX Energetic Crystals", *Philosophical Magazine A*, **78**, 907 (1998).
3. J. Sharma, C.S. Coffey, R.W. Armstrong, W.L. Elban, and S.M. Hoover, "Sub-Molecular Fracture Steps in Shock-Shattered RDX Crystals and Follow-on Nano-Indentation Evaluation of Early Stage Plasticity", in Shock Compression of Condensed Matter – 2001, M.D. Furnish, N.N. Thadhani and Y. Horie, eds. (AIP Press, N.Y., 2002) Conference Proceedings 620, Part 2, p. 837.

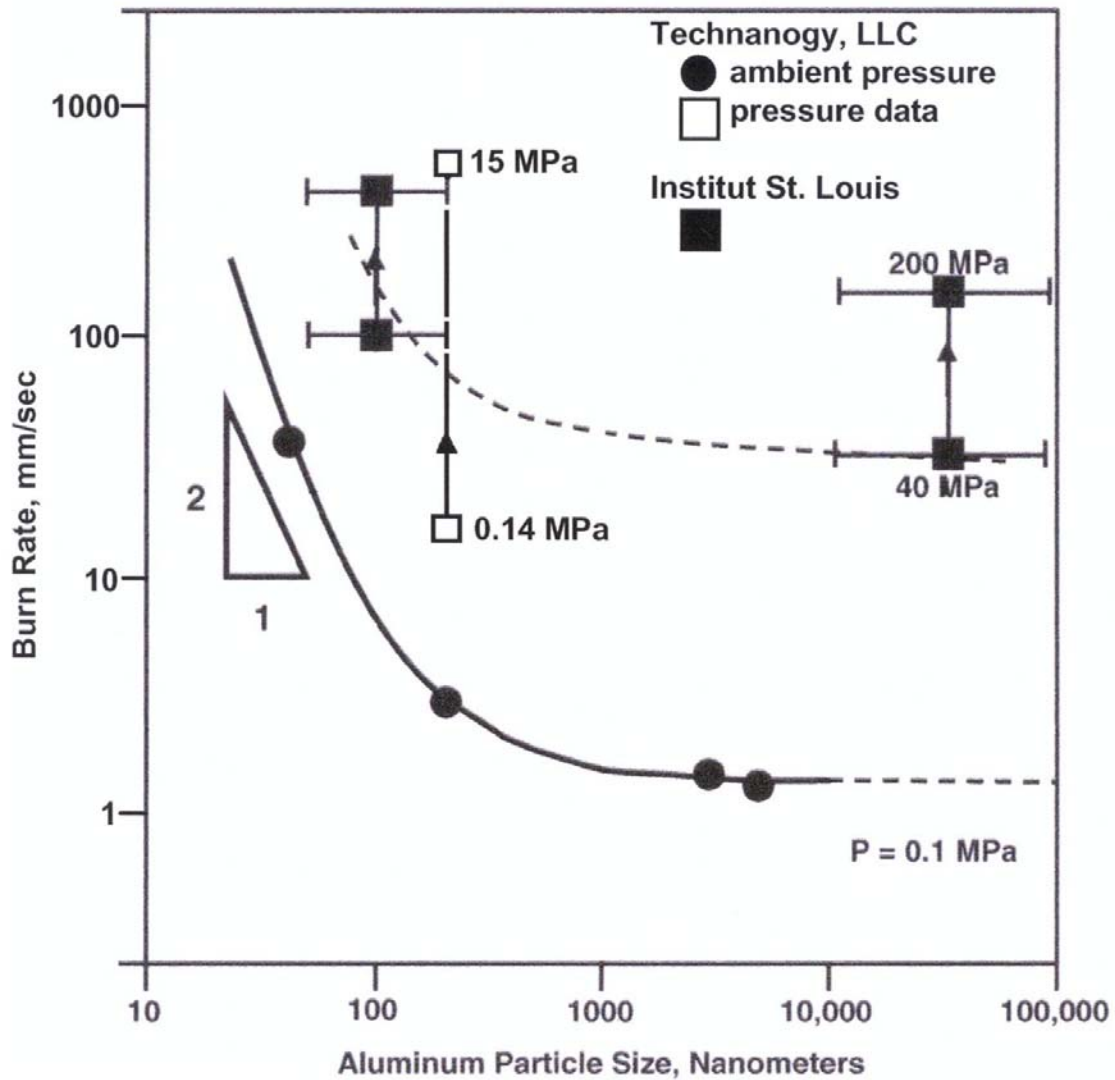


Figure 1. Burn rate as a function of aluminum particle size, also showing indicated pressure ranges for the vertical lines, and providing indication at the smallest particle sizes of an inverse square dependence of burn rate on particle diameter [1]. The Technanogy results are for strands 3.175 mm diameter and 6.35-8.47 mm length employing a standard ammonium perchlorate formulation in 88% solid condition after pressing to 80-85% density. The French-German Research Institute of Saint Louis results apply for a new double-base gun propellant containing 15% either of Alex or micrometer-sized aluminum particles in the same Pechiney YX 76 propellant formulation of 55% nitrocellulose and 30% dioxyethylnitramine dinitrate (DINA), as measured at different pressures in a high-pressure closed vessel of 50 cm³ volume.

Dislocation properties:
Pile-up/crack analogy; grain volume/boundary-controlled dynamics; and,
energetic crystal interpretations *

R.W. Armstrong
AFRL/MNME
2306 Perimeter Road
Eglin.AFB, FL 32542-5910

ABSTRACT

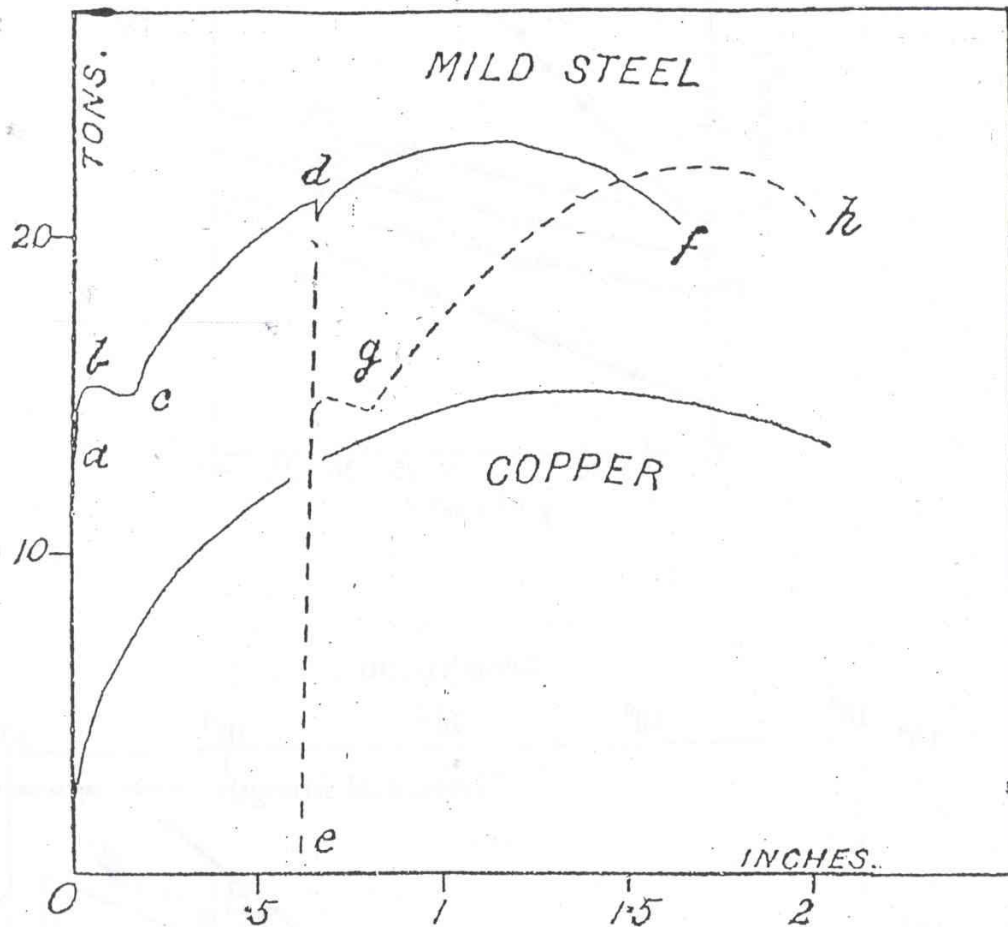
The analogous properties of dislocation pile-ups and sharp cracks [1] are employed recently to explain the increased indentation fracture mechanics stress intensities measured at small crack sizes for alumina polycrystals [2]. For Armco iron employed as a reference structural material, the twinning-stress-determined Hugoniot elastic limit (HEL) is shown to follow an Hall-Petch inverse square root of grain diameter dependence, in agreement with conventionally determined twinning stress measurements obtained at low temperatures and/or high strain rates [3]. Special dislocation properties for RDX and related energetic materials offer a rationale for the crystals being plastically hard and brittle, as compared with their otherwise "polymer-like" elastic compliances [4].

References

1. R.W. Armstrong, "Plasticity: Grain Size Effects", in Encyclopedia of Materials: Science and Technology, (Elsevier Science Publishers, Oxford, 2001), pp. 7103-7114.
2. R.W. Armstrong, "Grain size dependent alumina fracture mechanics stress intensity", *Intern. Journal of Refractory Metals and Hard Materials*, vol. 19 (2001), pp. 251-255.
3. R.W. Armstrong, W. Arnold, and F.J. Zerilli, "Grain size dependence of shock-induced twinning stresses in Armco iron", Intern. Workshop: "New Models and Hydrocodes for Shock Wave Processes in Condensed Matter", Chair: V. Klimenko, C.S. Coffey, A. Rajendran, and D. Swift, Edinburgh, Scotland, 19-24 May 2002.
4. R.W. Armstrong and W.L. Elban, "Dislocations in energetic crystals", submitted for Dislocations in Solids, Editor: F.R.N. Nabarro, Vol. 12 (Elsevier Science Publishers, Oxford, 2002).

* *Physics and Chemistry of Solids Colloquium, Cavendish Laboratory.*

W.C. Unwin, "On the Yield Point of Iron and Steel and the Effect of Repeated Straining and Annealing", Proceedings of the Royal Society (London) 58, 178 (1895).



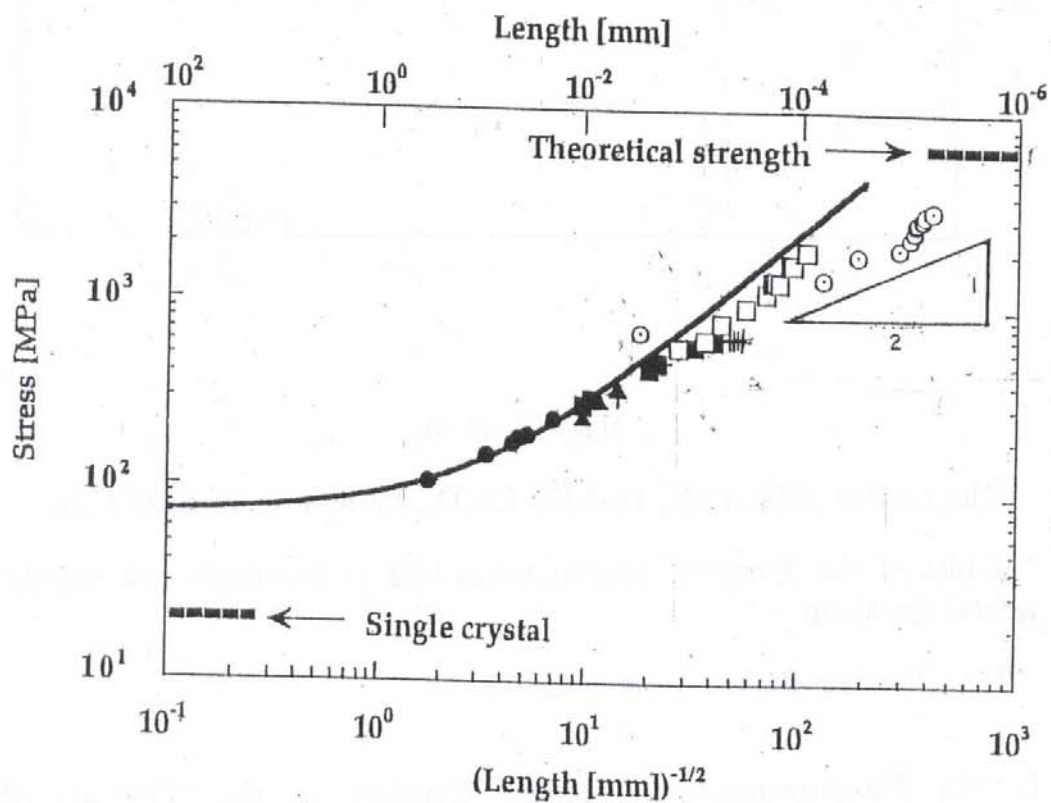
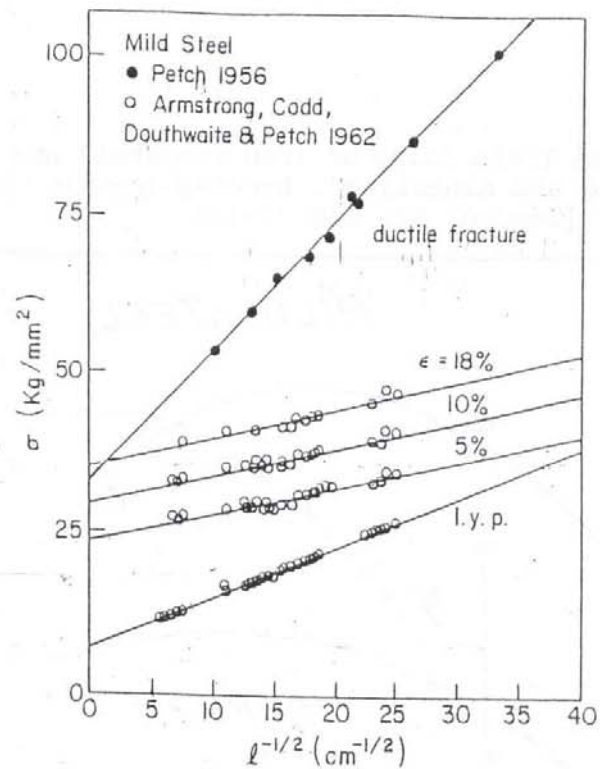
May 16, 1895.

The LORD KELVIN, D.C.L., LL.D., President, in the Chair.

A List of the Presents received was laid on the table, and thanks ordered for them.

The following Papers were read:—

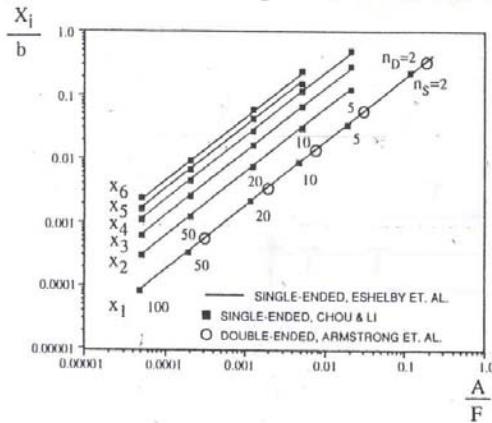
- I. "On Measurements of small Strains in the Testing of Materials and Structures." By J. A. EWING, M.A., F.R.S., Professor of Mechanism and Applied Mechanics in the University of Cambridge. Received April 24 1895



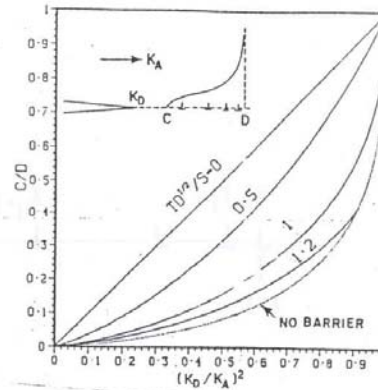
DISLOCATION PILE-UP DESCRIPTIONS OF SHEAR BANDING

I. Static pile-up results

J.C.M. Li and Y.T. Chou, "The Role of Dislocations in the Flow Stress/Grain Size Relationships", Metallurgical Transactions, 1, 1145 (1970); Wen-Lan Li and J.C.M. Li, "The Effect of Grain Size on Fracture Toughness", Philosophical Magazine, A59, 1245 (1989); Q. Gao and H.W. Liu, "Characterization of the Tip Field of a Discrete Dislocation Pile-up for the Development of Physically Based Micromechanics", Metallurgical Transactions, 21A, 2087 (1990).



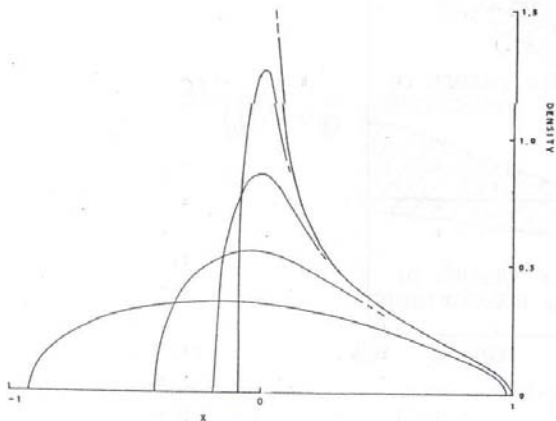
The position, X_i , of the i -th dislocation in a pileup.



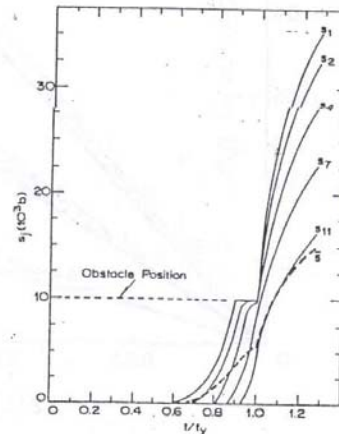
Dislocation-free zone at the crack tip; the effect of lattice friction and barrier distance.

II. Dynamic pile-up results

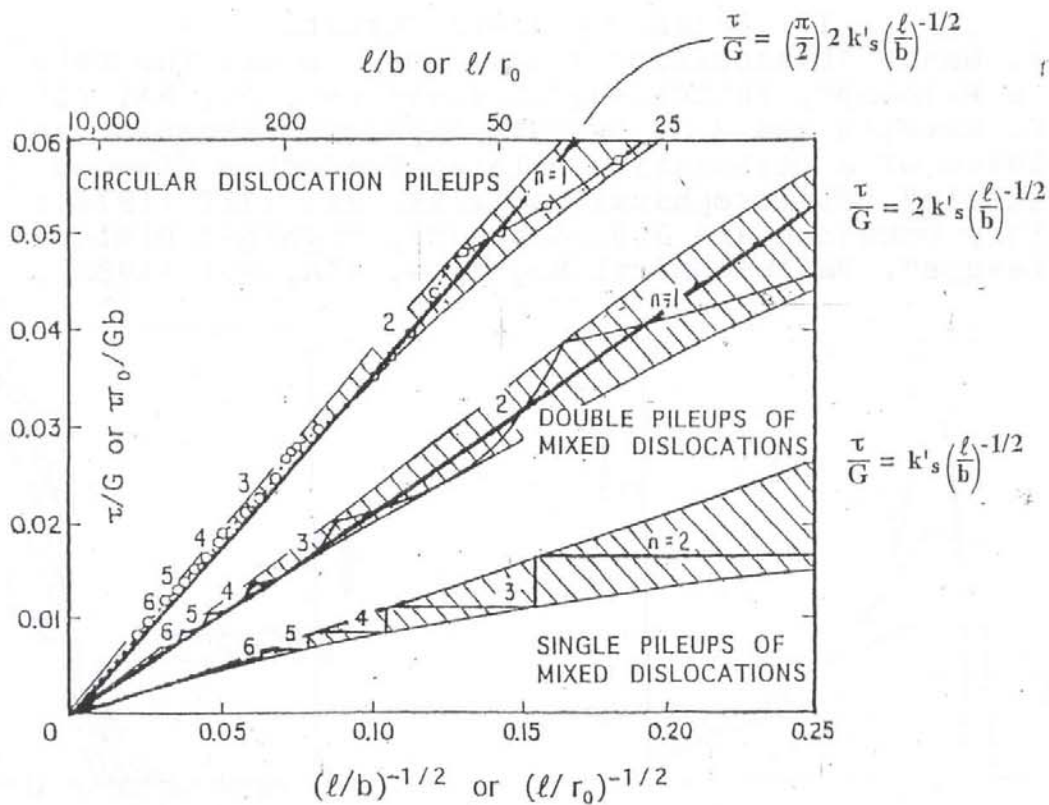
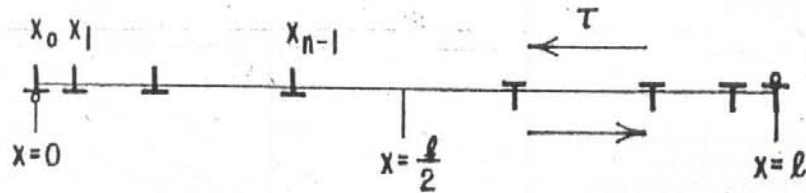
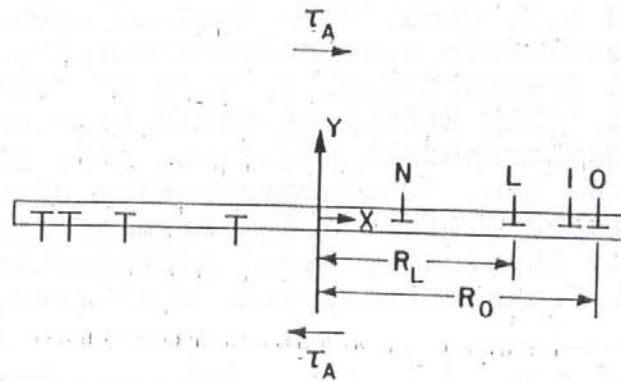
A.K. Head, "Dislocation Group Dynamics VI. The Release of a Pile-up", Philosophical Magazine, 27, 531 (1973); F.P. Gerstle and G.J. Dvorak, "Dynamic Formation and Release of a Dislocation Pile-up Against a Viscous Obstacle", Philosophical Magazine, 29, 1337 (1974); Hilary Ockendon and J.R. Ockendon, "Dynamic Dislocation Pile-ups", Philosophical Magazine, 47A, 707 (1983).

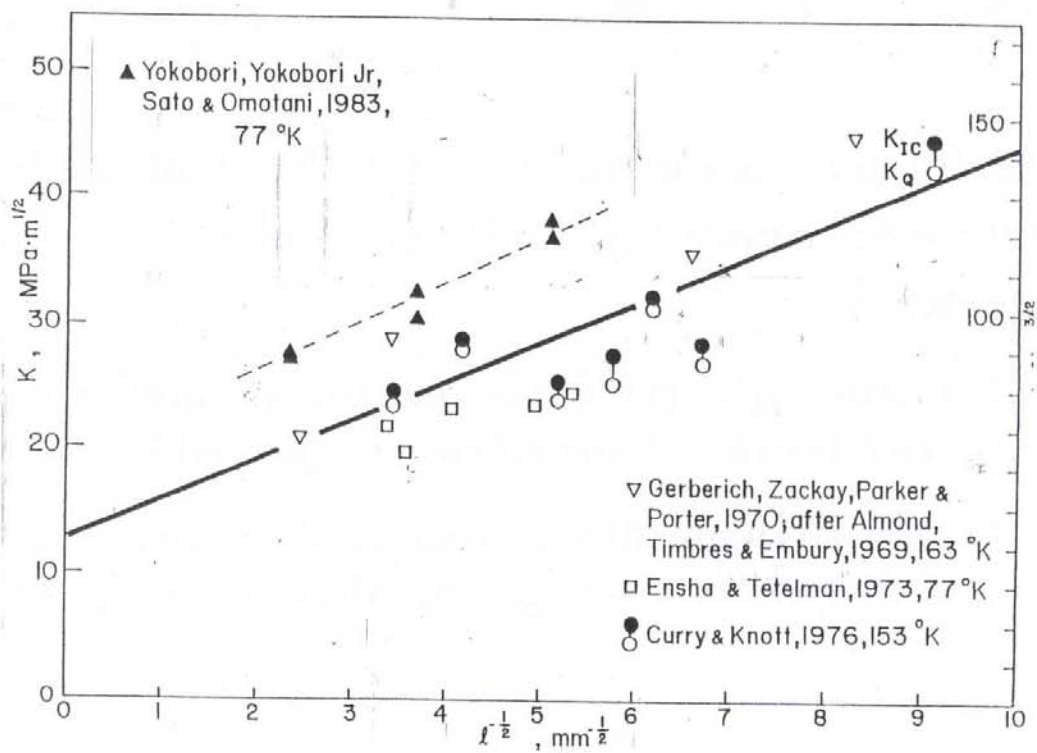
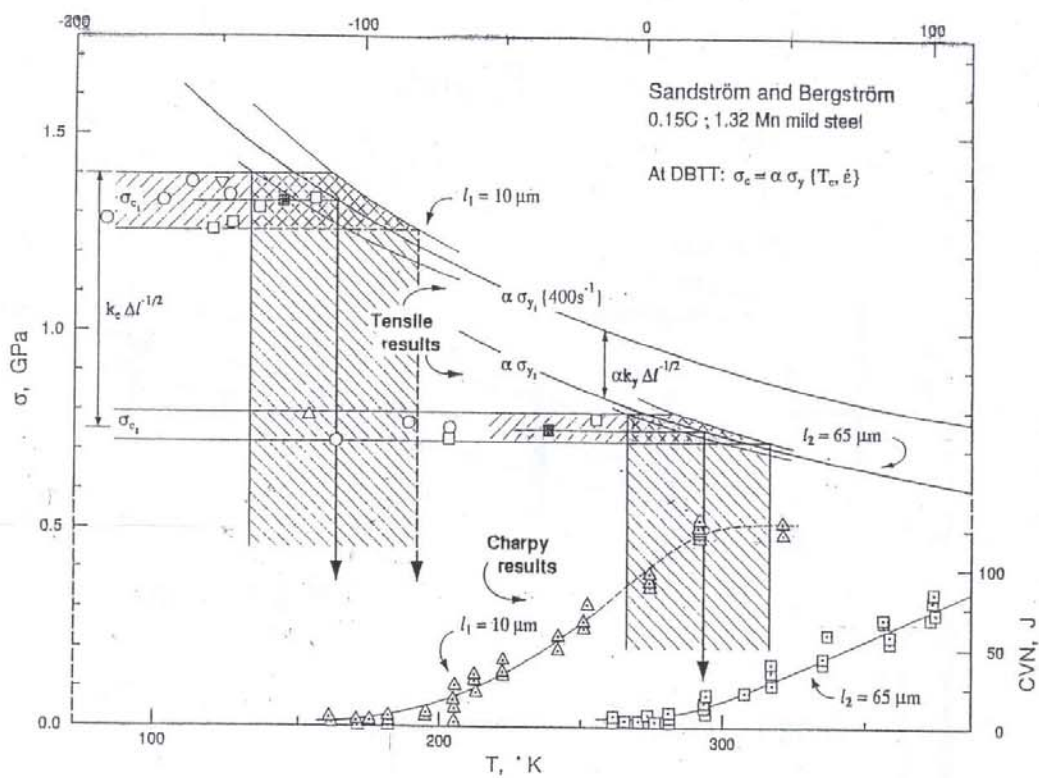


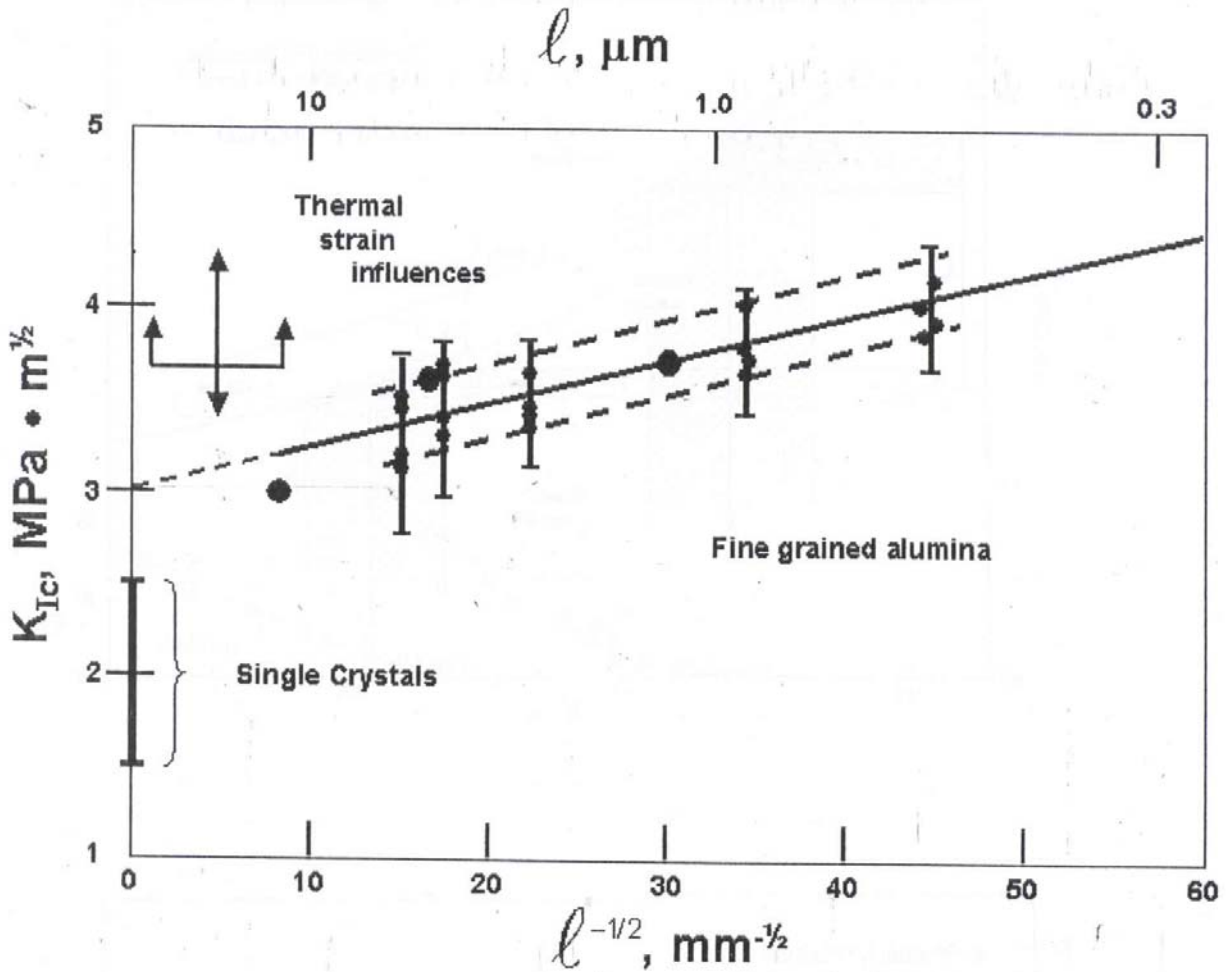
The shape of the dislocation distribution as it moves from right to left, at times



Positions s_i of individual dislocations during a constant strain-rate test ($t = 100$ sec)

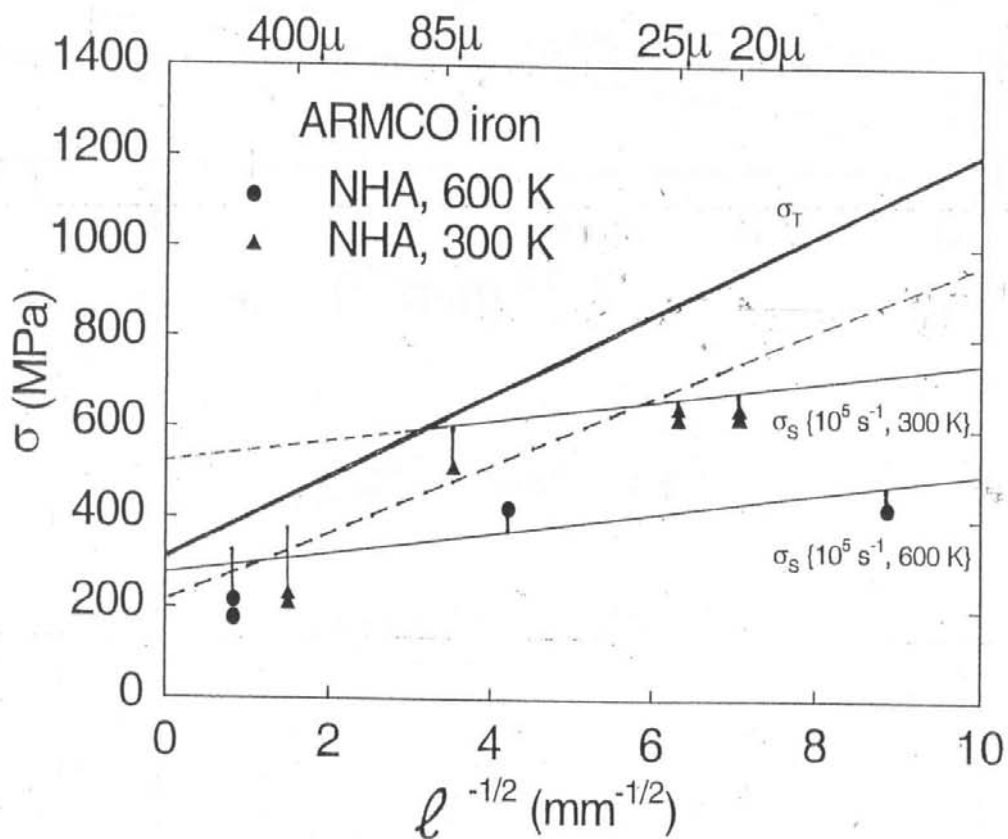
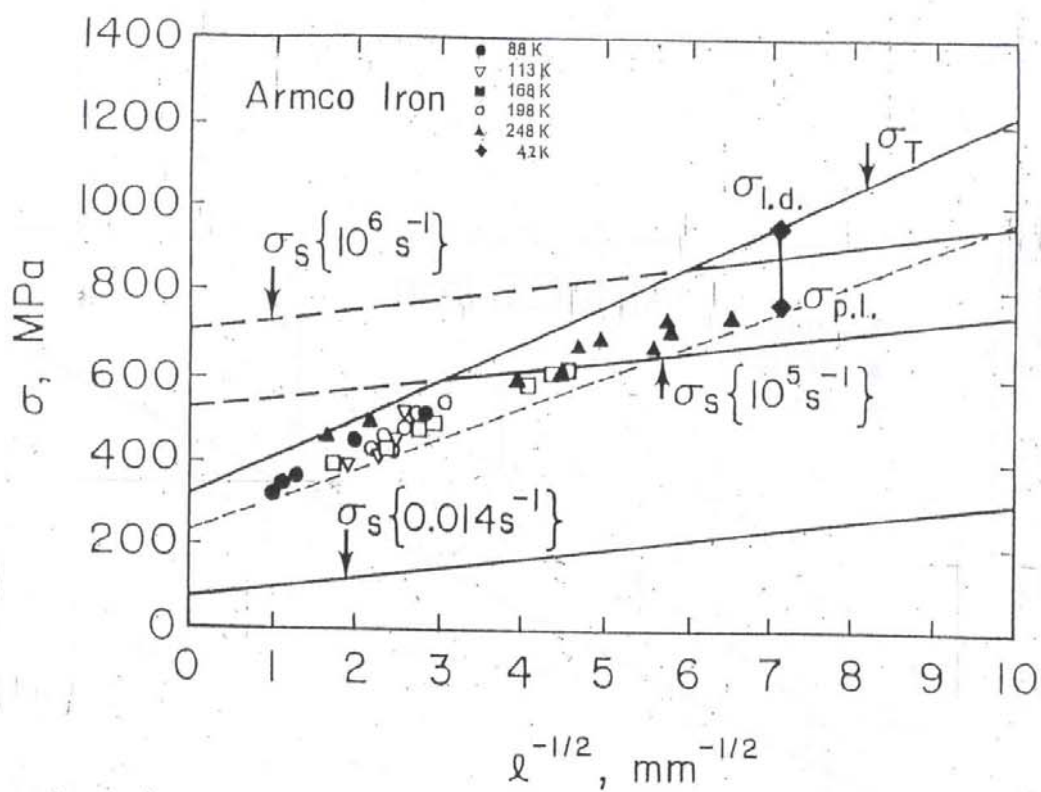


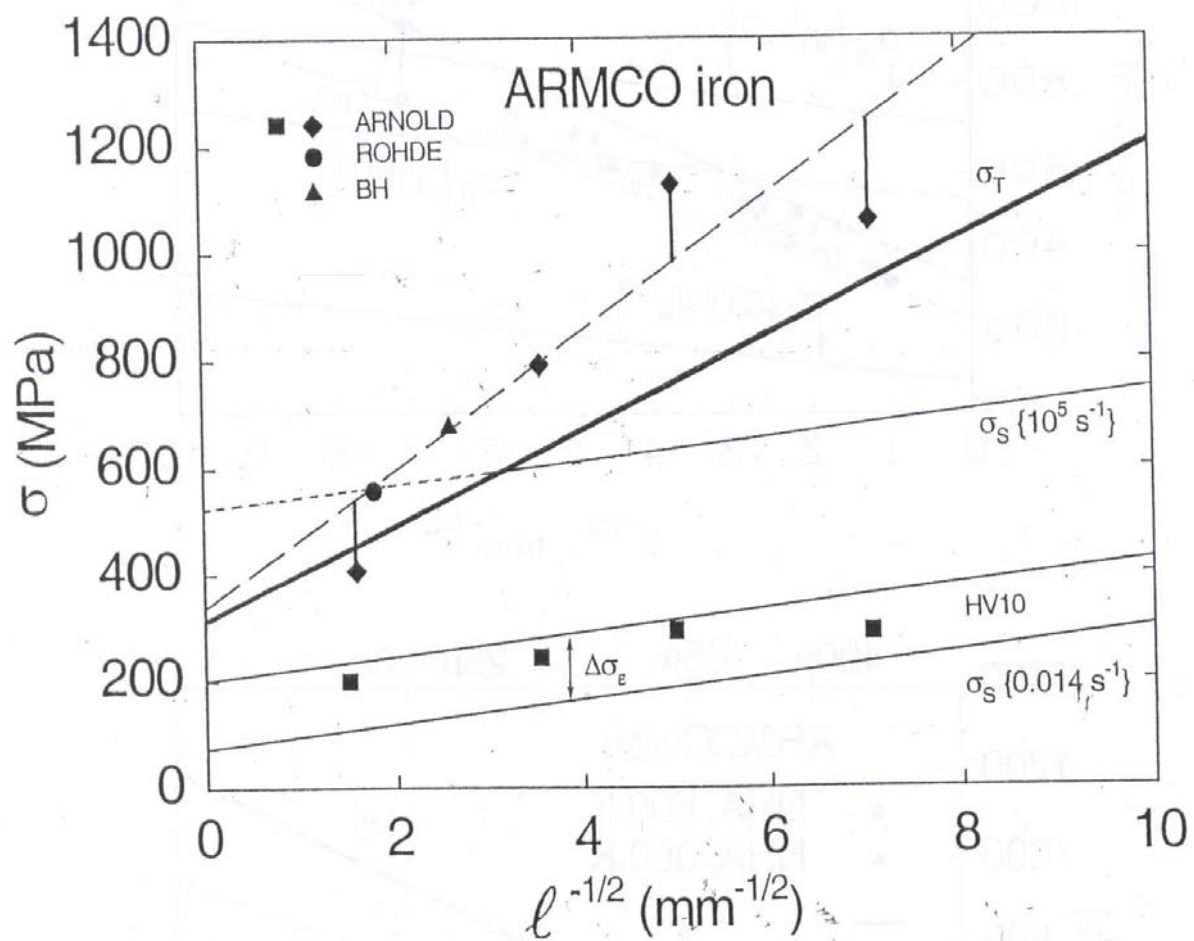




The fracture mechanics stress intensity at small grain sizes follows prediction of an H-P dependence:

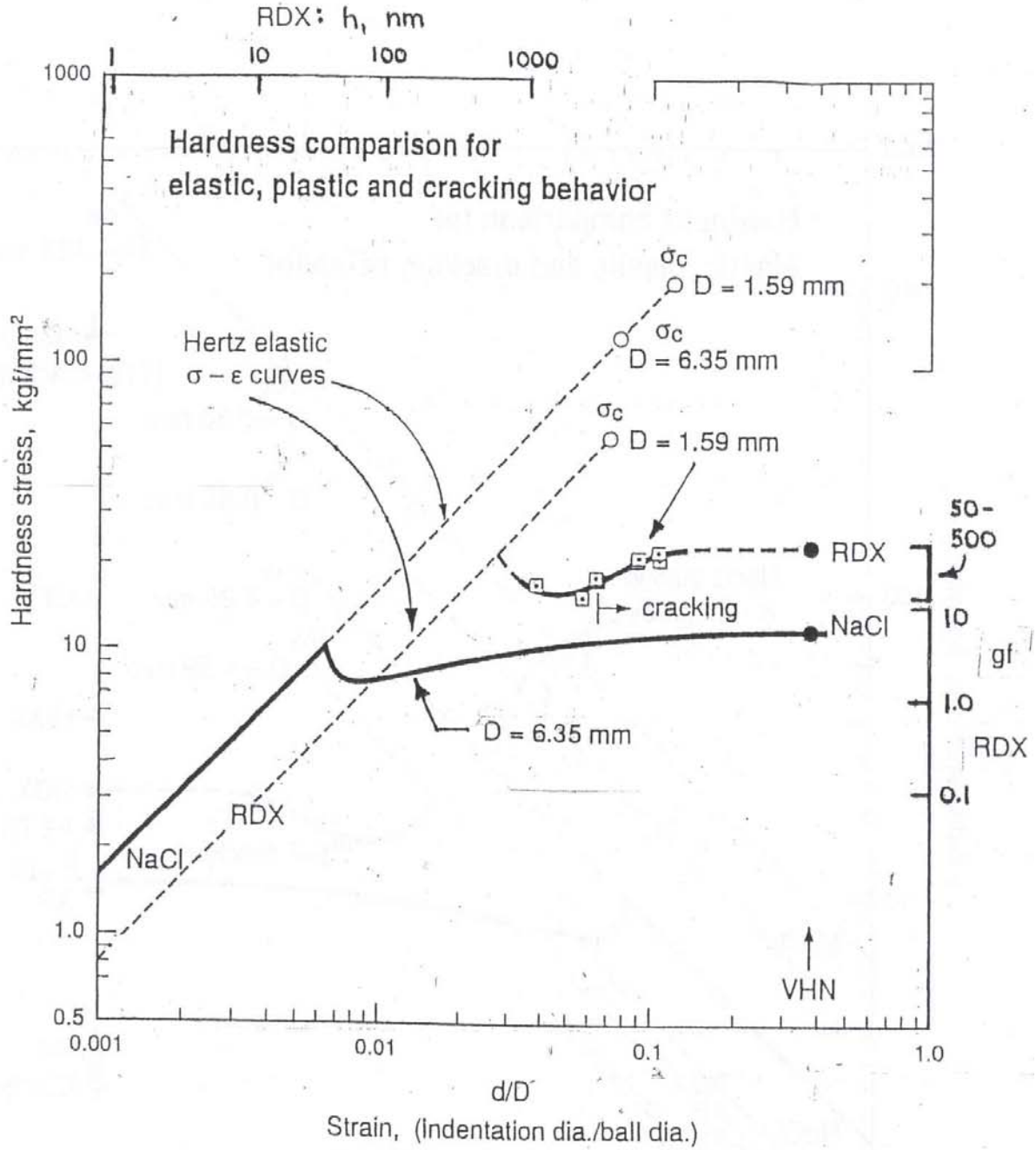
1. Lower single crystal stress intensity measurements occur because of orientation influence; and,
2. Thermal strain influences apparently reverse the grain size dependence at large grain sizes.





$$\sigma = \left\{ (1 - 2\nu) / (1 - \nu) \right\} \sigma_{HEL}$$

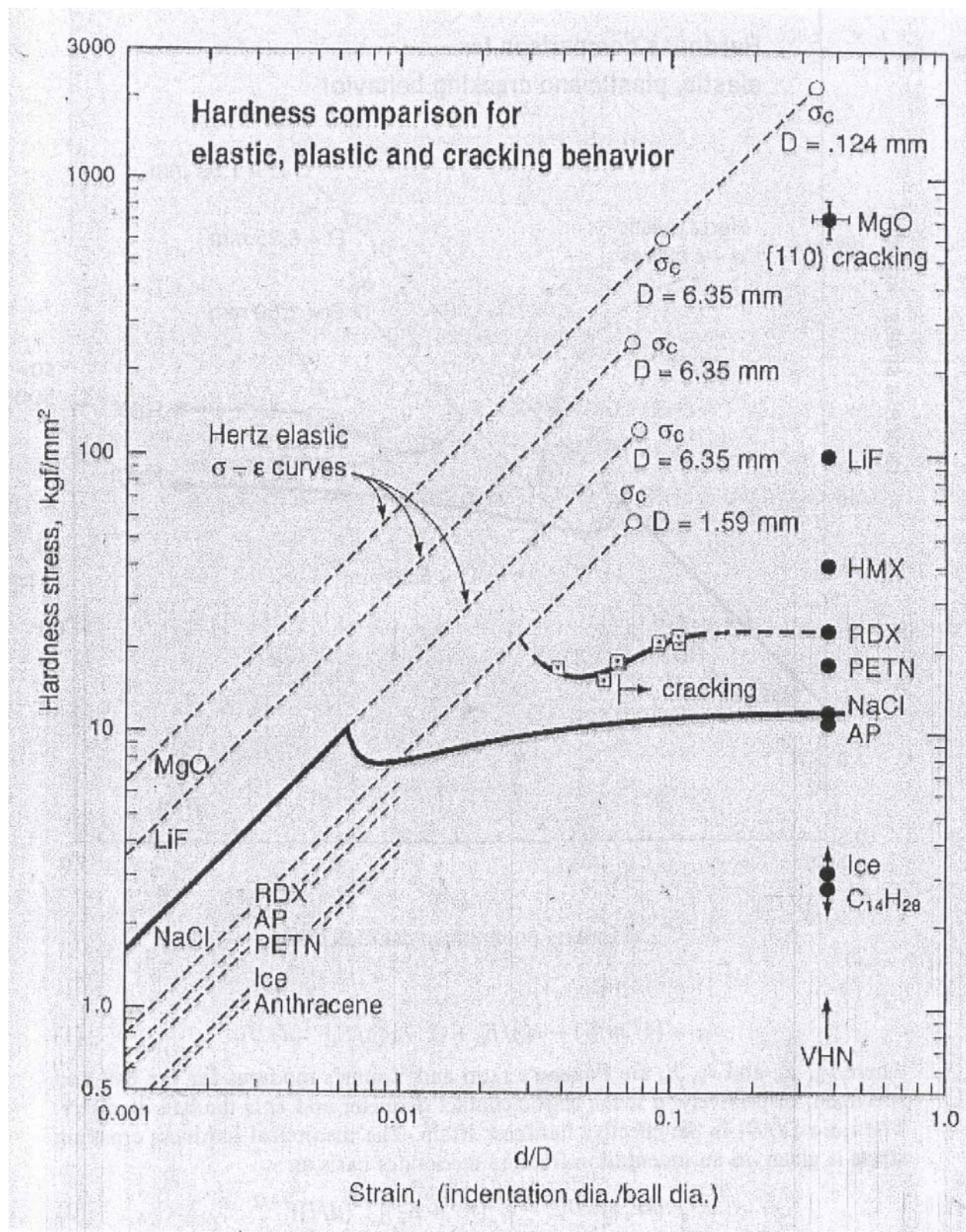
$$= E(V_0 - V) / V_0(1 + \nu)$$

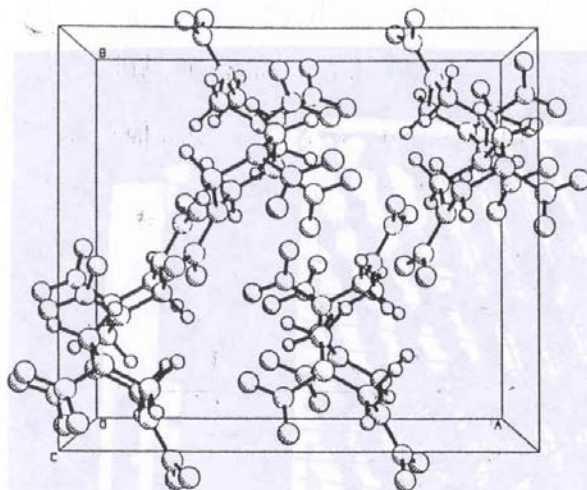


$$\sigma_H = (4/3\pi)[(1 - \nu_b^2)/E_b + (1 - \nu_s^2)/E_s]^{-1}(d/D), \quad (1)$$

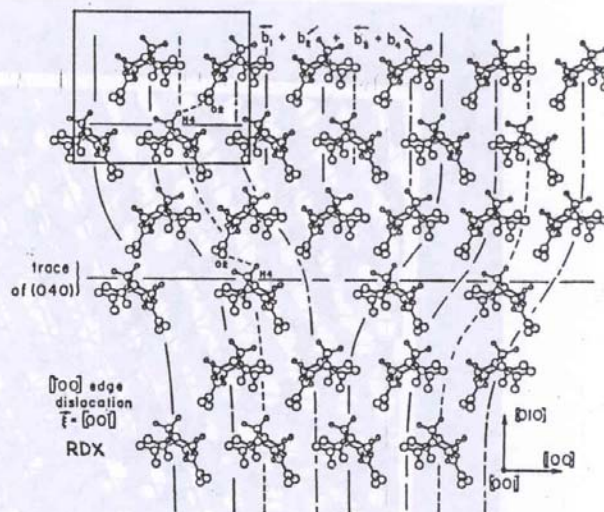
where ν_b , E_b and ν_s , E_s are Poisson's ratio and Young's modulus for the ball and specimen, respectively, d is the elastic contact diameter and D is the ball diameter. The ratio (d/D) is the effective hardness strain. The theoretical hardness cracking stress is given on an indentation fracture mechanics basis as:

$$\sigma_c \geq [4E_s\gamma/\pi D(1 - \nu_s^2)(K_1^2 + K_2^2)]^{1/2}(d/D)^{-1/2} \quad (2)$$

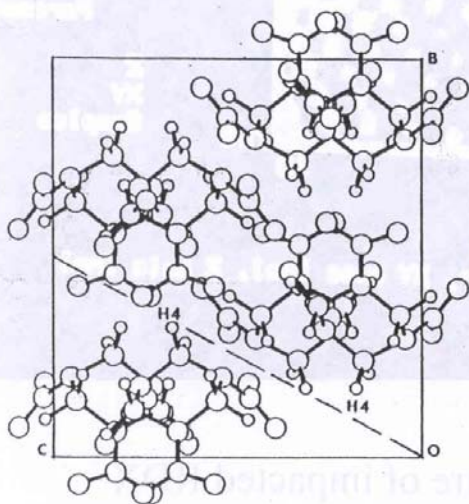




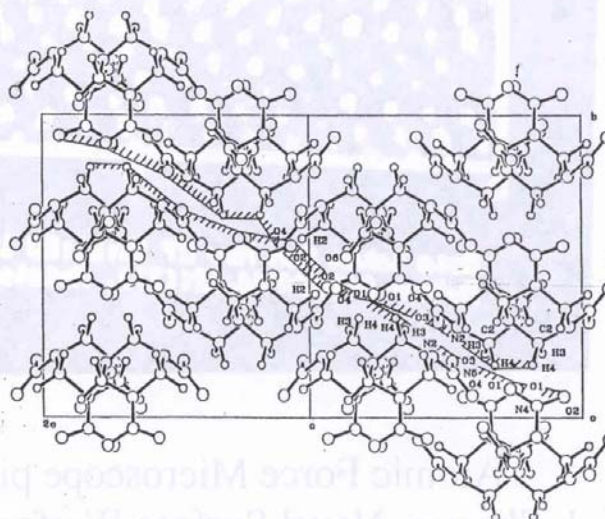
RDX ORTHORHOMBIC UNIT CELL



$[100] (040)$ EDGE DISLOCATION IN RDX



$\pm [012]$ SHEAR ON $(02\bar{1})$ SLIP PLANE



MOLECULE INTERACTIONS FOR $[100] (02\bar{1})$ SLIP

AMMON, ARMSTRONG, BODINE, ELBAN, HOFFSOMMER, & HUGHES

DISTRIBUTION LIST
AFRL-MN-EG-TR-2003-7111

*Defense Technical Info Center
8725 John J. Kingman Rd Ste 0944
Fort Belvoir VA 22060-6218

AFRL/MNME (6)
AFRL/MNOC-1 (STINFO Office)
AFRL/MN/CA-N